MEASUREMENTS OF ROCK CORE DISPERSIVITY AND TORTUOSITY FOR MULTI-PHASE SYSTEMS

Marco Zecca[a], Abdolvahab Honari[a], Sarah J. Vogt[a], Branko Bijeljic[b], Eric F. May[a] and Michael L. Johns[a]
[a] School of Mechanical and Chemical Engineering M050, University of Western Australia, 35 Stirling Highway, Crawley 6009, Western Australia, Australia.
[b] Department of Earth Science and Engineering, Imperial College London, Prince Consort Road, London SW7 2BP, United Kingdom.

This paper was prepared for presentation at the International Symposium of the Society of Core Analysts held in Snowmass, Colorado, USA, 21-26 August 2016

ABSTRACT
Known as CSEGR (Carbon Sequestration with Enhanced Gas Recovery), sequestered CO_2 can be used to re-pressurise partially depleted natural gas reservoirs to increase gas recovery, with the intention to also store the CO_2. Because natural gas and CO_2 are fully miscible, simulations require CO_2-natural gas dispersion at supercritical conditions to be accurately measured in order to quantify this mixing and hence establish the viability of CSEGR. We have designed and constructed a unique core flooding apparatus capable of accurately determining such supercritical gas dispersivity; this has been measured in two sandstones and two carbonates cores as a function of temperature, pressure and interstitial velocity. This is supplemented with Nuclear Magnetic Resonance (NMR) measurements of tortuosity to quantify the underpinning effective diffusion process. The resultant dispersivity data (K - Peclet number (Pe) plot) and tortuosity data are combined and presented in a format which is readily incorporated into CSEGR simulations.

INTRODUCTION
Even though enhanced oil recovery (EOR) via CO_2 flooding is a promising method to improve the recovery factor of oil reservoirs and geologically sequester CO_2, enhanced gas recovery (EGR) with CO_2 flooding/sequestration has not been widely considered by the oil and gas industry. The only current field-scale EGR project is the Rotliegend K12-B gas reservoir, located offshore of the Netherlands, which started in 2004 after 17 years of conventional gas production (Vandeweijer *et al.*, 2011). A Canadian depleted gas reservoir was also used for an EGR/CO_2 sequestration trial in 2002 but the operation was terminated after three years due to the early CO_2 breakthrough into the producing wells (Pooladi-Darvish et al., 2008).

EGR cannot only safely store CO_2 within the formation but also can improve the natural gas recovery by maintaining the reservoir pressure and enhancing sweep efficiency and production rates. However, natural gas and CO_2 are entirely miscible in all proportions and consequently the risks of extensive mixing of these fluids within the reservoir formation and early CO_2 breakthrough into production wells are the main hurdles for EGR implementation. These associated risks and uncertainties of EGR projects can be estimated by using reservoir simulations in which fluid flow in reservoir formations can be quantitatively modeled and, in principle, the mixing process between the injected CO_2 and natural gas captured. Doing so reliably, however, requires (1) adequate characterization of physical dispersion at all relevant length-scales, and (2) that numerical dispersion in such simulations be kept sufficiently small. Extensive studies of dispersion at the field scale have been published (Arya et al., 1988; Coats et al., 2009a; Lake, 1989) but generalizing the results of these studies is not straightforward. Physical dispersion at smaller length scales is also important because the description of transport at the core scale can play an important role in the prediction of mixing at the field scale.

In this work, a unique core flooding apparatus capable of accurately determining supercritical gas dispersivity has been designed and constructed. The measured dispersion coefficients (K_L) of CO_2 and CH_4 for two sandstone cores (Berea and Donnybrook) and two carbonate rock samples (Ketton and Estaillades) are presented over a range of pressure, temperature, and interstitial velocities. These highly reproducible data are used to obtain the characteristic mixing length-scale for the different rocks. These measurements were extended to also consider the effect of residual water on the dispersion process and were supplemented by an independent measurement of tortuosity using appropriate NMR methodology.

THEORY

Dispersion in floods of cylindrical core plugs with injection along the axis can be adequately described by the one-dimensional advective-dispersion (AD) equation:

$$\frac{\partial C}{\partial t} = K_L \frac{\partial^2 C}{\partial x^2} - u_m \frac{\partial C}{\partial x} \quad , \qquad (1)$$

where C is the concentration of the dispersing species, t is time, K_L is the longitudinal dispersion coefficient and u_m is the mean interstitial velocity in the direction of bulk flow, x, in the porous medium. We note the use of alternative models (continuous time random walks and multi-rate mass transfer models) to describe dispersion in more complex, heterogeneous porous media (e.g. Haggerty and Gorelick, 1995; Berkowitz et al., 2006). The ratio of the dispersion coefficient calculated from Eq. (1) to the diffusion coefficient, K_L/D, has been commonly plotted as a function of Peclet number. This is defined here as $\alpha u_m/D$ where α denotes the medium dispersivity. This differs from the classical definition in which grain/particle diameter replaces α as the characteristic length scale for mixing in the pores (Perkins and Johnston, 1963). Note that this latter definition is inappropriate for consolidated media such as the rock cores studied here.

Additionally, Eq.**(2)** has been frequently used to characterize the different dispersion behaviors evident in such correlated data:

$$\frac{K_L}{D} = \frac{1}{\tau} + \frac{\alpha u_m^n}{D}, \quad (2)$$

where τ is tortuosity, and n is an exponent. These three parameters characterize a given porous medium: generally $1 \leq n < 1.5$ (Brigham *et al.*, 1961; Gist et al., 1990; Legatski and Katz, 1967) and τ can range from $\sqrt{2}$ (for ideal packed beds only) to as much as 13 for certain consolidated media (Gist et al., 1990; Hurlimann et al., 1994). Generally for consolidated media these three parameters are treated empirically and must be determined from experiments with the rock; while τ can be determined via several methods, α and n can only be determined from core flooding experiments.

METHODOLOGY

Materials

The methane, carbon dioxide and nitrogen used in our experiments were supplied by BOC Scientific at purities greater than 0.999 mole fraction. Mixtures of CO_2 and CH_4 for pulse injection were prepared gravimetrically. Two types of 1.5 inch diameter sandstone cores, Berea and Donnybrook, and two carbonates, Estillades and Ketton were available. These cores were cleaned prior to use by Soxhlet extraction with a mole fraction mixture of 0.9 dicholormethane (Chem-Supply) + 0.1 methanol (Ajax-Finechem). The geometrical properties of the four cores used are listed in Table 1 with porosities, Φ, and permeabilities, k.

Core	Length (mm)	Diameter (mm)	$p_{confining}$ (MPa)	Φ	k (mD)
Berea sandstone	100.4	37.6	8	0.2043	463.3
			10	0.2039	460.7
			12	0.2036	458.2
Donnybrook sandstone	101	37.5	8	0.1576	12.07
			10	0.1573	12.01
			12	0.1572	11.95
Ketton carbonate	104.7	38.0	8	0.2277	2922.4
			10	0.2274	2912.2
			12	0.2270	2902.7
Estillades carbonate	105.6	37.9	8	0.2817	211.7
			10	0.0811	211
			12	0.2806	210.1

Table 1 Rock cores properties.

Apparatus and method

The specialized core flooding apparatus for $^{SC}CO_2$-CH_4 dispersion measurements was adapted from our previous experimental set-up for breakthrough measurements (Hughes *et al.*, 2012) to allow for pulse injection and to enable water delivery to, and drainage of, the rock core. A schematic of the apparatus is shown in Figure 1. A HPLC switching valve was included to allow for a controlled injection of a pulse of a 50% CH_4 and 50% CO_2 mixture. This composition was calculated as the best trade-off between minimizing density and viscosity contrasts between the fluids and maintaining an adequate signal to noise ratio. Analysis of the core effluent was conducted at measurement pressure using a HPIR cell and a syringe pump was used for effluent collection, ensuring better pressure regulation during the pulse displacement process. Details of the core holder, core wrapping, the core holder bath temperature control, pressure instrumentation and calibration of FT-IR spectrometer are included in our previous work (Hughes *et al.*, 2012). All experiments described below were conducted with the core in a vertical orientation.

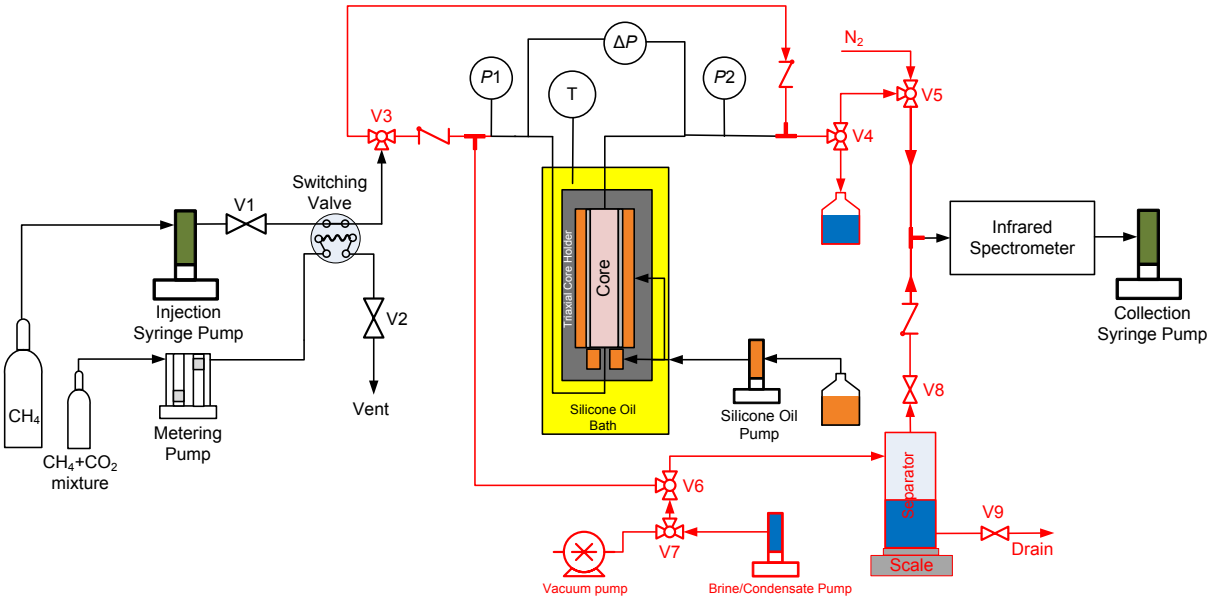

Figure 1 Simplified schematic of the core-flood apparatus for accurate dispersion measurements. The HPLC switching valve is shown in the sample loop filling position. To inject the pulse the valve is switched (rotated 180◦) so that the CH_4 flow flushes the sample out of the loop.

The flow from the injection pump was stopped when the dispersed pulse had passed completely through the IR cell. The experiments were conducted at core temperatures and pressures of 40 to 100 °C and 8 to 14 MPa, respectively, and with interstitial velocities between 0.004 and 1.908 $mm \cdot s^{-1}$.

Data analysis

For pulse experiments, the boundary conditions are:
$C(x > 0, t = 0) = 0$, $C(x = \infty, t) = 0$, $C(x = 0, 0 < t < \delta) = C_0$ and $C(x = 0, t > \delta) = 0$ where δ is the pulse duration. The solution to Eq. (1) with these boundary conditions (Levenspiel, 1999) is:

$$C = \frac{u_m}{\sqrt{4\pi K_L t}} \exp\left(-\frac{\left(L - u_m t\right)^2}{4K_L t} \right), \tag{3}$$

where L is the experimental length scale (core length). Eq.**(1)**, and its solution (Eq.**(3)**) are one–dimensional, as such they are unable to account for any velocity variations in the radial or cross-sectional direction.

However, Eq.**(3)** alone was not adequate for description of the effluent tracer concentration curves produced from the Ketton carbonate because of the non-Fickian/preasymptotic transport behavior associated with its heterogeneity in pore sizes. To describe this non-Fickian flow regime, several alternative models have been developed including the mobile-immobile model (MIM) (Deans (1963)), diffusion models, MRMT models (Haggerty and Gorelick, 1995) and CTRW models (Berkowitz *et al.*, 2006). In this case, it was found that the non-Fickian behavior of Ketton carbonate could be adequately modeled utilizing the MIM approach, which assumes the existence of two distinct regions in the rock, mobile and stagnant/immobile, and which describes the diffusional transport of species between these two zones using a first order mass transfer expression. This model was initially proposed by Deans (1963), who added two new parameters to Eq.**(1)**, namely the mass transfer coefficient and immobile volume fraction, but did not include the longitudinal dispersion coefficient. Coats and Smith (1964) modified Deans' version of Eq.**(1)** by adding this dispersion coefficient to produce (Coats and Smith, 1964; Van Genuchten and Wierenga, 1976)

$$\theta_m \frac{\partial C_m}{\partial t} + \theta_{im} \frac{\partial C_{im}}{\partial t} = \theta_m K_L \frac{\partial^2 C_m}{\partial x^2} - u_m \theta_m \frac{\partial C_m}{\partial x}, \tag{4}$$

$$\theta_{im} \frac{\partial C_{im}}{\partial t} = \beta\left(C_m - C_{im}\right) \tag{5}$$

where C_m and C_{im} are the concentrations of the dispersing solute species in the mobile and immobile regions, respectively; θ_m and θ_{im} are the mobile and stagnant fractions of the fluid in the porous media; β is a mass transfer coefficient; and u_m is the mean interstitial velocity in the mobile zone. To apply this solution to the measured effluent pulse profiles obtained for the Ketton core, the dispersion coefficient (K_L), the mobile fluid fraction (θ_m) and the mass transfer coefficient (β) were treated as the fitting parameters and the measured pulse breakthrough profiles were regressed to the analytical solutions of Eq. **(4)** and Eq.**(5)**.

The dispersion that occurs in the tubing leading to and from the core, and the inhomogeneous velocity profiles around the core entry and exit, both add to mixing and erroneously increase the apparent dispersion. As discussed in our previous work (Hughes *et al.*, 2012), to remove these effects measurements were conducted at the same conditions of T, P and flow rate with short and long Berea rock cores. The concentration profiles collected with the short core were used as inlet boundary conditions to a hypothetical undisturbed core of a length equal to the difference in length between our long and short core. Eq.**(1)** was solved numerically using a central finite difference method (the method of lines) implemented in Matlab within this hypothetical core and regressed to the experimental (long core) data in order to determine K_{corr}. In this manner this systematic error, between K_{long} extracted via Eq.**(3)** and the above methodology employing long and short core, was quantified. The modified setup produced a correction which was significantly dependent on velocity; a clear trend is shown in Figure 2. Consequently all K_{long} data measured for all the rock cores were corrected to account for these systematic errors as shown in Figure 2 to give the K_{corr} values listed in Table 2.

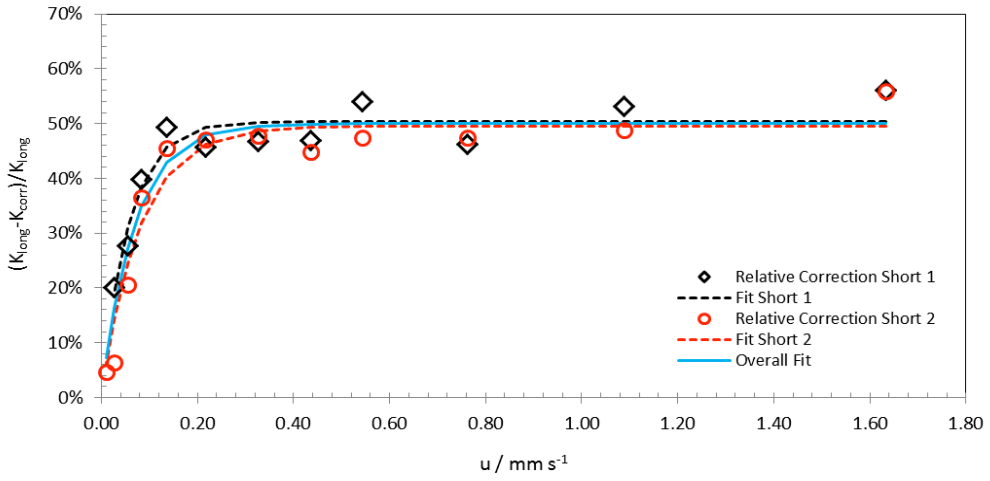

Figure 2 Relative size of dispersion coefficient correction as function of the interstitial velocity. The two data sets correspond to the two halves obtained from the cut of the original long core.

Independent measure of tortuosity

The diffusion coefficients D in Eq.**(2)**, which depend on pressure, temperature and composition, were obtained from the data of Takahashi and Iwasaki (1970). An error in the calculation of D would cause an offset in the value of (K_L/D) determined from the dispersion measurements, which would be most pronounced in the limit $u_m \rightarrow 0$. To confirm that no such offset was present, we measured the core's tortuosity, τ, using a second, completely independent technique. The Berea and Donnybrook rock core samples were evacuated and then saturated with distilled water at a pressure of 10 MPa and left for several hours to ensure complete saturation. These saturated cores were then placed in a 12.9 MHz nuclear magnetic resonance (NMR) rock core analyzer (Oxford Instruments) to

enable self-diffusion measurements via the application of pulsed field gradient stimulated-echo (PGSTE) techniques (Stejskal and Tanner, 1965). Measurement of the water's self-diffusion coefficient for a free liquid sample (D_0) and for the water in the saturated rock core (D), enables calculation of the system tortuosity ($\tau = D_0/D$) if a sufficiently long observation time is allowed to ensure the diffusion within the core is completely restricted. The same experiments were also run with methane at 3MPa providing a tortuosity consistent with the value obtained from water. In future, tortuosity will be measured as a function of the residual water content; D_2O will be adopted to avoid NMR signal from this wetting phase.

RESULTS AND DISCUSSION

'Dry' Sandstones and Carbonates

Table 2 summarizes all our experimental conditions (T, P and u_m), and a selection of dispersion coefficients (K_{corr}) for all the cores considered. The values of K_{corr} have been corrected for entry/exit and tubing effects as outlined above.

Core	T (°C)	P (MPa)	u (mm s^{-1})	D (10^{-8} m^2 s^{-1})	K_{corr} (10^{-8} m^2 s^{-1})
Berea	40	8	0.025	16.4	6.63
	40	8	0.499	16.4	22.12
	40	10	0.006	12.5	3.98
	40	10	0.140	12.5	9.58
	40	12	0.010	10.0	4.00
	40	12	0.199	10.0	10.37
	60	8	0.452	19.6	20.24
	60	10	0.012	15.2	5.39
	60	10	0.304	15.2	13.63
	60	12	0.004	12.3	3.21
	60	12	0.035	12.3	5.36
	80	8	0.034	23.1	8.00
	80	8	0.216	23.1	13.27
	80	10	0.016	18.0	6.18
	80	10	0.085	18.0	8.47
	80	12	0.120	14.7	8.45
	80	12	0.482	14.7	18.67
	100	8	0.085	26.6	10.17
	100	10	0.085	21.0	8.45
	100	10	0.142	21.0	9.64
	100	12	0.085	17.2	7.81
	100	12	0.207	17.2	10.18
Donnybrook	40	8	0.025	16.4	7.21
	40	8	0.140	16.4	18.22
	40	12	0.050	10.0	6.69
	40	12	0.141	10.0	18.66

	60	10	0.007	15.2	5.17
	60	10	0.304	15.2	39.95
	60	12	0.008	12.3	2.72
	60	12	0.035	12.3	5.36
Estillades	40	8	0.09	16.4	10.38
	40	10	0.004	12.5	3.79
	40	10	0.04	12.5	5.76
	40	12	1.151	10	140.03
	60	10	0.23	15.2	21.59
	60	10	1.149	15.2	133.65
	60	12	0.016	12.3	4.39
	60	12	1.646	12.3	214.59
Ketton	40	8	0.053	16.4	17.08
	40	10	0.011	12.5	8.49
	40	10	0.141	12.5	27.06
	40	10	1.124	12.5	212.49
	40	12	1.743	10	381.7
	40	14	1.908	8.1	424.03
	60	10	0.015	15.2	10.03
	60	10	0.745	15.2	115.94

Table 2 Dispersion coefficients of equimolar mixtures of CO_2–CH_4 into pure CH_4 or pure CO_2 for Berea, Donnybrook, Estillades and Ketton cores.

Application of Eq.**(2)** allowed the dispersivity (α) to be determined for the two sandstone cores. For the Berea and Donnybrook rocks, $\alpha = 0.35$ mm and 1.31 mm, respectively, with a relative statistical uncertainty in these parameters from the regression of less than 5%. These values are consistent with those reported for sandstones by Coats *et al.* (2009b), although in the case of the Berea sandstone, the dispersivity measured here is moderately lower than other values reported in the literature (1.2 mm (Gist et al. (1990)); 3.75 mm (Brigham et al. (1961)); 2.2 mm (Legatski and Katz (1967)); 1-6 mm (Schulze-Makuch (2005))). However, as demonstrated by the discussions above, the value of the apparent dispersivity obtained can readily be affected by systematic measurement errors, compounded by the effects on α due to variation in sample length employed and, of course, variability in the actual samples used.

In Figure 3 the pulse breakthrough profiles of Estillades and Ketton carbonates show the reproducibility of the data and the better fitting obtained for Ketton with the MIM model in comparison to the AD equation.

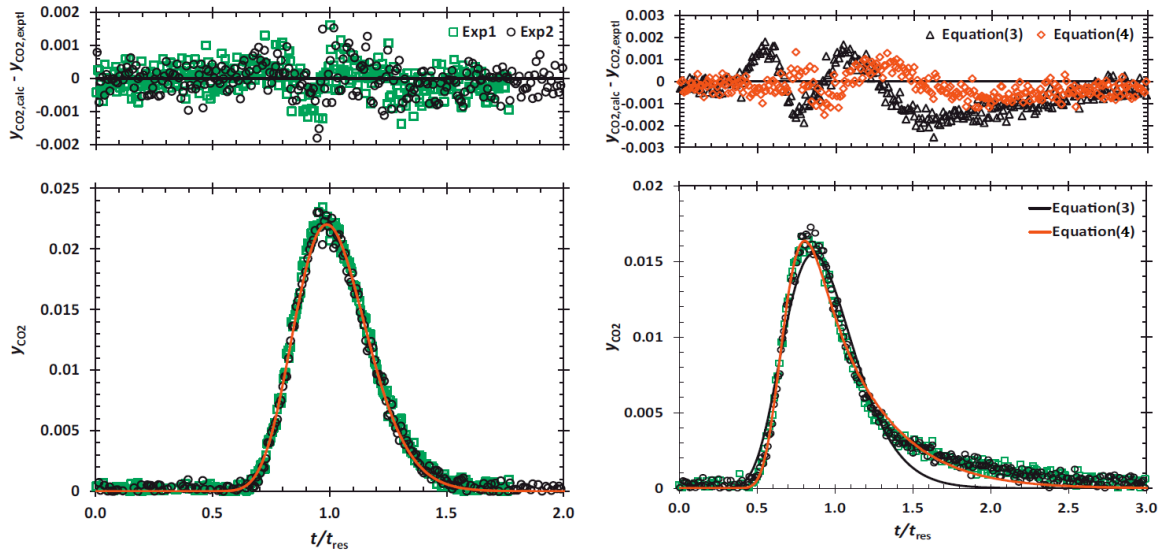

Figure 3 Left: repeatability of the pulse-breakthrough profiles for Estaillades carbonate core at 60°C, 10 MPa and 0.14 mm s^{-1}. Right: Ketton carbonate core at 60°C, 10 MPa and 0.28 mm s^{-1}. The lower panel demonstrates the breakthrough profiles and the fits achieved using Eq. (3) for Estaillades and both Eqs. (3) and (4) for Ketton. The upper panel shows the resulting residuals of the fits.

Our previous results showed the 1D-AD equation was adequate for the description of dispersion of CO_2-CH_4 system through sandstone cores. Larger dispersion coefficients at similar conditions for Donnybrook sandstone were reported, indicating a higher level of heterogeneity relative to the homogenous Berea sandstone. Because carbonate rocks are known as heterogeneous porous media, long tailing and early breakthrough profiles of the CO_2 together with comparatively higher dispersion coefficients were expected. After comparing several measured dispersion coefficients of the sandstones and carbonates at similar conditions, the dispersion coefficients for both carbonate samples were found to be larger than those for the homogeneous sandstone rock (Berea) whereas Estaillades showed similar dispersive behaviour to the more heterogeneous (Donnybrook) sandstone. Ketton exhibited the greatest dispersion among all the core samples used during this study. The pulse breakthrough profiles we observed for Ketton carbonate showed a more persistent long tail and an earlier breakthrough than for Estaillades carbonate.

The calculated dispersivities were then used to produce Figure 4 where the ratios of dispersion and diffusion coefficients, K_{corr}/D, were plotted against Pe_m. Also shown are two curves utilizing Eq.**(2)** where n was 1 for $Pe_m<1$ and 1.2 and 1.4 (power-law scaling) for $Pe_m>1$ (Bijeljic and Blunt, 2006; Bijeljic *et al.*, 2011). Figure 4 explicitly shows that the curves produced using Eq.**(2)** with n = 1.2 for sandstones and n = 1.4 for carbonates are an excellent fit with the Donnybrook and Ketton data respectively for $Pe_m>10$. This provides experimental validation for the power law exponents derived from transport simulations (e.g. Bijeljic and Blunt (2006) and Bijeljic et al. (2011)). Finally, the $Pe_m<100$ considered in the study is lower compared to other standard curves reported in literature

(e.g. Seymour and Callaghan (1997)) since this the IR spectrometer could not detect the breakthrough pulse for higher velocities due to the limited time resolutions of the instrument.

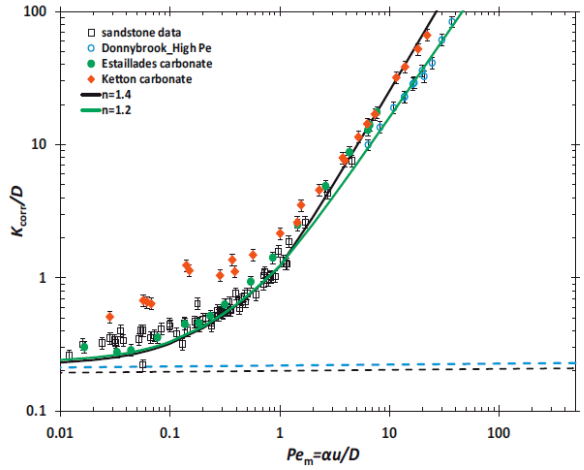

Figure 4 Measured K_{corr}/D vs. Pe_m for Berea and Donnybrook sandstone and Ketton and Estaillades carbonate cores. The dashed lines indicate the independent NMR measurements of sandstone rocks tortuosity. The fitted curves are produced by Eq. (2) for n equal to 1.2 and 1.4.

Inclusion of Residual Water

Figure 5 shows the impact of connate or residual water on the breakthrough profiles for Donnybrook. The presence of this second phase clearly increases the dispersion significantly, the corresponding dispersion coefficients are 5.7×10^{-7} and 39.0×10^{-7} $m^2\cdot s^{-1}$ respectively. Future work will quantitatively measure the dependence of medium properties such as dispersivity on the residual water content.

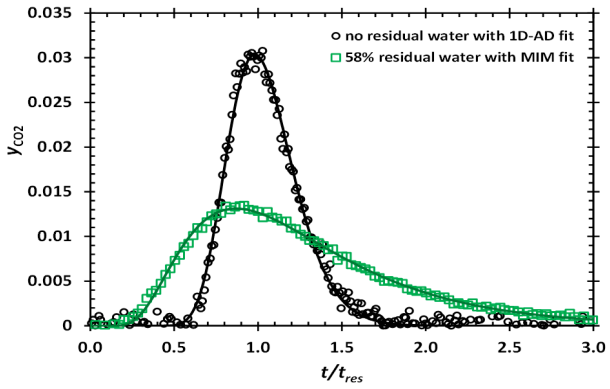

Figure 5 Pulse breakthrough profiles obtained for Donnybrook dry and 58% saturated with water. The measurements were made at 40 °C, 10 MPa and with an interstitial velocities 0.34 $mm\cdot s^{-1}$.

Measurement of Tortuosity

The NMR measurements of tortuosity (τ), using water with diffusion times between 10ms and 1s, were 4.3 and 4.8 for Berea and Donnybrook sandstone cores, respectively. In literature, lower values of tortuosities have been reported from electrical measurements (Zhan et al. (2011)). The tortuosity value for the Berea rock core was also calculated by measuring the self-diffusion coefficient of methane at 3MPa; the tortuosity value in this case was 4.5 which is broadly in agreement with the water measurement. In Figure 6 we show the raw signal attenuation NMR data – the slope of these data provides the diffusion coefficient according to the Stejskal-Tanner equation (Stejskal and Tanner, 1965) and the ratio of the free to restricted diffusion coefficient provides the tortuosity, τ. The diffusion time for these measurements was 100 ms, ensuring the diffusion to be fully restricted ((Hurlimann (1994). In future we will measure τ as a function of water content.

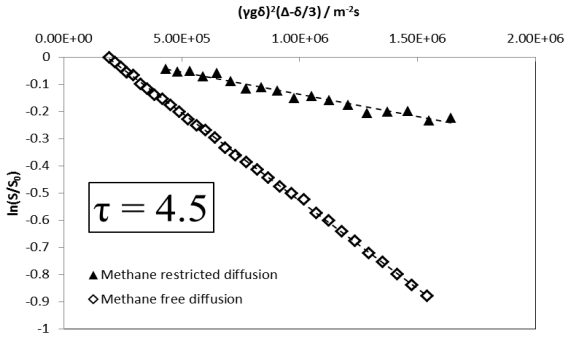

Figure 6 NMR diffusion measurements of free and restricted methane at 3MPa.

CONCLUSIONS

A pulsed measurement apparatus was established for the measurement of the dispersion coefficient (K) for $^{SC}CO_2$ and CH_4 and successfully applied to two sandstones and two carbonates samples. The methodology was adapted to minimize the effects of density and concentration contrasts; the reproducibility obtained were excellent. By using 1D- ADE approach for sandstones and Estillades carbonate and a mobile-immobile model to analyse the breakthrough profiles observed for the Ketton carbonate, asymptotic dispersion coefficients were obtained and compared. All acquired data collapsed onto a common curve when K/D was plotted as a function of Pe_m, capturing variation with temperature and pressure. Preliminary results showed the impact of residual water on the dispersion mechanism and independent measurements of tortuosity with water and methane also produced consistent results.

ACKNOWLEDGEMENTS

This work was supported by the Western Australian Department of Environment and Conservation through the Low Emissions Energy Development fund.

REFERENCES

Arya, A., Hewett, T. A., Larson, R. G., Lake, L. W., 1988. Dispersion and reservoir heterogeneity SPE Reservoir Engineering 3, 139-148.

Berkowitz, B., Cortis, A., Dentz, M., Scher, H., 2006. Modeling non-fickian transport in geological formations as a continuous time random walk, Reviews of Geophysics 44, 1-49.

Bijeljic, B., Blunt, M. J., 2006. Pore-scale modeling and continuous time random walk analysis of dispersion in porous media, Water Resources Research 42, W01202.

Bijeljic, B., Mostaghimi, P., Blunt, M. J., 2011. Signature of non-Fickian solute transport in complex heterogeneous porous media, Physical Review Letters 107, 204502.

Brigham, W. E., Reed, P. W., Dew, J. N., 1961. Experiments on mixing during miscible displacement in porous media, SPE Journal 1, 1-8.

Coats, K. H., Smith, B. D., 1964. Dead-end pore volume and dispersion in porous media, SPE Journal 4, 73-84.

Coats, K. H., Whitson, C. H., Thomas, L. K., 2009a. Modeling Conformance as Dispersion, SPE Reservoir Evaluation & Engineering 12, 33-47.

Coats, K. H., Whitson, C. H., Thomas, L. K., 2009b. Modeling conformance as dispersion, SPE Reservoir Evaluation & Engineering 12, 33-47.

Deans, H. A., 1963. A mathematical model for dispersion in the direction of flow in porous media Society of Petroleum Engineers Journal 3, 49-52.

Gist, G. A., Thompson, A. H., Katz, A. J., Higgins, R. L., 1990. Hydrodynamic dispersion and pore geometry in consolidated rock, Physics of Fluids A 2, 1533-1544.

Haggerty, R., Gorelick, S. M., 1995. Multiple-rate mass transfer for modeling diffusion and surface reactions in media with pore-scale heterogeneity, Water Resources Research 31, 2383-2400.

Hughes, T. J., Honari, A., Graham, B. F., Chauhan, A. S., Johns, M. L., May, E. F., 2012. CO_2 sequestration for enhanced gas recovery: new measurements of supercritical CO_2-CH_4 dispersion in porous media and a review of recent research, International Journal of Greenhouse Gas Control 9, 457-468.

Hurlimann, M. D., Helmer, K. G., Latour, L. L., Sotak, C. H., 1994. Restricted diffusion in sedimentary rocks. determination of surface-area-to-volume ratio and surface relaxivity, Journal of Magnetic Resounance, Series A 111, 169-178.

Lake, L. W., 1989. Enhanced oil recovery Prentice Hall 550, New Jersey, USA.

Legatski, M. W., Katz, D. L., 1967. Dispersion coefficients for gases flowing in consolidated porous media, SPE Journal 7, 43-53.

Levenspiel, O., 1999. Chemical reaction engineering 3rd ed. John Wiley & Sons.

Perkins, T. K., Johnston, O. C., 1963. A review of diffusion and dispersion in porous media, SPE Journal 3, 70-84.

Pooladi-Darvish, M., Hong, H., Theys, S., Stocker, R., Bachu, S., Dashtgard, S., 2008. CO_2 injection for enhanced gas recovery and geological storage of CO_2 in the long Coulee Glauconite F pool, Alberta. In SPE (Ed.), SPE Annual Technical Conference and Exhibition, Denver, Colorado.

Schulze-Makuch, D., 2005. Longitudinal dispersivity data and implications for scaling behavior, Ground Water 43, 443-456.

Seymour, J. D., Callaghan, P. T., 1997. Generalized Approach to NMR Analysis of Flow and Dispersion in Porous Media, AIChE Journal 43, 2096-2111.

Stejskal, E. O., Tanner, J. E., 1965. Spin diffusion measurements: spin echoes in the presence of a time dependent field gradient The Journal of Chemical Physics 42, 288-292.

Takahashi, S., Iwasaki, H., 1970. The diffusion of gases at high pressures. III. The diffusion of $^{14}CO_2$, in the $^{12}CO_2$-CH_4 system, Bulletin of the Chemical Research Institute of Non-Aqueous Solutions, Tohoku University 20, 27-36.

Van Genuchten, M. T., Wierenga, P. J., 1976. Mass transfer studies in sorbing porous media I. analytical solutions, Soil Science Society of America Journal 40, 473-480.

Vandeweijer, V., van der Meer, L. G. H., Hofstee, C., Mulders, F., Graven, H., D'Hoore, D., 2011. Monitoring CO_2 Injection at K12-B http://www.co2geonet.com/UserFiles/file/Open%20Forum%202011/PDF-presentations/2-10_Vanderweijer.pdf.

Zhan, X., Zhu, Z., ToksoZ, M. N., 2011. Quantitative DC and high frequency AC seismoelectric measurement on Berea sandstone, SEG Technical Program Expanded Abstracts 30, 2246-2250.

FLUID-FLOW DURING EOR EXPERIMENTS IN CHALK: INSIGHTS USING SEM-MLA, EMPA AND NANOSIMS APPLICATIONS

Mona W. Minde [1,2,3], Udo Zimmermann[1,3], Merete V. Madland[1,3], Reidar Inge Korsnes[1,3], Bernhard Schulz[4], Jean-Nicolas Audinot[5]
(1) University of Stavanger, Norway, (2) IRIS AS, Stavanger, Norway, (3) The National IOR Centre of Norway, (4) TU Bergakademie Freiberg, Germany, (5) LIST, Luxembourg

This paper was prepared for presentation at the International Symposium of the Society of Core Analysts held in Snow Mass, Colorado, USA, 21-26 August 2016

ABSTRACT

Water injection has been applied with great success on the Norwegian continental shelf (NCS) and has in addition to maintaining pore-pressure a significant EOR effect. Understanding rock-fluid interactions during flooding experiments with synthetic seawater under reservoir conditions comparable to the NCS, are of importance in order to decide on the best-suited water-composition and to predict and control compaction-effects. For this objective fractured chalk samples are analysed with Scanning Electron Microscope Mineral Liberation Analyzer (SEM-MLA), Electron MicroProbe Analyses (EMPA) and nano Secondary Ion Mass Spectrometry (nano-SIMS) techniques to observe chemical and mineralogical changes on smallest scale. The results point to a significant influence of rock texture on fluid flow mechanisms and propagation through the sample. Micro- and nano-sized silicates and minute grains of magnesium-rich carbonates most likely grow on larger micron-sized calcite crystals and/or precipitate in pore-spaces. The new grown inner-fracture minerals show higher magnesium-concentrations than those of the surrounding matrix and minute Si-rich minerals have been detected. Remarkable is the observation that shell fragments from macrofossils, orientated perpendicular to the fluid flow, influence the rock-fluid interactions. Moreover, shell fragments of macrofossils resist fluid flow and its effects on mineralogy stronger than micro- and nanofossils and their fragments. This study shows that fluid flow and flooding movements are, even in seemingly homogeneous rocks like chalk, strongly dependent on the texture, which reflects in this case the environmental conditions during deposition of the carbonate or later induced fractures. This has, in turn, a significant effect on the distribution of mineral alteration caused by flooding at micron- and nanoscale. The formation of secondary minerals has a significant effect on the surface properties of the rock, such as surface charge, specific surface area, thus wettability, permeability and porosity, which are control factors for the recovery of hydrocarbons.

INTRODUCTION

Flooding by non-equilibrium brines is an efficient EOR-method in chalk-reservoirs. The composition and temperature of the brine seem to have an effect on oil recovery through chemical and mineralogical alterations as well as changes in mineral surface complexes,

thus surface-charge and -potential of the rock [1-4]. The primary composition of the rock controls these interactions and studies have suggested that especially the silica-content in carbonate rocks, may play an important role [5]. Chemical and textural alterations have shown to affect the mechanical strength of the rock and the compaction of chalk, thus the recovery of oil [2, 6-8]. A large variety of experiments carried out on flooded chalk cores has led to a large dataset and reveals an extraordinary complexity of reactions even though the mineralogy of the rock itself seems rather simple. Understanding the mechanisms behind the water induced compaction, often called water weakening of chalk, and its EOR effects is a multi-scale work, ranging from nano- to field-scale. To understand these alterations at larger scale, one must also understand them at smaller scale and as such pore-scale studies are carried out (e.g. [2] and [9]) When flooding samples with synthetic seawater (SSW), anhydrite or gypsum have been found to precipitate together with magnesium-bearing carbonates and silicates. This is linked to dissolution of calcite [2]. The chalk core, which has been the subject of this experiment, is from the Late Campanian to Early Maastrichtian Gulpen Formation [10], sampled from an outcrop near Liège (Belgium). The chalk from this outcrop has a very clean nature, with a non-carbonate content mostly below 5 weight% (wt%). Diagenesis did not affect the rock significantly as such the preservation of mircofossils and pore-space is fairly good. Calcite cementation is absent, however contact cement is commonly found [11]. Most of the oil in chalk reservoirs is trapped in the matrix. In fractured carbonate reservoirs, displacement of oil is mostly related to spontaneous imbibition of water into the matrix [4]. Hence, it is important to understand how fractures in the reservoir behave during flooding to maximize the effect of the injected water, improving the sweep.

EXPERIMENTAL SET-UP AND METHODOLOGY

For this experiment, the chalk-core was fractured in two directions (Figure 1). One perpendicular to the flow, cut by a saw, and one along the core-axis, induced by uniaxial stress in a so-called Brazilian test cell. Parts of the latter fracture is the focus of this paper. The experiment was performed in a tri-axial cell at 130°C, pore pressure of 0.7 MPa and two injection brines, NaCl and Synthetic seawater (SSW). After an initial loading phase beyond the yield stress, a creep phase at 11.4 MPa followed with NaCl injection for 5.7 days, before SSW was flooded through the core at the rate of one pore-volume a day (PV/D) for 34 days. After this phase, the core clogged and was bypassed with SSW for another 24 days and was subsequently cleaned by distilled water. Before flooding, porosity was measured to 40.1 % and permeability to 5 mD. More detailed description of the experimental set up can be found in [2].

The here presented data is based on the following analytical methods; field emission gun Scanning Electron Microscope (SEM) with Energy-Dispersive X-ray Spectroscopy (EDS), Mineral Liberation Analysis software (MLA; FEI Quanta 650 FEG with EDAX-EDS and Quantix Esprit 1.8 software; 25 kV acceleration voltage 12 mm working distance at TU Freiberg/Saxony), Electron MicroProbe Analyses (EMPA; JEOL JXA-8900RL; 15 kV acceleration voltage, 20 nA current and 2 µm beam; TU Freiberg/Saxony) and nano Secondary Ion Mass Spectrometry (NanoSIMS 50; 16 kV

impact energy, 2 pA current and 150 nm probe size; LIST). Detailed methodologies are described in [9]. In fine-grained chalk, it is difficult to resolve the composition of all minute grains by MLA, and areas with different content of magnesium (Mg), were classified into two so-called "mixed spectra", in addition to minerals such as calcite, magnesite, quartz, clay minerals, and feldspars. The names of the mixed spectra are denoted "Low Mg calcite" (Mg wt% <1%) and "High Mg calcite" (Mg wt% >1%). The spatial resolution is between 1 and 2 μm per pixel.

RESULTS

MLA-images show that inside fractures there is in general a higher concentration of magnesium (Mg), silicon (Si) and aluminium (Al). Shells of micro- and macrofossils stand out as to have very low Mg content, even contain pure calcite, while the matrix of the rock has a mixture of high and low Mg concentrations. Figure 2 shows the fracture running from the bottom to the top of the figure with fluid-flow direction along the fracture. A shell from a macrofossil is embedded perpendicular to the fracture. This texture provokes a significant difference in Mg content between the concave side of the shell, with higher Mg concentrations, and the area of the convex side of the obstruction. This trend is confirmed by EMPA data along the profile A-A' in Figure 2, showing higher values for MgO, SiO_2 and Al_2O_3 on the concave side of the shell (Figure 3). Analyses by nanoSIMS show that another fragment of a shell embedded in the matrix, also exhibit different behavior than the surrounding particles (Figure 4). It does not seem altered by flooding of SSW and the shell shows a clear depletion of Si and Mg while, compared to the matrix, it seems to have kept its original calcitic composition. With the methods used, no precise evidence of calcite dissolution is identified in the core, but as at least part of the newly precipitated material is assumed to be Mg-bearing carbonate, dissolution of calcite is a pre-requisite for having CO_3^{2-} available in the fluid. In addition, dissolution is confirmed by presence of calcium (Ca^{2+}) in the produced water from the experiment (not shown in this paper).

DISCUSSION

In the fracture, enrichments of Mg, Si and Al could be observed, measured as either oxides, elements or isotope clusters. This is compatible with the results from studies identifying precipitated clay-minerals and/or Mg-rich carbonates in fractured areas [12]. Even though the resolution of MLA measurements does not enable identification of the mineralogy of single grains in every case, the increase in concentrations of Mg, Al and Si corresponds to an increase in silicates and alumo-silicates, most probably clay precipitates, in addition to Mg-rich carbonates including minute particles of magnesite. A general increase in Mg content in the sample after flooding agrees with the information from studies using effluent profiles in chalk-flooding experiments which show retention of Mg^{2+} and production of Ca^{2+} [9, 12]. Remarkable is how the concentration of Mg, Si and Al varies between the concave and the convex side of the shell-fragment perpendicular to fluid flow and how the shells in Figures 3 and 4 resist to the effect of the fluid. The flow is clearly obstructed by the shell-fragments (Figure 2 and Figure 4) and

cannot infiltrate the shell during the here used flooding time. Although most of the surrounding matrix seems affected by the flooding of SSW, the shells and microfossils seem inert to the flooding agent and show to much less degree, if any, mineralogical changes. There may be several reasons for this differentiation: 1) The size of the carbonaceous particle matters for the chemical stability of the grain. Smaller particles may be more prone to alteration and mineralogical changes than larger ones. 2) The initial composition of the fossils differs from the finer-grained matrix, such as Mg/Ca ratio depending on e.g. age, seawater composition and temperature at formation. 3) Curvature and surface properties affect the dissolution rates of the initial grains and fossils [13]. 4) The increase in Mg-, Si- and Al-concentration may be due to precipitation of smaller crystals/grains in the pore-spaces or in the fractures where there is more free space and the stress state is different. If all these points would be deciding factors, then the mineralogical composition of the rock itself is paramount for the fluid flow in chalks. Without the knowledge of the micro-facies, fluid flow is barely predictable even on core scale for the length of the experiment here. It is possible that these criteria are of less significance when massive fluid flow affects entire rocks over a longer time. However, they affect definitely simulation and modelling at core scale, assuming homogeneous rock and rock-fluid interactions, which function for the entire rock in a similar way. Chalk with large amounts of micro- or macrofossil shells, will react differently than those rocks with fewer shell fragments. Furthermore, these chemically more resistant components influence the fluid flow through the core and play an important role to understand the progression of fluid in a core sample. As the rock-fluid interactions are the key components controlling compaction in chalk during flooding, this factor is important when studying the geo-mechanical behaviour of chalk. Obstruction of fluids may also cause unpredicted high concentrations of ions in the fluid, which in turn would change the equilibrium and influence the rock-fluid interactions in certain locations, enhancing coupled dissolution and precipitation locally. At macro-scale this may cause sealing of fractures, thus affecting the sweep and imbibition of water into the matrix.

CONCLUSION

The results from this study show clearly that chemical and textural alterations do take place when flooding non-equilibrium synthetic seawater (SSW) through an onshore Liège chalk-core with two fracture systems. Fluid flow through the core is significantly influenced by the fractures and the texture of the rock. Microfossils and shell debris of macrofossils play an important role in the rock-fluid interplay and affect estimates of rock-fluid interaction as they react differently from the much finer-grained matrix in chalk. Measurable differences in Mg-, Si- and Al-concentrations on either side of the shell lying perpendicular to the fluid flow in the natural fracture, proves disturbances of the fluid flow and variable alterations of the core at micro-scale. Hence, the presented results imply that occurring heterogeneities in chalk after flooding can occur and should be controlled before modelling the impact on a larger scale. This accounts also for the texture and the pattern of existing fractures. Such alterations may lead to sealing of fractures or heterogeneous alterations and may therefore be important to control fluid-flow and imbibition of water and compaction in reservoirs.

ACKNOWLEDGEMENTS

The authors would like to thank the Research council of Norway and the industry partners; ConocoPhillips Skandinavia AS, BP Norge AS, Det Norske Oljeselskap AS, Eni Norge AS, Maersk Oil Norway AS, DONG Energy A/S, Denmark, Statoil Petroleum AS, ENGIE E&P NORGE AS, Lundin Norway AS, Halliburton AS, Schlumberger Norge AS, Wintershall Norge AS of the National IOR Centre of Norway for support.

REFERENCES

1. Hiorth, A., E. Jettestuen, L.M. Cathles, and M.V. Madland, "Precipitation, dissolution, and ion exchange processes coupled with a lattice Boltzmann advection diffusion solver". *Geochimica Et Cosmochimica Acta*, 2013. 104: p. 99-110.
2. Madland, M., A. Hiorth, E. Omdal, M. Megawati, T. Hildebrand-Habel, R. Korsnes, S. Evje, and L. Cathles, "Chemical Alterations Induced by Rock–Fluid Interactions When Injecting Brines in High Porosity Chalks". *Transport in Porous Media*, 2011. 87(3): p. 679-702.
3. Megawati, M., M.V. Madland, and A. Hiorth, "Probing pore characteristics of deformed chalk by NMR relaxation". *Journal of Petroleum Science and Engineering*, 2012. 100: p. 123-130.
4. Zhang, P., M.T. Tweheyo, and T. Austad, "Wettability alteration and improved oil recovery by spontaneous imbibition of seawater into chalk: Impact of the potential determining ions Ca^{2+}, Mg^{2+}, and SO_4^{2-}". *Colloids and Surfaces A: Physicochemical and Engineering Aspects*, 2007. 301(1): p. 199-208.
5. Halleux, L., C. Detiege, B. Poot, C. Schroeder, A. Monjoie, G. Debande, and F. Da Silva, "Mechanical behavoiur of chalk". *North Sea Chalk Symposium May 1985*, 1985. 3: p. 152 - 178.
6. Risnes, R., "Deformation and Yield in High Porosity Outcrop Chalk". *Physics And Chemistry Of The Earth Part A-Solid Earth And Geodesy*, 2001. 26(1 - 2): p. 53 - 57.
7. Risnes, R., H. Haghighi, R.I. Korsnes, and O. Natvik, "Chalk - Fluid interactions with glycol and brines". *Tectonophysics*, 2003. 370: p. 213 - 226.
8. Korsnes, R.I., M.V. Madland, T. Austad, S. Haver, and G. Røsland, "The effects of temperature on the water weakening of chalk by seawater". *Journal of Petroleum Science and Engineering*, 2008. 60(3): p. 183-193.
9. Zimmermann, U., M.V. Madland, A. Nermoen, T. Hildebrand-Habel, S.A.R. Bertolino, A. Hiorth, R.I. Korsnes, J.-N. Audinot, and P. Grysan, "Evaluation of the compositional changes during flooding of reactive fluids using scanning electron microscopy, nano-secondary ion mass spectrometry, X-ray diffraction, and whole-rock geochemistry". *AAPG Bulletin*, 2015. 99(5): p. 791-805.
10. Molenaar, N. and J.J.P. Zijlstra, "Differential early diagenetic low-Mg calcite cementation and rhythmic hardground development in Campanian-Maastrichtian chalk". *Sedimentary Geology*, 1997. 109(3): p. 261-281.

11. Hjuler, M.L. and I.L. Fabricius, "Engineering properties of chalk related to diagenetic variations of Upper Cretaceous onshore and offshore chalk in the North Sea area". *Journal of Petroleum Science and Engineering*, 2009. 68(3): p. 151-170.
12. Megawati, M., Geochemical Aspects of Water-Induced Compaction in High-Porosity Chalks, PhD Thesis, 2015, University of Stavanger: Stavanger.
13. Levenson, Y. and S. Emmanuel, "Pore-scale heterogeneous reaction rates on a dissolving limestone surface". *Geochimica et Cosmochimica Acta*, 2013. 119: p. 188 - 197.

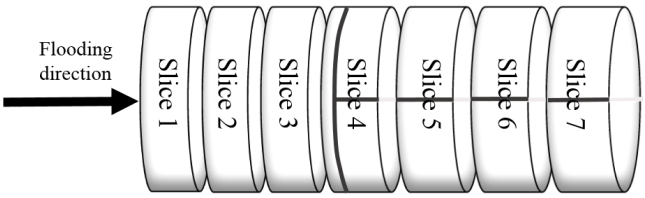

Figure 1. Sketch of the chalk core and how it was cut after flooding. Dark grey lines showing the positions of the fractures created before flooding

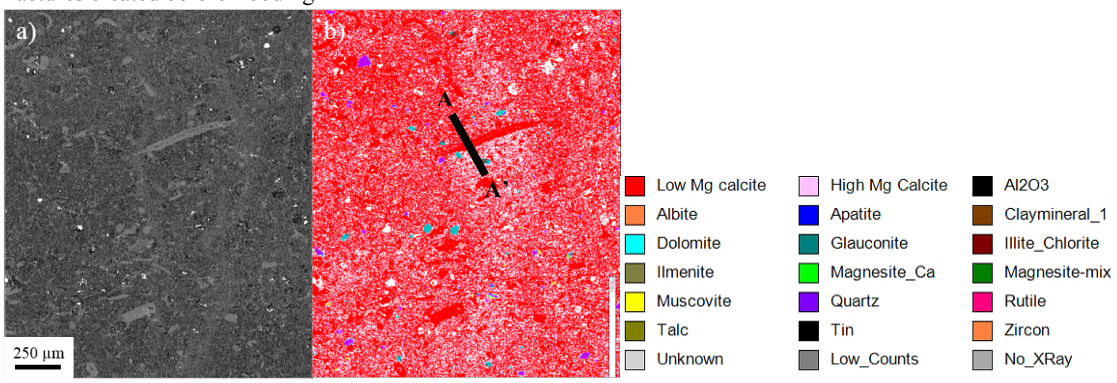

Figure 2: SEM-BSE micrograph (a) and MLA scan (b) of the same area of the fracture. The Mg-content is higher on the concave side (below) of the shell than on the convex side (above). White areas relate to pore space.

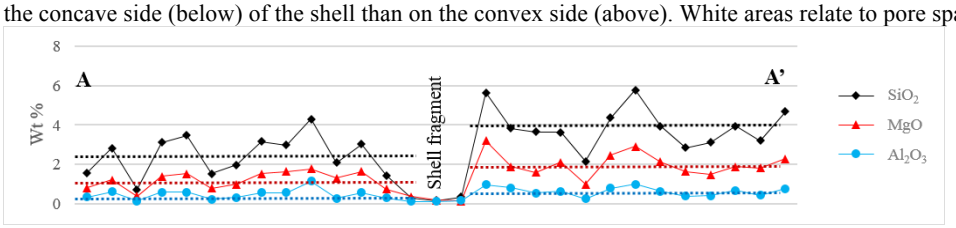

Figure 3: Oxide values measured by EMPA along the profile A - A' in Figure 2. Dotted lines are average values

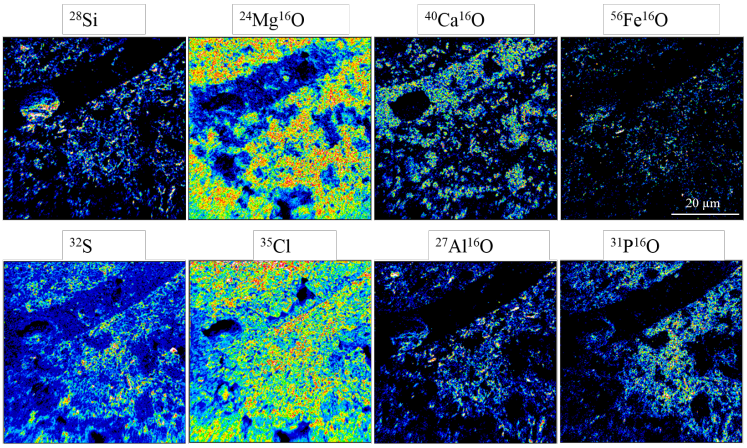

Figure 4: NanoSIMS images showing relative concentrations of elements between a shell-fragment and the surrounding matrix in fractured Liège chalk flooded with synthetic seawater (SSW). Notice the enrichment of Mg in the surrounding matrix compared to the concentration of Mg in the shell-fragment

THE IMPACT OF MINERAL DISSOLUTION ON THE CHARACTERIZATION OF PORE STRUCTURE AND MULTIPHASE FLOW PROPERTIES IN CARBONATES

Ben Niu[1,3] and Sam Krevor[2,3]
[1]Department of Chemical Engineering, Imperial College London
[2]Department of Earth Science & Engineering, Imperial College London
[3]The Qatar Carbonates and Carbon Storage Research Center (QCCSRC), Imperial College London

This paper was prepared for presentation at the International Symposium of the Society of Core Analysts held in Snowmass, Colorado, USA, 21-26 August 2016

ABSTRACT

In this study, we used core flooding techniques to mimic the uniform dissolution in carbonate rocks. Tests sequentially induced mineral dissolution and characterized the impact on multiphase flow properties. Temperature retarded acid was used to uniformly dissolve calcite in Ketton and Estaillades carbonate rock cores. A single dissolution stage removed approximately 0.5% of the mass of the rocks and measurements of relative permeability and residual trapping were made after each stage along with mercury injection capillary pressure (MICP) measurements to quantify the variation of pore throat size distribution. Multiple Stages were performed on each of carbonates rocks. Images from x-ray micro-CT and medical CT were used to describe the porosity variation and observe the changes in pore structure and multiphase flow properties at scales from the μm to the cm.

The pore throat size distribution of the rocks was observed to both increase and become less uniform with progressive dissolution. For Ketton, the micro-pores, with size range from 0.01μm to 0.1μm, have less been involved in the reaction than the macro-pores (10μm to 100μm). A larger spread in capillary trapping was seen around a characteristic initial-residual curve.

INTRODUCTION

During CO_2 injection into aquifers, the injected CO_2 will progressively dissolve into formation brine and leads to a decrease in pH (as a consequence of increasing CO_2 partial pressure), which changes the geochemical equilibrium between the formation water and the minerals [1]. Therefore, the strong dissolution of rock matrix can be expected in the carbonate dominated reservoir. This will result in the alternation of both the intrinsic properties of rock such as porosity and pore throat size distribution, and further the change of fluid flow properties, in terms of the permeability and residual trapping. There are essentially two main types of dissolution: uniform dissolution, where a simple uniform increase in porosity along the samples is observed, and non-uniform dissolution, where the dissolution is concentrated in the upper part of the sample close to the injection sites (compact dissolution) or the certain flow path along the sample (wormholes or

channelling). Although, the above theory was developed initially for single phase flow, it is still applicable to two phase flow, when the saturation-dependent flow velocity of the brine phase is considered [2].

At the core scale (the sample size in cm), the non-uniform dissolution features were observed in depth. The formation of wormhole and channelling occurred preferentially at the core inlets regardless of the sample orientation, the temperature and the injection rates [3]. To date, little experimental data regarding the impact of dissolution on petrophysical properties as relative permeability and residual trapping exist. The former is an important descriptor in the reservoir model to predict the subsurface flow [4]. The latter is the key process for maximizing capacity and ensuring the integrity of CO_2 sequestration at the industrial scale [5].

The petrophysical properties measurements must be performed on the samples that can be considered as the representative elementary volume (REV) to ensure that the macroscopic petrophysical parameters are uniform at the core scale [6]. Therefore, the samples have non-uniform dissolution cannot be used for measuring relative permeability and porosity. Furthermore, although the uniform dissolution can be achieved at the pore-scale samples (sample size in mm) [7], the samples are not large enough for the direct measurement of the properties. One of the possibility of creating the uniform dissolution at core scale is to upscale the flow conditions directly from the pore-scale experiment. However, this approach usually requires high injection flow rates or long experimental time. Therefore, in most laboratory cases at core scale, the flow regime is governed by the non-uniform dissolution.

In this study, we used temperature retarded acid (RA), described below, to develop the uniform dissolution [6]. The test program sequentially induced mineral dissolution and characterized the impacts on the multiphase flow properties in Ketton and Estaillades carbonate rock cores, which are characteristic of different pore structures. We examined the pore structure variation at the scales from micron to centimetre scale, by imaging rock sample with x-ray micro-CT and medical CT. A sequence of MICP measurements were conducted to characterizing the evolving pore throat size distribution.

EXPERIMENTAL CONDISTIONS AND PROCEDURES

Two carbonate rocks were used and their properties were summarised in table 1. These two rock samples were mainly used in the core-scale experiments for the measurement of fluid flow properties. Smaller samples (4mm diameters and 10mm length) for micro-CT observation and the MICP measurements were also drilled from the same rock blocks separately. These two types of rocks were composed of more than 99% calcite. The pore throat size distribution of both Ketton and Estaillades, interpreted from the MICP tests, showed a bimodal distribution, in the figure 1. The size of inter-granular pores in Ketton was larger than the size of inter-aggregate pores of Estaillades. Nitrogen (N_2) and distilled water (DI) were used in our experiment (100bars and 20^{o}C). The interfacial tension between N_2 and DI water was 73mN/m.

The temperature retarded acid used in this experiment was the solution composed of ester and enzyme, named Acidgen FG® (a trademark of Cleansorb Ltd.), which is an in-situ organic acid production system. The solution was usually diluted with water as a mixture of 10% w/v. It took 10.5hours for the completion of hydrolysis of the ester at temperature 65^{o}C. The pH of solution went up to 3.

The relationships between relative permeability/residual trapping and porosity were still uncertain in current literature. Therefore, we carefully chose small amount dissolution to catch any possible significant variation of fluid flow properties due to little change of rock porosity. In this paper, a single dissolution stage indicated that the sample was saturated with 10w/v RA and heated for the dissolution reaction. During each stage, approximate 0.5% mass of rock sample was dissolved.

The relative permeability curves were measured by using the steady state approach. The total injection rate as high as 20cc/min was used to lower the negative influence of capillary end effect, minimize the impact of minor heterogeneity of rock and measure the intrinsic relative permeability [4]. The residual trapping was measured by our novel technique, in which the use of capillary end effect resulted in a rapid construction of the initial-residual curves [5].

The samples were initially saturated with RA solution, and heated at 65^{o}C for more than 14hours to guarantee the completion of hydrolysis of the ester (The batch reactor experiment from the supplier indicated that 13.5hours were sufficient.). After two dissolution stages, the large samples shown in the table 1 were used for the measurement of relative permeability and small samples were used for the MICP analysis and the micro-CT imaging. Tests continued and sequentially induced the mineral dissolution and characterized the impacts on multiphase flow properties. The rock properties as permeability, porosity and pore throat size distribution were measured after each dissolution stage. The relative permeability and residual trapping were measured after every two dissolution stages.

RESULTS AND DISCUSSION

The variation of porosity in Ketton after different dissolution stages was shown in the figure 2. The homogeneously increasing porosity indicated that RA approach was an efficient way to create the uniform dissolution. The porosity increased around 0.017 for both rocks, in table 2. The permeability did not increasing monotonously with the porosity in Ketton. This was possibly due to the pore blockage by the large dissociated particles released by the dissolution of grain contact parts or the cementation materials of the rock [7], and needed further investigation. In the figure 3, the residual trapping properties of Estaillades almost did not change with dissolution. However, the residual trapping capacity of Ketton slightly decreased. This indicated that less gas could be trapped in Ketton with increasing porosity, which was mainly due to the fact that the macro-pores (10μm to

100μm) became larger and the micro-pores (0.01μm to 0.1μm) almost remained the same during the dissolution, as shown in the figure 4. The error source for the residual trapping measurement was mainly from the noise in the images, and detailed analysis on images could be found in our previous research [5]. The micro-CT images with resolution 4μm also supported the observation of pore throat size distribution, in the figure 5. The macro-pores became larger with more gran materials dissolved. The pore size distribution of Estaillades remained unchanged, which needed further repeated tests. The relative permeability of Ketton were fitted by the power law, as shown in the figure 6. With little variation of porosity (from 0.219 to 0.236), the rock became more preferable to gas flow, competing with water.

CONCLUSION

In this pioneered study, we have successfully generated uniform dissolution along the core sample and measured the change of flow properties due to the mineral dissolution. Our initial results suggested that the small amount increase on porosity could possibly result in noticeable changes on relative permeability and residua trapping in Ketton and almost no variation in Estaillades, which were heavily dependent on the evolving pore throat size. In the future, more work on experiments need to be fine-tuned and error considered in more detail to quantitatively understand any changes due to acid dissolution.

ACKNOWLEDGEMENTS

The authors gratefully acknowledge funding support for this work from the Qatar Carbonates and Carbon Storage Research Centre provided jointly by Shell, Qatar Petroleum and the Qatar Science and Technology Park. The authors also thank Cleansorb Limited (Guildford, UK) for the supply of chemical samples.

REFERENCES

1. Oleg, C. P., S. V. Golubev, J. Schott and A. Castillo, “Calcite, dolomite and magnesite dissolution kinetics in aqueous solutions at acid to circumneutral pH, 25 to 150 °C and 1 to 55 atm pCO_2: New constraints on CO_2 sequestration in sedimentary basins”, *Chemical Geology*, (2009) **265**, 20-32.
2. Ott, H., S. Oedai, C. H. Pentland, K. Eide-Engdahl, A. J. van der Linden, O. Gharbi, A. Bauer and A. Makurat, “CO_2 reactive transport in limestone: flow regimes, fluid flow and mechanical rock properties”, Paper 029 presented at the International Symposium of the Society of Core analysis held in Napa Valley, California, USA, 16-19 Sept., 2013.
3. Svec, R. K. and R. B. Grigg, “Physical effects of WAG fluids on carbonate core plugs”, Paper SPE 71496 presented at the 2001 SPE Annual Technical Conference and Exhibition held in New Orleans, Louisiana, 30 Sept. 4. Oct., 2001.
4. Reynolds, C. A. and S. Krevor, “Characterizing flow behavior for gas injection: Relative permeability of CO_2-brine and N_2-water in heterogeneous rocks”, *Water Resources Research*, (2015) **51**, 12, 9464-9489.

5. Niu, B., A. Al-Menhali and S. C. Krevor, "The impact of reservoir conditions on the residual trapping of carbon dioxide in Berea sandstone", *Water Resource Research*, (2015) **51**, 4, 2009-2029.
6. Egermann, P., E. Bemer and B. Zinszner, "An experimental investigation of the rock properties evolution associated to differential levels of CO_2 injection like alternation processes", Paper SCA2006-34 presented at the International Symposium of the society of core analysts held in Trondheim, Norway 12-16 Sept., 2006.
7. Luquot, L., O. Rodriguez and P. Gouze, "Experimental characterization of porosity structure and transport property changes in limestone undergoing different dissolution regimes", *Transport in Porous Media*, (2014) **101**, 3, 507-532.

Table 1 Sample properties

Sample	Diameter [cm]	Length [cm]	Porosity [-]	Permeaiblity [D]	Pore volume [cm3]
Ketton	3.800	16.400	0.218	2.840	40.530
Estaillades	3.800	16.400	0.279	0.196	52.180

Table 2 The change of porosity and permeability in Ketton and Estaillades

	Ketton		Estaillades	
	Porosity [-]	Permeability (D)	Porosity [-]	Permeability (D)
Initial	0.219	2.840	0.279	0.196
1st dissolution	0.224	2.937		
2nd dissolution	0.228	3.613	0.287	0.204
3rd dissolution	0.231	3.484		
4th dissolution	0.236	2.786	0.295	0.235

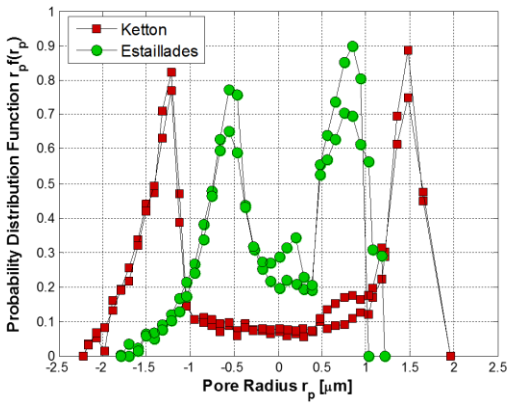

Figure 1 Pore throat size distribution of Ketton and Estaillades without dissolution experiments.

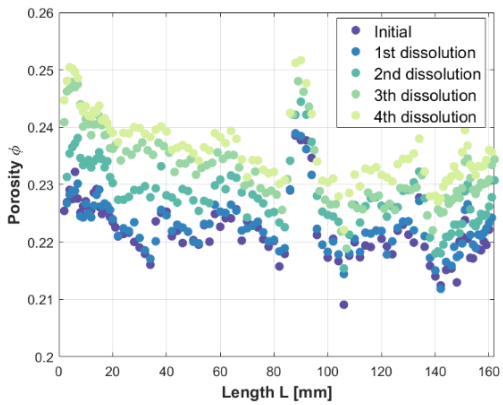

Figure 2 The variation of porosity at different dissolution stages: Ketton

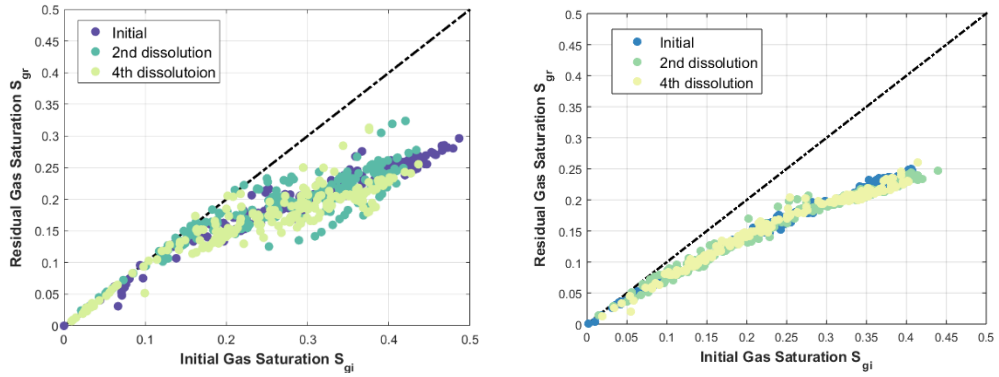

Figure 3 The Initial-residual curves at different dissolution stages: Ketton (right), Estaillades (left)

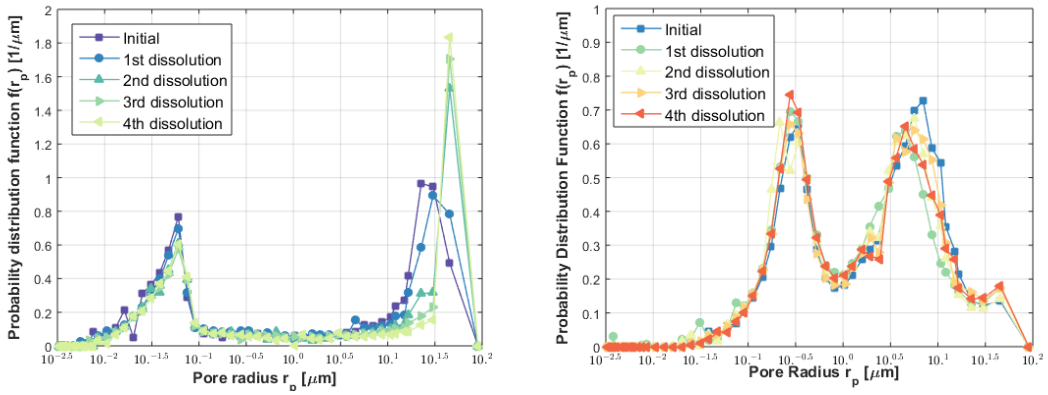

Figure 4 The pore throat size distribution interpreted from MICP tests at different dissolution stages: Ketton (right), Estaillades (left)

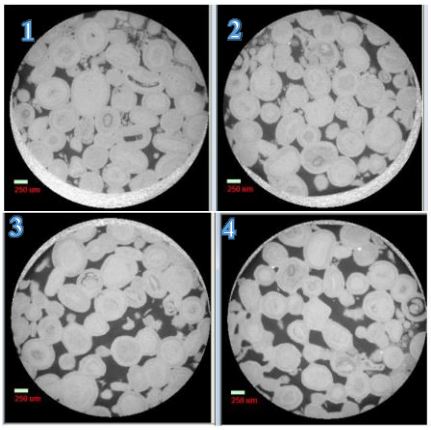

Figure 5 Micro-CT images of Ketton at different dissolution stages: 1. Initial, 2. 1st dissolution, 3. 2nd dissolution, 4. 3rd dissolution. Dark color: pore space, Grey color: grain, bright color: rubber sleeve.

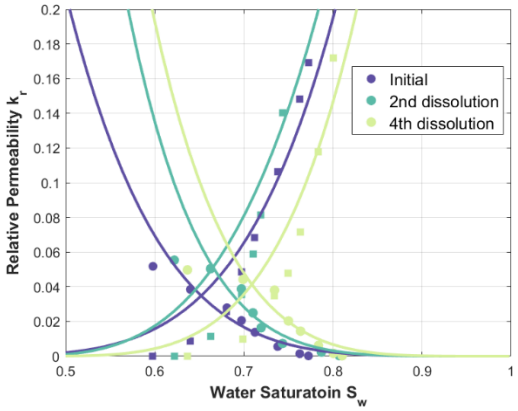

Figure 6 Relative permeability of Ketton at different dissolution stages: Round: gas, Square: water

EVALUATION OF GAS BUBBLE DURING FOAMY OIL DEPLETION EXPERIMENT USING CT SCANNING

Weifeng LV, Zhenpeng LENG, Xingmin LI, Heping CHEN, Jiru YANG, Ninghong JIA

Research Institute of Petroleum Exploration and Development, Beijing, China

This paper was prepared for presentation at the International Symposium of the Society of Core Analysts held in Snowmass, Colorado, USA, 21-26August 2016

ABSTRACT

Solution gas drive is an effective way to yield large oil recovery in some heavy oil reservoirs, and it is also identified as foamy oil. Due to the high viscosity of heavy oil that prevents gas bubbles to move, bubbles do not form a continuous gas phase compared with those in conventional oil reservoirs. Although many laboratory investigations and field observations were published around this phenomenon, the mechanism of gas bubble motion remained an essential issue. In this study, a sandpack study is designed to investigate foamy oil displacement mechanism by CT scanning. According to oil and gas production during the entire process, there are 3 stages corresponding to compressibility single oil flow, foamy oil flow and channel gas flow and foamy oil flow accounts for the major recovery. Combining oil saturation images and their histograms, the size and volume of bubbles is determined. Gas bubbles are formed in the foamy oil flow stage, and the quantity of bubbles increases exponentially with depletion pressure decreasing. When it enters into gas channelling flow stage, a continuous gas phase develops. Analyzing oil saturation images of inlet and outlet sections turn out that the low oil saturation regions expand together near the inlet but shows a dispersed distribution at the outlet, which indicates that free gas phase may formed near the inlet and gas bubbles are not connected and foamy oil energy is still effective to enhance oil recovery at the outlet.

INTRODUCTION

Successful heavy-oil reservoir development by solution gas drive has been reported recently. Different from conventional reservoir, heavy oil reservoir with solution gas drive presents unusual development characteristic such as low producing oil-gas ration, high oil recovery rate and more than expected recovery[1]. Studies show some special mechanisms and foamy oil drive is one of them: due to high viscosity of crude oil, gas releases slowly from the liquid phase and starts to flow in relative low gas saturation; at the same time the gas phase mobility doesn't increase with the increasing in saturation. Gas, showing up as tiny bubbles and representing in discontinuous phase, distributes in crude oil and flows in the porous medium. Such dispersed system (e.g. gas bubble surrounded by oil) is called foamy oil and this fluid type is foamy oil fluid[2].

Although the understanding of foamy oil has been deepened in recent years, the flow mechanism of foamy oil in porous medium is still not clear enough[3-6]. Using visual glass micro model can observe the micro-phenomenon and flow mechanism, however,

there is a certain difference between real pores and glass model in temperature and pressure. This study based on real core sample to simulate reservoir pressure and temperature and applies CT scan process to evaluate foamy oil depletion recovery method, focusing on foamy oil production characteristic and establishing a bubble generation evaluating system for bubble quantity, size and other factors.

EXPERIMENTAL

A 45mm (D) ×450mm (L) sandpack filled with 100-120 mesh quartz was used. Its porosity was 36.5% and air permeability was 5541mD, which was similar to the target reservoir. The test live oil was made by CO_2 and CH_4 (mole ratio 13:87), which has a solution gas oil ratio (GOR) of 18.0m^3/m^3, viscosity of 6151mPa·s, density of 0.98 g/cm^3, bubble point pressure (BBP) of 6.07MPa and pseudo bubble point pressure (PBBP) of 4.44MPa at reservoir conditions of 53.7°C.

A GE medical CT scanner is used under 120 kV and 130 mA conditions, and foamy oil analysis software based on CT data was developed by Beijing Digian-Sim Technology Co., Ltd. A set of Quizix pumps was used for fluid injection and backpressure control.

The experimental process can be described as followed: Vacuum the prepared sandpack and saturate it with live oil, and the pressure was maintained at 7.0 MPa during this process. Then close the inlet and step down the backpressure of the outlet. Reduce the pressure by 0.2 MPa each step until the backpressure was stable and no more fluid came out. Terminate the experiment when the outlet pressure reached atmosphere pressure. Maintain the whole system at reservoir temperature, and scan the sandpack and measure the produced oil and gas of every pressure drop.

RESULTS AND DISCUSSIONS

Characteristic of Foamy Oil Depletion

In the initial stage of the experiment, only oil was produced due to the compressibility, where collected gas was escaped from oil at ambient condition. When the pressure dropped slightly lower than the BBP (6.07MPa), oil and gas were produced simultaneously, and a large amount of oil was produced until the pressure reached PBBP (4.44MPa). After that, only a great pressure drop, a little oil can be produced. Meanwhile, bursting gas channelling was shown up intermittently. Accordingly, there were 3 stages corresponding to compressibility single oil flow (Stage I), foamy oil flow (Stage II) and channel gas flow (Stage III).

The production data of oil and gas from experiment were shown as Fig1 (the COP represents cumulative oil production and SOP represents stage oil production, meanwhile, CGP implies cumulative gas production and etc.). It can be seen from Fig 1 that stage I had very limited effect on foamy oil recovery that the accumulated oil production was only 4.8% of the entire experiment. Stage II took the major contribution for the whole system, which occupied 72.3% oil recovery of the entire system. The recovery percent increased rapidly in Stage II after the slow grow in Stage I, but substantially declined in Stage III. It meant that the ultimate recovery, 17.4% in this experiment, relied on the span

of Stage II which determined by the differences between the BBP and the PBBP. Fig 1 (b) showed that the GOR maintained at 18.0m^3/m^3 in Stage I, and slightly rose to 20~35.0m^3/m^3 in Stage II. It can be explained that there were a few dispersed gas in the foamy oil fluid and they acted as discontinued micro bubbles in the oil phase. However, the GOR increased significantly in Stage III, which can reach to 300.0m^3/m^3 and then decline to 60.0m^3/m^3 in the end. The cumulative gas production curve had several increases in this stage, and each change maintained longer than the former one. It indicated that with the increase of degassed oil viscosity, the energy that required for gas bubble to create channel gas flow was also increased. Accordingly, lots of bubbles were trapped in the porous media and channel gas flow was difficult to occur.

Flow Mechanism for Foamy Oil Depletion

In the foamy oil depletion process, the development of gas phase from dissolved gas bubbling out of solution will lead to change of the effective density of the oil / gas-bubble mixture, which is imaged by the medical CT scanner at a resolution of 1 millimeter as an effective phase. CT scanning can monitor the fluid saturation throughout the experiment so to understand the flow mechanism for foamy oil depletion more deeply. Fig 2 and Fig 3 display the oil saturation images and its saturation distribution in each stage.

In Stage I, the total oil saturation was close to100% but a little lower at the inlet (the blue lines from Fig 2). This may due to the escaped gas with local pressure drop caused by live oil injection. In addition, as this position was far away from the outlet, a huge flow resistant kept these gas stay where they were and lead to a small decline of oil saturation, which meant that small bubbles had been formed near inlet position.

In Stage II, the oil saturation was significantly decreased around BBP (the red cures in Fig 4), which indicated that the optimum production period was the combination of compressibility and foamy oil fluid energy. After that, the oil saturation curves along the sandpack decreased uniformly, which meant that the production effect was proportional to the amplitude of the step- down pressure drop. Comparing the CT images of different positions, it can be seen that the oil saturation showed a uniform decline trend near the outlet, which meant that bubbles were relative small and highly disconnected in this area. While the inlet showed a low oil-saturation zone, which indicated bubbles were generally gathered and grew larger. This phenomenon can be explained that the bubbles formed near the outlet can be produced by foamy oil flow timely, so it is difficult to gather but distributed uniformly. However, the bubbles near the inlet were too far from the end to be produced, so they were trapped by degassed oil with high viscosity and expanded with the pressure drop, and finally gathered into a connected gas phase.

In Stage III, the oil saturation did not decrease obviously with the pressure drop, and the bubbles grew bigger and spread stronger comparing to the previous stage. At the end of this experiment, a connected gas phase was also established near the outlet. After a large number of degassing, the viscosity of oil increased significantly, which lead to the trapping of a large amount of the bubbles. These bubbles expanded and gather into a connected gas phase, even caused bursting gas channelling.

Evaluation of Gas Bubbles in Foamy Oil

In CT scanning, the porosity and saturation of every pixel can be calculated from CT number. Gas bubbles can be identified by setting saturation threshold of pixels considering saturation distribution frequency and images change. This method can be described as followed: When the pressure is lower than BPP, gas will escape and present as unconnected micro-bubbles dispersed in the oil phase. The gas saturation at this moment is called minimal bubble generation gas saturation (MBGGS), accompanied by the sharp decline in the oil saturation distribution frequency (Fig 4). With the pressure continuous decreasing, these micro-bubbles expand and gather. When the pressure is lower than PBBP, the connected gas phase starts to move, and the gas saturation at this moment is called critical gas saturation (CGS). The color of images changes uniformly until CGS, low-oil-saturation zone appears (blue spots on Fig 5), and the distribution frequency of gas saturation that higher than CGS, quite small and even close to zero before, increases rapidly (Fig 4).According to the saturation data of every pixel, gas bubble can be identified and its properties can be analysis by following rules: (1) Gas saturation lower than MBGGS, no bubble; (2) Gas saturation between MBGGS and CGS, discontinuous bubble, and its volume can be calculated by formula (a); (3) Gas saturation higher than CGS, large bubble or continuous gas phase, and its volume can be calculated by formula (b).

$$V_{\text{discontinuous}} = \Delta V_{pixel} \cdot \emptyset_i S_{gi} \quad (a)$$

$$V_{continuous} = \Delta V_{pixel} \cdot \sum \emptyset_i \cdot S_{gi} \quad (b)$$

$V_{single} - discontinuous\ bubble\ volume, ml$ $\quad$ $\Delta V_{pixel} - \ pixel\ volume, ml$

$V_{continuous} - continuous\ bubble\ volum, ml$ $\quad$ $\emptyset_i - pixel\ porosity, \%$

$S_{gi} - pixel\ gas\ saturation, \%$

In this experiment, considering the propagation of the pressure, a CT image slice close to the outlet was analysis. The threshold of MBGGS and CGS were 2.3% and 17.0%, respectively. The volume of discontinuous bubbles was range from 0.00142ml to 0.0141ml, and the volume of continuous bubbles was range from 0.104ml to 12.36ml. Take this slice for example, in Stage II the quantities of bubbles increased exponentially with pressure drop and reached the top of 3592 at PBBP, while these bubbles were all discontinuous. In Stage III the quantities of bubbles showed a little decrease. When the pressure dropped to 4.0MPa, the quantities rose to 3437, but still presented as discontinuous bubbles with a few large bubbles. After that the quantities of bubbles decreased drastically to form large bubbles, and finally there were only 896 bubbles and large bubbles took the main position around 87.4% at ambient condition. In general, the foamy oil stage (Stage II) was the main period for single bubbles to form and the expansion energy of gas perform well displacement of oil, which was the major production period. With a large depletion in pressure, the residual oil has less potential to

produce gas while existing small bubbles gathering into continuous gas phase even to cause gas channelling, which result in reducing oil production.

CONCLUSION

In this study, a foamy oil depletion experiment was conducted to understand the flow mechanism and evaluate the gas bubble by the aid of CT scanning. Some conclusions can be drawn. There were 3 stages in foamy oil depletion process corresponding to compressibility single oil flow, foamy oil flow and channel gas flow. The oil saturation maintained 100% throughout the sandpack in the compressibility single oil flow stage. It was significantly decreased around BBP, which indicated that the optimum production period was the combination of compressibility energy and foamy oil fluid energy, and the foamy oil flow stage accounts for 72.3% accumulated oil recovery of the whole process and the length of this stage directly affects the ultimate oil recovery. In the channel gas flow stage, the isolated gas bubbles expanded and gathered into continuous gas phase even caused bursting gas channelling, which would reduce oil production. The volume of discontinuous bubbles was range from 0.00142ml to 0.0141ml and that of continuous bubbles was 0.104ml to 12.36ml. Bubbles occurred in the foamy oil flow stage and the quantities of discontinuous bubbles increased with the pressure drop. However, when the gas channelling came into being, the quantities of discontinuous bubbles decreased but gather into large bubbles and continuous gas phase, which resulted in reducing oil production.

REFERENCES

1. SHENG,J.J., MAINI, B.B., HAYES, R.E. and TORTIKE, W.S. Critical Review of Foamy Oil Flow, *Transport in Porous Media, Vol.35, p.157-187, 1999*.
2. TANG, G.Q., SAHNI, A., GADELLE, F., KUMAR, M., and KOVSCEK, A.R., Heavy-Oil Solution Gas Drive in Consolidated and Unconsolidated Rock, *SPE 87226, International Thermal Operations and Heavy-Oil Symposium and Western Regional Meeting, Bakersfield, California, 2004*.
3. MAINI, B.B. Effect of Depletion Rate on Performance of Solution Gas Drive in Heavy Oil System, *SPE 81114 presented at the Latin American and Caribbean Petroleum Engineering Conference, Port-of-Spain, Trinidad and Tobago, April 27-300, 2003*.
4. SMITH, G.E., Fluid Flow and Sand Production in Heavy-Oil Reservoirs Under Solution-Gas Drive, *SPE, P169-180, May, 1988.*
5. AKIN, S., and KOVSCEK, A.R., Computed Tomography in Petroleum Research. *Applications of X-ray Computed Tomography in the Geosciences, Geological Society of London, Special Publications, 215, 23-38, 2003.*
6. KOWALEWSKI, E., RENNAN, L., SOLBAKKEN, K., GILJE, E., MELHUUS, K., and RINGEN, J.K., Foamy Oil Experiments Monitored by Computed Tomography Scanning, *World Heavy Oil Congress 2008, Paper 2008-309.*

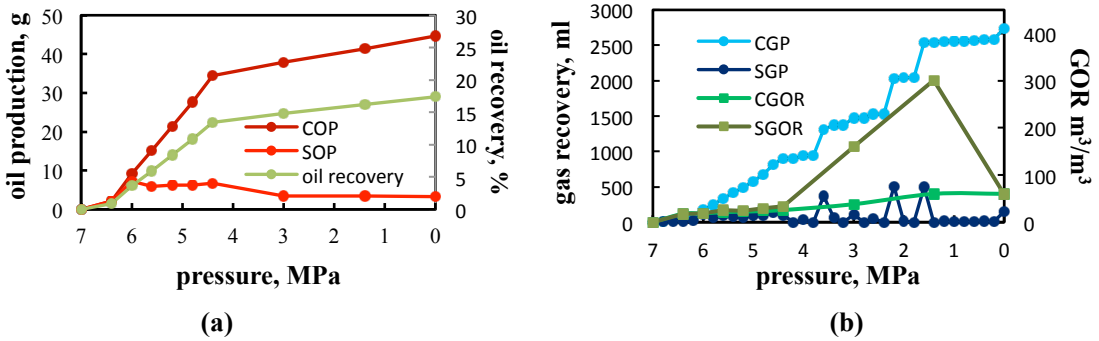

(a) (b)

Figure 1. Different Production Parameters with Pressure Change

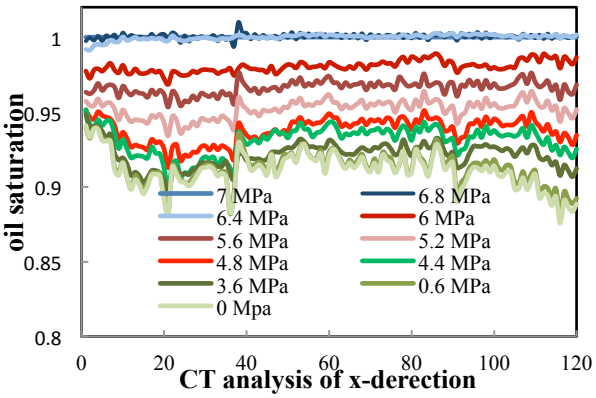

Figure 2. Oil Saturation Changes from Different Stages

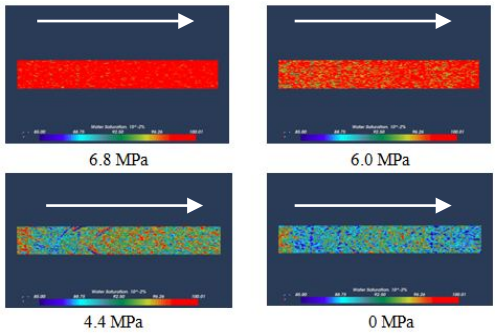

Figure 3. Oil Saturation from CT Images

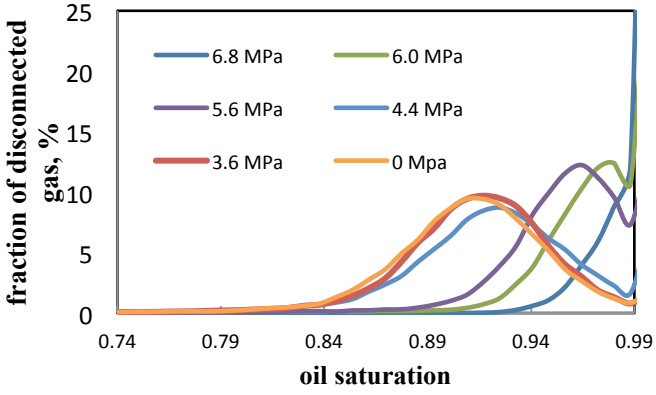

Figure 4. Fraction of disconnected (and immobile) gas v.s. Oil Saturation

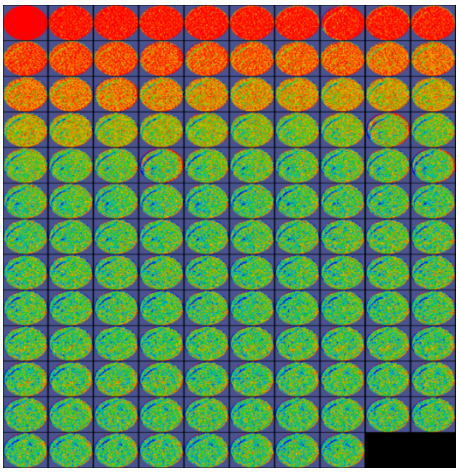

Figure 5. A sample of oil saturation evolution

Comparative core analysis from a Wolfcamp formation well; a case study

Joel Walls*, Anyela Morcote*, Tiffany Hintzman*, Michael Everts**
*Ingrain Inc., Houston, TX; **Halliburton, Houston, TX

This paper was prepared for presentation at the International Symposium of the Society of Core Analysts held in Snow Mass, Colorado, USA, 21-26 August 2016

ABSTRACT

The Permian Basin Wolfcamp shale formation is a prolific producer of oil and gas from horizontal wells. The formation is over 1000 feet thick in most areas and has multiple prospective completion targets. The Wolfcamp formation is also highly variable in mineralogy, total organic content (TOC), porosity and other key reservoir properties. For this project, a full diameter core of 246 feet length was obtained, and a multi-faceted core analysis program was conducted. The program included spectral gamma logging, dual-energy CT imaging, plug sample selection, geochemistry, traditional shale core analysis, and digital rock analysis. Digital rock data from plug sample was upscaled to the whole core scans and continuous vertical curves were computed for mineralogy, brittleness index, TOC, porosity, and permeability.

Plug samples were taken from 34 depth locations selected to be representative of the key lithologies as indicated by the bulk density (RHOB) and photo-electric factor (PEF) computed from dual-energy CT imaging. Preserved plug samples were sent to three different labs for physical lab testing, geochemistry, and digital rock analysis. One objective of this project was to obtain key reservoir and completion quality data to aid in selecting an optimum horizontal landing zone and to quantify hydrocarbon in place. Another goal was to enable comparisons between physical lab and digital rock experiments. Using ion-milled SEM images and 3D FIB-SEM data, TOC, intergranular porosity, and porosity associated with organic matter (PAOM) were determined. Of particular interest was to understand the importance of PAOM and to explore the similarities and differences between SEM derived porosity and helium porosity from traditional physical lab test.

INTRODUCTION

The subject well for this project was drilled in the Delaware Basin in west Texas, USA, and was sampled in the upper Wolfcamp formation. In order to gain a more thorough understanding of reservoir and completion-related rock properties, an extensive suite of core and well log data was obtained. Approximately 246 feet (75 meters) of full diameter core was recovered and it was immediately cut into 3 foot long sections while still inside the aluminum inner core barrel liner. These individual tubes were sealed with rubber end caps to reduce sample loss and drying, then shipped directly from the field to the digital rock lab.

METHODS

For this project, the entire core was CT and spectral gamma ray (SGR) scanned while still sealed in the aluminum core barrel liners. From this imaging, a continuous high-resolution (about 1000 points per linear foot) log was computed of RHOB and PEF using a process described by Vinegar, 1986 and Coenen and Maas, 1994. By combining SGR with RHOB and PEF, estimations of rock mineral volumes, clays, silicates, and carbonates were computed, as well as TOC. X-ray fluorescence (XRF) data was acquired at discrete points along the core for mineral volume calibration purposes.

In order to select plugs and ensure adequate characterization of the rocks with greatest reservoir potential, the data was divided into classes as described by Walls and Sinclair, 2011. From each of the 34 selected plugs, a half inch end trim was removed and used for digital rock analysis. The remaining portion of the plug and the second plug taken at the same depth was used for quantitative XRD, LECO, TOC and other tests.

To aid with sub-sample selection for SEM imaging, Archimedes bulk density was measured from the end trim, bulk TOC and mineralogy was measured from homogenized material using Fourier Transform Infrared Spectroscopy (FTIR) and a three component mineralogy classification was computed based on XRF measurements. From each sub-sample, a 1 millimeter by 0.5 millimeter argon ion polished area was SEM imaged using both secondary electron (SE2) and back-scatter electron (ESB1) detectors at 10 nanometers per pixel. The sets of high resolution images were combined and segmented for porosity, organic matter, higher density minerals, and matrix grains. The porosity was further analyzed and separated into PAOM, intergranular and intragranular porosity.

For this project, 8 of the 34 plug samples had a 3D image data set acquired with a FIB-SEM imaging system by alternately removing 15 nanometers of material with the Ga+ ion beam and then acquiring SE2 and ESB1 images simultaneously at a resolution of 15 nanometers per pixel. Each 3D volume was segmented into grain, porosity, and organic matter. From the effective pore volume, connected and isolated porosities were computed as well as PAOM. Horizontal and vertical absolute permeability was computed with the use of Lattice-Boltzmann methods on the connected pore volume.

RESULTS

Mineral composition was measured with XRF and XRD from 34 samples. From each analysis, a 3 component mineralogy group comprising of clays, silicates, and carbonates was normalized and plotted onto a ternary diagram. The results from both techniques are in good agreement with each other. The datasets show similar mineralogy distribution with silica to clay ratio of about 70/30 and the carbonate content ranging from 0-90% by weight. Each data point in Figure 1 represents the mineralogy for one sample. The data points are also colored by rock classes characterized by the high resolution RHOB and PEF obtained from the dual energy CT scan of the core.

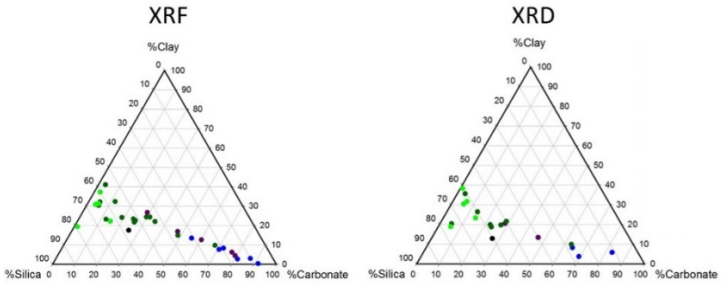

Figure 1: Comparison of mineralogy results from XRF (left) and XRD (right).

From the 34 plug samples, PHIE, organic matter, and PAOM were segmented and measured from 10 SEM image data sets per sample. Each of the 10 pairs of images (secondary and backscatter electron) span an area of approximately 20 X 30 microns. The results were averaged per sample and are used for observations and comparisons. The 34 samples show a wide range of porosity, organic matter and mineralogy. Each data point in Figure 2 represents the average for a sample. The data points are also colored by rock classes. The more siliceous samples (green and black data points) range in porosity from 1 to 6% by volume and range in PAOM from 0.5 to 2% by volume. The more calcareous samples (blue and purple data points) range in porosity from 0.5 to 5% and range in PAOM from 0 to about 1% by volume. Most samples have a combination of mineral bounded (intergranular plus intragranular) porosity and porosity associated with organic matter. In Figures 3 the segmented PAOM from the image to the left is shown in blue and the segmented intergranular porosity is in red.

LECO TOC from geochemical lab analysis was measured and compared to organic matter from SEM for 13 samples with closely matching depths. The results in Figure 4 show that the SEM total organic matter and LECO TOC form a linear trend that has a non-zero intercept. The higher LECO TOC values in the cluster of four low TOC samples may have been caused by incomplete calcite dissolution as these were all high calcite samples. Also we do not know the kerogen density exactly so it isn't possible to convert weight % to volume % exactly, but a factor of 2 is a common assumption. The dashed line in Figure 4 shows the line of equality (slope = 1) between SEM and LECO with the factor of 2 assumption. For 13 samples, the average equivalent Vro is 1.18 and the average Tmax is 463 (late oil to early gas window).

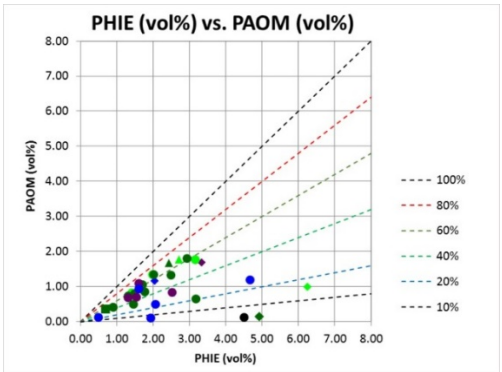

Figure 2: Crossplot of PHIE and PAOM from SEM. Data points colored by CT class.

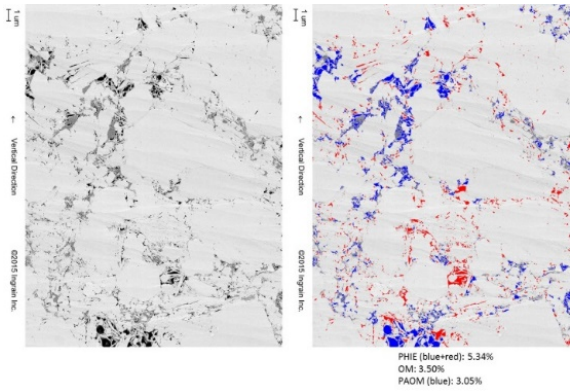

Figure 3: Left is an original 10 nm/pixel SE2 image, and right is a segmented image with intergranular porosity in red and organic porosity in blue.

The clay bound water volume cannot be resolved from SEM images and gets counted as part of the clay mineral volume during image analysis. Therefore the SEM porosity can be considered as porosity available for free water or hydrocarbons, which is a common definition of effective porosity (PHIE). Clay in these samples is about 19% smectite and 81% illite as determined by XRD. The weighted average clay bound water porosity is equal to about 0.18 times total clay volume using Chitale's published clay porosity for different clay species. This clay bound water (CBW) porosity was added to effective porosity from SEM imaging to get an approximate total porosity.

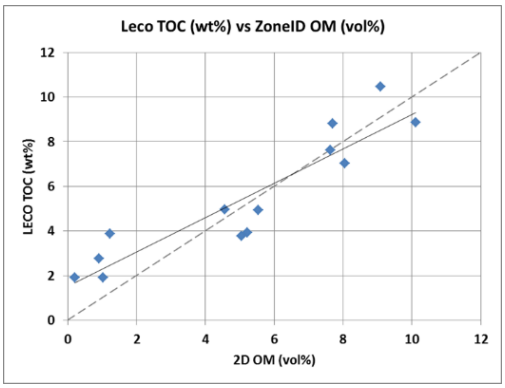

Figure 4: Comparison of organic matter from 2D SEM to LECO TOC for subset of samples with exactly matching depths. Low TOC samples had high calcite content which may have increased LECO TOC if there was incomplete calcite dissolution.

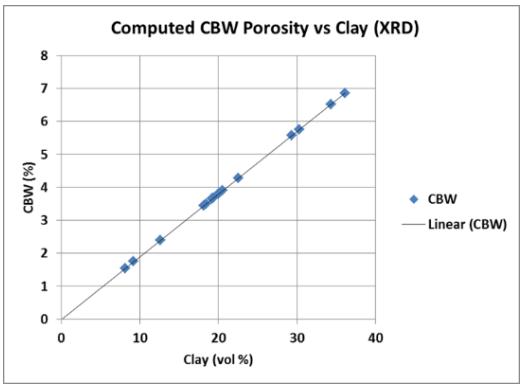

Figure 5: Computed clay bound water (CBW) porosity using results from Chitale, 2010 combined with clay analysis from XRD.

From eight 3D FIB-SEM volumes, the properties computed were connected porosity, isolated porosity, PAOM, organic matter, and absolute permeability in both the vertical and horizontal directions. The porosity from these 3D volumes ranged from 4 to 11% by volume. The horizontal absolute permeability ranged from about 40 to 1900 nD. The porosity versus horizontal permeability trend was determined and compared to porosity and permeability from GRI crushed sample analysis. The porosity ranges for both types of data are similar and so are the porosity-permeability trends (Figure 6). We could not cross plot porosity vs porosity or permeability vs permeability for the two methods because none of the depths of the FIB-SEM and GRI samples matched.

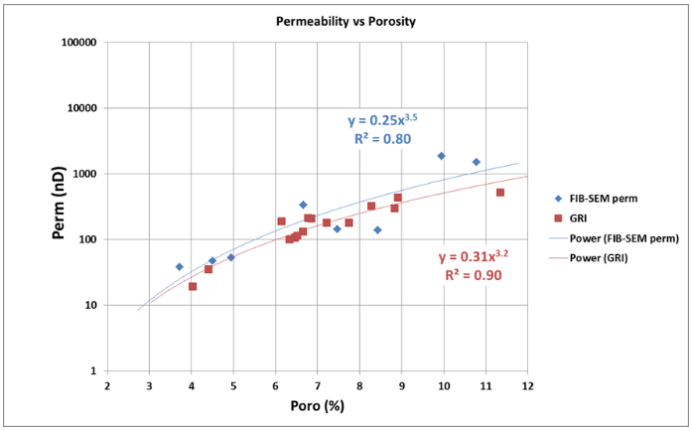

Figure 6: FIB-SEM computed porosity and permeability trend compared to GRI data. (not matching depths)

Petrophysical Integration and Upscaling:

The SEM and FIB-SEM analysis and results from selected plugs were incorporated into the petrophysical analysis as calibration points. Thus, we were able to estimate total porosity (PHIT), effective porosity (PHIE) and PAOM as continuous logs along the cored interval. Since matrix permeability was computed at various depths from a 3D FIB-SEM volume using a Lattice Boltzmann method (Tolke, et al., 2010), a matrix permeability log was obtained from the correlation between FIB-SEM porosity and computed permeability. Using a combination of X-ray CT data, SGR, SEM, and FIB-SEM analysis, key shale reservoir rock properties were computed along the entire cored interval (Figure 7). This analysis contributed to a better understanding of this well at an early stage of the study process.

These rocks have a wide variability in mineralogy, porosity, and TOC over short vertical distances. The CT scan data was able to detect and resolve the thin layers. Brittleness index (BI), was based on a relationship between Young's modulus and Poisson's ratio, similar to that of Rickman, et al., 2008. Estimation of BI shows that the most calcareous rocks are generally more brittle than the more clay rich rocks. However, the tight, high calcite layers also have high rock strength which can act as a barrier to vertical fracture growth depending on the layer thickness and spacing.

OBSERVATIONS AND CONCLUSIONS

Some key findings from this project are;

- LECO TOC from geochemical lab analysis matches organic matter from SEM with a correlation coefficient R^2 of 0.84.
- SEM image derived porosity is analogous to effective porosity (hydrocarbon plus free water plus capillary water).
- Porosity vs permeability trends computed using FIB-SEM data and traditional "GRI" type data are similar.
- Data from plug samples, including SEM and FIB-SEM, can be upscaled by applying trends and correlations to the continuously sampled dual energy CT and SGR data.

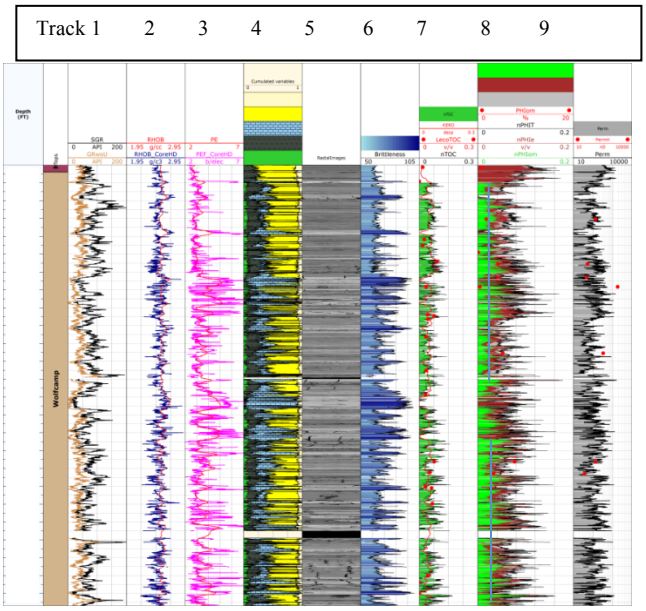

Figure 7: SGR, CT data, and computed curves. Track 1, spectral gamma; Track 2, RHOB, Track 3, PEF, Track 4, computed mineralogy; Track 5, radial images, Track 6, brittleness index; Track 7, TOC; Track 8, PAOM, PHIE, PHIT ; Track 9, permeability. Red curves are from well log data. Red data points are from plug samples. Cored interval is about 247 feet.

REFERENCES

1. Vinegar, Harold, X-ray CT and MR Imaging of Rocks, Journal of Petroleum Technology, March, 1986.
2. J.G.C. Coenen, J.G. Maas, Material classification by dual-energy computerized X-ray tomography, Proc. Int. Symp. on Computerized Tomography for Industrial Applications, 8–10 June 1994, Berlin, DGZfp, pp 120-127
3. Rickman, Rick, Mike Mullen, Erik Petre, Bill Geiser, Donald Kunert; A practical use of shale petrophysics for stimulation design optimization: all shale plays are not clones of the Barnett shale, presented at the SPE Annual Technical Conference and Exhibition, Denver, CO, 2008, SPE 115258.
4. Tolke, J., Baldwin, C., Mu, Y., Derzhi, N., Fang, Q., Grader, A., et al.: "Computer Simulations of Fluid Flow in Sediment: From Images to Permeability," The Leading Edge, Vol. 29, No. 1, January 2010, pp. 68-74.
5. Chitale, Vivek D., 2010; Simplified and More Accurate Clay Typing Enhances the Value Added by Petrophysical Evaluation of Shale and Tight Gas Sand Plays, Search and Discovery Article #40487 (posted 2010), adapted from oral presentation at AAPG Convention, Denver, Colorado, June 7-10, 2009
6. Walls, J.D. and Sinclair, S.W.: "Eagle Ford Shale Reservoir Properties from Digital Rock Physics," First Break, Vol. 29, No. 6, June 2011, pp. 97-101
7. Driskill, Brian, Joel Walls, Steven W. Sinclair, Juliana DeVito, "Applications of SEM Imaging to Reservoir Characterization in the Eagle Ford Shale, South Texas, USA", from Electron Microscopy of Shale Hydrocarbon Reservoirs, Co-editors: Wayne Camp, Elizabeth Diaz, Barry Wawak, AAPG Memoir 102, April, 2013

EVALUATION OF THE IMPULSE HAMMER TECHNIQUE FOR CORE MECHANICAL PROPERTIES PROFILING

P. Gramin[1], R. Fisher[1], R., A. Frooqnia[1], A. Ai[1], P. Hojnacki[2], G. Boitnott[3], L. Louis[3], J. Hampton[3]

[1]BP, Houston, TX, United States
[2]ALS Reservoir Laboratories, Houston, TX, United States
[3]New England Research, Inc., White River Junction, VT, United States

This paper was prepared for presentation at the International Symposium of the Society of Core Analysts held in Snowmass, Colorado, USA, 21-26 August 2016

ABSTRACT

As a part of an evaluation program conducted on several of BP's cores from deepwater Gulf of Mexico fields, a new probe was used to assess its potential as a non-destructive solution for geomechanical profiling. This mechanical probe measures the force-time relationship of a mass (referred to as Impulse Hammer) while it is freely falling onto the surface of a core from a known height. The force-time function is subsequently analyzed by an elastic Hertzian solution to obtain a reduced Young's modulus E^*, which is then used as a first-order strength indicator. Twenty one feet of slabbed core were analyzed for variations in E^* and compared with Scratch Test results. For comparison, we grouped the data into several litho-facies while each group retained a minimum number of representative data points. We observed that E^* reliably captured the variability of mechanical properties throughout the data. Results showed that the Impulse Hammer method provides a nondestructive alternative to the Scratch Test as a mechanical profiling tool. The Impulse Hammer data analysis also generates a second parameter that quantifies the deviation of core from a purely elastic behavior. Even though the use of this parameter is not thoroughly reviewed in the present study, its potential to yield a more complete picture of the core's mechanical properties and to improve the scratch test comparison is briefly discussed.

INTRODUCTION

Historically, when a whole core is collected for analysis, some form of vertical variability characterization is used to focus on sampling locations for special core analysis (SCAL). For petrophysical SCAL, this process normally involves cutting routine core analysis (RCA) plugs at a regularly sampled interval (1.0 or 0.5 foot are common depth increments). The routine plugs are then used to determine porosity and gas permeability as storage and flow capacity parameters to be employed in SCAL sample selection. Until 2008, the process by geomechanics specialists to characterize vertical variability included the use of porosity and permeability, petrophysical rock typing, core gamma ray, and/or a log-derived rock strength [1].

Starting in 2008, Terratek (now a Schlumberger company) introduced a rock strength profiling technique, known as the Scratch Test, which has been calibrated to unconfined compressive strength (UCS) core tests [5]. This technique has proven reliable and trustworthy in characterizing vertical variability in mechanical properties and approximating unconfined compressive strength. Because the method results in the cutting of a small furrow roughly 8 mm wide by 0.2 to 2 mm deep along the core face, geologists and sedimentologists have typically been unwilling to allow this strength profiling to occur on the geologic slab due to the concerns that the process damages the core. Alternatively, the Scratch Test methodology can also be run on core butts (3/4 sections) before or after the routine core plugging process. If before, the scratch test delays the cutting of the RCA plugs, geochemistry sampling, and/or petrophysical SCAL plugs, which may be sensitive to oil-based mud invasion or mechanical degradation of the rock strength (particularly in weakly consolidated sands). If after, the Scratch Test is collected over short intervals and in between core plugs could be impacted by the removal of core material.

In 2013, a new and non-damaging strength profiling technique was introduced by New England Research (NER) onto their AutoScan platform. The technique, known as Impulse Hammer, measures the reduced Young's modulus, or E*, by measuring the force-time response at the tip of a small instrumented sensor dropped on a core surface from a specified height and sampling interval. The technique was designed to provide a non-destructive option for mechanical profiling that can also be used to map 1 and 2D variability in mechanical properties such as elastic stiffness. To evaluate this new mechanical properties profiling process for incorporation into BP's core analysis workflows, BP worked with ALS Reservoir Laboratories (ALS) and New England Research (NER) to trial the Impulse Hammer technique on core where Scratch Test results were also available. More specifically, this study sought to answer the following questions:
(1) Are Impulse Hammer and Scratch Test techniques consistent between each other in capturing the variations of the core mechanical properties (i.e. what level of heterogeneities is each testing platform sensitive to)?
(2) Can empirical relationships be formulated between the rock strength index values obtained from the Scratch Test and the reduced Young's modulus E* obtained from the Impulse Hammer?

MATERIALS AND METHODS

Material Tested

The material tested consists of core sections and plugs selected by BP from three different formations encountered in GoM deepwater fields. All the original sections had previously been analyzed with a Scratch Test probe. For Fields A and B, the core sections were still available for impulse hammer profiling, while plugs that had been extracted from the scratched core were used for field C. The table below provides a description of the core material.

Table 1. Summary of tested core material

Field ID	Rock Properties		Experimental Dataset	
	Brief lithological description	Strength	Type	Amount
A	Well Consolidated, Fine Grained Sandstones Interbedded with Thin Shale	Strong	slabbed core	13.3 ft
B	Moderately Consolidated, Fine Grained Sandstone and Shale	Medium to Strong	slabbed core	7.8 ft
C	Loosely Consolidated, Medium Grained Sandstone	Weak	plug sample	7 plugs

Terratek Scratch Test

The Scratch Test was developed in the late 1990's at the University of Minnesota as a fast rock mechanical profiling technique to provide a strength index (Terratek Strength Index – TSI) that is positively correlated with UCS [2, 3, 4, and 5]. The Scratch Test consists of creating a continuous groove of constant depth on the surface of a rock sample at a constant velocity. The amplitude of the force acting on the cutter head are recorded continuously. An intrinsic specific energy parameter is sought throughout scratch testing which is a function of (a) the cutting process, (b) the inclination of the force acting on the cutting face, and (c) the friction coefficient across the cutter flat. Depending on rock type, mechanical properties, and cutter depth, the area of investigation and depth of damage will vary significantly. Also, the depth of cut impacts the type of failure process observed throughout testing, i.e., differing depths produce ductile and brittle failure. For ductile failure, the energy consumed is related to the volume of removed rock, while in the brittle mode, the energy consumed is related to the surface of the cracks while forming rock chips [6].

The scratch testing technique is based on a model of rock/cutter interaction in the ductile regime [7]. The model has four key assumptions: (1) the forces on the cutting face, which is suitably averaged over a long distance compared to the depth of the cut, is proportional to the cross-sectional area of the groove traced by the cutter, (2) the inclination of the average force on the cutting face is constant, (3) there is a frictional contact between the cutter flat and rock interface, and (4) the cutter wear is negligible.

Impulse Hammer Technique

The Impulse Hammer probe used is integrated to a petrophysical core scanning system manufactured by New England Research. This system also allows for routine scanning of gas permeability, P- and S-wave velocity, electrical resistivity and infrared absorbance. The scanner platform, shown in Figure 1(a), can accommodate up to 12 feet of whole or slabbed core material at a time. The computer-controlled gantry system first maps the core surface with a laser to identify edges and fractures and exclude them from the measurement grid. Then the system can run automatically with no further operator assistance and map the selected physical properties according to the defined layout.

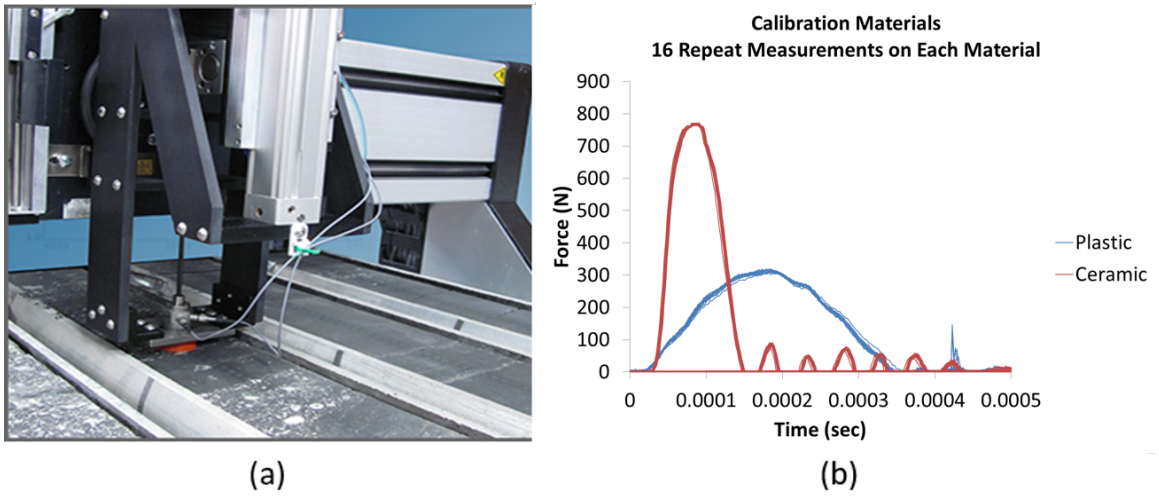

Figure 1. (a) A photograph of the measurement platform used in this study, with several sample types on the table. (b) Example of the Impulse Hammer response on two different elastic materials. 16 repeat measurements are made on each sample, illustrating the level of repeatability.

The Impulse Hammer was developed to provide a non-destructive mechanical profiling method. It was also designed to be fully automated for use on standard slabbed core without the need for special surface preparation. The area of investigation for the Impulse Hammer measurement is on the order of a millimeter and is commonly used with a measurement spacing of 2mm or greater depending on the application. Unlike more traditional rebound hardness techniques, the Impulse Hammer method can be used to extract both an elastic stiffness and a hardness index.

The measurement consists of dropping a mass equipped with a tip of known radius of curvature onto the core surface while continuously measuring the force applied at the tip at a very high sampling rate. A purely elastic Hertzian contact model is used to describe the impact of a sphere with an infinite sheet [8, 9]. The observed force-time function is fit to the model described in Equation (1).

$$f(t) \cong H\left(\frac{4}{3}\right) R^{\frac{1}{2}} \varepsilon^* d^{\frac{3}{2}} \quad ; \quad d(t) \cong \sin\left(\frac{\pi(t-t_0)}{2T^*}\right) d_{max} \tag{1}$$

where t is the time along the force-time function, R is the tip radius, and ε* is related to the tip properties and the reduced Young's modulus of the sample, E*. The parameter H is a dimensionless hardness parameter, which for the case of elastic impact has a value of 1. The displacement-time function is approximated as shown in (1), where t_0 is the time of impact.

$$d_{max} = \left(\frac{15MV^2}{\frac{1}{16R^2\varepsilon^*}}\right)^{\frac{2}{5}} \; : \; T^* = 2.94\frac{d_{max}}{2V} \quad ; \quad \frac{1}{\varepsilon^*} = \frac{(1-\nu_{tip}{}^2)}{E_{tip}} + \frac{1}{E^*} \quad ; \quad E^* = \frac{E}{(1-\nu^2)} \qquad (2)$$

where, M is the mass of the impactor, V is the velocity of impact, ν_{tip} is the Poisson's ratio of the tip, E_{tip} is the Young's modulus of the tip, and E and ν are the material Young's modulus and Poisson's ratio of the test sample.

Thus the measured force-time function of impact is fit to elastic theory and allowed two free parameters, E* and the impulse hardness parameter H, which can be related to the kinetic energy loss during impact.

Figure 1(b) shows several Impulse Hammer force-time functions for two different elastic materials, polyetherimide (plastic) and macor (ceramic). The plastic sample has a low Young's modulus and exhibits much lower force amplitude and longer period of indentation, while the ceramic sample has a high Young's modulus and provides a much higher force response in a relatively shorter time interval.

Procedures for Data Acquisition and Analysis

In the following, only the procedures that pertain to the Impulse Hammer work performed at ALS are described:

For Fields A and B, where slabbed 1- and 2-foot long core sections were available, E* was measured along the core axis at 5 mm spacing using NER's standard medium curvature tungsten carbide tip with R=3.8 mm, E_{tip}=545 GPa, and ν_{tip}=0.23.. All measurements were made using a fixed drop height of 12.5 mm and a total sensor mass of 69.7 grams, The data were processed using NER's default routine processing, yielding E* and H. Due to different sampling rates and volume sensitivities for the Scratch Test and Impulse Hammer outputs, the comparison between TSI and E* was initially carried out using histograms from common depth ranges.

For Field C, where original core sections were not available, RCA plugs were secured to the measurement table and mapped with the laser to delineate samples edges. A grid pattern of several measurements was performed on the end surface of every plug to provide a statistically representative data set. The data obtained were reduced by calculating average E* values per plug and these were compared against TSI values from the parent core at the same depth.

It is worth noting that although the Scratch Test provides a finer length resolution than the Impulse Hammer, the volume effectively investigated by the Scratch Test itself is larger than the mm scale footprint of the Impulse hammer.

RESULTS

Fields A and B

Figure 2 shows a data set obtained on one of the core sections from Field A, together with a core photograph. The reduced Young's modulus and TSI values are plotted as a function of depth using two different vertical scales. The comparison demonstrates a visually good consistency between the two data sets, with some contrast in a few intervals. Also, note that locations where plugs had been taken could not be probed by the Impulse Hammer. In order to conduct a global comparison between the two data sets across a number of core sections studied, histograms were used, as shown in Figure 3. The same procedure was followed for all the core sections studied from Fields A and B. Some results are showed in Figures 4 and 5.

Field C

Impulse Hammer data for Field C was obtained on RCA core plugs. Comparison between average E* per plug and TSI obtained at the same location is listed in **Table 2**. In this case, the strength measured by both methods was much lower than for Fields A and B. Yet, reasonable correlation is observed between the two measurements.

Table 2. Summary of Field C plug properties and test results.

Plug ID	Gas K, md	Helium Porosity, % PV	TSI from core MPa	*E**, GPa
1	278.	27.3	0.500	1.329
2	419.	28.8	1.500	0.833
3	742.	29.4	1.000	0.656
4	1290.	29.7	0.500	0.396
5	1140.	30.0	0.700	0.717
6	763.	27.5	0.400	0.561
7	1350.	28.3	0.600	0.361

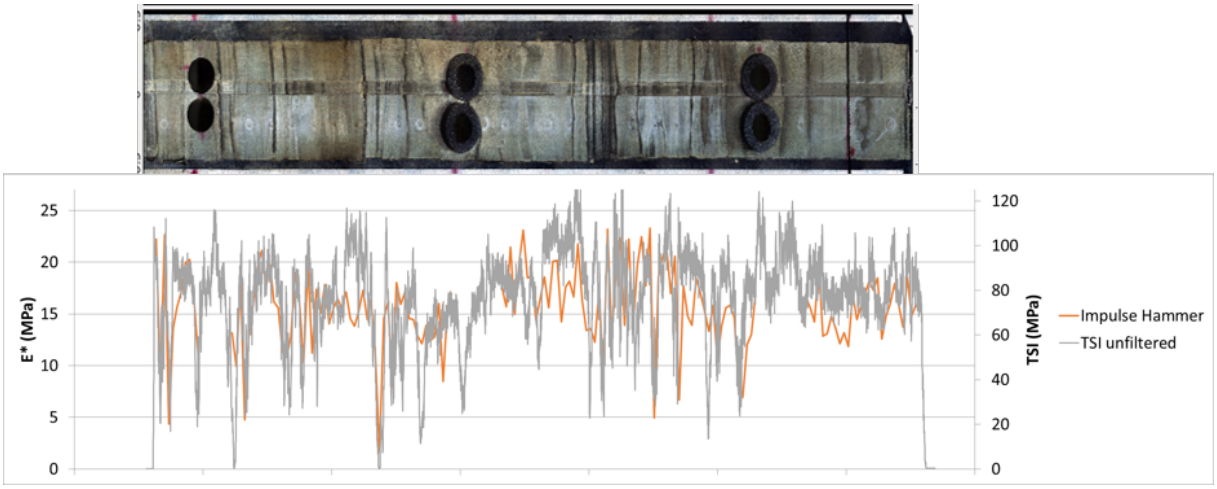

Figure 2. Field A slabbed core photograph (above) and measured E* and TSI values along the core length. This two foot interval consists of thin-bedded consolidated sand (tan color) and then shale (gray color). Note the sensitivity of both properties to variability in strength.

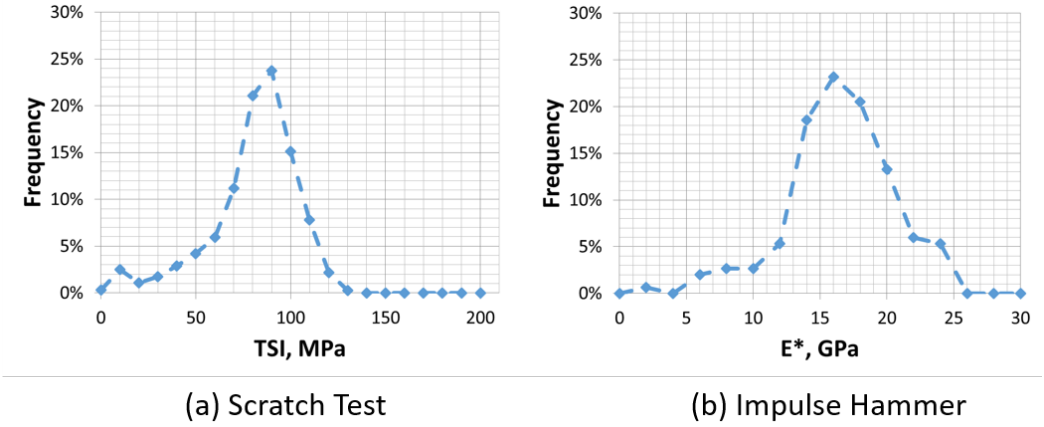

Figure 3. Field A: Histograms of all data showed in Figure 2. (a) TSI. (b) E*.

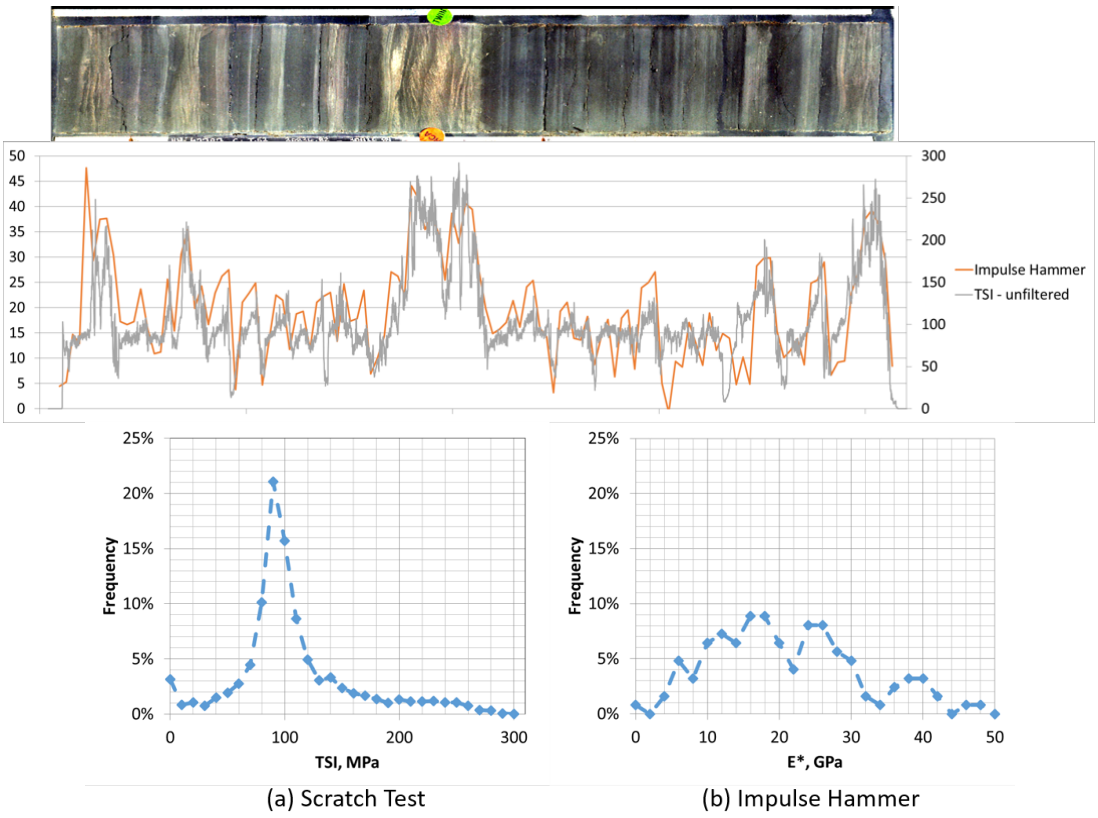

Figure 4. Field A slabbed core photograph and measured E* and TSI values along the core length (above). This two foot interval consists of shale (gray color) and thin-bedded consolidated sand (tan color). The tan-colored cross-bedded sandstone exhibits substantially higher strength than the rest of the core per both methods. Below: Histograms for above data. (a) TSI. (b) E*.

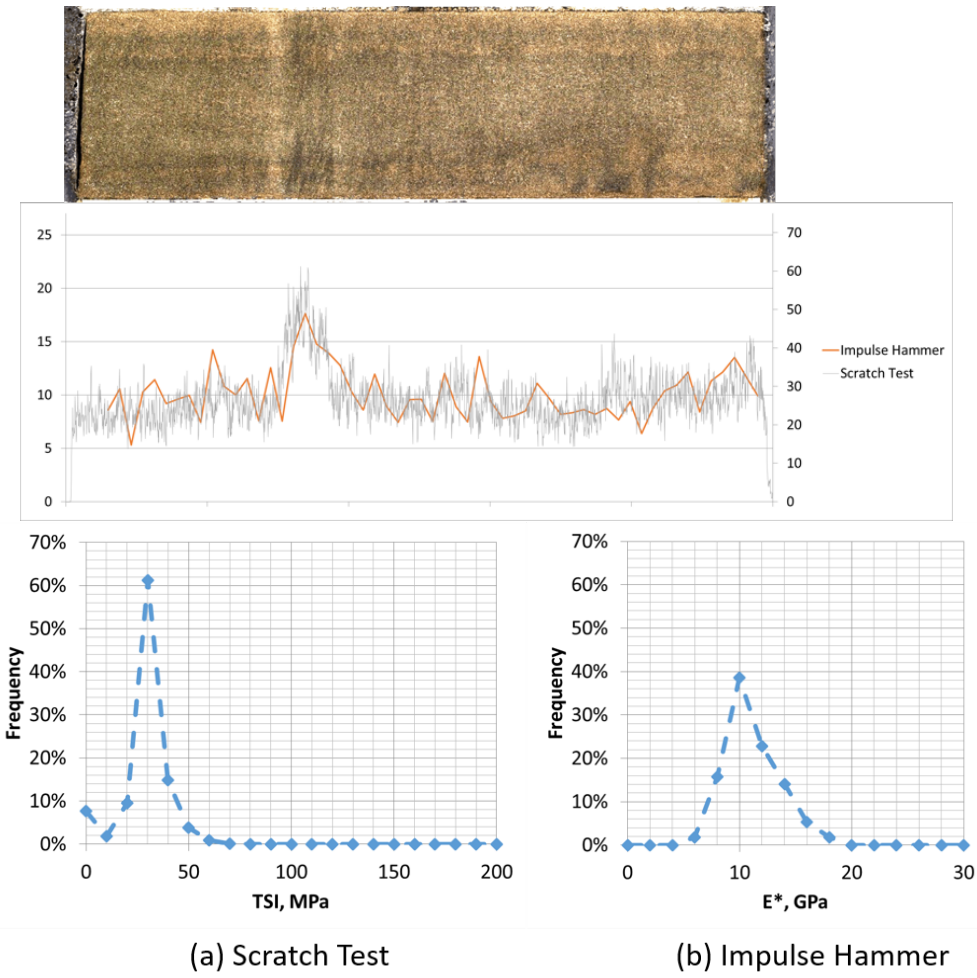

Figure 5. Field B slabbed core photograph and measured E* and TSI values along the core length (above). This one foot section consists of moderately consolidated sandstone. Relatively high strength interval associated with more bedded lithology is observed by both methods. Below: Histograms for above data. (a) TSI. (b) E*.

DISCUSSION AND CONCLUSION

Impulse Hammer as a TSI predictor

The data acquired and discussed in the previous section allows us to conduct a global comparison between the Scratch-Test-derived Terratek Strength Index (TSI) and the Impulse-Hammer-derived reduced Young's modulus E*. Based on our observations on cores and data sets, all the measured sections were divided into several internally-homogeneous subsets to perform the comparison. For each of those subsets, a separate histogram of both TSI an E* values was traced and the averages of those histograms were used as representative TSI-E* pairs for a global comparison. The result of this analysis is shown in **Table 3**. Note that in Field A some intervals display very similar pairs of average properties. In the case of Field C, each plug was considered as its own group.

Table 3. Summary of results obtained from histogram analysis for each individual rock type with lithological description.

Field	Length/ Quantity	Peak TSI, Mpa	Peak IH, Gpa	Comment
A	2 ft	70.000	16.000	sand w/shale laminae
A	3 ft	260.000	45.000	shale w/sand laminations
A	3 ft	70.000	16.000	massive sand
A	3 ft	40.000	6.000	Combination of silt and sand interbedded with shale laminae.
		90.000	16.000	
A	3 ft	10.000	2.000	Alteration of clean sand and silt with lower shale content
		60.000	14.000	
		70.000	16.000	
B	3 ft	40.000	6.000	shale
B	3 ft	10.000	4.000	massive sand
B	1 ft	60.000	18.000	massive sand
B	1 ft	30.000	10.000	massive sand
C	1 plug	2.000	1.200	sand
C	1 plug	1.500	0.833	sand
C	1 plug	1.000	0.656	sand
C	1 plug	0.500	0.396	sand
C	1 plug	0.700	0.717	sand
C	1 plug	0.400	0.561	sand
C	1 plug	0.600	0.361	sand

shale	sand

The breakdown of Table 4 helps us to establish the global correlation between TSI and E*, which is shown in Figure 8. The sands in Fields A, B and C appear to show very strong TSI-E*correlation. Best fitting power laws given below show similar factors and exponents:

$$\text{Field A sand:}\quad TSI = 2.1226\ E^{*1.263} \tag{3}$$

$$\text{Field B sand:}\quad TSI = 1.9194\ E^{*1.192} \tag{4}$$

$$\text{Field C sand:}\quad TSI = 1.4131\ E^{*1.159} \tag{5}$$

The shales from Fields A and B are fit with the polynomial:

$$\text{Field A and B shales:}\quad TSI = -0.1786\ E^{*2} + 8.9286E^{*} - 7.1429 \tag{6}$$

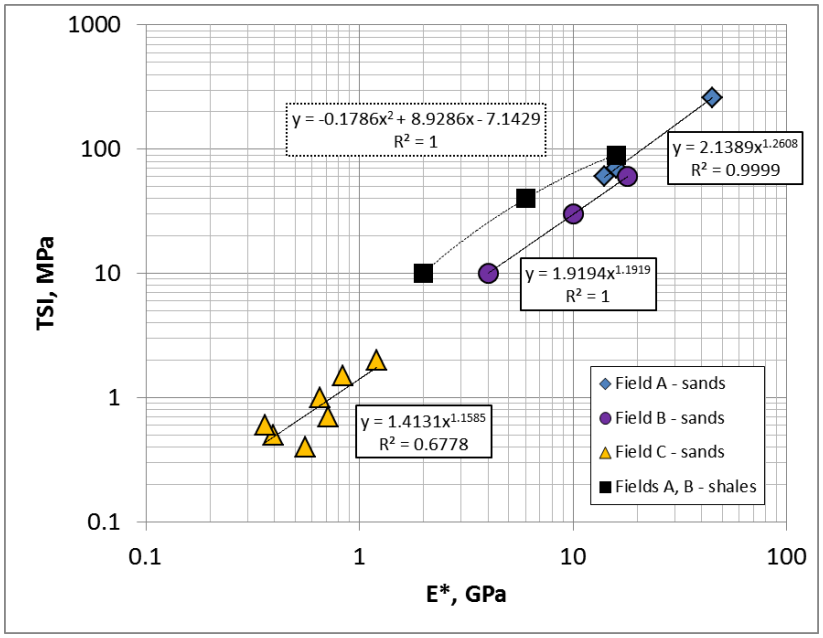

Figure 6. Group-wise correlation between TSI and E* with best fits per lithology

The obtained fits show that the correlation between TSI and E* for GoM sands is very good over a wide range of strengths. More complex mechanical behavior may explain the different trend observed in shale, although more data points might lead to finding a power law equally relevant.

Based on these results, we find that the TSI and E* parameters are adequately comparable in representing the variations of mechanical properties along a given profile (as shown in Figures 3-5). In addition**,** those parameters are very consistent in their relationship of magnitude, especially in sands. This provides a comparatively attractive method as the impulse Hammer is non-destructive and provides independent measurements at mm scale.

Impulse Hardness H

As described in the methods section, the Impulse Hammer produces an additional parameter which is sensitive to the permanent deformation experienced by the material during impact. This parameter, the impulse hardness, offers a more complete description of the mechanical behavior of the material during the test. The impulse hardness H operates in the numerical inversion as a scaling factor on the initial impact velocity and reflects the contrast between the velocities at impact and after rebound. Therefore, it correlates with another strength index known as the Leeb rebound hardness. Although H essentially allows to draw a more complete picture of the elasto-plastic mechanical response of the material during Impulse Hammer testing, it may also be used in the context of the present study to achieve a TSI prediction that does not necessitate the definition of rock types based on core observation. To explore that possibility, the data

set presented here was first reworked to allow for a one-to-one correspondence at each depth between TSI and pairs of E* and H values. That was achieved by averaging the TSI data over entire Impulse Hammer depth spacings. Doing so, one can use the trends that were defined in Figure 6 to cross-plot the predicted TSI versus the measured TSI for all individual Impulse hammer data points. This comparison is shown in Figure 7a. Without changing anything to the results obtained using the histogram analysis, we observe that the predicted TSI values lie within a factor of two of the measured ones over three orders of magnitude. In Figure 7b, instead of using the rock types of Table 3, the impulse hardness was used to distinguish between two populations which can be loosely defined as sands and shales. As can be seen on the plot, this procedure leads to a very similar result, suggesting that in regard to the objective set here of recovering TSI values from Impulse Hammer measurement, the use of both E* and H yields a result that is as satisfactory as the one of E* and rock types defined from core observation.

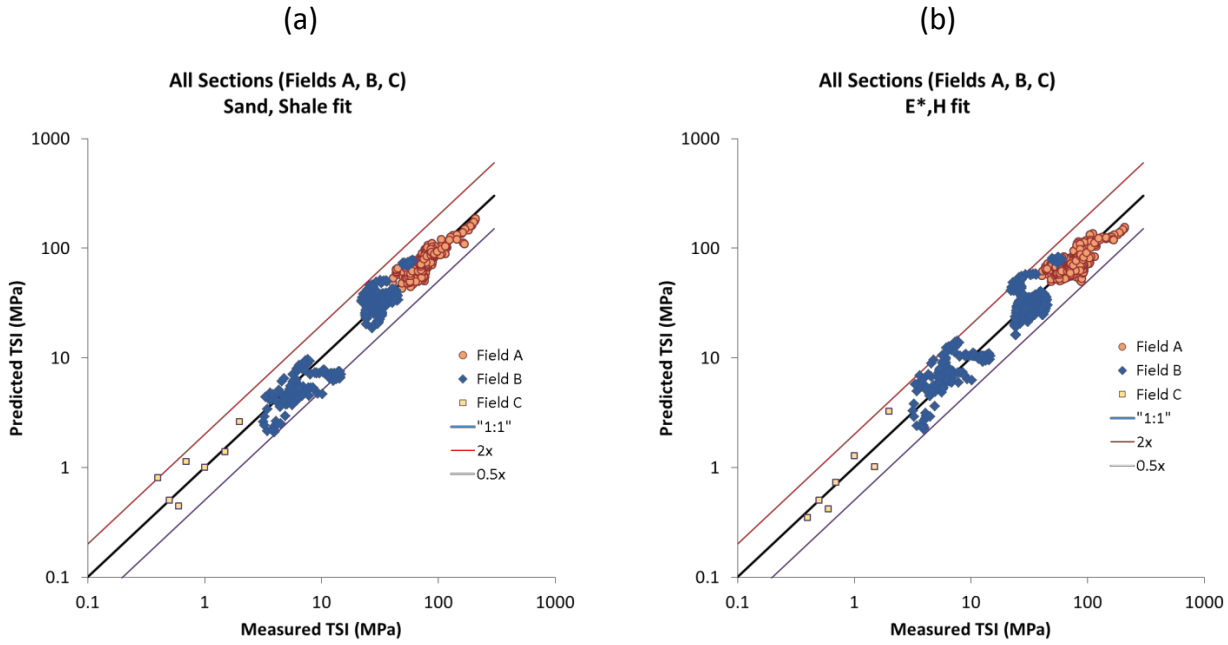

Figure 7. Comparison between predictions realized using the Impulse hammer data. (a) Using the fits of Figure 6 which use a lithology-based separation. (b) With Impulse Hammer data only but using the hardness H as a rock type indicator.

In conclusion, the trial conducted on various BP GoM core to validate the Impulse Hammer as a mechanical profiling tool can be considered successful as benchmarked against existing TSI data. Both rock-type specific and rock-type independent correlations are shown to fit the GOM dataset spanning 3 orders of magnitude in strength. It is worth noting here that this study implicitly assumes that the Scratch Test results are a representation of the variations that would be observed for uniaxial compressive strength data. Comparing the Impulse Hammer directly with UCS data, and extending the dataset to include a wider range of rock-types and compositions, could constitute another worthwhile validation step. Looking forward in time, it appears that Impulse Hammer

provides a more complete set of mechanical parameters that should therefore be tested against more complex data sets such as a combination of UCS and acoustic velocity in order to explore its potential for a wider applicability. Modifications to tip geometry and impact force are being explored as ways to characterize additional mechanical properties, including terms such as brittleness, tensile strength, and mechanical anisotropy.

ACKNOWLEDGEMENTS

The authors would like to thank BP America, ALS Reservoir Laboratories, BHP Billiton Petroleum, Chevron, Conoco Phillips, Exxon, New England Research and Petrobras companies for permission to publish this work.
This paper reflects the views of the authors and does not necessarily reflect or represent those of their employing companies.

REFERENCES

1. Chang, C., Zoback, M.D. et al. 2006. Empirical relations between rock strength and physical properties in sedimentary rocks. *Journal of Petroleum Science and Engineering*, **51**, 223-237.
2. Adachi J., and E. Detournay. 1996. Drescher A. Determination of rock strength parameters from cutting tests. *2nd North American Rock Mechanics Symposium*.
3. Detournay E., A. Drescher, P. Defourny, and D. Fourmaintraux. 1995. Assessment of rock strength properties from cutting tests: Preliminary experimental evidence. *Proc Of the colloquium Mundanum on Chalk and Shales*, Brussels. p. 11–3.
4. Detournay E, A. Drescher, and D.A. Hultman. 1997. Portable rock strength evaluation device. US Patent 5,670,711. U.S. Patent; 5, 670, 711.
5. Richard T, E. Detournay, A. Drescher, P. Nicodeme, and D. Fourmaintraux. 1998. The scratch test as a means to measure strength of sedimentary rocks. *SPE/lSRM EUROCK 98*.
6. Naeimipour, A., J. Rostami, E. Keller, O. Frough, S. Wang. 2015. Estimation of rock strength by means of scratch probe. 49th US Rock Mechanics/Geomechanics Symposium. San Francisco, California, 28 June-1 July.
7. Detournay E, and P. Defourny. 1992. A Phenomenological Model for the Drilling Action of Drag Bits. *Int J Rock Mech Min Sci Geomech Abstr*.
8. Rathbun, A.P., S.R. Carlson, R.T. Ewy, P.N. Hagin, C.A. Bovberg, G.N. Boitnott. 2014. Non-destructive impulse based index testing of rock core. 48th US Rock Mechanics/Geomechanics Symposium. Minneapolis, Minnesota, 1-4 June.
9. Johnson, K. 1985. *Contact Mechanics*. Cambridge: Cambridge University Press.

A CASE STUDY FOR EFFECTIVE LABORATORY EVALUATION OF MEOR TECHNOLOGY IN SULFIDE CONTAMINATED MATURE OIL FIELDS

Cicha-Szot R.[1], Falkowicz S. [1], Launt P. [2], Nelson S. [2], Grzesiak J. [3]
[1]Oil and Gas Institute – National Research Institute, Kraków, Poland
[2] RAM Biochemicals, Inc. Research Triangle Park, North Carolina, USA
[3] EIT+ Wrocław Research Centre, Poland

This paper was prepared for presentation at the International Symposium of the Society of Core Analysts held in Snowmass, Colorado, USA, 21-26 August 2016

ABSTRACT
This paper describes an extensive MEOR experimental program for sulfide contaminated mature oil fields comprised of a series of core flooding and glass model experiments and measurements of fluid properties using sulfide contaminated reservoir fluids to determine if the selected microbial system could be effective for enhanced oil recovery and potentially effective to inhibit souring. The selected microbial composition demonstrated positive growth in a sulfide contaminated environment, and core flooding tests produced increases in oil recovery 2% to over 10% above waterflooding. Core and sand pack studies confirmed that the MEOR displacement mechanisms were not inhibited by sulfide levels in the Grobla oil field.

INTRODUCTION
The occurrence of poisonous and corrosive hydrogen sulfide in aqueous systems is a major problem in upstream and downstream oil and gas production. In addition to corrosion and iron sulfide plugging it can lead to environmental hazards and reduced oil value. Moreover, it limits the use of standard MEOR technology. Among the Sulfate Reducing Bacteria (SRB) mitigation methods found to be useful in MEOR work, competitive exclusion emerges as the most efficient. This method uses fast growing microbes, both facultative anaerobes (nitrate respiration) and fermentative anaerobes that can out-compete the SRB's sulfate respiration. Since the role microbes play in MEOR is strongly correlated with growth and the production of primary and secondary metabolites, a dual role of enhanced oil recovery and SRB mitigation is conceivably possible.

Grobla, a mature oil field located in the northern part of central Carpathian Foredeep was selected for the current field trials. Two types of reservoir rocks are present and hydrocarbons are accumulated in a structural stratigraphic (the Oxfordian carbonates sealed by the marly Senonian – Turonian deposits) and stratigraphic (the pinching out of the Cenomanian sandstones) type traps [1]. The field produces light oil with gravity 38.36 - 42.97 ºAPI. Production is in decline and undergoing reinjection of production brine in a waterflood configuration. Challenges to effective MEOR treatment in this field arise from the levels of hydrogen sulfide (H_2S) and sulfide in production fluids (43g/m^3

of extracted gas and from 300 to 350 mg/dm^3 of formation water) which could alter or inhibit growth of the microbial composition selected for this field trial. Additionally, we needed to investigate whether the sulfide would diminish other aspects of microbial modes of action requisite to increase Recovery Factors necessary for economic success.

EXPERIMENTAL

The microbial system (MS) selected for the Grobla pilot was similar in composition to the one used earlier for the Plawowice MEOR project. Bacterial strains selected for Grobla were adapted to grow in sulfide free sterile brine that otherwise matched Grobla water analysis both chemically and osmotically. Sugar beet molasses was used as carbohydrate and nitrogen sources. Microbial materials for Grobla were batch produced in 30L and 300L Sartorius fermenters at the BTEC facility in Raleigh, NC, USA. The final 300L batch was concentrated in disc bowl centrifuges to produce the Grobla microbial system inoculum (MSI) which was cryo-protected and air shipped frozen to the INiG-PIB laboratory in Krakow, Poland for laboratory studies and field application.

A novel, but simple closed system using plastic syringes in anaerobic bags was developed to incubate oil and brine with the microbial materials. Multiple tests were conducted; three series contained 5% MSI (microbial system inoculum / bacterial concentrate) and two series each with 2.5% and 0.5% MSI. Tables 2 and 3 show the results of serial analyses of the two liquid phases by LSRV (low shear rate viscosity) and interfacial tension (IFT) measurements. Basically, lab procedures consisted of serial inoculations of oil (Fig.1), followed by 144 hours of anaerobic incubation at reservoir temperature (35ºC). Further examination of inoculated and control oil using full computational rotational viscometer (Anton Paar Physica MCR 301) generated quantitative indexes describing the degree of oil compositional alteration such as: Newtonian Index (NI), the Delta Viscosity Index (DV) and Enhanced Oil Recovery Index (EOR) related only to viscosity (Table 4). Additional experiments using core plugs and sand pack models were conducted to evaluate microbial system performance. All tests were carried out under anaerobic conditions on TEMCO® core flooding system using original reservoir fluids under simulated reservoir conditions (pressure, temperature, flow rate). Five core plugs and 4 sand packs (1 inch in diameter and 11.8 inches in length) were prepared with different grain size and/or layering and marked as Z1-Z4 (Table 1).

After determining the basic petro physical parameters of absolute permeability and porosity, core plugs and sand packs were saturated with Grobla Formation Water (GFW) by vacuum, aged for one month and then evacuated by a displacement method using high pressure gradients, after which they were saturated with reservoir oil until irreducible saturation of GFW (Swi,) was obtained. This allowed for estimation of oil saturation of the cores and packs. Waterflooding and MEOR treatment were then simulated to produce recovery factor (RF) volumes. Core plugs and sand packs were then injected with one pore volume of bio-product and incubated for 4 days at 35°C under anaerobic conditions. Microbial enhanced waterflood simulation displaced additional oil (Table 1).

To confirm microbial activity in plugs cryo-SEM and energy-dispersive X-ray (EDX) mapping were performed. Cores were thin sliced and immediately mounted on microscope stubs without any adhesives. Samples were immersed in liquid nitrogen until they reach its boiling temperature to avoid evaporation of oil remnants. Frozen samples were quickly transferred to the preparation chamber (Quorum) to coat them with platinum. The temperature at the preparation chamber and at the microscope chamber was -140 C. Samples were sputtered with platinum for 80 sec/10uA and then transferred to the cross-beam field-emission scanning electron microscope chamber (Auriga60, Zeiss). Observations were made at 25kV of electron beam voltage using the SE2 and InLens detectors (Pic. 1,2). Cross-sections made with FIB were visualized at 2kV with ESB detector. The SEM-EDX mapping was performed at 25kV and -140 C using the Oxford instrument and Aztec software.

RESULTS AND DISCUSSION

Initial experiments were designed to verify the hypothesis that a dual role of microbial enhanced oil recovery and H_2S mitigation is possible. Laboratory tests of Grobla production fluids show high levels of sulfide and low levels of indigenous SRB's. This suggest that at least some H_2S at Grobla may be due to a combination of biotic and abiotic processes from deeper in the Grobla formation rather than SRB activity in the near well bore and producing formation's water. However, SRB's are present in Grobla brine which has an alkaline pH of 7.6-8.0, and therefore conducive to SRB growth.

The first step in verifying a possible dual role was to confirm that the selected microbial system is capable of displacing additional oil under simulated oil field conditions. One sees from Table 1 that microbial treatment after initial waterflooding recovered additional oil. The average coefficient obtained in the laboratory from simulation microbial waterflooding is 5.2% and per individual cores it range from 2.5% to 10.6%.

A second confirmation step was aimed at mitigating the biotic component of sulfide generation using known SRB mitigating methods judged compatible with MEOR. This step used nitrite and/or a nitrite proxy (nitrate). It it required additional RF testing with using various SRB Mitigants, authentic field samples of Grobla brine and oil and microbial system materials. Shown in Table 2 are increases in reservoir brine viscosity with the addition of MSI (microbial system inoculum), N (Nitrogen) and Mo (Molybdate). This is a very positive factor when assessing the potential effectiveness of the proposed microbial treatment technology.

The best results from waterflooding are obtained when the viscosity of the oil recovery displacement fluid is close to the viscosity of the fluid being displaced [3,4]. Quantitatively, the mobility factor (M) expresses the impact of changes in viscosity of resorvoir fluids as a ratio. Ideally, the value of M should approach unity. All microbially treated samples had lower values of M than the baseline value for crude oil / brine. The incubated sample that included molybdate salt produced the lowest M value of 1.41.

Another means of evaluating MEOR treatability is by oil viscosity analysis [2]. Oil is a very complex liquid that exhibits typical non-Newtonian behavior. Viscosity is shear rate sensitive (pseudo plastic model) and it correlates strongly with the fluid dynamics occurring in the pore space. Specific quantitative lab procedures were conducted to measure the shift in rheological properties in treated (inoculated) and untreated (control) samples. One can see from Table 4 that all obtained indexes for bio-treatability show positive changes in fluid characteristics after microbial treatment. The comparison between control and inoculated oil samples clearly shows microbial cracking in that all EOR values are greater than 1.10. A global change in viscosity is also indicated by DV values greater than 0.10. Cryo-SEM images combined with EDX mapping also confirm positive bacterial growth activity in a sulfide contaminated environment and show clogging of pores by the biofilm produced by the bacteria strains (Pics.1,2).

CONCLUSION

Laboratory studies point to the possibility of a dual role for microbial enhanced oil recovery; 1) increased oil recovery, and 2) inhibition of oil field souring. The selected microbial composition demonstrated positive growth in a sulfide contaminated environment, and core flooding tests produced increases in oil recovery 2% to over 10% above waterflooding. Core and sand pack studies confirmed that the MEOR displacement mechanisms were not inhibited by sulfide levels in the Grobla oil field production fluids. Laboratory studies tested the hypothesis that H_2S mitigation and microbial enhanced oil recovery at Grobla are not mutually exclusive. The Grobla pilot field project which commenced on March 25th may further validate a dual role of microbial EOR and H_2S mitigation.

ACKNOWLEDGEMENTS

We wish to thank the Biomanufacturing Training and Education Center at North Carolina State University and RAM Biochemicals for producing microbial materials for the Grobla project, and to RAM Bio for collaboration on laboratory testing and field application protocols. Thanks as well go to the Polish Oil and Gas Company management for their cooperation and permission to publish this paper.

REFERENCES

1. Golonka J. and Picha F. J., *Carpathians and their Foreland: Geology and Hydrocarbon Resources*, AAPG Memoir 84 (2006), 351–393, ISBN Number: 0891813659
2. Maure M. A., Dietrich F. L., Diaz V. A., Argañaraz H., "Microbial Enhanced Oil Recovery Pilot Test in Piedras Coloradas Field, Argentina*"* SPE 53715, 1999, Paper presented at SPE Latin American and Caribbean Petroleum Engineering Conference held in Caracas, Venezuela, 21–23 April 1999.
3. Lake, L. W., Johns R. T., Rossen W. R., Pope G. A, *Fundamentals of enhanced oil recovery*, Society of Petroleum Engineers, 2014.
4. Kantzas A., Bryan J., and Taheri S. *Fundamentals of Fluid Flow in Porous Media*,http://perminc.com/resources/fundamentals-of-fluid-flow-in-porous-media/

Table 1. Core and sand pack test results

Plug/Sand Pack	Initial Recovery Factor (RFi) [%]	volume of displaced oil in MEOR [cm3]	final recovery factor (RF_f) [%]	Increment of recovery factor E_{mwf} [%]
1-C	24.4	0.00	24.4	**0.0**
Gr-5	17.8	0.20	22.2	**4.4**
Gr-8	14.5	0.20	18.2	**3.6**
Gr-9	15.4	0.55	26.0	**10.6**
Gr-10	19.0	0.20	23.8	**4.8**
Gr-11	19.6	0.13	22.2	**2.5**
Z-1	71.0	3.10	76.8	**5.8**
Z-2	81.8	1.50	84.5	**2.7**
Z-3	70.7	1.50	74.4	**3.7**
Z-4	82.2	1.05	84.6	**2.3**

Initial Recovery Factor (RF) from saturated cores and sand pack columns, volume of oil displaced by MEOR, final RF of waterflood and MEOR flood combined, and percent of incremental oil recovered.

Table 2. MEOR viscosity, surface tension and pH alteration

Fluid	Viscosity	Surface tension	pH	Viscosity	Surface tension	pH
	[mPas]	[mN/m]	[-]	[mPas]	[mN/m]	[-]
	Base measurement			After 6 days of incubation		
Oil	3.220	26.00	-	-	-	-
Brine	0.973	59.70	5.60	0.973	59.70	5.60
MSI	1.157	52.77	6.70	1.361	41.20	4.87
MSI+N	1.173	52.45	6.73	1.270	35.00	4.80
MSI+N+Mo	1.128	52.20	6.72	2.035	40.57	4.85

Table shows changes from baseline values for viscosity, surface tension and pH after 6-day incubation period. MSI = Microbial System Inoculum, N = Nitrogen, Mo = Molybdate

Table 3. Percentage change in IFT

Phase	Interfacial tension [mN/m]	Change [%]
Brine/oil	15.4	-
MSI/oil	6.8	55.8
MSI+N/oil	10.7	30.5
MSI+N+Mo/oil	12.4	19.5

MSI = Microbial System Inoculum, N = Nitrogen
Mo = Molybdate

Table 4. MEOR Indexes

Oil after contact with:	MEOR Indexes		
	NI	DV	EOR
MS	3.2	0.17	1.21
MS+N	3.8	0.15	1.18
MS+N+Mo	3.9	0.16	1.19

A positive test for bio-treatability results when the value of NI > 1.10, DV > 0.10, and EOR > 1.15

NI = Newtonian Index

$$NI = \left(\frac{(\mu app^{control})^{minSR} - (\mu app^{control})^{maxSR}}{(\mu app^{inoculated})^{minSR} - (\mu app^{inoculated})^{maxSR}}\right) TMD \quad \text{..... Eq. 1}$$

DV = Delta Viscosity Index

$$DV = \left(\frac{\sum_{i=minSR}^{maxSR}(\mu appi)^{control} - \sum_{i=minSR}^{maxSR}(\mu appi)^{inoculated}}{\sum_{i=minSR}^{maxSR}(\mu appi)^{control}}\right) \quad \text{..... Eq. 2}$$

EOR = Oil Recovery Index

$$EOR = \frac{1}{1-DV} \quad \text{..... Eq. 3}$$

TERMS for Eq. 1-3: Control = original sample (pre-inoculation), minSR = minimum explored shear rate [1/s], maxSR = maximum explored shear rate [1/s], i = data point, spatial reference, TMD = Temperature of maximum discrimination of rheological properties [ºC]

OTHER TERMS: GFW = Grobla Formation Water, SRB = Sulfate Reducing Bacteria, IFT – Interefacial Tension, RF = Recovery Factor, Swi = irreducible saturation, MSN = Microbial System Nutrient, MSI = Microbial System Inoculum, MS = Microbial System

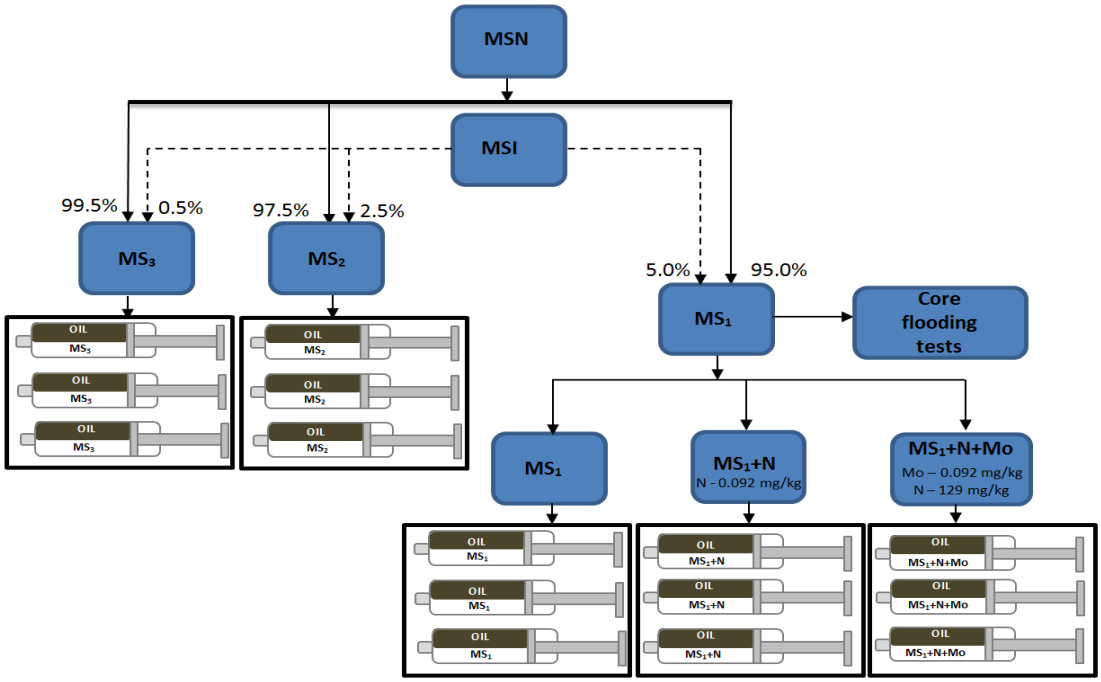

Fig. 1. Scheme of laboratory incubation tests (MS – microbial system, MSN – microbial system nutrient, MSI – microbial system inoculum, N – nitrogen, Mo – molybdate)

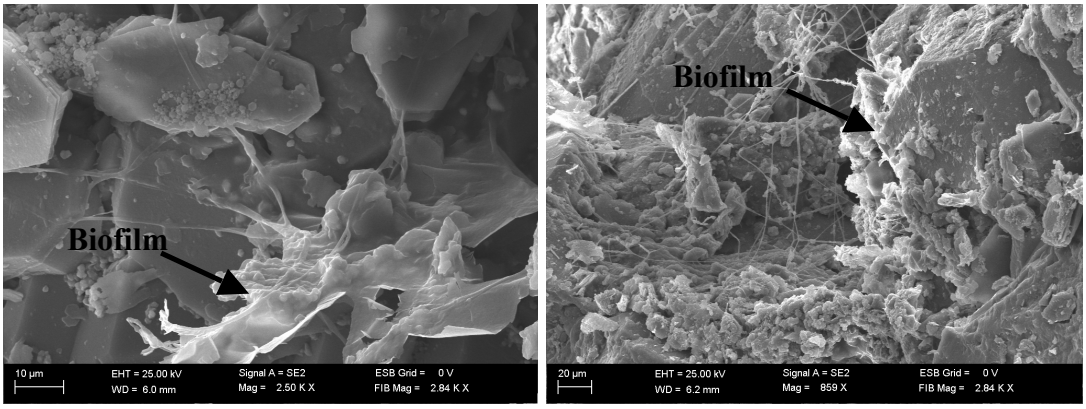

Pics. 1 and 2. Cryo-SEM observation made at 25kV using the SE2 and InLens detectors of an Auriga60 Zeiss cross-beam field-emission scanning electron microscope. Image show microbial growth in the core after incubation.

INACCESSIBLE POROSITY – INSIGHT TO PORE DEVELOPMENT AND SOLUTIONS TO MICP DATA INTERPRETATION

Leśniak G.[1], Such P.[1], Komorowska K.[2]
[1] Oil and Gas Institute – National Research Institute, Poland,
[2] EIT+ Wrocław Research Centre, Poland

This paper was prepared for presentation at the International Symposium of the Society of Core Analysts held in Snowmass, Colorado, USA, 21-26 August 2016

ABSTRACT
Shale is the most abundant sedimentary rock, which under certain conditions might be both source and reservoir rock. A Micrometer to nanometer scale pore system has been found in organic matter and inorganic matrix of shale reservoirs, which can have significant influence on storage and fluid transport. Peculiar MICP results are observed in 5-15% of the investigated Silurian shales from the Central European formations. These samples have calculated porosity that is greater than total porosity measured with the use of helium pycnometry on powdered samples. This effect is visible only for pores of diameters smaller than 10 nm and produces a characteristic shape of cumulative pore size distribution curves. The combination of helium pycnometry, MICP and adsorption investigations as well as a set of mineralogical measurements (XRD, thin section microscopic investigations, SEM analyses) were performed in order to describe pore space. The results show that inaccessible porosity is created by a large number of isolated pores, which collapse under great pressure of mercury exerted during measurements. The results show that isolated nanopores can create up to 4% of MICP porosity.

INTRODUCTION
A problem of inaccessible porosity was mentioned by several authors. Clarkson at.al. [1] estimated the volume of this part of pore space in the range of 15-30%.Typical situation is presented in Figure 1A and 1B. During laboratory investigations of the Polish shale rocks about 5% of investigated samples show the effect presented in Figure 1C For pore diameters smaller than 10 nm cumulative curve sharply goes up and reaches the volume of porosity greater than open porosity calculated with the use of helium pycnometry, or even greater than total porosity (which is performed using powdered sample). The hypothesis is that this effect is caused by closed porosity which collapsed under very high pressure applied during MICP measurements.

INVESTIGATIONS
More than 2000 samples from the Polish shale basin were investigated. A workflow consisted of density measurements, total and connected porosity investigations as well as nitrogen adsorption [5] and high pressure MICP analyses and petrographical analyses with the use of thin sections and SEM [2,3,8]. This set of analyses was done for all samples.

Special attention was paid to prepare homogeneous samples to all analyses. Total porosity was performed with the use of powder sample while connected porosity, MICP and adsorption low pressure analyses were done using granulated samples (0.5-1 mm) [4,8]. Such granulation conserves porosity and specific surface of investigated rocks (correctness and reliability was checked during independent investigations). Total porosity was measured with the use of powdered sample and this analysis shows some volume of closed pores in great part of investigated samples. These both analyses were done with the use of helium and mercury pycnometry. During MICP analysis full intrusion and drainage curve are completed. In the figures only part of intrusion curve is presented. From 40 m of core analyzed during petrophysical investigations 6 samples were chosen to cover a broad range of properties (Table 1). Additionally, for all selected samples a thin section was prepared and for 3 of them SEM analyses were performed. One can see from Table 1 that sample 2 shows an extreme value of MICP porosity in comparison with total and open. To a lesser degree this phenomenon is also present in sample 5 (helium porosity is almost equal to MICP porosity). Sample 1, 3, 4 and 6 were used in order to prepare reliable pore space characteristics of over 80 % of shale rock matrix. The mineral composition of all samples is very similar. The main minerals are quartz (29-45%), minerals from group muscovite/illite (33-45%), chlorite (6-17%), carbonates (calcite, dolomite, ankerite) (2-6%), feldspar (2-5%), minerals from illite/smectite group (2- 8%) and pyrite and marcasite (3-8%). Generally the analyzed rocks can be described as silty clays (clays with a large admixture of thicker detrital material).

These samples contain from 1 to 7% of TOC. A degree of thermal transformation of organic matter reached the level of gas window. SEM analyses were performed for samples number 2, 3 and 5. These samples were chosen because of their extreme MICP and porosity analyses (total and open porosity). In these samples a mixed pore network is dominant with the presence of interparticle pores (interP), intraparticle pores (intraP) and pores in organic matter (OM) [6,7].

DISCUSSION

MICP measurements show generally low calculated porosity. All factors present during analyses decreased it. These are compressibility of rocks and bad penetrability of mercury. The effect is that 60-70% of the investigated samples show calculated porosity lower than 2,5%. For the rest this parameter could reach 5%.

The results presented for sample 2 from Table 1 show, that in shale rocks there must exist closed porosity, not penetrable even to helium (even for powdered sample). Of course there are no isolated pores in geological time because of molecular diffusion but we are interested in exploitation time. In this time these pore can be treated as isolated (eventually the volume of transport is negligible. Typical shape of such cumulative curve shows inflexion point for diameter lower than 10 nm – it means it is connected with the pressures greater than 1000 at and covers one or two points of cumulative curve (it mean that time is 1-3 min). These parameters indicate that the observed phenomena must depend only on invades of mercury into closed objects.

After reaching inflexion point, cumulative volume occupied by mercury rapidly grows. The key word to this situation is high pressure. When the pressure produced by

porosimeter becomes greater than 50 000 psi and still increases, the closed pores start to squeeze and break providing additional volume of pore space. Such great pressure is necessary to displace mercury through nanopore space and additionally break the pore in organic matter. For those types of rocks MICP shows in fact rather total than dynamic porosity.

In order to confirm above stated hypothesis three questions must be answered:

- Is really such part of pore space closed/inaccessible?
- Why do such pores occur only in 5-8% of investigated samples?
- Which element of shale rock is responsible for closed pore space (residual matter or some kinds of minerals)?

Answers to above mentioned questions might be found analysing MICP data and SEM images. For discussed samples (sample 2 and 5) MICP data do not show distribution of diameters (below 10 nm) but only the pressure of collapse. The results show that the only restriction for inaccessible pores is diameter of powdered grains (too big to open that pore space). All surface effects were precisely removed from MICP curves. Figure 2 shows cumulative curves of selected investigated samples. Collapse of sample 2 and 5 started near pore diameter equal to 10 nm. Figure 3 shows incremental curves for the same set of samples. Open part of its pore space is built with pores of diameter 1 – 0.1 μm. The interpretation is that the dominant peak in samples 2 and 5 consists of inaccessible pores, closed accessible pores (open by powdered sample) and even part of open pores. The significance of this effect is even greater because porosity built with pores greater than 10 nm is less than 2% for these samples so the rest of pore space (over 8 and 6%, respectively) is included in great peak below 10 nm. More precise and direct answer to the stated questions is given by SEM images analysis which indicates main differences between pore space in analyzed shale rocks (resolution of instrument equal to 5 nm). Figure 4 shows SEM images of pore space of investigated samples (sample 2 - A, B, sample 3 - C, D and sample 5 - E, F). In sample 2 all OM pores, interP pores and intraP pores were found, which suggests mixed pore network [7]. Pores observed in organic matter (1.9%), which is highly dispersed in a rock sample, achieve the size of 300 nm and are mainly in the center part of the OM grains. Arrangement of pores inside the grains of OM, with no contact with the grains of mineral framework (Figure 4 A), allows for a statement that the pores occurring in OM, in the majority of cases, are isolated. Organic matter is pressed into ductile clay mineral packages, which provide also isolation of OM from interparticle pore space. Moreover, in pyrite framboids interparticle pores between crystals of pyrite were found and pores in OM, which fill and surround framboid structures. A part of pores in framboids might be also isolated by OM. Sample 2 shows also a number of intraparticle pores located in the plaques of clay minerals and detrital grains and interparticle pores (intrerP) between detrital grains. Presented SEM images suggest that differences between MICP and helium pycnometry might be associated with isolated pores in OM and framboidal pyrites. Pore space of sample 5 (Figure 4 – E, F), in which similar effect like in sample 2 is observed, can also be described as mixed pore network. Both pores in OM, interP and intraP pores were distinguished. Differences from the sample 2 are associated with the location of the pores in the OM. Most of these pores adhere to the detrital grain boundaries and clay minerals, and probably creates the system

connected to the system of interparticle pores. These pores are larger than the pores observed in sample 2 (the size reaches 800nm). OM (3.66%) is also highly dispersed in the rock matrix. Differences are also observed in the pores of the pyrite framboids, which are filled with less OM resulting in fewer pores isolated. Such structure of the pore space results in lower number of isolated pores what consequently leads to slight difference between MICP (8.25%) and helium porosity (6.12%). In sample 3 inerP and intraP pores are two main types of pores observed. Although most of the OM do not contain pores, very few pores in OM might be distinguished. The size of such pores is in the range of several nm. The position of OM (7.16%) in the rock matrix indicates strong compression of OM between detrital grains and ductile clay minerals. Often thin laminas of OM are observed. No pores in OM indicates a different type of OM, requiring a greater activation energy for the generation of hydrocarbons. Rock-Eval studies showed that very high content of residual carbon (RC) indicating a very low transformation of OM in discussed sample.

Analyzing such samples another question arises: is existence of such isolated pores possible? In geological time it is not. Molecular diffusion is fast enough to connect all empty spaces in rocks. But this scale is not interesting for us. Our problem is: are such pores accessible during exploitation of shale well (up to three years). The first visible effect is difference of porosity between granulated and powdered sample. Difference between total and connect porosity shows volume of pores opened in powdering process. Empty spaces opened during collapse of pore space were also inaccessible by helium even for powdered sample. Dimensions of these closed pores are restricted only by dimensions of powder grains not by Washbourne formula. Taking into consideration very short path of migration in powdered sample and helium penetrability we can conclude that possible influence of this part of pores space on total flux will be negligible.

CONCLUSION

1. In part of examined samples there exists closed porosity, inaccessible even to helium. These pores can be opened only by collapse of rock due to high pressure. It manifests during high pressure MICP on the cumulative curve as a great peak of pores below 10 nm range of diameter. However, interpretation of MICP data needs to be performed very carefully, because as the results show, the pore sizes reflected by that peak are much higher than 10 nm. That is why, in order to depict pore size distribution, additional investigations are needed.
2. Inaccessible porosity is found in dispersed organic matter and in framboidal pyrite. Single pores can reach diameters of several hundreds of nanometers.
3. Higher value of MICP porosity than of open porosity might be considered as a parameter that indicates the occurrence of dispersed organic matter (highly thermally transformed) in the rock sample.
4. A lower value of MICP porosity than open porosity in the shale samples suggests the presence of OM that is considered as a low thermal maturity OM (another type of OM) or in this sample pores are filled with asphaltenes (as a result of bitumen migration).

ACKNOWLEDGEMENTS
This article is the result of research conducted in connection with a project funded by the National Centre for Research and Development as part of programme BLUE GAS – POLISH SHALE GAS. Contract no. BG1/MWSSSG/13

REFERENCES
1. Clarkson C.R., Solano N., Bustin R.M., Bustin A.M.M., Chalmers G.R.L., He L., Melnichenko Y.B., Radlinski A.P., Blach T.P., "Pore structure characterization of North American shale gas reservoirs using USANS/SANS, gas adsorption, and mercury intrusion" *FUEL*, (2013) 103, 606-616
2. Clarkson C.R., Wood J., Burgis S., Aquino S., Freeman M. "Nanopore-Structure Analysis and Permeability Predictions for a Tight Gas Siltstone by Use of Low-Pressure Adsorption and Mercury –Intrusion Techniques." *SPE* (2012) -155537
3. Curtis M.E., Cardott B.J., Sondergeld C.H., Rai Ch., S., "Development of organic porosity in the Woodford Shale with increasing thermal maturity." *International Journal of Coal Geology, (*2012*),* no 103, 23-31
4. Howard J.J., "Porosimetry Measurement of Shale Fabric and Its Relationship to Illite/Smectite Diagenesis." *Clays and Clay Minerals*, (1991) v.39, no.4, 355 – 361
5.Kuila U., Prasad M. 2011: Surface area and pore size distribution in clays and shales, SPE-146869
6. Loucks R. G., Reed R. M., Ruppel S. C., Jarvie D. M., "Morphology, genesis, and distribution of nanometer-scale pores in siliceous Mudstones of the Mississippian Barnett shale." *Journal of Sedimentary Research* (2009), v. 79, 848-861
7. Loucks R.G., Reed R. M., Ruppel S. C, Hammes U., "Spectrum of pore types and networks in mudrocks and a descriptive classification for matrix-related mudrock pores." *AAPG Bull*. (2012), v.96 no 6, 1071-1098
8. Such P., "Porosity: what does it mean in shale gas reservoirs." *Nafta-Gaz*, (2014) no7, 411-415

Table1. Porosity data

Sample ID	MICP porosity (%)	Total porosity (%)	Open porosity (%)
1	4.98	5.49	2.56
2	10.22	4.62	0.70
3	1.76	8.57	3.29
4	2.88	8.41	8.40
5	8.25	8.53	6.12
6	4.19	8.00	1.85

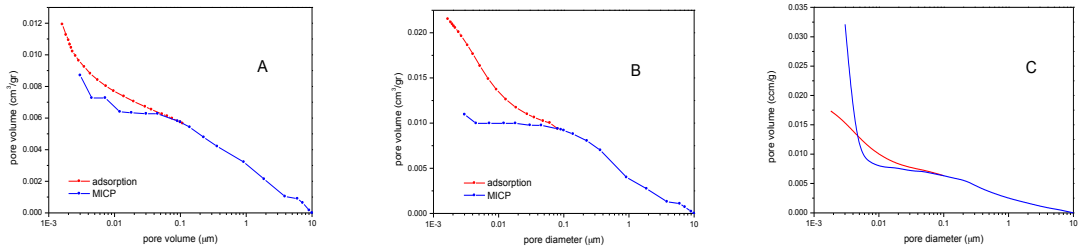

Figure 1. Comparison of MICP and adsorption pore size distributions cumulative curves calculated using BHJ and Halsey theory. MICP – blue curve, Nitrogen adsorption – red curve. Merging procedures was applied to combine both cumulative curves. Of course MICP curves shows volume of porosity in a function of pore throats while adsorption shows pore bodies. Obtained results are similar to results obtained by Clarkson at al. Typical curves are presented in Fig A and B. Adsorption curve in fig A could be shifted during greater values of diameter but because of plateau or near plateau part of MICP curve total volume of penetrated pores can be reliably estimated. Fig B shows the same run of both curves in some range of diameters and it also give us opportunity to calculate pore volume. Figure 1C – calculated total volume is lower than calculated MICP porosity

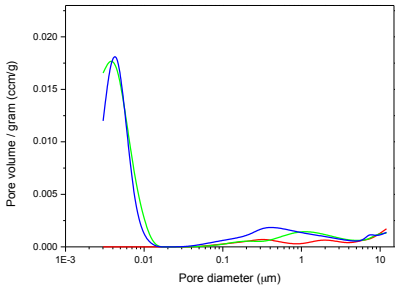

Figure 3. Incremental curves
(sample 2 – green, sample 3 – red sample 5 – blue)

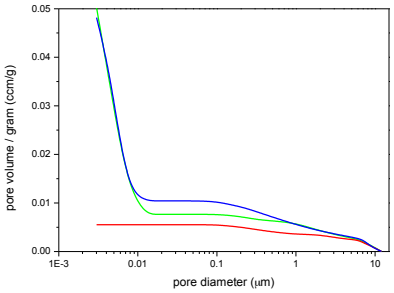

Figure 2. Cumulative curves for 3 investigated samples
(sample 2 – green, sample 3 – red sample 5 – blue)

Figure 4 Types of pore space in analyzed samples. A, B – sample 2, B, C sample 3, E, F – sample 5.

INJECTIVITY AND RETENTION OF NANOCELLULOSE DISPERSIONS IN BEREA SANDSTONE

Reidun Cecilie Aadland[(1)], Katherine R. Aurand[(1)], Ole Torsæter[(1)], Ellinor Bævre Heggset[(2)] and Kristin Syverud[(1,2)]
1) Norwegian University of Science and Technology, Trondheim, Norway
2) Paper and Fibre Research Institute, Trondheim, Norway

This paper was prepared for presentation at the International Symposium of the Society of Core Analysts held in Snowmass, Colorado, USA, 21-26 August 2016

ABSTRACT
In this study, the main objective was to examine the interactions between nanocellulose dispersions and Berea sandstone through retention studies using a vertically-oriented particle mobility coreflooding (PMC) procedure. The type of nanocellulose evaluated was cellulose nanocrystals (CNC).

The results showed that CNC in low salinity water (LSW) was able to transport through the core causing moderate rock impairment (permeability reduction between 17 % to 25 %). Furthermore, it was observed an increase in differential pressure as CNC concentration increased. Indicating that retention increases as a function of concentration. A higher pressure was obtained when injecting with a high flow rate (3.0 ml/min) compared to a low rate (0.3 ml/min). CNC at higher salt concentration (3.53%) was not stable and plugged the inlet of the core. More research is required to improve the stability of CNC in brine and thus increase its mobility through the core.

INTRODUCTION
Chemical flooding with polymers is considered one of the most promising enhanced oil recovery (EOR) methods and has been researched for over 40 years. The main objective with polymer flooding is to improve the macroscopic displacement efficiency by increasing the viscosity of the aqueous phase. A higher viscosity of water results in a favorable mobility ratio, which reduces viscous fingering effects and changes the flow pattern in the reservoir.[5,7,8] Polymers will also help to increase microscopic efficiency due to their viscoelastic nature.[5]

When polymer flooding is applied to a reservoir, water-soluble polymers are added to the water prior to injection. Today, two main polymers are used commercially; the biopolymer xanthan gum and the synthetic polymer hydrolyzed polyacrylamide (HPAM).[2] The disadvantages with HPAM are that they are sensitive to high reservoir temperatures and shear degradation. Xanthan gum on the other hand is less sensitive to shear degradation, but the polymer is susceptible to bacterial degradation. In addition, it has a significantly higher cost than HPAM.[7]

This study examines the potential of using a novel additive derived from cellulose for chemical flooding. Cellulose is a renewable, non-toxic and biodegradable biopolymer obtained from wood. A particle character is obtained by utilizing cellulose in the nanoscale (nanocellulose). Particle characteristics at this size attain an advantage in the micron sized pore throats compared to

dissolved polymers. The cellulose polymers occurs as bundles, not as single molecules, and they exhibit a high crystallinity. This makes them less vulnerable for degradation. It is therefore assumed that nanocellulose have a higher thermal stability and are less susceptible to bacterial degradation, compared to HPAM and xanthan gum.

Formation damage could be a problem when injecting polymers into a reservoir, as polymer molecules adsorb well at solid interfaces. Retention of particles inside the core creates an extra layer inside the pores and pore throats, which might lead to flow resistance. Furthermore, the adsorption is practically irreversible because it takes a large pore volume of displacing fluid to desorb the polymer.[8] Such a process might not be economically feasible. Hence, the polymeric additive is lost. Another option is to inject polymers with a higher initial concentration to take into account that some will be adsorbed by the rock. This will also cost more money and might not be the best solution. The most promising EOR additives have little to no adsorption. If the polymers exhibit high retention, they need to be modified to alleviate the issue; otherwise they will be excluded from further EOR research. Polymer chemistry, reservoir rock composition, temperature, salinity and polymer composition are the main factors influencing polymer retention.[5] A retention study on xanthan gum in a sandstone core showed that retention increased with increasing polymer concentration, and it also increased somewhat with the flow velocity.[4]

In this study, cellulose nanocrystals were flooded through a dry core plug to evaluate particle mobility. Ionic strength of the dispersion fluid and CNC concentration were varied to see if they displayed a trend with increasing or decreasing retention. The effect of flow rate was also evaluated.

EXPERIMENTAL MATERIALS

Base Fluids

Low salinity water (LSW) and synthetic North Sea water (NSW) were used as base fluids. LSW consisted of 0.1 wt.% sodium chloride (NaCl), while NSW comprised deionized water and seven different salts, resulting in a salinity of 3.53%. The base fluids were used as the aqueous phases into which CNC was dispersed.

Nanocellulose

Cellulose nanocrystals are rod-like particles with sizes in the nanometer range. The CNC used in this study were purchased from the University of Maine. This material was manufactured at the US Forest Service's Cellulose Nano-Materials Pilot Plant at the Forest Products Laboratory in Madison, Wisconsin. The cellulose nanocrystals were produced using 64 % sulphuric acid to hydrolyze the amorphous regions of the cellulose material, resulting in acid resistant crystals.[3] After washing, dialysis and sonication, a dispersion of 12 % CNC was obtained. This suspension was then diluted to 0.5 wt.% and 1.0 wt.% in the LSW and to 1.0 wt.% in the NSW.

Porous Media

The core plugs were extracted from a Berea sandstone block, which is considered to be strongly water-wet. Six core plugs were used in the study and their properties are listed in Table 1.

X-ray diffraction (XRD) analysis was performed for five samples taken from the same block as the core plugs used in this study. The results showed that the rock is composed of three main minerals: quartz (93.7 wt.%), microcline (5 wt.%) and diopside (1.3 wt.%).

Table 1. Properties of Berea sandstone core plugs. Porosity was measured with a helium porosimeter, and permeability was measured with air and corrected by use of the Klinkenberg effect.

Core #	Length [cm]	Diameter [cm]	Pore volume [ml]	Porosity [%]	Permeability [mD]
1	4.5	3.8	9.5	18.1	435
2	4.5	3.8	9.1	17.4	413
3	4.5	3.8	8.5	16.4	307
4	4.5	3.8	8.8	16.8	354
5	4.5	3.8	8.7	16.6	316
6	4.5	3.8	9.2	17.8	307
7	4.5	3.8	8.8	17.0	275
Average	4.5	3.8	9.0	17.2	344

EXPERIMENTAL METHOD

The standard PMC rig set-up was used for this study.[1] A dry core plug was mounted in a vertically-oriented core holder with 20 bar sleeve pressure. The base fluid or nanocellulose fluid was then injected from the bottom of the core. Effluent was collected from the top of the core holder every pore volume (PV) for 5 PV. A pressure gauge measured the pressure drop across the core. The core's final saturation was measured after flooding was complete. The cores were cleaned with methanol using a soxhlet extraction apparatus and dried in an oven at 60°C after flooding. Pre- and post-flooding porosity and permeability measurements were conducted to determine possible rock impairment.

Effluent samples were analyzed for concentration and pH. The concentrations of CNC will be determined quantitatively at a later point. However, CNC solutions become whiter and more opaque with increasing concentration, so it is possible to qualify concentration using visual observation. Therefore, the original injection fluid was placed in a vial and compared to the effluent samples. If the effluent had the same opacity as the original solution, it was concluded that little to no retention had taken place. As the transparency of the effluent increased, more retention was occurring. The retention results from the visual inspection were compared with the differential pressure curves for validation.

An overview of the experimental plan is displayed in Table 2. Concentration of CNC, dispersing fluid, and injection rate were the parameters that were changed for each experiment. The low flow rate was chosen to mimic the typical flow velocity in a reservoir (1 ft/day, which corresponds to 0.24 ml/min with the core's cross-sectional area).

Table 2. The different fluid types that were tested with the corresponding injection rates.

Core #	CNC concentration [wt.%]	Dispersing fluid	Flow rate [ml/min]
1	---	LSW	0.3

2	0.5	LSW	0.3
3	1.0	LSW	0.3
4	0.5	LSW	3.0
5	1.0	LSW	3.0
6	---	NSW	0.3
7	1.0	NSW	0.3

RESULTS AND DISCUSSION

A total of seven PMC experiments were conducted, where two of them were regarded as base cases. The LSW and NSW base cases were pure brines; they did not contain any nanocellulose particles. Therefore, no retention was occurring. The pressure curves from the experiments with nanocellulose particles were compared to the base cases. If the differential pressure was significantly higher than the base case, retention was assumed to occur, causing the pressure increase. On average, the cores were saturated 60 % at the end of the experiment. The pH was measured prior to injection and for the first and fifth pore volume of the effluent samples. It remained constant for all experiments.

LSW as Dispersing Fluid

Both concentrations that were used with LSW were considered stable solutions. The stability of 1.0 wt.% CNC with LSW was also confirmed in the research conducted by Molnes et al.[6] From the experimental results where the low rate was applied, it was observed a higher pressure for the case where 1.0 wt% CNC was used compared to 0.5 wt.% CNC (Figure 1A). The same trend was also observed when the high rate was used (Figure 1B). This indicates that particle retention increases with increasing CNC concentration. The same observation was also found in the retention experiments conducted on xanthan gum by Huh et al.[4]

For the low rate, both fluid systems follows the same trend as the base case, where the low concentration (0.5 wt.% CNC) is almost identical to the pressure curves of pure LSW (Figure 1A). The only difference is a slightly increased pressure at the end (pressure increased from 0.10 bar to 0.12 bar). This could be a result of particles adsorbing onto the rock grains leading to a tighter flow path and hence an increase in pressure. At the very end the pressure dropped to 0.10 bar again, which could mean that these particles were pushed further out or that a new flow path opened in the core.

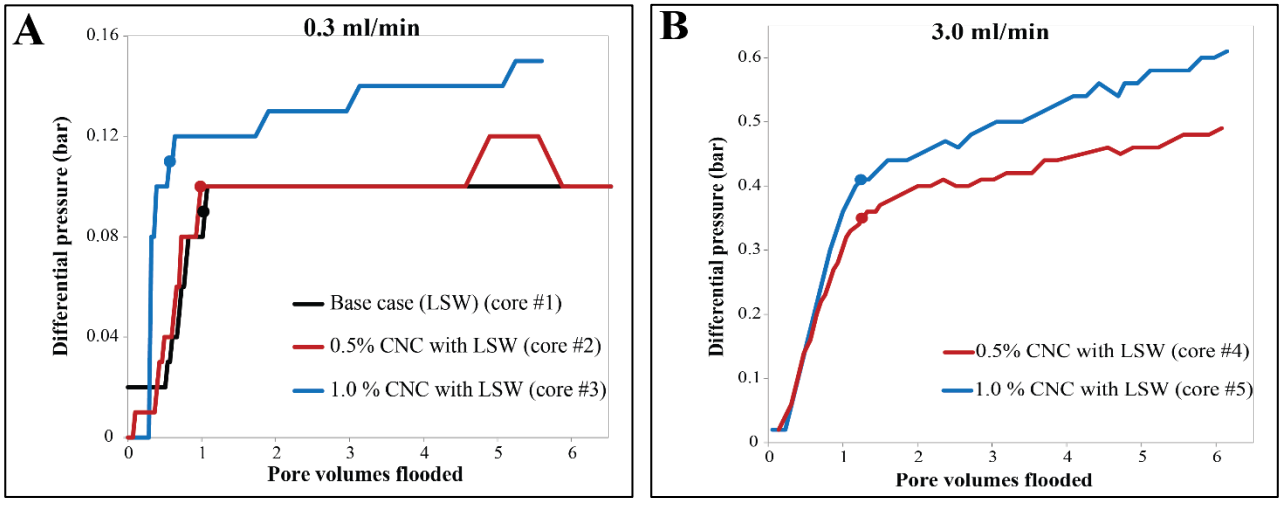

Figure 1. Pressure curves for the low rate (A) and high rate (B) using LSW as dispersing fluid for CNC. The points illustrate the breakthrough times for the water.

A base case was not conducted for the high rate in this particular study. However, Aurand et al.[1] did a PMC study where different rates were tested using NSW as base fluid. In the case where 3 ml/min was used as the rate, the differential pressure reached its maximum at 0.36 bar. It is therefore assumed that the base case for LSW would follow the same trend as NSW. This assumption is based on the fact that NSW and LSW do not contain any particles, and they had the same pressure curve when the low rate was applied. 0.5 wt% CNC and 1.0 wt.% CNC have a higher differential pressure than the base case for the high rate, and particles could be retained within the core.

NSW as Dispersing Fluid

For the solution where NSW was used as dispersing fluid, larger particles were visible with the eye, indicating that the CNC aggregated throughout the duration of the experiment. This caused particle accumulation at the inlet face of the core (Figure 2), inhibiting injection. Differential pressure increased throughout the experiment to a final, maximum pressure of 3.5 bar. This is over 20 times greater than the maximum pressure of the flooding experiments conducted with the low rate. The PMC test cannot be accurately run with particle aggregation, so this test does little more than to show that more work needs to be done on the stabilization in the presence of synthetic saltwater.

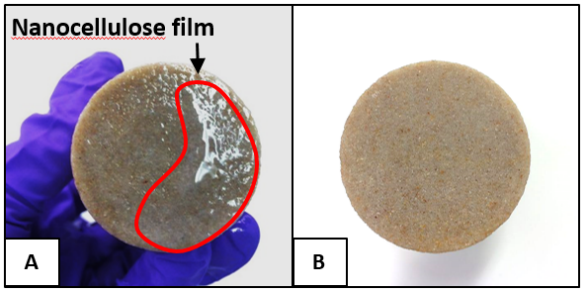

Figure 2. A) Picture of the core inlet for 1.0 wt.% CNC with NSW taken after PMC. A thin film of nanocellulose is observed. B) The other tests did not display this effect, which is illustrated by the core that was flooded with 0.5 wt.% CNC with LSW.

Porosity and Permeability

The permeability was altered during the PMC tests, and lead to a moderate impairment (ranging from 17% to 25%) for the majority of the cores. Core 6 (1 wt.% CNC with NSW) had a significant permeability reduction of 61 %, which could be explained by the nanocellulose film that was created on the inlet of the core. The porosity of the core plugs did not change during the PMC tests.

Effluent Analysis

The effluent analysis confirmed the observations from the pressure curves. From sample 1 PV to 5 PV it is seen that nanocellulose has been transported through the core in the cases where LSW was used as dispersing fluid (Figure 3). However, it is not possible to determine the exact amount of particles by visual analysis only. It is difficult to determine the extent of retention as a function influent concentration and flow rate without a quantitative measurement of the effluent

concentrations. The observations from the effluent study therefore just give an indication of which system will perform best for further EOR research.

In the case where NSW was used as dispersing fluid, it is observed that PV 1 to 4 is quite transparent when compared to PV 0 (Figure 3). This indicates that CNC is retained within the core. In the fifth PV it is possible to see that CNC has had a breakthrough in the core because a small amount of CNC is observed in the bottom of the sample.

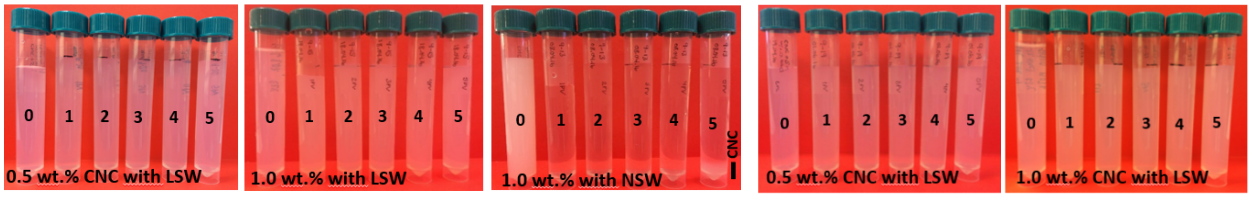

Figure 3. Effluent samples from flooding experiments, where sample 0 is the original fluid prior to injection and sample 1 to 5 illustrates PV 1 to 5, respectively. From left to right: 0.5 wt.% CNC with LSW (0.3 ml/min), 1.0 wt.% CNC with LSW (0.3 ml/min), 1.0 wt.% CNC with NSW (0.3 ml/min), 0.5 wt.% CNC with LSW (3.0 ml/min) and 1.0 wt.% CNC with LSW (3.0 ml/min).

CONCLUSIONS

- The studies show that there is a trend between CNC concentration and retention. Retention is increasing as CNC concentration increases.
- CNC exhibits a greater retention in the core when dispersed in a fluid with high ionic strength (3.53% salinity), which was evident from pressure data, permeability impairment and effluent analysis. This could be a result of an unstable solution. Thus, more research concerning the stability of the nanocellulose dispersions in salt is needed in order to prevent aggregation and plugging of pores.
- A higher flow rate might lead to more particles being retained, but this statement needs to be confirmed by running more parallel experiments together with accurate measurement of effluent concentration.

ACKNOWLEDGEMENTS

The authors would like to thank the Research Council of Norway for their financial support through the grant 244615/E30 in the Petromaks2 programme.

REFERENCES

1. Aurand K., Flatås V. and Aadland R. "Analyzing retention via particle mobility coreflooding". In International Symposium of the Society of Core Analysts, (2016).
2. Chang, H. L. (1978). Polymer flooding technology yesterday, today, and tomorrow. *Journal of Petroleum Technology*, *30*(08), 1-113.
3. Dong, X. M., Revol, J. F. and Gray, D. G. "Effect of microcrystallite preparation conditions on the formation of colloid crystals of cellulose". Cellulose, (1998) **5(1)**: 19-32.
4. Huh, C., Lange, E. A., & Cannella, W. J. "Polymer retention in porous media". In *SPE/DOE Enhanced Oil Recovery Symposium*, (1990), Society of Petroleum Engineers.

5. Kamal, M.S., Sultan, A.S., Al-Mubaiyedh, U.A., & Hussein, I.A. “Review on polymer flooding: rheology, adsorption, stability, and field applications of various polymer systems”. *Polymer Reviews*, (2015) ***55*(3),** 491-530.
6. Molnes, S.N., Torrijos, I.P., Strand, S., Paso, K.G and Syverud, K. “Sandstone injectivity and salt stability of cellulose nanocrystals (CNC) dispersions—Premises for use of CNC in enhanced oil recovery”. Ind. Crops Prod.(2016).
7. Raney, K. H., Ayirala, S., Chin, R. W., & Verbeek, P. “Surface and subsurface requirements for successful implementation of offshore chemical enhanced oil recovery”. *SPE Production & Operations*, (2012) ***27(03),*** 294-305.
8. Sheng, J. J., Leonhardt, B., & Azri, N. «Status of polymer-flooding technology”. *Journal of Canadian Petroleum Technology*, (2015) ***54*(02)**, 116-126.

INVESTIGATION OF THE PHYSICS OF INERTIAL EFFECTS AND THE FORCHHEIMER EQUATION UTILIZING THE LATTICE BOLTZMANN METHOD

Rasoul Arabjamaloei[1], Douglas W. Ruth[1]

[1]Centre for Engineering Professional Practice and Engineering Education, University of Manitoba, Canada

This paper was prepared for presentation at the International Symposium of the Society of Core Analysts held in Snowmass, Colorado, USA, 21-26 August 2016.

ABSTRACT

The Darcy law provides the basic linear equation for fluid flow in porous media in an ideal, simplified condition. The Darcy's equation has been shown to be valid in flow processes happening in sufficiently low Reynolds number regimes. At higher Reynolds numbers, the inertial effect causes extra pressure drop and a decrease in the apparent permeability of the porous media. The Forchheimer's equation is a semi-empirical relationship which accounts for the inertial effects on the flow characteristics.

In this research, high Reynolds number flow through two-dimensional pore-throat combinations were simulated by the Lattice Boltzmann method. The effect of the geometry on the extent of the inertial effects was studied based on the outputs of the simulation. The validity and sensitivity of the Forchheimer's correlation was tested in this work.

1. INTRODUCTION

Permeability is defined as the capability of a porous medium to pass a single phase, single component flow. For a natural porous medium such as a natural hydrocarbon reservoir, the porous medium consists of a wide range size of pores and the connecting pore throats.

The first basic mathematical model to study fluid flow in porous media is the empirical relationship known as the Darcy's law. This equation relates the fluid viscosity μ, the rock permeability k, the flow area A, the sample length L and the piezometric pressure difference $\Delta\Phi$ of the fluid flow rate through the sample Q as

$$Q = \frac{kA}{\mu}\frac{\Delta\Phi}{L}, \qquad \Delta\Phi = \Delta P + \rho g \Delta z \tag{1}$$

At higher Reynolds numbers, the relationship between the pressure gradient and flow velocity becomes non-linear. Forchheimer (1901) was one of the first people to provide a quadratic empirical correlation for the velocity and pressure gradient relationship

$$-\frac{dP}{dx} = \frac{\mu u}{k_F} + \beta \rho u^2 \tag{2}$$

where β is termed the Forchheimer coefficient, u is the average velocity of the fluid, k_F is the Forchheimer permeability and ρ is the fluid density. There has been some research works that propose a cubic relationship for the velocity and pressure gradient (Mei and Auriault 1991; Coulaud et al. 1998; Balhoff and Wheeler 2009). However, the range of the applicability of the cubic relationship is not wide.

Ruth and Ma (1992) proposed an alternative form of representing the inertial effects on the permeability as

$$\frac{1}{k} = \frac{1}{k_o}\left(1 + \frac{\beta k_o \rho u}{\mu}\right) \tag{3}$$

where k is the permeability, and k_o is the apparent permeability. The Forchheimer coefficient β is measured experimentally for each type of fluid and porous media by multi-rate flow tests and there is no generally accepted theory to predict its value. However, there are empirical correlations relating the Forchheimer coefficient to permeability and porosity.

Considering a porous medium to be a bead pack, Ergun (1952) derived a correlation for the Forchheimer coefficient as

$$\beta = ab^{-0.5}(10^{-8}k)^{-0.5}\emptyset^{-3/2} \tag{4}$$

where a and b are constants depending on the porous structure surface, and ϕ is the porosity. MacDonald et al. (1979) modified Ergun's correlation and defined ranges for a and b. There are also some other correlations obtained for natural porous media. Table 4 presents a few of the correlations found in the literature.

Flow test experiments on regular shaped sphere packs have shown the applicability range of the Forchheimer equation (Dybbs and Edwards 1984; Fand et al. 1987). This ranges differ for each type of the packings.

2. MODEL ANALYSIS AND RESULTS

Natural porous media consists of a wide range of pores and pore throats of different sizes and shapes. In natural porous media the pores could be connected to any number of throats. In this study a simple circle in 2D is chosen to represent the pore and channels are assumed to represent the pore throats. Figure 1 shows the schematic of the simplified pore.

The purpose of this study is to investigate the onset of the non-Darcy flow and the pressure loss and velocity relationship in the pore-throat combination by simulating the hydrodynamics of flow in pore bodies by the Lattice Boltzmann method. The Lattice Boltzmann method is a popular fluid dynamics simulation method. For a detailed explanation of the method, the paper by Arabjamaloei & Ruth (2016) is suggested.

It is known that the sudden change in the flow path width causes a shift of the laminar flow from the Darcy regime (creeping flow) to non-Darcy regime (Forchheimer or turbulent). Turbulent flow happens at very large velocity and rarely innatural porous media flow. The dimensionless Reynolds number (*Re*) is typically the main indicator of the onset of the flow regime change. Studies on the onset of non-Darcy flow in sphere packs have shown that assigning a unique *Re* onset for all types of porous media is not possible due to the sensitivity of the fluid flow to the geometrical properties of the porous medium (Hassanizadeh and Gray 1987).

Reforming equation 2, for gravity driven flow, by inserting the kinematic viscosity v instead of the dynamic viscosity μ, results in another form of the Forchheimer equation as

$$g = \frac{vu}{k_F} + \beta u^2 \tag{5}$$

The flow processes in all the pore-channel combinations at varying gravity force was simulated. The plot of gravity (g) and the average exit velocity (u) for 4 different pore-throat combinations is provided by figure 2. As it is seen in figure 2, a second order Forchheimer type polynomial fits the data well but the trend of the velocity profile is more like a third order polynomial with an obvious critical point that could be related to the critical *Re*. The velocity and gravity force in lattice Boltzmann units show a well behaved cubic relationship for each combination. However, the effectiveness of this relationship depends on its applicability to the whole range of aspect ratio combinations. To investigate this issue, the plot of the velocity and gravity for 10 different pore-channel combinations with varying aspect ratio was produced, as shown in figure 3. The mass flow rate is also a characteristic of the flow process and the inertial effects extent. The permeability for all the different cases was scaled by dividing the calculated permeability to the absolute permeability for all the data 10 combinations. The absolute permeability was calculated at vanishing Reynolds number. Scaled permeability (*Ks*) was plotted versus the mass flow rate in figure 4. Comparing figures 3 and four illustrates that the mass flow rate and scaled permeability provide a well behaved relationship for the whole ranges of pore-throat geometries while the velocity and head loss relationship foe all the geometries is not correlating well.

4. DISSCUSSIONS AND CONCLUSIONS

- As it is seen in figure 3, neither third order nor second order polynomial can perfectly predict the velocity and gravity relationship. This indicated the weakness of the Forchheimer type equation for the pore network combinations.
- A second order polynomial precisely predicts the permeability change as a function of mass flow rate due to the inertial effects in the simplified geometries used for this research.
- The Forchheimer equation seems to work for some pore-throat combinations, however it doesn't work well for all size combinations.
- The third order form of the Forchheimer equation works better than the second-order form in the two dimensional models studied (Figure 2).

ACKNOWLEGEMENTS

This work was supported in part by a grant from the Natural Sciences and Engineering Research Council of Canada.

REFERENCES

1. Arabjamaloei, R., & Ruth, D. W. (2016). Lattice Boltzmann based simulation of gas flow regimes in low permeability porous media: Klinkenberg's region and beyond. *Journal of Natural Gas Science and Engineering*, *31*, 405-416.
2. Balhoff, M. T., & Wheeler, M. F. (2009). A predictive pore-scale model for non-Darcy flow in porous media. *SPE Journal*, *14*(04), 579-587.
3. Coulaud, O., Morel, P., & Caltagirone, J. P. (1988). Numerical modelling of nonlinear effects in laminar flow through a porous medium. *Journal of Fluid Mechanics*, *190*, 393-407.
4. Dybbs, A., & Edwards, R. V. (1984). A new look at porous media fluid mechanics—Darcy to turbulent. In *Fundamentals of transport phenomena in porous media* (pp. 199-256). Springer Netherlands.
5. Ergun, S. (1952). Fluid flow through packed column. Chemical Engineering Progress, 48, 89-94.
6. Fand, R. M., Kim, B. Y. K., Lam, A. C. C., & Phan, R. T. (1987). Resistance to the flow of fluids through simple and complex porous media whose matrices are composed of randomly packed spheres. *Journal of fluids engineering*, *109*(3), 268-273.
7. Forchheimer, P. (1901). Wasserbewegung durch boden. *Z. Ver. Deutsch. Ing*, *45*, 1781- 1788.
8. Hassanizadeh, S. M., & Gray, W. G. (1987). High velocity flow in porous media. *Transport in porous media*, *2*(6), 521-531.

9. Macdonald, I. F., El-Sayed, M. S., Mow, K., & Dullien, F. A. L. (1979). Flow through porous media-the Ergun equation revisited. Industrial & Engineering Chemistry Fundamentals, 18(3), 199-208.
10. Mei, C. C., & Auriault, J. L. (1991). The effect of weak inertia on flow through a porous medium. *Journal of Fluid Mechanics*, *222*, 647-663.
11. Ruth, D., & Ma, H. (1992). On the derivation of the Forchheimer equation by means of the averaging theorem. *Transport in Porous Media*, *7*(3), 255-264.

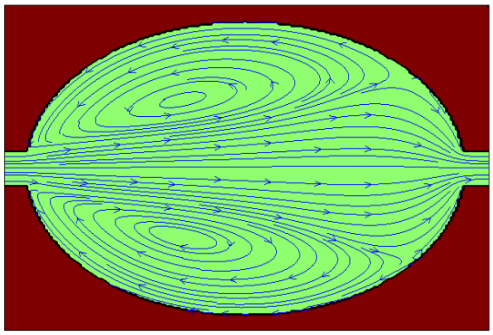

Figure 1: Schematic of the velocity streamlines in simple pore (the green circle) and two connecting channels (the green channels) surrounded by solid impermeable medium (the red color)

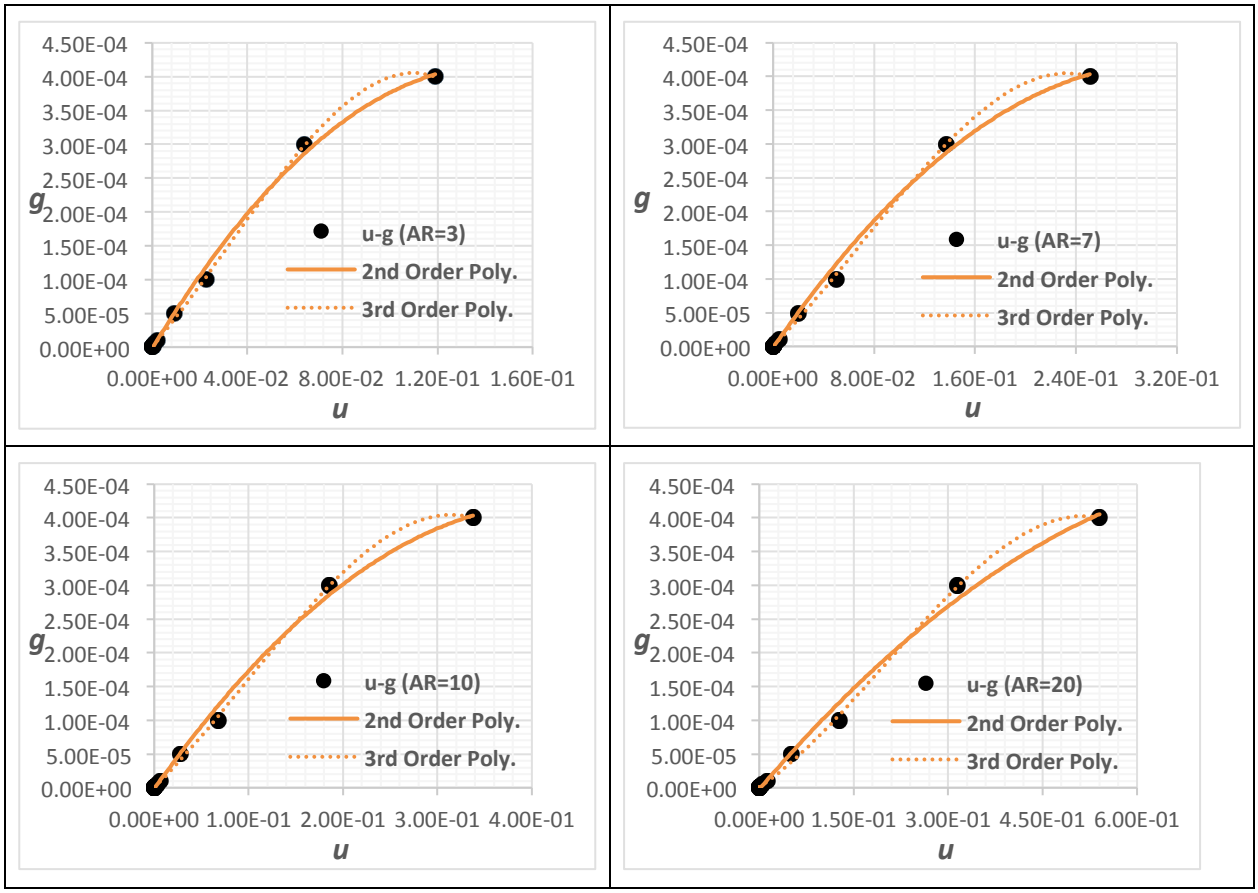

Figure 2: Average exit velocity (u) versus dimensionless gravity acceleration and two orders of polynomial fits for 4different pore-throat combinations. Data points show the simulation results and the line shows the fitted polynomial.

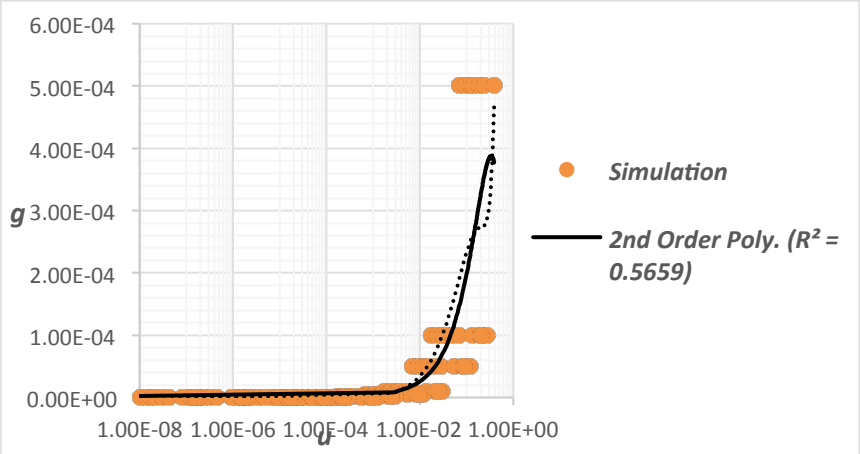

Figure 3: Plot of average exit velocity (u) versus dimensionless gravity (g).

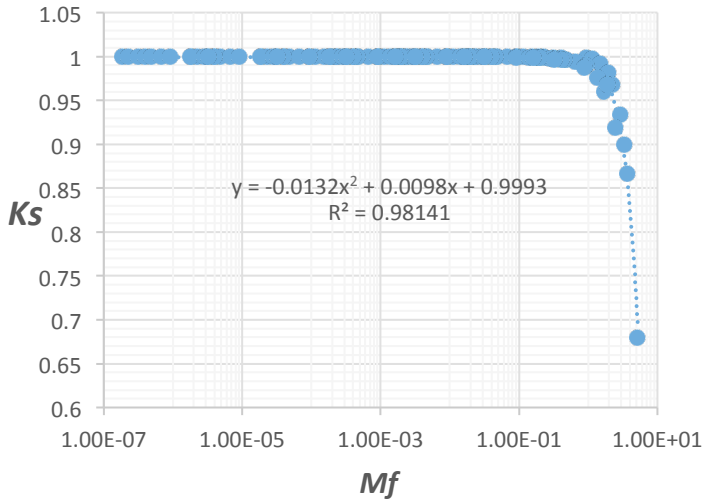

Figure 4: Scaled permeability (Ks) and mass flow rate (Mf) relationship for 10 different combinations of pore and throat with different aspect ratios and the polynomial fitting all the data points

STUDY OF THE THREE-PHASE FLUID FLOW MECHANISM IN LOW PERMEABILITY AND HIGH GOR RESERVOIRS

JIA Ninghong[1], LV Weifeng[1*], LIU Qingjie[1], QIN Jianhua[2], XU Changfu[2], Danyong LI[3], LENG Zhenpeng[1]

1. State Key Laboratory of Enhanced Oil Recovery, Research Institute of Petroleum Exploration and Development, Beijing, China; 2. Research Institute of Exploration And Development of Xinjiang Oilfield Company, CNPC, Karamay, China; 3, iRock Technologies, Beijing, China

This paper was prepared for presentation at the International Symposium of the Society of Core Analysts held in Snowmass, Colorado, USA, 21-26 August 2016

ABSTRACT

Multiphase flow induced by solution gas evolution impacts water flooding performance, such as drastically decline of oil and liquid production, which raises the necessity to take into account the gas evolution effect when designing oilfield development plan and optimizing oilfield development model. In this work a three-phase flow experiment was conducted to simulate water flooding process in a core sample from one low permeability reservoir with high GOR located in northwestern China and the impact of solution gas evolution was studied quantitatively. By imaging the flooding process in a core sample with an X-ray CT facility and recording the variance profile of gas saturations on multiple locations of the core sample was observed. Also, relative permeability of oil phase is reduced by 27.5% from that of two-phase (oil/water) flow where solution gas evolution effect is omitted. On the other hand, reduction of relative permeability of water phase is only 1.4%, indicating that water phase flow is less impacted by solution gas evolution, assuming a water-wet reservoir where water-phase has little direct contact with gas-phase.

INTRODUCTION

Water flooding is often approached as an effective way for oil production in low permeability reservoirs featuring low formation energy. However, rapid dissipation of the injected energy due to high flow resistance of low permeability reservoirs makes it difficult to supplement adequate energy in time to support the formation pressure. Solution gas tends to come out of crude oil as the formation pressure drops below the saturation pressure point, which is a prevalent occurrence near wellbore area, particularly for low permeability reservoirs with high GOR (Gas/oil ratio). [1-2]

Higher saturation pressure would be beneficial in solution gas drive since it permits higher drawdown pressure. The effect of increased GOR at a constant saturation pressure due to compositional effects is not obvious. Increased GOR would give lower live oil viscosity and increased gas flow. [3]

In all solution gas drive reservoirs, gas is released from solution as formation pressure declines, initially in the form of tiny bubbles within individual pore bodies. As formation pressure declines further, the tiny bubbles expand to occupy connected pores. Eventually the bubbles expand large enough due to very low pressure and merge each other into a continuous gas phase. [4]

Although the understanding of solution gas drive has been intensively studied in recent years, the flow mechanism of solution gas drive in porous medium still remains unclear enough [5-6], although microscopic flow behavior can be observed in micro-models by various approaches. There still exists certain representative issue of microscopic pore spaces to realistic pore spaces, as well as different temperature and pressure between underground formation condition and at room conditions. This study uses core sample of realistic length scale at reservoir pressure and temperature and applies CT scanning process to identify the place where solution gas appears and to observe the solution gas evolution.

EXPERIMENTAL

Core Samples and Fluids

Two core plugs, 5 inches in length and 1 inch in diameter, were drilled from a block of conglomerate using liquid nitrogen as coolant, dried in an oven at 110°C for 3 days and cooled in a desiccator for 2 days. The plugs (Sample XJ1 and Sample XJ2) were then imaged by X-ray CT facility to investigate their homogeneity and comparability. The three-dimensional images of the samples demonstrated that they were heterogeneous. Air permeabilities of Samples XJ1 and XJ2 were 1.6mD and 1.4mD, respectively, and they have close average CT number which shows Sample XJ1 and Sample XJ1 can be used as parallel reference samples. Figure 1 shows the distribution of porosity along the length of the core for both sample XJ1 and sample XJ2 and the petrophysical parameters are shown in Table 1. The test live oil was made by dissolving CO2 and CH4 into crude oil with mole ratio 19:97, which has a solution gas oil ratio (GOR) of 179.0m3/m3, viscosity of 26.12mPa·s, density of 0.7165 g/cm3, bubble point pressure (BBP) of 10.07MPa at reservoir conditions of 53.7°C.

Experimental Set-up and Conditions

The scheme of the experimental set-up is illustrated in Figure 2. A medical CT scanner manufactured by GE was used as a base platform where a set of core flooding experimental equipment was attached to realize the function of simultaneous scanning and flooding. The core samples and the fluids were scanned at low energy (100kV) and high energy (140kV) respectively by changing the volt of the X-ray source, and the filament current was fixed at 150mA. Helical mode was adopted to reduce the scanning time. CT images were processed by CT image analysis software (CTIAS 2.0, developed by RIPED). Two sets of QUIZIX pumps were employed to control the injection of water and oil. A set of ISCO pumps was used to control the back pressure. Image slices from the scanning were taken as platforms for the three-phase saturation calculations [7].

PROCEDURES

A workflow of simulating the evolved gas-driving flooding experiment by displacing the crude oil containing solution gas with injected brine is designed and carried out on the proposed experimental configuration. This workflow is a modification and extension of our previous traditional water flooding experiment on core samples with the aid of Dual-energy X-ray CT scanning and imaging processing. The procedures of the workflow are proposed as following:

1. A core sample is vacuumed within the core holder with a confining pressure of 20MPa. The same gas as the solution gas in oil is injected into the vacuumed core sample till full saturation. Then, X-ray CT imaging is performed and the image slices obtained are taken as 'dry model'.
2. The gas saturated core sample is re-vacuumed and white oil is injected until it reaches full saturation. Then, the live crude oil *is* injected into the core sample to displace the white oil. The reason that live crude oil displaces white oil instead of being directly injected into the vacuumed pore space is to avoid that the unexpected gas is coming out due to extremely low pressure in the vacuumed pore space. X-ray CT images obtained by scanning the core sample with fully saturated crude oil are taken as 'oil-wet model'.
3. After core sample with saturated crude oil is scanned by X-ray CT, the sample is then cleaned by alternately injecting petroleum ether and air into the sample until it is believed that no petroleum ether remains within the core sample.
4. The vacuumed core sample is once again saturated by injecting brine and the X-ray CT image slices obtained are taken as 'water-wet model'.
5. A pressure-controlled live crude oil injection is carried out on the brine saturated core sample, with initial pressure starting from 12MPa. The pressure is incremented until no water is produced at the outlet of the sample. X-ray CT image slices obtained at this stage are considered to be the initial reservoir condition prior to production, hence labelled as 'initial-model'
6. Production stage is simulated by injecting brine into the crude-oil-saturated sample while the pressure and flow rate is measured at the outlet end. The injection is controlled to maintain a constant flow rate during the whole procedure and injecting pressure is gradually incremented till the maximum pressure of 17MPa. Various injecting stages are scanned by X-ray CT and are labelled as 'intermedia models'. This procedure stops as no more oil and gas are produced at the outlet.

RESULTS AND DISCUSSION

Gas saturation of sample XJ1 calculated from the CT image slices shows in Figure 3 that no gas coming out in the first half section of the sample. As back pressure declines from 12MPa to 8MPa, gas begins to come out near the outlet end and the region where dissolved gas can be detected occupies the second half section of the core sample. It is obvious that gas saturation increases as pressure goes down, which is consistent with the reservoir observation that more gas evolves from the solution as pressure declines.

With permeability and porosity close to sample XJ1, sample XJ2 is taken as a parallel reference sample and performed with the same workflow except that on XJ2 the back pressure declines to 4MPa, instead of 8MPa on XJ1. Figure 4 compares the gas production of the two samples with different declining pressures. It can be observed that gas evolution in XJ2 occupies larger section of a core sample than that in XJ1. Further, the effect of higher declined pressure leads to higher gas production from XJ2 (16%) than that of XJ1 (10%).

Overlapping relative permeability curves of XJ1 and XJ2 and comparing them with regular two-phase relative permeability curves can obviously shows in Figure 5 the effect of higher declined pressure at the outlet end. The reduction of the oil-phase relative permeability by the impact of gas evolution is proportional to the magnitude of the declined pressure. Relative permeability of oil phase is reduced by 27.5% on XJ2 from that of two-phase (oil/water) flow. On the other hand, reduction of relative permeability of water phase is only 1.4%, indicating that water phase flow is less impacted by solution gas evolution, assuming a water-wet reservoir where water-phase has little direct contact with gas-phase.

As mentioned already, Three-phase saturations in this study were measured in-situ using computed tomography. To calculate three phase saturations, the cores were scanned at two different energy levels during the experiments and three phase relative permeability was obtained by assuming that relative permeability of each phase was a function of its own saturation. Combining with the measured gas production at the outlet end, the flow ability of oil phase in the core sample is significantly depressed by large volume of gas evolved into the pore space, which is consistent with the microscopic explanation of 2-phase flowing mechanism in porous media. On the other hand, the dissolved gas has little impact on the relative permeability of water phase through the whole production stage except on the residual water saturation.

CONCLUSION

A modified flooding experiment, combined with X-ray CT scanning, is proposed to study the characteristic of gas evolution occurrence within the pore space during production stage. It can be concluded that three-phase flowing, which implies the gas coming out occurs mainly near the outlet end of a flooded core sample.

Comparison between 2-phase (oil/water) flow and 3-phase relative permeability shows that gas evolved will depress the previous 2-phase oil-water flowing channels, hence leads to a significant reduction of oil-phase production by about 20%, while water-phase production remains much less impacted, which is consistent with the theoretical model of 3-phase flowing in channels.

ACKNOWLEDGEMENTS

We gratefully acknowledge financial support from PetroChina Research Project (2014A-1003) and Research Institute of Exploration and Development, Xinjiang Oil field Company.

REFERENCES

1. TANG, G.Q., SAHNI, A., GADELLE, F., KUMAR, M., and KOVSCEK, A.R., Heavy-Oil Solution Gas Drive in Consolidated and Unconsolidated Rock, *SPE 87226, International Thermal Operations and Heavy-Oil Symposium and Western Regional Meeting, Bakersfield, California, 2004*.
2. MAINI, B.B. Effect of Depletion Rate on Performance of Solution Gas Drive in Heavy Oil System,*SPE 81114 presented at the Latin American and Caribbean Petroleum Engineering Conference, Port-of-Spain, Trinidad and Tobago, April 27-300, 2003*.
3. Baibakov, N. K. and Garushev, A. R., Thermal Methods of Petroleum Production, *Developments in Petroleum Science* 25, *Translated by W. J. Cieslewicz, Elsevier Science, Amsterdam, pp. 6–21, 1989.*
4. SHENG, J.J., MAINI, B.B., HAYES, R.E. and TORTIKE, W.S. Critical Review of Foamy Oil Flow, *Transport in Porous Media, Vol.35, p.157-187,1999*.
5. AKIN, S., and KOVSCEK, A.R., Computed Tomography in Petroleum Research. *Applications of X-ray Computed Tomography in the Geosciences, Geological Society of London, Special Publications, 215, 23-38, 2003.*
6. SMITH, G.E., Fluid Flow and Sand Production in Heavy-Oil Reservoirs Under Solution-Gas Drive, *SPE, P169-180, May, 1988.*
7. Coles M. E., Muegge E. L., et al. "The Use of Attenuation Standards for CT Scanning," *SCA 1995-13*, (1995).

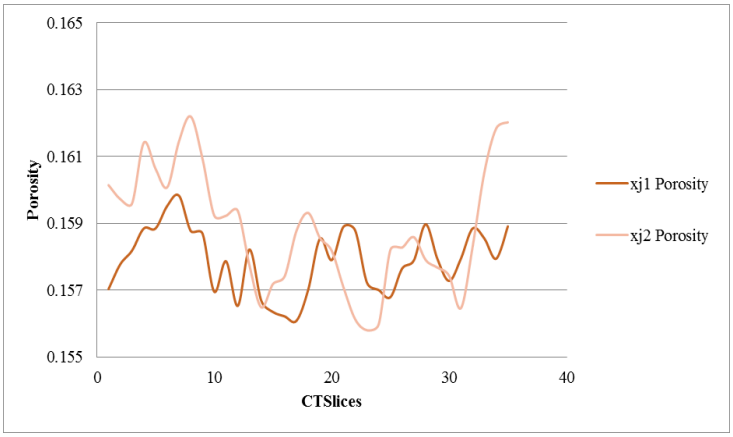

Figure 1. Slice-averaged porosity distribution along the length of the core samples determined using X-ray imaging.

Table 1. Petrophysical Parameters of Core Samples

Sample No.	Porosity,%	K_{air},10^{-3} μm^2	CT number
XJ1	15.7	1.6	2053
XJ2	16.1	1.4	2098

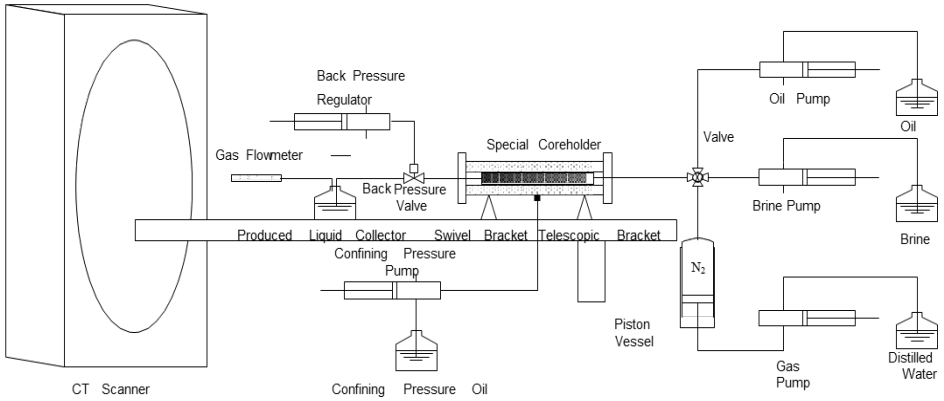

Figure 2. Experimental Schematic

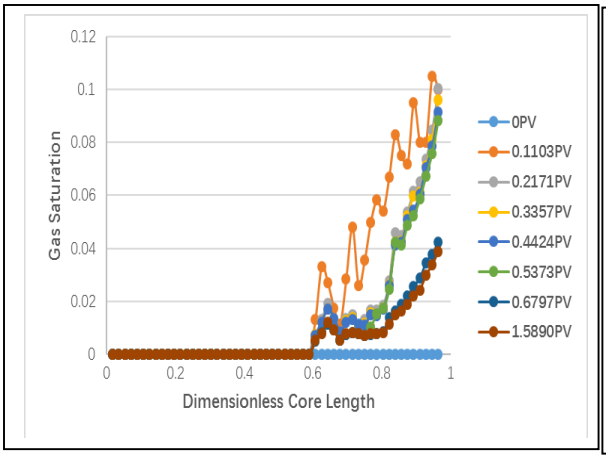

Figure 3. Gas Saturation distribution changes along the length of the sample XJ1 when back pressure declines from 12MPa to 8MPa

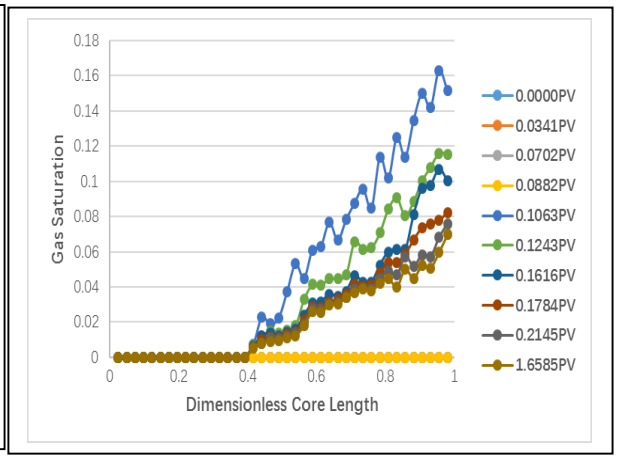

Figure 4. Gas Saturation distribution changes along the length of the sample XJ2 when back pressure declines from 12MPa to 4MPa

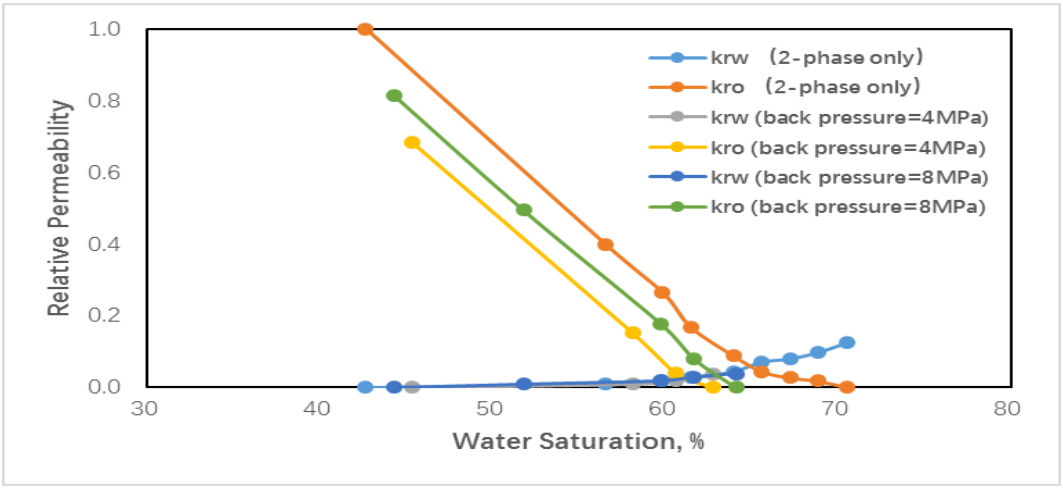

Figure 5. Comparison of relative permeability for 2-phase flow and 3-phase flow

An Experimental Investigation of Performance Evaluation for Seawater and CO_2 Injection Using Dual Cores Methodology at Reservoir Conditions

Xianmin Zhou, Fawaz AlOtaibi, Almohannad Alhashboul and Sunil Kokal, Saudi Aramco

This paper was prepared for presentation at the International Symposium of the Society of Core Analysts held in Snowmass, Colorado, USA, 21-26 August 2016

ABSTRACT

In this study, a novel methodology of dual core flooding was first developed and described in detail, and applied to evaluate displacement efficiency and performance of seawater and supercritical CO_2 (sc-CO_2) injection for two carbonate core plugs with different permeabilities at reservoir conditions. The dual core flooding apparatus consists of seven components and can be used to inject individually or simultaneously for one or two phases fluids into core plugs with variety of length in a single or dual core flooding configuration. The orientation of single or dual core holder with test core plugs can change horizontally or vertically for the different experiments. The experimental conditions of this new apparatus are up to 150^{o}C for temperature, up to 6000 psi for pore pressure and 10,000 psi for confining pressure.

As an example of application of dual core flooding experiments, the different oil recovery schemes of seawater flooding, as a secondary EOR process followed by a sc-CO_2 injection, as a tertiary EOR process was conducted at reservoir conditions. The results from the dual core flooding experiments are discussed for high and low permeability carbonate rocks, and show the potential of CO_2-EOR projects. Experimental procedures are provided for conducting these dual core experiments, and show the potential to become a gold standard for such studies.

INTRODUCTION

Development of core flooding apparatus started in the 1940s. There is various equipment in laboratories experiments for reservoir engineering processes. Some examples of the classical steady-state method are the Penn State method [1], the Hassler method [2], the single-core dynamic method [3], the stationary fluid method [4] and the Hafford's method [3]. With development of laboratory testing techniques, the apparatus included in-situ saturation imaging techniques by X-ray to measure saturations when two or three fluids are injected into core. Based on research objectives, the components of core flooding apparatus have to be changed to meet the requirements of the investigation. The utilization of core flooding apparatus covers many research areas such as oil recovery by

seawater and Low-Salinity waterflooding [5], Chemical Flooding [6] and CO_2 injection [7]. A review of the core flooding apparatus described in areas above found that one core holder was used, no matter which research objectives were investigated.

In this paper, dual core flooding apparatus (DCFA) is proposed and designed to apply to oil recovery and performance studies by different oil recovery schemes of seawater flooding and initial and post sc-CO_2 injection at reservoir conditions as an evaluation of the practicability of a dual core flooding system.

Dual Core Flooding Apparatus

A dual core flooding apparatus (DCFA) is custom designed to perform tests on stacked or composite core plug samples to study oil recovery by IOR and EOR processes and evaluate the impact of reservoir heterogeneities such as permeability contrast and gravity override on performance of oil/water production at reservoir conditions. The schematic of the core flooding apparatus are presented in Figure 1. The core holders are placed horizontally with high permeable core plug (HPCP) on top of low permeable core plug (LPCP) core-holder. A detailed description of dual core flooding system has been presented [8].

Application of Dual Core Flooding Apparatus

As an example of application of the dual core flooding experiments the different oil recovery schemes of seawater flooding, as secondary EOR and sc-CO_2 injection, as tertiary EOR were conducted for carbonate core plugs with different permeabilities at reservoir conditions.

Properties of fluids

Brines: Two types of brines were used in this study, field connate water and seawater. The field connate water was used to saturate the core plugs for brine permeability measurement and acquiring the initial water saturation (S_{wi}). Seawater was used to displace live oil for evaluating displacement efficiency by injecting seawater simultaneously into both HPCP and LPCP. The compositions, density and viscosity of both brines were described [8].

Dead and live crude oils: A dead crude oil from a carbonate reservoir was used in this study to set up initial water saturation (S_{wi}) and age core plugs at reservoir conditions. Separator crude oil and gas were collected from the same reservoir to recombine the live crude oil sample. The live oil was then used to age the core plugs and to represent the oil phase for the seawater flood and sc-CO_2 miscible flooding experiments. The viscosity and density of dead and live crude oils at reservoir temperature were described [8].

Supercritical CO_2 (sc-CO_2): sc-CO_2 was also used as a displacing agent for tertiary oil recovery at a pressure of 3200 psi and temperature of 102^{o}C. This created the miscible flooding condition with the live crude oil in reservoir. The minimum miscible pressure (MMP) between live oil and sc-CO_2 was 2600 psi. The viscosity and density of sc-CO_2 were described [8].

Preparation of Core plugs

Core plugs: The core plugs were selected from a carbonate reservoir and scanned to ensure consistency, i.e. no fractures or permeability barriers in single core plug. The length (L) and diameter (D) of core plugs show in Table 1.

Set up initial water saturation (S_{wi}) and original oil in core (OOIC):

Before running dead crude oil flooding for setting up initial conditions, S_{wi} and S_{oi}, several tests were done to saturate the core plugs with field connate water and measure brine permeabilities. Core plugs were assembled using Teflon Tape, aluminum foil and 1 layer of Teflon shrink tube as a stack. The aluminum foil functioned as a diffusion barrier between the core plug and the overburden sleeve. The procedure of setting up initial conditions was described in detail [8]. Table 1 shows these data.

Table 1 Initial Date of live oil flooding at reservoir conditions

Composite ID	L (cm)	D (cm)	PV (cc)	K_b (mD)	S_{wi} (%)	S_{oi} (%)	K_{eo} at S_{wi} (mD)
Composite 1 (HPCP)	6.394	3.8	20.6	967	24.6	75.4	104
Composite 2 (LPCP)	6.018	3.8	14.1	22.3	17.6	82.4	3

Aged composite core plugs with live crude oil: After initial water and original oil saturation was set up, live oil flooding was conducted at reservoir condition of pore pressure 3200 psi, confining pressure of 4500 psi and temperature of 102^{o}C for both HPCP and LPCP. One pore volume of live oil was injected into each composite core at a flow rate of 1.0 cc/min in order to check stabilization of injection pressure and effective oil permeability of core plugs every day for three weeks. The initial water saturation (S_{wi}) and original oil in core (OOIC) were 24.6% and 75.4% for HPCP and 17.6% and 82.4% for LPCP, respectively.

Oil Recovery by Seawater and sc-CO_2 Injection

Oil recovery by seawater flooding: Once both composites were aged with live oil at reservoir conditions, seawater was injected simultaneously into both HPCP and LPCP at injection rates of 0.5, 1.0 and 2.0 cc/min until the water cut reached 99%. The recovered oil was collected separately from the two composites as a function of pore volumes of seawater injected. The differential pressures across both composites and injection pressure were also recorded as a function of time.

Oil recovery by initial sc-CO_2 miscible flooding: After the initial seawater flooding and the remaining oil saturation was established, the inlet and outlet valves of both composites were closed. All the lines which were filled with seawater were first displaced with sc-CO_2. Thereafter the two composites were opened again and sc-CO_2 was injected simultaneously into both at a rate of 0.2 cc/min. The recovered oil was collected from the

two composites separately. Differential pressures and injection pressure for each composites was also recorded as a function of time.

Injection of a diverting system: To investigate the effect of permeability contract and to mitigate its impact on oil recovery, a diverting system was injected into the HPCP composite. The main idea was to block the HPCP composite so that the subsequent sc-CO_2 would travel through the LPCP composite and recover the bypassed oil. The diverting system used for this experiment was described [8].

2nd sc-CO_2 miscible flooding: After accomplishing the diverting system injection, both HPCP and LPCP composites were opened for the 2nd sc-CO_2 miscible flooding at injection rate of 0.2 cc/min. Oil production and differential pressure across composites and injection pressure were recorded individually for HPCP and LPCP.

Results and Discussion

Profile of differential pressure during seawater and sc-CO_2 injection

The differential pressure across the high and low permeable core plugs vs total pore volume of seawater injection is presented in Figure 2 (left). At breakthrough of injection fluid, the differential pressure across the HPCP core reached a maximum value of 0.8 psi and then dropped to a value of about 0.2 psi at an injection rate of 0.5cc/min. For the LPCP, the differential pressure across the core reached a maximum value of 11 psi and then dropped down to same value as the HPCP. This phenomenon is due to the seawater bypassing through HPCP and the effect of rock heterogeneity. Figure 2 (right) presents the differential pressure drop across both cores during initial sc-CO_2 injection. The performance of initial sc-CO_2 injection was quite different to that of the seawater injection for LPCP composite. After sc-CO_2 breakthrough, the differential pressure drop across the two cores was different (unlike the case during in the seawater flood). A second peak value of differential pressure was observed for LPCP, and the value was greater than 5psi. This was due to two-phase and three-phase flow in the LPCP. Slow continuous oil production was observed beyond 0.2 PV sc-CO_2 injected.

Oil recovery during seawater and sc-CO_2 injection

Figure 3 shows the overall oil recovery with seawater, sc-CO_2 before and after the diverting system slug injection. The results show exceptional recovery (98%) in the HPCP composite after the seawater and first CO_2 injection cycles. Due to seawater and sc-CO_2 bypassing through the HPCP, the performance of the LPCP composite was relatively poor. By plugging the HPCP with the diverting system slug, the subsequent CO_2 was able to extract some of the remaining oil from the LPCP composite.

Conclusions

Based on results and observations of seawater and sc-CO_2 flooding using dual core flooding apparatus at reservoir conditions, the following conclusions can be drawn:

1. A novel apparatus and experimental procedure for dual core flooding experiments were first developed and then applied successfully to study oil recovery by seawater and sc-CO_2 as well as conformance control using a diverting system at reservoir conditions.

2. Novel methodologies of dual core flooding are an effective technique, and dual core flooding apparatus is a very useful tool to study oil recovery and performance by IOR and EOR processes, and to evaluate the effect of permeability contrast, reservoir heterogeneities and injection flow rate on oil recovery at reservoir conditions.

Acknowledgement

The authors would like to thank Saudi Aramco and EXPEC Advanced Research Centre for the permission to publish this paper. Special thanks Amin M. Alabdulwahab and Sentbilmurugan Balasubramanian for the preparation of a diverting system.

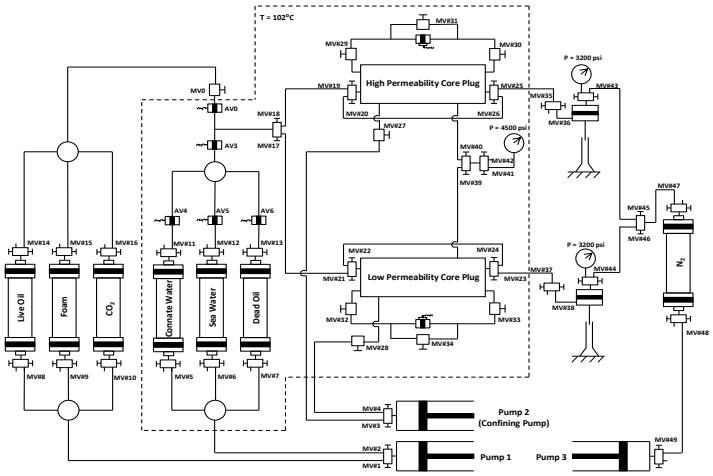

Fig.1 flow chart for dual core flooding apparatus at reservoir conditions

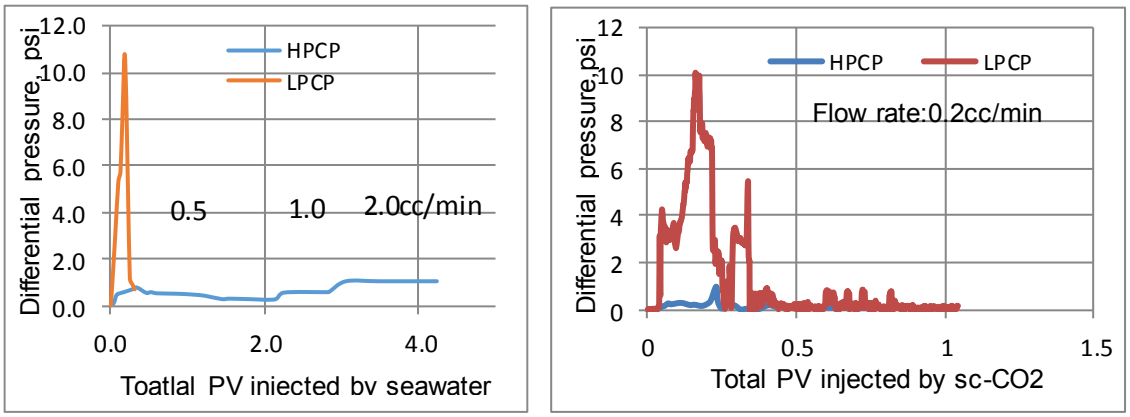

Fig.2 Comparison of differential pressure vs. the sum of PV injected during simultaneous seawater injection for LPCP and HPCP composites, Left: Seawater flooding; right: sc-CO2 injection

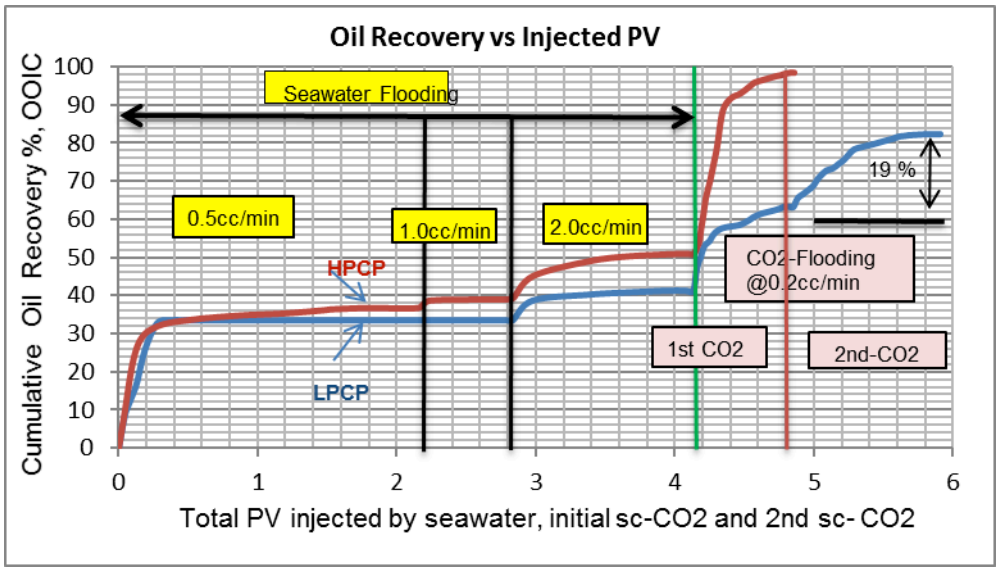

Fig.3 Overall oil recovery by seawater, initial sc-CO_2 and 2nd-sc-CO_2 flooding after diverting system slug injection at reservoir conditions

References

1. Morse, R. A., Terwilliger, P. L. and Yuster, S. T.: "Relative permeability measurements on small Sample," Oil and Gas Journal, (Aug. 23) 109, 1947.
2. Hassler, G.L.: "Method and Apparatus for Permeability Measurements." U. S. patent No. 2,345,935, April, 1944.
3. Richardson, J. G., Kerver, J. K., Hafford, J. A., and Osoba,J . S.: "Laboratory determination of relative permeability," Trans. AIME, 195, 187, 1952.
4. Leas, W. J., Jenks, L. H. and Russell, C. D.: Trans AIME, 189, 65, 1950.
5. Yousef, A. A., Al-Saleh, S. H., Al-Kaabi, A. and Al-Jawfi, M. S.: "Laboratory Investigation of the Impact of Injection-Water Salinity and Ionic Content on Oil Recovery From Carbonate Reservoirs", Society of Petroleum Engineers. doi:10.2118/137634-PA, 2011.
6. Shedid, S. A.: "Experimental Investigation of Alkaline/Surfactant/Polymer (ASP) Flooding in Low Permeability Heterogeneous Carbonate Reservoirs", Society of Petroleum Engineers. doi:10.2118/175726-MS, 2015.
7. Zhou, X, Al-Otaibi, F. and Kokal, S. L.: "Laboratory Evaluation of Performance of WAG Process for Carbonate Rocks at Reservoir Conditions", Society of Petroleum Engineers. doi:10.2118/167646-MS, 2013.
8. Zhou, X., Al-Otaibi, F., Kokal, L. S., Alhashboul, A., Balasubramanian, S. and Alghamdi, F.: **"**Novel Insights into IOR/EOR by Seawater and Supercritical CO2 Miscible Flooding Using Dual Carbonate Cores at Reservoir Conditions," Presented at 18th European Symposium on Improved Oil Recovery, Dresden, Germany, April 14-16, 2015

Residual Oil Distribution in Sandstone with Different Permeability Scale During Water Flooding Process

Xin WANG[a], Qi ZHANG[ab], Jun YAO[b], Yongfei YANG[b], Zhonghai ZHOU[a], Liya Duan[a]
[a]Institute of Oceanographic Instrumentation, Shandong Academy of Sciences (SDIOI)
[b]School of Petroleum Engineering, China University of Petroleum (East China)

This paper was prepared for presentation at the International Symposium of the Society of Core Analysts held in Snowmass, Colorado, USA, 21-26 August 2016

ABSTRACT

Recently with the rapid development of digital core technology, applications are used in the practical oil and gas field production. To illustrate the effect of pore structure on micro-distribution of residual oil, sandstones with different kinds of pore structure were imaged under the resolution of 3.78μm during water flooding process using X-ray tomography. Based on cluster-size distribution of oil segmented from the tomography images and classification using shape factor and Euler number, transformation of oil distribution pattern in different injection stages has been studied for the samples with different pore structures, which demonstrated distinctly different evolution behaviors of oil cluster. In general, distribution patterns of oil cluster constantly change during imbibition. Large connected oil clusters break off into smaller segments. Residual oil saturation tends to increase as the pore structure becomes more complicated where large oil blobs are trapped in such systems. For cores with good pore connectivity, which showed the largest change of distribution pattern, the oil distribution is relatively simple, and clusters are always concentrated on one or two kinds of distribution patterns. Meanwhile, some disconnected clusters merge and lead to re-connection at the stage of a high water cut. While pore structure becomes compact and complex, residual nonwetting phase becomes static and is difficult to move, so that all distribution patterns coexist during whole displacement process. As EOR methods for reservoirs containing residual oil are greatly influenced by pore scale entrapment characteristics of the oil phase, this study improves our ability to further enhance oil recovery.

INTRODUCTION

With advancement in X-ray computed micro tomography (μCT) and increase in computational power, detailed information extracted from 3D CT images of rocks can be used to accurately study multiphase flow in porous media at representative conditions. Started with glass bead packs[1-4], reseachers obtained the images of cores after both drainage and imbibition in real rock systems.The experimental examinations focus on relative permeability[5], fluid distribution[6-11], capillary pressure measurements[12], oil recovery[13], or wettability [14-16]. When displacement is carried out by usual

waterflooding, the complex pore structure is responsible for trapping a large portion of the oil phase within the pores of the rock. This in turn impacts the overall flow behaviour, such as oil recovery. Therefore, understanding of transport properties in porous materials and their dependence on pore geometry is critical. In the earliest studies, clusters of all sizes were observed, with approximately power-law distributions[17]. Cluster size has been found that can range from a single pore to multiple-pore configurations[4, 10, 18]. More recently, a tendency for residual nonwetting-phase saturations to increase as porosity decreased was noted[9]. However, these experiments do not reveal the morphology change of trapped cluster.

To overcome this, We focus here on two-phase flow of high water cut period in sandstones at pore-scale in 3D with micro-computed tomography(μ-CT). Four sandstones samples of different permeability scale were selected to representative of different reservoir sandstones. We have imaged sequences of water flooding production steps to study on changes of residual oil distribution and improve fundamental understanding with which it will be possible to reduce S_{or} further.

METHODOLOGY

Experiments

To introduce the effect of pore structure on residual oil distribution in the investigation, relatively homogeneous sandstone samples of different permeabilities were used to model the different kinds of porous media. Permeability and porosity of the four water-wet systems are 48.53mD, 110.84mD, 430.03mD, 520.81mD, and 0.25, 0.23, 0.21, 0.20, respectively. As the rapid development of pore network model, this method can be used to determine pore body and throat size locations and distributions from high-resolution tomographic images. Characterizations of pore structure, such as pore radius, throat radius, and coordination number etc. are calculated based on pore network model.

Brine doped with 10wt% potassium iodide (to enhance CT contrast) is the brine, and crude oil mixed with 52.1wt% kerosene is used as oil phase. The viscosity of aqueous phase is 1.2 mPa·s and for oil phase it is 0.75 mPa·s. Initially, the dry samples were scanned in order to obtain an accurate mapping of pore structure. Then the cores saturated with brine were displaced by oil until water production ceased. After ageing, the cores were scanned again to obtain the distribution of oil phase at connate oil saturation (So) state. Thirdly, the core plug was waterflooded by brine with a velocity of 0.1ml/min, and μCT images with a resolution of 3.78μm at 1PV, 5PV, 15PV, 50PV injection stages were then acquired respectively. All experiments were conducted at 297.15K and 0.1MPA.

The raw CT images were filtered and segmented by image filters and segmentation algorithms available within the commercial software package Avizo. Note that for each process step the same areas of $300\times300\times300 pixel^3$ are compared.

Characterization of residual oil

Residual oil distribution we got from the experimental CT images can be separated into a new image of the oil phase only, where disconnected blobs are labeled by distinct numerical values starting from the value of one to the maximum number of individual

blobs in the image. Then, attributes of every individual oil blob such as volume and interfacial area can be computed by performing operations on these sets of voxels.

There are two important parameters that we use to classify the distribution pattern. One is the sphericity index(G) which describes how closely an oil blob resembles a sphere. For a perfect sphere, G=1. It is computed as follows[19]:

$$G = \frac{6\sqrt{\pi}V}{S^{1.5}}$$

Where S is the surface area of the oil cluster and V is the volume of the oil cluster.

Another is the Euler number(E) which can be used as a characteristic describing the topological properties of the residual oil clusters. Euler number can be expressed by three Betti number[20].

$$E = b_0 - b_1 + b_2$$

Where E is the Euler number of oil cluster, b_0 is the number of isolated components, b_1 is the number of tunnels, b_2 is the number of cavities.

Combine the sphericity index (G) and Euler number(E) so that distribution pattern of residual oil can be defined(Table 1), as shown in Fig. 1.

Distribution pattern	
Network	G<0.1
Branch	0.1<G<0.3
Multiple	0.3<G<0.7 & E_N<1
Singlet	G>0.7
Film and tubular	0.3<G<0.7 & E_N≥1

Table 1 Classification of distribution patterns of micro residual oil

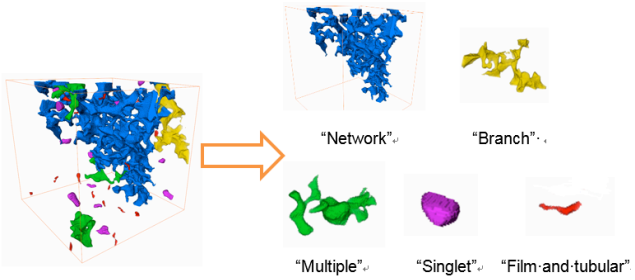

Fig. 1 Distribution patterns of oil cluster

RESULTS AND DISCCUSION

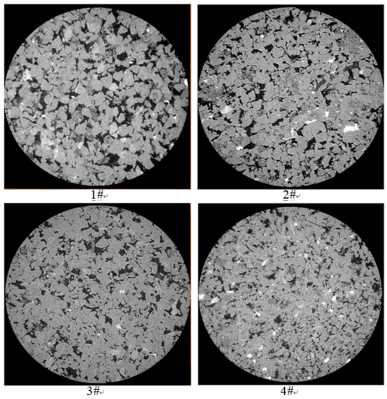

Fig. 2 Cross sections of the 4 sandstone samples

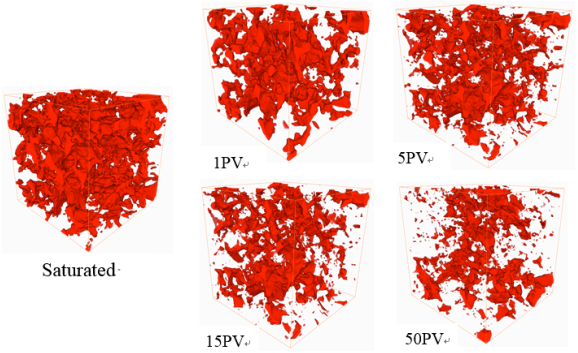

Fig. 3 Three-dimensional visualization of residual oil (sample 1#)

Fig. 2 shows the cross sections of the samples. As the permeability and porosity of the samples reduce, the pore structure getting complex, the pore connectivity poor, middle pores, small pores and fine throats develop and are short of big pores. Then portion of the original CT images of 300×300×300 voxels were extracted to segment and built into pore network. Table 2 shows parameters obtained by pore network characterization. As the

permeability and porosity of the samples reduces, the pore structure changes. Mean volume of pore and throat decreases, mean tortuosity has a tendency to increase, and mean coordination shows a decrease tendency. Mean pore radius and throat radius get smaller, and throat radius changes more than pore radius.

Table 2 Parameters of the samples abtained by pore network characterization

	1#	2#	3#	4#
Number of pores	598	4102	3175	3981
Mean pore radius(um)	25.37	11.30	10.99	8.15
Number of throats	1061	7649	5832	6718
Mean throat radius(um)	17.06	8.43	7.99	6.63
Mean coordination number	3.47	3.70	3.64	3.34
Mean Tortuosity	2.26	2.20	2.31	2.35
porosity(%)	22.29	20.33	18.47	13.67

As the complication pore structure, the decreased tendency of residual oil saturation become slower during water flooding process. Three-dimensional visualization of residual oil(Fig. 3) shows that the volume of residual oil reduces and its distribution patterns constantly change. The volume fraction of each pattern at each stage is calculated

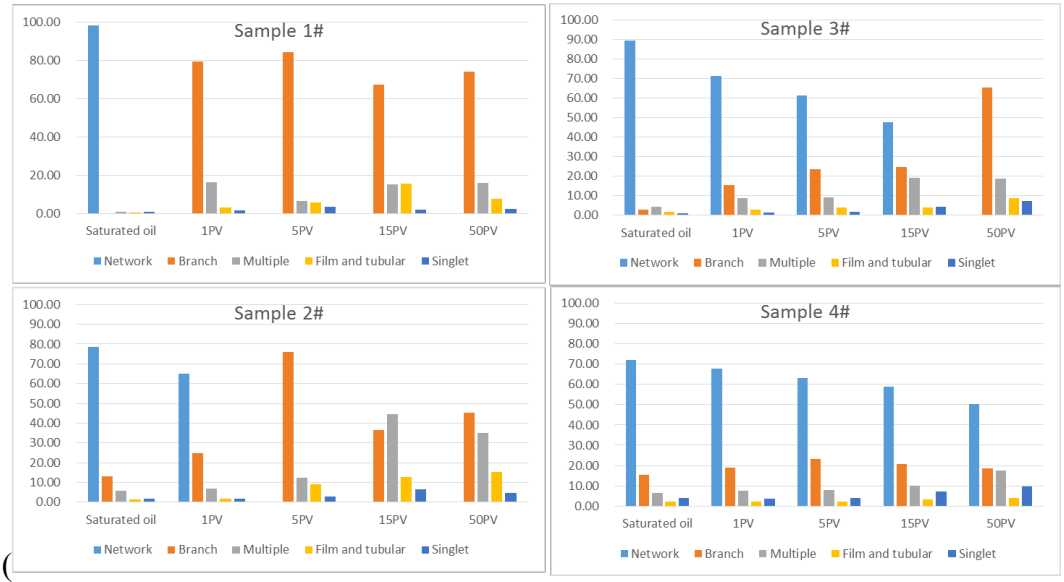

(Fig. 4).

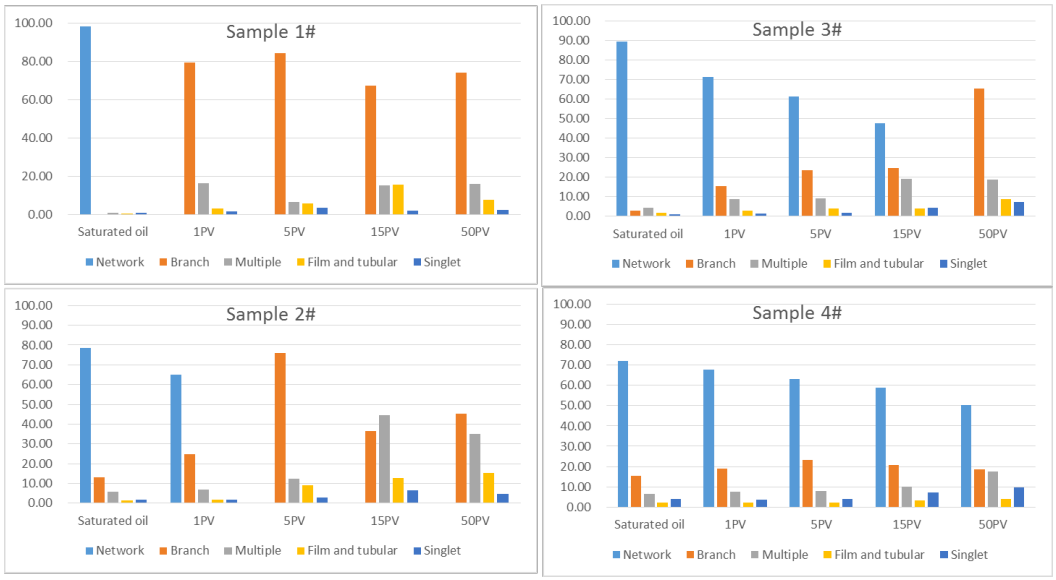

Fig. 4 Change of distribution pattern during water displacement

Sample 1# which has good connectivity between pores and throats has biggest changes in terms of the distribution pattern of residual oil. There is one dominating oil cluster in "network" form, which initially contains 99% of the total oil volume and is connected across the whole sample, disappeared after displacement. This could be because of the oil cluster breakup affected by snap-off events. Distribution pattern mainly is "branched" form after injection of 50PV brine.

Sample 2#, similar to sample 1#, due to affection of pore structure, prime distribution patterns are "branched" form and "multiple" form after injection of 50PV brine. We also observed a transition from a connected oil phase flow to disconnected clusters. In this process, the oil volume of "branched" rises sharply when "network" form of oil disappeared. Furthermore, redistribution of residual oil can be observed after 15 pore volume of water flooding displacement. Volume of "branch" form increases when the volume of "multiple" form decreases, this may be because of the coalescence events.

By contrast, water flooding displacement do not work well on sample3# and sample 4#which have more complicated pore structure. Their residual oil distribution patterns change less while oil clusters distribution is more complex. Especially 4# sample. All five distribution patterns coexist during whole displacement process, and mainly is "network" form.

CONCLUSION

Digital core technology is used to investigate the characteristics of residual oil clusters. The finding indicate that distribution of residual oil is influenced by pore structure and injected fluid volumes. Low permeability sandstones cores were more likely to have smaller pore radius, smaller throat radius, and poor coordination number which making process of oil production encounter greater resistance.

In imbibition, volume of residual oil in the pore space reduce, distribution patterns of oil clusters constantly change during displacement process. Cores with good pore

connectivity have biggest changes in terms of the distribution pattern of residual oil. Transition from a connected oil phase to disconnected clusters can be observed during water flooding. Oil volume of "branched", "multiple" rise sharply when "network" form of oil disappeared at the stage of a high water cut. Residual oil distribution pattern of cores with compact pore structure has smaller change while oil clusters distribute more complex. All five distribution patterns coexist during whole displacement process, and mainly is "network" form. As EOR methods for reservoirs containing residual oil are greatly influenced by pore scale entrapment characteristics of the oil phase, this study should result in improvements in our ability to further enhance oil recovery.

ACKNOWLEDGEMENTS

We would like to express appreciation for the following financial support: International Science & Technology Cooperation Program of China (2014DFR60490), Chinese National Natural Science Foundation (51504146), Youth Scholar Foundation of Shandng Academy of Scienses (2014QN030) & (2015QN016).

REFERENCES

1. Culligan, K., et al., *Pore-scale characteristics of multiphase flow in porous media: a comparison of air–water and oil–water experiments.* Advances in water resources, 2006. **29**(2): p. 227-238.
2. Culligan, K.A., et al., *Interfacial area measurements for unsaturated flow through a porous medium.* Water Resources Research, 2004. **40**(12).
3. Geistlinger, H., et al., *Quantification of capillary trapping of gas clusters using X‐ray microtomography.* Water Resources Research, 2014. **50**(5): p. 4514-4529.
4. Karpyn, Z.T., M. Piri, and G. Singh, *Experimental investigation of trapped oil clusters in a water‐wet bead pack using X‐ray microtomography.* Water Resources Research, 2010. **46**(4).
5. Ghosh, J. and G.R. Tick, *A pore scale investigation of crude oil distribution and removal from homogeneous porous media during surfactant-induced remediation.* Journal of contaminant hydrology, 2013. **155**: p. 20-30.
6. Rücker, M., et al., *From connected pathway flow to ganglion dynamics.* Geophysical Research Letters, 2015.
7. Krummel, A.T., et al., *Visualizing multiphase flow and trapped fluid configurations in a model three‐dimensional porous medium.* AIChE Journal, 2013. **59**(3): p. 1022-1029.
8. Berg, S., et al. *Multiphase Flow in Porous Rock imaged under dynamic flow conditions with fast X-ray computed micro-tomography*. in *EGU General Assembly Conference Abstracts*. 2013.
9. Al-Raoush, R.I., *Experimental investigation of the influence of grain geometry on residual NAPL using synchrotron microtomography.* Journal of Contaminant Hydrology, 2014. **159**(0): p. 1-10.
10. Kumar, M., et al., *Visualizing and quantifying the residual phase distribution in core material.* Petrophysics, 2010. **51**(05).

11. Georgiadis, A., et al., *Pore-scale micro-computed-tomography imaging: Nonwetting-phase cluster-size distribution during drainage and imbibition.* Physical Review E, 2013. **88**(3): p. 033002.
12. Youssef, S., et al., *Investigation of Pore Structure Impact on the Mobilization of Trapped Oil by Surfactant Injection.*
13. Iglauer, S., et al. *In-situ Residual Oil Saturation And Cluster Size Distribution In Sandstones After Surfactant Flooding Imaged With X-ray Micro-computed Tomography*. in *International Petroleum Technology Conference*. 2014. International Petroleum Technology Conference.
14. Andrew, M., B. Bijeljic, and M.J. Blunt, *Pore-scale contact angle measurements at reservoir conditions using X-ray microtomography.* Advances in Water Resources, 2014. **68**: p. 24-31.
15. Al-Raoush, R.I., *Impact of wettability on pore-scale characteristics of residual nonaqueous phase liquids.* Environmental science & technology, 2009. **43**(13): p. 4796-4801.
16. Kumar, M., et al. *Quantifying trapped residual oil in reservoir core material at the pore scale: Exploring the role of displacement rate, saturation history and wettability*. in *International Petroleum Technology Conference*. 2009.
17. Iglauer, S., et al., *Comparison of residual oil cluster size distribution, morphology and saturation in oil-wet and water-wet sandstone.* Journal of Colloid and Interface Science, 2012. **375**(1): p. 187-192.
18. Iglauer, S., A. Paluszny, and M.J. Blunt, *Simultaneous oil recovery and residual gas storage: A pore-level analysis using in situ X-ray micro-tomography.* Fuel, 2013. **103**(0): p. 905-914.
19. Li, F., et al., *CT Experiments and Image Processing for the Water-Oil Displacement at Pore Scale.* Procedia Engineering, 2012. **29**: p. 3831-3835.
20. Kong, T.Y. and A. Rosenfeld, *Digital topology: Introduction and survey.* Computer Vision, Graphics, and Image Processing, 1989. **48**(3): p. 357-393.

RAPID ESTIMATION OF HYDRAULIC FLOW UNIT PARAMETERS RQI AND FZI FROM MAGNETIC MEASUREMENTS IN SOME SHOREFACE RESERVOIRS

Carl Egiebor and David K. Potter

Department of Physics, University of Alberta, Edmonton, Canada

This paper was prepared for presentation at the International Symposium of the Society of Core Analysts held in Snowmass, Colorado, USA, 21-26 August, 2016

ABSTRACT

Petrophysical analysis of reservoirs often involves calculating key hydraulic flow unit parameters, such as the reservoir quality index (RQI) and the flow zone indicator (FZI), from core porosity and permeability measurements. The purpose of the present study was to see whether there were correlations between these hydraulic unit parameters and magnetic susceptibility measurements on core plugs from two oil wells in shoreface reservoirs in the North Sea. Good correlations could potentially allow future rapid estimation of RQI and FZI from magnetic measurements long before the conventional core porosity and permeability data normally becomes available. The main control on permeability in the two oil wells was illite clay, and the results showed good correlations between magnetically derived illite content (from the magnetic susceptibility measurements) and each of the parameters RQI and FZI in both wells. In one of the wells, where we had additional mineralogical data from X-ray diffraction (XRD), we obtained slightly improved estimates of the magnetically derived illite content by correcting for the presence of pyrite. This in turn led to slightly better correlations with RQI and FZI than the raw uncorrected values. Significantly poorer relationships were observed between XRD derived illite content and each of the parameters RQI and FZI. This may in part be because XRD is generally regarded as a semi-quantitative technique, whereas the magnetic method is extremely sensitive at quantifying the mineral components if the mineralogy is known. Also the XRD analyses required powdered samples that were much smaller than the core plugs used for the magnetic measurements, and therefore were not volumetrically identical to the core plug scale. The magnetic method is very rapid, non-destructive, easy to undertake and inexpensive. The good relationships generated in this study demonstrate its potential usefulness for rapidly estimating the hydraulic flow unit parameters RQI and FZI in these shoreface reservoirs. These measurements potentially allow field development decisions to be made at an earlier stage (before the conventional porosity and permeability data become available) in future cases in similar reservoirs, and this may have associated economic benefits.

INTRODUCTION AND METHODOLOGY

Recent studies have shown correlations between magnetic susceptibility, clay content and key petrophysical properties such as permeability [1,2]. The purpose of the present study

was to see if rapid, non-destructive magnetic susceptibility measurements also correlate with the key hydraulic flow unit parameters reservoir quality index (RQI) and flow zone indicator (FZI). These parameters were first proposed by Amaefule et al [3] as a means of splitting a reservoir into quantifiable hydraulic flow units, and the methodology has been widely adopted in the industry. All samples in a particular hydraulic flow unit have similar values of FZI, which is related to porosity and permeability as follows:

$$FZI = RQI / \Phi_z \quad (1)$$

where RQI is the reservoir quality index (= $0.0314 \sqrt{\{K/\Phi_e\}}$ where K is the permeability and Φ_e is the effective porosity), and Φ_z is the pore volume to grain volume ratio (= $\Phi_e/1-\Phi_e$). The present study determined the FZI and RQI values for several hundred core plugs from the conventional core porosity and permeability data in two wells (Well 2 and 2a) containing shoreface reservoirs in a North Sea oilfield. The FZI and RQI values were then compared to the illite content derived from magnetic susceptibility measurements on the identical conventional core plugs. These measurements were obtained using a Molspin magnetic susceptibility bridge. Each measurement, which requires a background reading followed by a core plug sample reading, can be acquired in about 5 seconds. Thus many samples can be measured extremely rapidly. Assuming a simple mixture of quartz and illite (which was a reasonably good assumption according to our XRD data), then following the procedure of Potter et al [1,4] the fraction of illite, F_I, is given by:

$$F_I = (\chi_Q - \chi_T) / (\chi_Q - \chi_I) \quad (2)$$

where (1- F_I) is the fraction of quartz, and χ_I and χ_Q are the magnetic susceptibilities per unit mass of illite and quartz (15×10^{-8} m^3 kg^{-1} and -0.62×10^{-8} m^3 kg^{-1} respectively). In Well 2a we were also able to compare XRD derived illite content with RQI and FZI. The XRD data was acquired using the Siroquant technique, which quantifies clay and non-clay minerals in one run.

RESULTS AND DISCUSSION

Figure 1 shows crossplots of magnetically derived illite content against RQI (top) and FZI (bottom) for the nearly 300 core plugs in Well 2. The R^2 regression coefficients are relatively high (0.73 and 0.67 respectively) demonstrating good correlations between the hydraulic unit parameters and the magnetically derived illite content. The correlations might be expected given that a correlation was previously identified between permeability and magnetically derived illite content [1], and porosity is relatively constant. **Figure 2** shows crossplots of magnetically derived illite content (corrected for the presence of pyrite) against RQI (top) and XRD derived illite content against RQI (bottom) for the 87 core plugs in Well 2a. Whilst the R^2 regression coefficient is quite high (0.80) for the magnetic data, it is significantly lower (0.31) for the XRD data. A similar pattern is evident in **Figure 3**, which shows crossplots of magnetically derived illite content (corrected for the presence of pyrite) against FZI (top, with $R^2 = 0.76$) and XRD derived illite content against FZI (bottom, with $R^2 = 0.27$) for the 87 core plugs in Well 2a. Whilst XRD is good at identifying which minerals are present, it is a semi-quantitative technique, which may partly explain the poorer correlations with RQI and FZI. It may also partly be due to the XRD analyses requiring powdered samples that

were much smaller than the core plugs used for the magnetic measurements, however, since the magnetic measurements indicate several samples with low illite content it seems unlikely that many of the XRD samples merely sampled the more illite rich zones. We have greater confidence in the magnetic measurements that are extremely sensitive to small amounts of illite clay (with uncertainties of less than ± 0.1%, compared to at least ± 0.5% for the XRD measurements). Note also that the differences between the magnetic and XRD values at low illite content appear exaggerated due to the logarithmic scale. There are also instances where the magnetic measurements give a higher illite content than XRD. This may partly be due to a very small amount of ferrimagnetic material in the samples (causing a slight overestimate in magnetically derived illite content), or that XRD may not see some very fine grained amorphous illite within the samples.

CONCLUSIONS

1. Good correlations exist between the hydraulic flow unit parameters (RQI, FZI) and magnetically derived illite content in Wells 2 and 2a. Hence, the magnetic method shows good promise for rapidly and non-destructively estimating the hydraulic unit parameters in this type of shoreface reservoir where porosity remains fairly constant and permeability varies with illite content.
2. Significantly poorer relationships were observed between the hydraulic flow unit parameters and the XRD derived illite content. This may be due to some of the reasons suggested in the Results and Discussion section. Unlike the XRD technique, which is more expensive and requires extra time for preparation, the magnetic method is rapid, sensitive, easy and less expensive for predicting the hydraulic flow unit parameters.
3. The correlations between the hydraulic flow unit parameters and magnetically derived illite content in Well 2a were very slightly better after the magnetic susceptibility results were corrected for the presence of paramagnetic pyrite (identified from XRD data).

ACKNOWLEDGEMENTS

The support of an NSERC Discovery Grant to DKP is gratefully acknowledged.

REFERENCES

1. Potter, D. K., 2007. Magnetic susceptibility as a rapid, non-destructive technique for improved petrophysical parameter prediction. *Petrophysics*, **48** (issue 3), 191-201.
2. Ali, A., Potter, D. K. and Tugwell, A., 2014. Correlation between magnetic properties and permeability: results from a new case study in the North Sea. *2014 International Symposium of the Society of Core Analysts***,** Avignon, France. Paper SCA2014-077.
3. Amaefule, J., Altunbay, M., Tiab, D., Kersey, D., & Keelan, D., 1993. Enhanced reservoir description: Using core and log data to identify hydraulic flow units and predict permeability in uncored intervals/wells. *SPE paper 26436*, p. 205-220.
4. Potter, D. K., Corbett, P. W. M., Barclay, S. A and Haszeldine, R. S., 2004. Quantification of illite content in sedimentary rocks using magnetic susceptibility - a rapid complement or alternative to X-ray diffraction: *Journal of Sedimentary Research, Research Methods Papers Section*, **74**, p. 730-735.

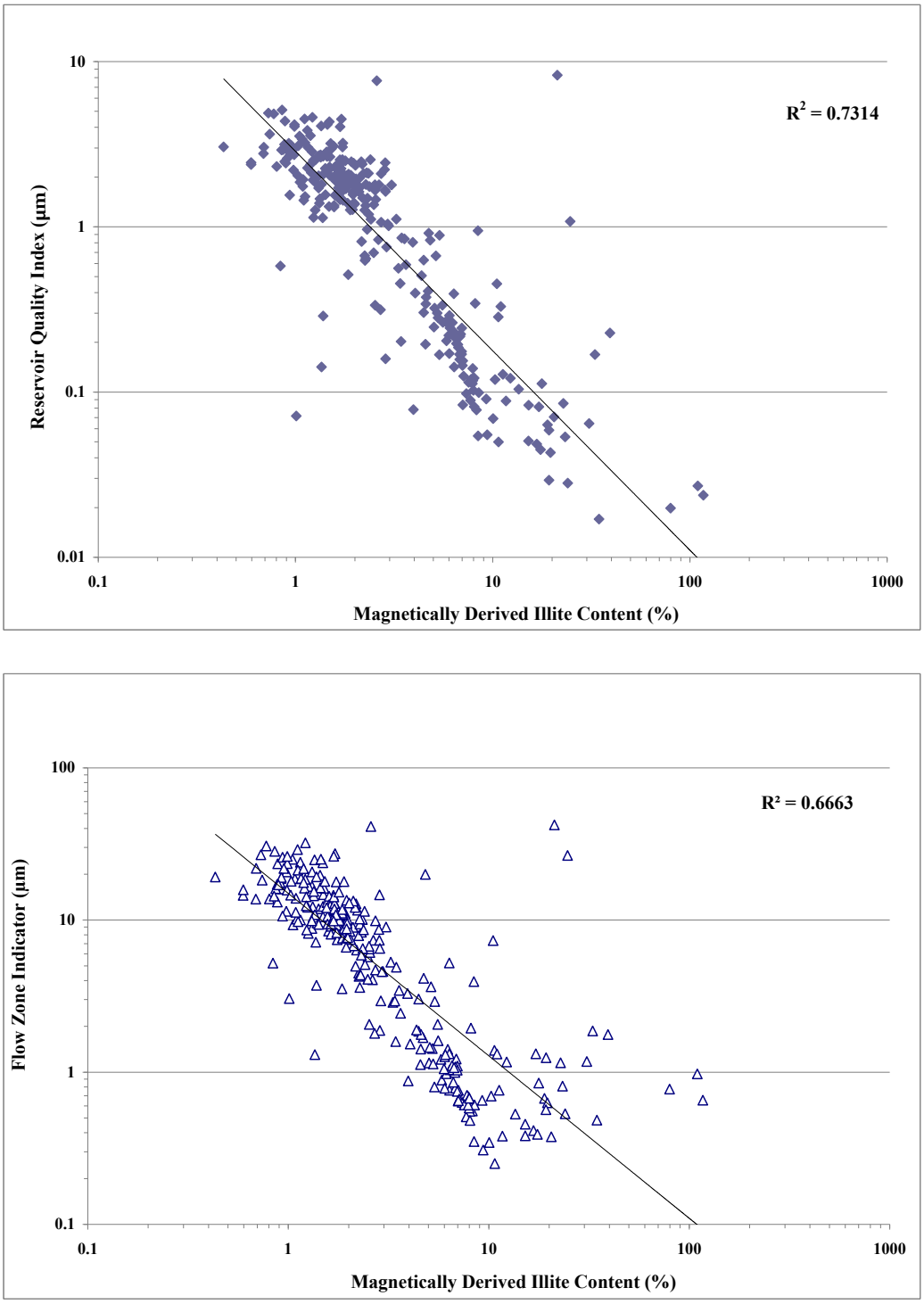

Figure 1. Crossplots of magnetically derived illite content against RQI (top) and FZI (bottom) for the nearly 300 core plugs in Well 2. The cause of the two samples that exhibit "illite" contents just over 100% is most likely due to the samples containing extremely small amounts of ferrimagnetic material.

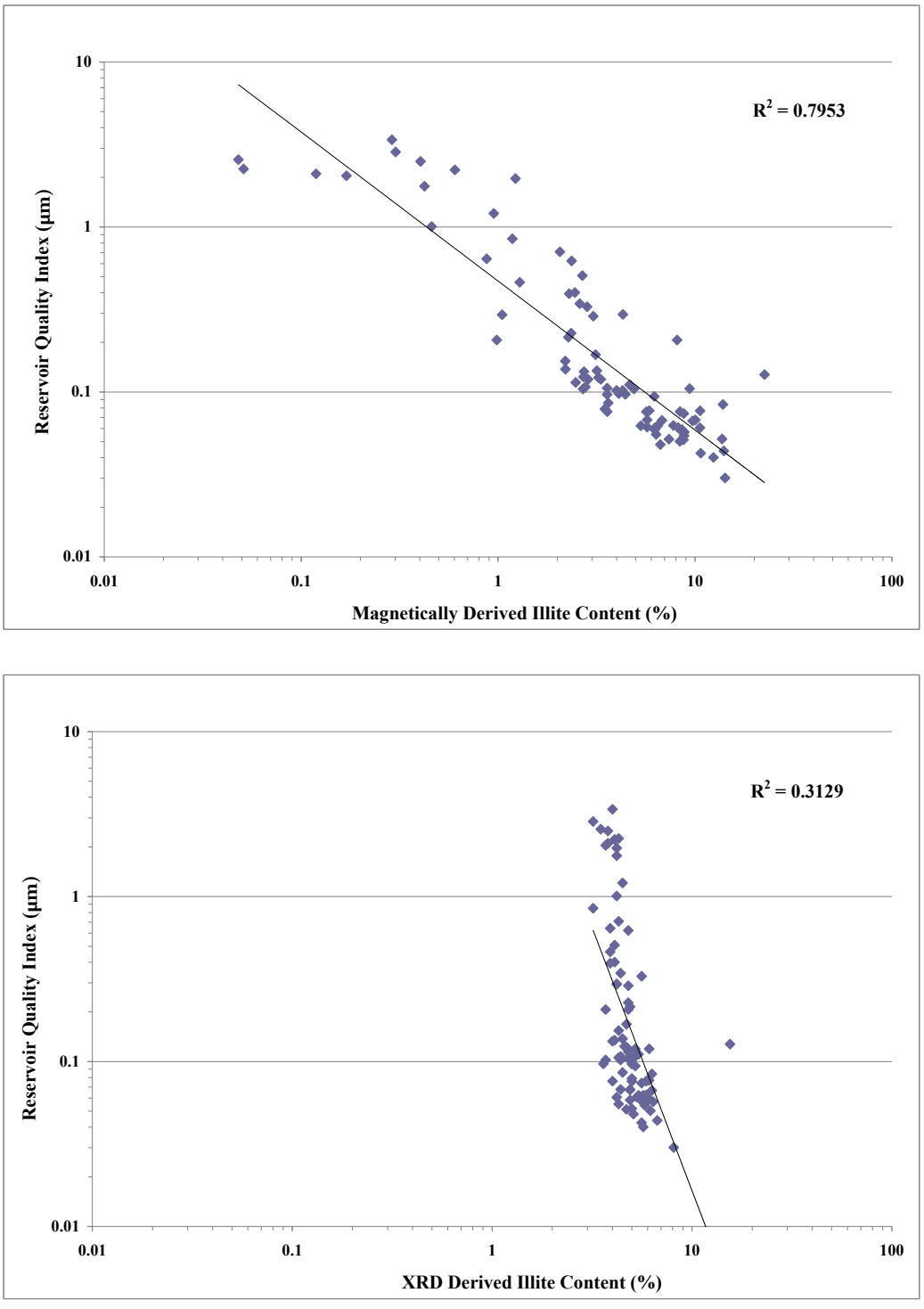

Figure 2. Crossplots of magnetically derived illite content against RQI (top) and XRD derived illite content against RQI (bottom) for the 87 core plugs in Well 2a. The magnetically derived illite content was corrected for the presence of small amounts of pyrite (identified from XRD). This made only a slight difference to the regression, since the R^2 value for the uncorrected data for the top figure was 0.7933.

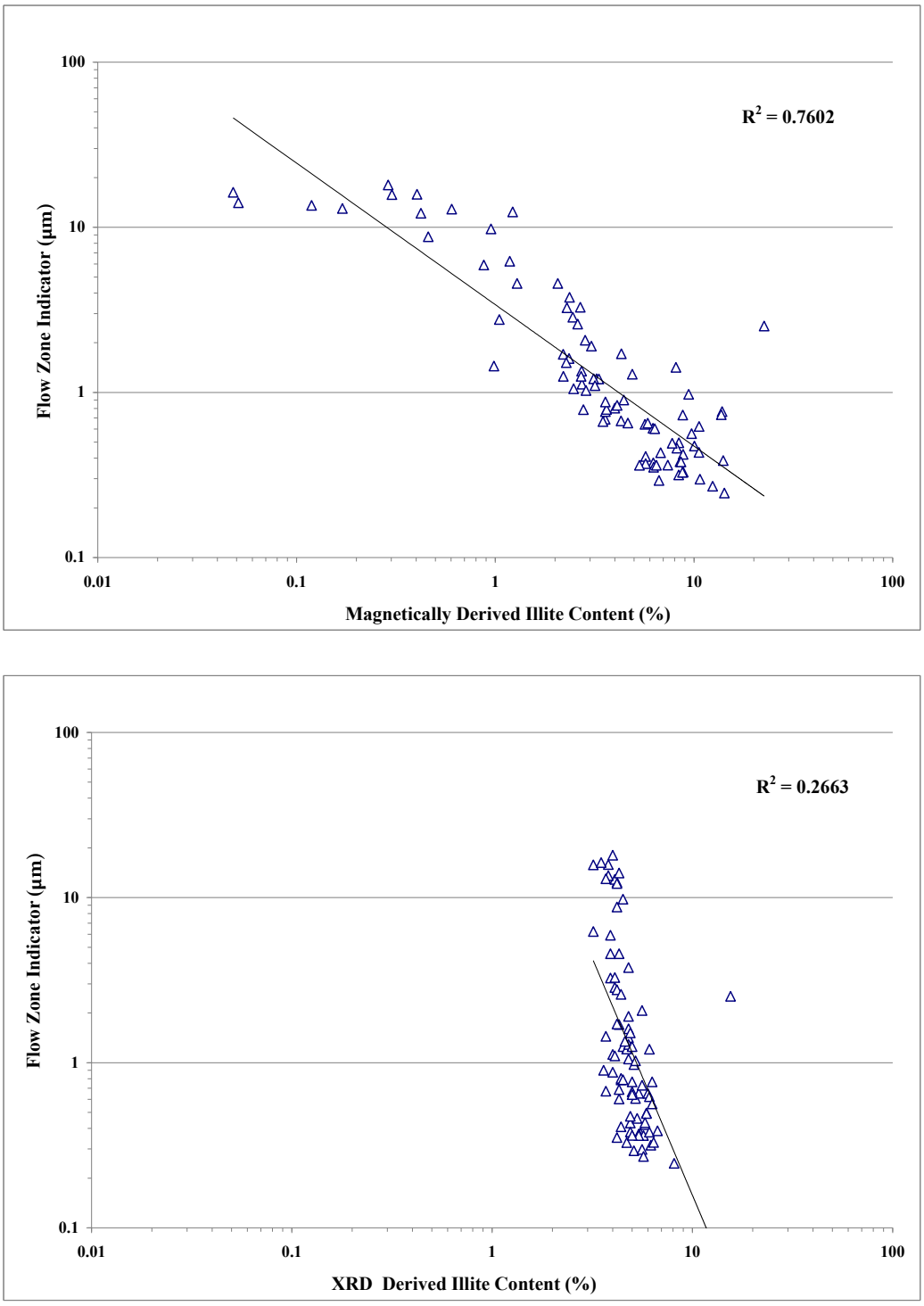

Figure 3. Crossplots of magnetically derived illite content against FZI (top) and XRD derived illite content against FZI (bottom) for the 87 core plugs in Well 2a. The magnetically derived illite content was corrected for the presence of small amounts of pyrite (identified from XRD). This made only a slight difference to the regression, since the R^2 value for the uncorrected data for the top figure was 0.7579.

ALTERNATIVE APPROACHES FOR TRANSIENT-FLOW LABORATORY-SCALE PERMEAMETRY

Michael J. Hannon, Jr.
The University of Alabama at Birmingham

This paper was prepared for presentation at the International Symposium of the Society of Core Analysts held in Snowmass, Colorado, USA, 21-26 August 2016

ABSTRACT

Although pressure-pulse-decay permeametry has been in wide use for the past 50 years, its standard configuration and design have remained largely intact, with performance optimizations based mostly on sample geometry and reservoir volumes. For characterizing ultra-low permeability materials like shales or caprocks, where the pulse-decay methodology often becomes problematic, many have turned to unsteady-state analyses on crushed fragments. A paucity of models exists in the public literature for the latter scenario, most of which are analytical approximations of very simple cases. This study addresses both issues by proposing analytical flow models for alternative experimental schemes. First, new unidimensional flow scenarios are considered as substitutes for the classical pulse-decay techniques on cylindrical core samples. Such strategies can decrease testing times by more than an order of magnitude as compared to conventional pressure-pulse-decay strategies with similar fidelity. Second, a model is presented here that relaxes a key simplifying assumption inherent to publicly available models for crushed media, namely that the entire collection of particles is of uniform size. Rather, an analytical model for a discrete distribution of sizes is presented that more accurately represent the broad range of particle sizes that are typically seen in crushed materials.

INTRODUCTION

Site characterization of geologic formations begins with the collection of native core samples and their analysis by bench-top laboratory experiments. Although these analyses occur on a minute sample size with respect to the reservoirs under investigation, they are used as the "ground truth" against which field-scale data are calibrated. Perhaps nowhere is this approach more important than in the assessment of permeability. Conventional steady-state measurements performed on samples from highly porous and permeable storage formations provide accurate estimates of permeability in a reasonable amount of time. But for the ultra-tight formations interlaced between them, measuring permeability is much more difficult. The ability to perform such measurements in a way that is both reproducible and timely continues to elude interested parties, who require them for applications such as unconventional hydrocarbon recovery [1] or geological contaminant storage [2].

The most prevalent rapid permeametry techniques for shale and caprock materials are based upon the pressure-pulse-decay experimental scheme [3]. Offshoot approaches of this baseline strategy, most notably the pulse-decay analysis performed on crushed samples [4], provide estimates of very low permeability quite rapidly. But they do not always do so within a level of certainty that meets industry needs [5]. A technique that could resolve core-scale permeabilities reliably in a reasonable amount of time would be a significant technological leap forward. As a step in that direction, this report considers alternative approaches to the standard pressure-pulse decay on cylindrical core samples and an additional flow model for pulses applied to crushed media.

ALTERNATIVE FLOW SCENARIOS

To address many of the limitations inherent to the models outlined in the current art, this section considers alternative unidimensional flow scenarios which can be reduced to analytical models. It begins by describing slight modifications to the classical techniques involving flow along the axial direction of cylindrical core samples, followed by models for flow in the radial direction of cylindrical specimens. These approaches could form baseline alternatives to the industry-standard pulse-decay. The most prevalent of these variant approaches is crushed-core transient-flow permeametry, which has a shortage of publicly available flow models to compare against its experimental data. Toward that end, a model is presented for a pulse applied to a discrete size distribution of porous spherical particles.

In order to linearize the governing equations in the presence of changing fluid viscosity μ, compressibility c, and compressibility factor Z, the pressure variable p and temporal variable t were transformed to the pseudo-pressure (p^*) and pseudo-time (t^*) domains defined in Equations 1 and 2, respectively [6].

$$p^* \equiv \int_{p_i}^{p} \frac{p'}{\mu(p')Z(p')}dp';\ \ dp^* = \frac{p}{\mu Z}dp \tag{1}$$

$$t^* \equiv (\mu c)_{ref}\int_0^t \frac{dt'}{\mu\big(p(x,t')\big)c\big(p(x,t')\big)};\ \ dt^* = \frac{(\mu c)_{ref}}{\mu c}dt \tag{2}$$

The subscript "ref" denotes properties evaluated at a reference condition, such as their average values over the duration of the test. The dependent variable is non-dimensionalized to its final form p_D^* by the pseudo-pressure evaluated under pulse conditions p_p^* (i.e., $p_D^* \equiv p^*/p_p^*$) and the independent temporal variable is normalized by the time constant τ_ℓ (i.e., $t_{D,\ell}^* \equiv t^*/\tau_\ell$). Defined by Eq. 3, this time constant depends on the thermo-physical properties of the permeant $(\mu c)_{ref}$, the length scale of each scenario ℓ, the porosity of the sample ϕ, and the apparent permeability k (assumed constant) of the sample to the gaseous permeant under the pressure conditions of a given experiment.

$$\tau_\ell \equiv \frac{\phi(\mu c)_{ref}\ell^2}{k} \tag{3}$$

Axial Flow in Cylindrical Samples ($\ell = L$)

One slight change to the standard pressure-pulse decay would be to apply a step disturbance in both reservoirs (having volumes V_0 and V_1) simultaneously, as shown in Figure 1. By doing so, the time required for the system to reach equilibrium decreases significantly. A four-fold decrease in time can be attributed to effectively cutting the characteristic length scale (in this case, chosen as the sample length L) in half (see Equation 3), and equilibration no longer requires filling the downstream reservoir. Figure 1 provides example pressure responses to a simultaneous pulse applied to both ends of a homogenous sample with apparatuses having various reservoir volumes ($\gamma_0 \equiv V_0/V_p$, $\gamma_1 \equiv V_1/V_p$, where V_p indicates the pore volume of the sample). Applying a simultaneous pressure increase in both reservoirs also enables a rapid characterization of core-scale longitudinal heterogeneity [7] from a single test. Toward

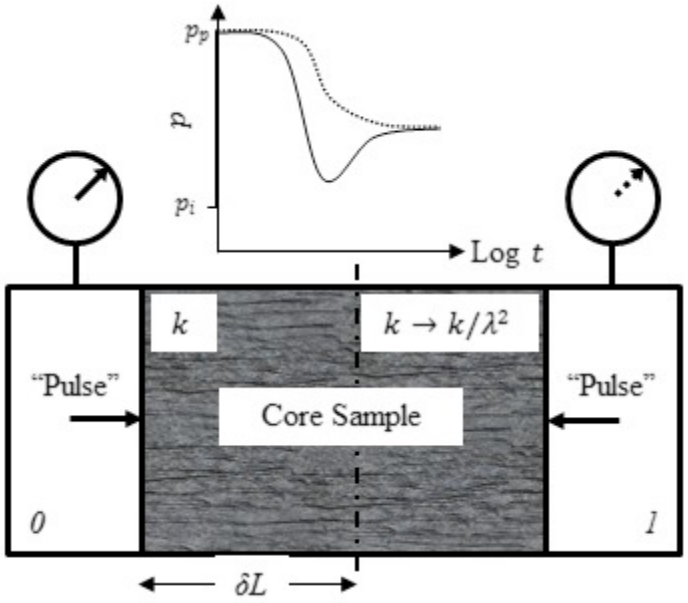

Figure 3. Schematic of a bi-directional pressure-pulse-decay model for a sample having a discrete discontinuity of permeability at a distance δL from the upstream face.

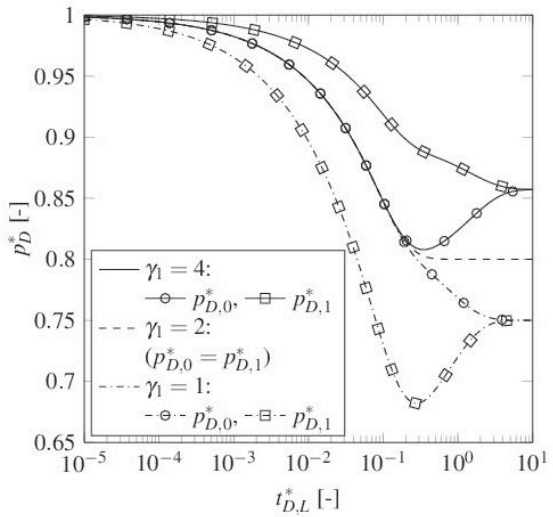

Figure 1. Bidirectional pressure-pulse decay of a homogeneous sample (i.e, $\lambda^2 = 1$) with one reservoir-volume ratio fixed ($\gamma_0 = 2$) and the other (γ_1) variable.

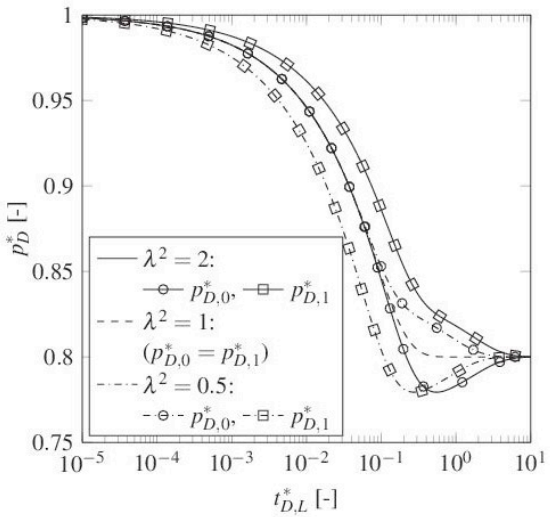

Figure 2. Bidirectional pressure-pulse decay with fixed reservoir volumes ($\gamma_0 = \gamma_1 = 2$) of a heterogeneous sample with varying permeability ratio λ^2 and fixed discontinuity location ($\delta = 0.5$).

that end, an analytical solution for the case of a discrete permeability discontinuity imposed at an arbitrary plane (located a distance δL from the upstream face) within a sample having uniform porosity is presented in Figure 2.

Radial Flow in Cylindrical Samples ($\ell = R$)

Another technique for decreasing the length of the flow path for the permeant, and therefore the equilibration time, is to invert the normal pulse-decay apparatus by sealing the circular ends of a cylindrical sample and allowing the fluid to infiltrate its circumferential surface (Figure 4). The underlying assumption here is a uniform-permeability fabric along the radial direction r of the sample. At the core scale, this is reasonable for many varieties of lithologic samples extracted perpendicular to their native bedding planes under uniform radial confining stress, which is the only stress state achievable in cylindrical core-holder apparatuses. Figure 5 shows pressure-response curves from the outer reservoir ($p_D^*|_{r=R}$) and along the sample centerline ($p_D^*|_{r=0}$), plotted for various reservoir volumes ($\gamma \equiv V/V_p$, where V is the volume of the reservoir). Although the latter of these pressures could not be measured directly, they are shown here to indicate equilibration of the system.

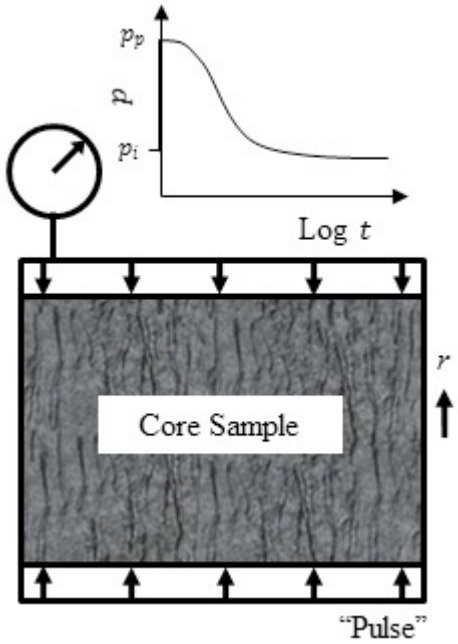

Figure 4. Schematic of a radially oriented pressure-pulse-decay experiment.

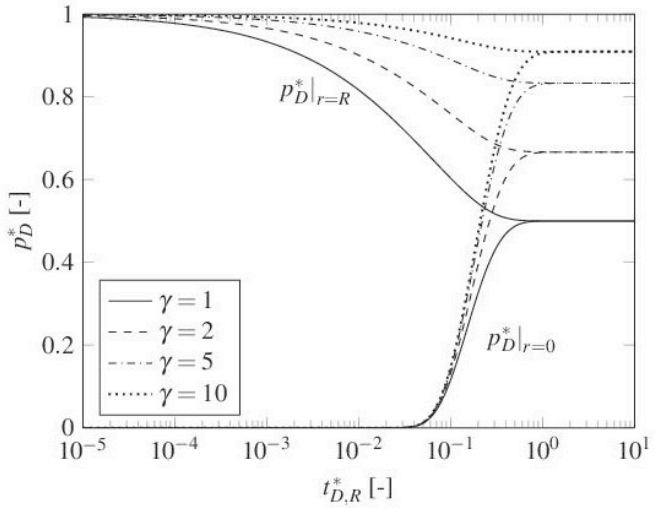

Figure 5. Radial pressure-pulse decay in apparatus having various reservoir volumes.

Radial Flow in a Discrete Size Distribution of Spherical Particles ($\ell = R_{eq}$)

Publicly available models predicting the pressure response from pulse-decay tests on crushed particles assume them to be a collection of uniformly sized homogeneous, isotropic spheres [8]. While this may be a suitable approach for a select portion of crushed materials (such as those collected from a single sieve layer), permeability estimates are known to decrease with decreasing particle size [4]. To analyze a wider

array of particle sizes, an analytical model was generated for a pressure disturbance applied to a collection of spherical particles having a discrete distribution of M different sizes, the i^{th} of which has particles of radius R_i and contains fraction χ_i of the overall volume (or mass, assuming constant grain density) of the particles. The characteristic length is chosen as the equivalent radius R_{eq} of a single sphere having identical volume as the entire collection of particles. Pressure-decay curves from these solutions are plotted in Figure 6 for a discrete particle size distribution comparable to those typically seen in industry, as given in Table 1.

Table 1. Typical particle size distribution for crushed shale samples, provided by Weatherford International, Ltd. (personal communication, 2015).

Sieve Size	χ_i [%]	R_i [mm]
>60	9.20	0.088
60	5.47	0.177
35	6.73	0.324
20	29.4	0.594
12	21.7	0.996
8	27.5	1.53

$$\bar{R} = \sqrt[3]{\sum_{i=1}^{M} \chi_i R_i^3} = 1.08 \text{ mm}$$

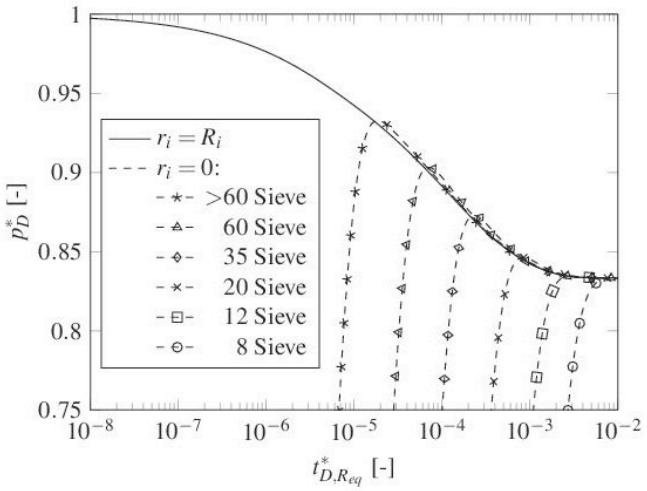

Figure 6. Pressure-pulse decay for a distribution of spherical particles collected from a cylindrical core having diameter equal its length, partitioned in a typical sieve-size distribution (Table 1) in a typical reservoir volume ($\gamma = 5$).

COMPARISONS AMONG EXPERIMENTAL SCHEMES

Error! Reference source not found. shows the anticipated pressure responses from the multiple pulse-decay techniques discussed previously, based on a homogeneous,

Table 2. Comparison of the times required by each flow condition demonstrated in Figure 11 to decay the pressure disturbance to within 0.01% of equilibrium. The "crushed" case indicates the pressure response to a pulse applied to spherical particles collected by crushing the same cylindrical plug into the size distribution of particles described in Table 1.

Experiment	$t^*_{D,L}$	× Faster
Unidirectional	5.17	1.0
Bidirectional	0.665	7.77
Radial	0.294	17.6
Crushed	0.00203	2,550

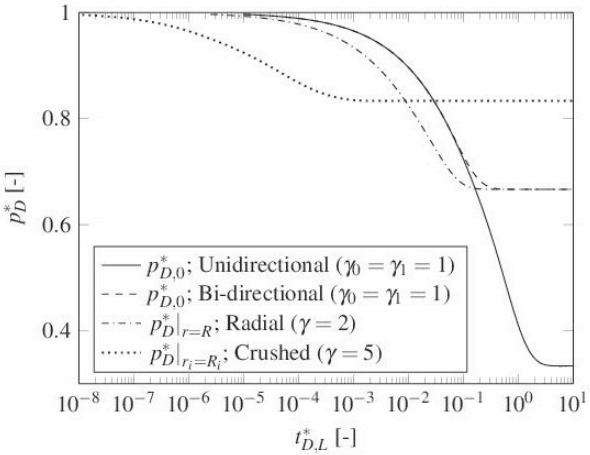

Figure 7. Comparison of various unsteady-state permeametry methodologies based on a cylindrical sample having diameter equal to its length.

cylindrical sample having a diameter equal to its length. **Error! Reference source not found.** compares the amount of time necessary for the pressure disturbance to decay to within 0.01% of its final equilibrium value for each experimental scheme, with similar comparisons noted for various stages of partial equilibrium. Reservoir sizes (provided in the legend of **Error! Reference source not found.**) were selectively chosen to draw appropriate comparisons among the various experimental schemes. The bi-directional- and radial-flow cases would provide more than a 7.5- and 17.5-fold reduction, respectively, in test time compared to the conventional approach. These benefits come at the cost of a more limited range on the observed pressure response, but transducers are available having sufficiently high precision to provide satisfactory measurements over this range. A much faster (>2,500×) reduction in equilibration time is noted from the crushed-sample approach, but it has well-documented limitations in the accuracy of its permeability estimates [5]. The bi-directional and radial transient-flow schemes provide means for low-permeability assessment with a combination of speed, reliability and representativeness far more practical to many industrial applications.

ACKNOWLEDGEMENTS

This work was supported by the U.S. National Energy Technology Laboratory. It summarizes a manuscript currently in review by *Transport in Porous Media*.

REFERENCES

1. Chhatre, S.S., Braun, E.M., Sinha, S., Passey, Q.R., Zirkle, T.E., Wood, A.C., Boros, J.A., Berry, D.W., Leonardi S.A., and Kudva, R.A., "Steady state permeability measurements of tight oil bearing rocks," SCA 2014-12.
2. Hannon, Jr., M.J. and Esposito, R.A., "Screening considerations for caprock properties in regards to commercial-scale carbon-sequestration operations," *International Journal of Greenhouse Gas Control*, (2015) **32**, pp. 213-223.
3. Brace, W.F., Walsh, J.B., and Frangos, W.T., "Permeability of granite under high pressure," *Journal of Geophysical Research*, (1968) **73**, 6, pp. 2225-2236.
4. Luffel, D.L., "Advances in shale core analysis," Technical Report GRI-93/0297, Gas Research Institute, 1993.
5. Spears, R.W., Dudus, D., Foulds, A., Passey, Q.R., Sinha, S., and Esch, W.L., "Shale gas core analysis: strategies for normalizing between laboratories and a clear need for standard materials," SPWLA-2011-A, presented at the *52nd Annual Logging Symposium*, 2011.
6. Haskett, S.E., Narahara, G.M., and Holditch, S.A., "A method for simultaneous determination of permeability and porosity in low-permeability cores," *SPE Formation Evaluation*, (1988) **3**, 3, pp. 651-658.
7. Kamath, J., Boyer, R.E., and Nakagawa, F.M., "Characterization of core scale heterogeneities using laboratory pressure transients," *SPE Formation Evaluation*, (1992) **7**, 3, pp. 219-227.

8. Profice, S., Lasseux, D., Jannot, Y., Jebara, N., and Hamon, G., “Permeability, porosity and Klinkenberg coefficient determination on crushed porous media,” SCA 2011-32.

CORE ANALYSIS AS A KEY TO UNDERSTANDING FORMATION DAMAGE AFTER HYDRAULIC FRACTURING TREATMENT

Wilk, K.[1], Kasza, P.[1], Labus, K.[2]
[1]Oil and Gas Institute – National Research Institute, Poland, klaudia.wilk@inig.pl
[2]Silesian University of Technology, Poland

This paper was prepared for presentation at the International Symposium of the Society of Core Analysts held in Snowmass, Colorado, USA, 21-26 August 2016

ABSTRACT

Hydraulic fracturing is the most effective stimulation method of hydrocarbon reservoirs. The main goal of this treatment is to increase production rate and recovery factor of oil and/or gas. Originally fracturing has been developed for conventional reservoirs and has been performed successfully in different oil and gas formations for decades. This technology has also become invaluable for completion of unconventional hydrocarbon deposits. It has been proved, that so far it is the only, effective method to allow hydrocarbons drainage and commercial production from gas shales and tight gas sandstones. Thanks to hydraulic fracturing it is possible to increase the recovery rate of hydrocarbons.

Just like any other technology along with benefits it also has drawbacks. One of the key drawbacks is the impact of technological fluids on reservoir rock. Any interference of technological fluids with stable reservoir system (rock – water - hydrocarbons) may result in undesirable effects. During the fracturing treatment, fracking fluids are injected also into pores and natural fractures of reservoir rock. In many cases the contact and interaction of these fluids with the formation may generate serious problems like clays swelling and precipitation of secondary minerals. Each of these phenomena may cause temporary or permanent formation damage and reduce its permeability.

There are several different field and laboratory methods designed to assess the degree and range of formation damage. In this area many possibilities is offered by comprehensive analysis of the core material. In our study, several techniques to evaluate the formation damage have been used. At first routine core analysis was applied and permeability and porosity coefficients were measured. Next, auxiliary analyses were performed, including fluorescence microscopy and Scanning Electron Microscopy in order to confirm the structural effect of formation damage by fracturing fluids. Presented results and conclusions of this research may be very useful to design more “clean” and efficient fluids for hydraulic fracturing.

INTRODUCTION

Hydraulic fracturing is now the most popular method of stimulating gas and oil reservoirs in non-conventional formations. Fracturing is necessary to enable production of hydrocarbons from formations of very low permeability, i.e. tight gas, coal and gas-bearing shales deposits that cannot be exploited without fracking [1]. When fracking fluids used are based on water, the so-called permeability damage is likely to occur caused by, among others, swelling of clay minerals, or by other physical and chemical mechanisms taking place in a formation being fractured. [2] The role of fracking fluid is to generate and propagate fractures. Any applied fracking fluid should transport the proppant in suspension, and then to leave it in the fracture made in the reservoir. It turns out, that in many Polish shale formations, swelling clay minerals occur, preventing the use of traditional water-based fracturing liquids due to the permeability damage hazard.

PERMEABILITY DAMAGE IN FRACTURING

In practice, fracking fluids based on water are most often used in hydraulic fracturing operations. They include water solutions of natural or synthetic linear and cross-linked polymers. Fracking fluid used for hydraulic fracking treatments in conventional deposits (cross-linked linear polymer technology) should have in surface conditions apparent viscosity in the range of thousands of mPa* s. And in formation conditions, apparent viscosity in the range of at least 100 mPa* s, at shear rate 40 s^{-1}, because it is assumed that such a shear rate occurs in a fracture [3]. In non-conventional deposits, in particular in shale formations, the role and types of fracking fluids are somehow different. From technological point of view, US onshore American experience shows that obtaining high number of fractures in the largest possible volume is achievable even when using low-viscosity fluids of several mPa* s at high pumping rate, however, its friction, when flowing in pipes, is high. As a result, small amount of synthetic polymer is added to water, usually polyacrylamide, which significantly, due to its low viscosity reduces the flow resistance. Shale fracturing in some cases also uses more "conventional" fracking fluids (linear and cross-linked polymer). Sometimes it is necessary to perform so-called hybrid fracturing. Fracturing of unconventional tight gas deposits also uses fluids based on gels, and foams [4,5].

During fracking, considerable amounts of technological fluid is injected (thousands of m^3), with a very high flow rate, even up to 25 m^3/min [2,6]. As a result, the fracturing pressure of the formation is exceeded, the fracture propagation is maintained, proppant in the fracking fluid of low viscosity is kept in the form of a suspension, in order to transport it to the fracture.

An important parameter that characterizes a fracturing fluid is its leak off into the rock matrix. Hydraulic fracking operations are always performed at high pressure. The difference of fracturing pressure and deposit pressure causes filtration of the fracking fluid into the matrix of formation. When using polymer fluids, the filtrate that infiltrates the matrix is water, and the filtration cake is formed on the fracture wall. Filter cake on a sandstone during laboratory filtration tests is shown on Figure 1

.

Figure 1. Filter cake example

The degree of filtration significantly affects the efficiency of a fracking fluids and is one of the main parameter taken into consideration in the fracturing treatments design. Too high, uncontrolled filtration of fracturing fluid into the rock matrix during fracking can lead to screen out of proppant. Sandstone and carbonate reservoirs of low permeability have slightly different leak off nature of a fracking fluid. This difference stems mainly from the porosity and permeability. Sandstones have usually porous structure. Polymer on the surface of a porous rock creates filter cake and filtrate fills the pores. With low permeability of sandstone, the filtration range and the thickness of the filter cake are significantly limited. In reservoirs that have fracture porosity and permeability, frack fluid will rather fill fractures and micro-fractures, causing their further propagation. Classic filtration with filter cake shall be in this case marginal. In the process of filtration, the type of the reservoir fluid that fills the porous volume is also significant. Gas, as a compressible medium, will limit filtration to a very small extent, and oil, as less compressible, will limit it to much greater extent.

Another phenomenon that negatively affects the appropriate conductivity of a fracture is the insufficient cleaning of a fracture from polymers present in the fracking fluid. Also, insoluble residues included in the fracking fluid or formed during fluid breaking may remain in a fracture or in the porous space, thus reducing the primary conductivity of a fracture. It shows in particular during the flow of fracturing liquid filtrate into the reservoir rock (creating filter cake), and hence polymer thickening in a fracture filled with proppant [3].

PROCEDURES

When preparing the formulation for a fracturing fluid, its possible interaction with components of rock structure and the cement of the rock should be taken into account. The research was supposed to evaluate such interaction based on the results of experimental tests. In order to test formation damage with selected fluids, the following laboratory tests have been planned:

- how the prepared fracking fluids are damaging the rock formations (based on flow tests on natural cores)

- identification, analysis and assessment of rock formation damage

The tests have been conducted on natural rock cores from Rotliegend samples.
The impact of three fracking fluids on rock formation damage has been tested:

- fluid based on synthetic polymer - slick water
- fluid based on natural linear polymer
- fluid based on natural cross-linked polymer

Fig. 2 presents the core face after the flow tests with the use of cross-linked polymer, linear polymer, and slick water liquid. The core flow tests of the fracturing fluids have been conducted on AFS Core Flood System at ambient temperature using low backpressure (140 psi).

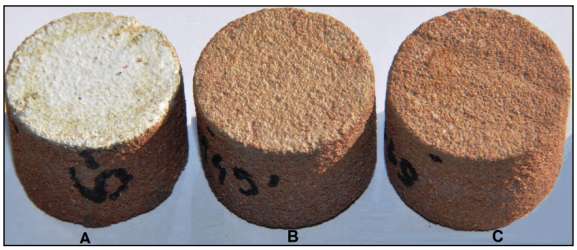

Figure 2. The Rotliegend Sandstone cores after the injection of A-cross-linked polymer, B-linear polymer, C-slick water.

RESULTS

The level of damage to rock pores after the flow tests has been defined using:

- permeability and porosity tests,
- SEM analysis
- fluorescence tests in UV light

According to our results –Table 1, the permeability of the cores significantly decreased after the application of the technological fluid with linear polymer and cross-linked polymer. The permeability has been reduced mainly by the filter cake, formed on the face surface of the cores. The permeability was reduced on the samples' surface, as visible in the microscopic photos. In the case of these cores, the porosity slightly increased as a result of solid particle elution. The sample core permeability increased after the injection of the slickwater-based fluid. Probable increase in permeability and porosity of the samples might be attributed to the washing out of solid particles from the cores, visible also in the received filtrate.

Table. 1 Porosity and permeability coefficient measured before and after the core flow tests.

Type of Fluid	k_0 initial core permeability [md]	k_k final core permeability [md]	ϕ_0 initial core porosity [%]	ϕ_k final core porosity [%]
slick water	78,09	99,39	24,77	26,28
linear polymer	146,64	15,47	26,88	27,01
cross-linked polymer	155,01	19,45	21,15	21,58

To identify the mineral phases in the samples, a FEI Quanta-650 FEG electron microscope (15 kV, 8–10 nA, 50 Pa) was used before and after the experimental tests. Below are the example images of the pore space after the linear polymer-based, and cross-linked polymer-based fluid injection into the core. The observation of fine clayey fractions, that were present in the intergranular space, and traces of the fracturing fluid, under the scanning electron microscope is important from the point of view of stimulation procedures.

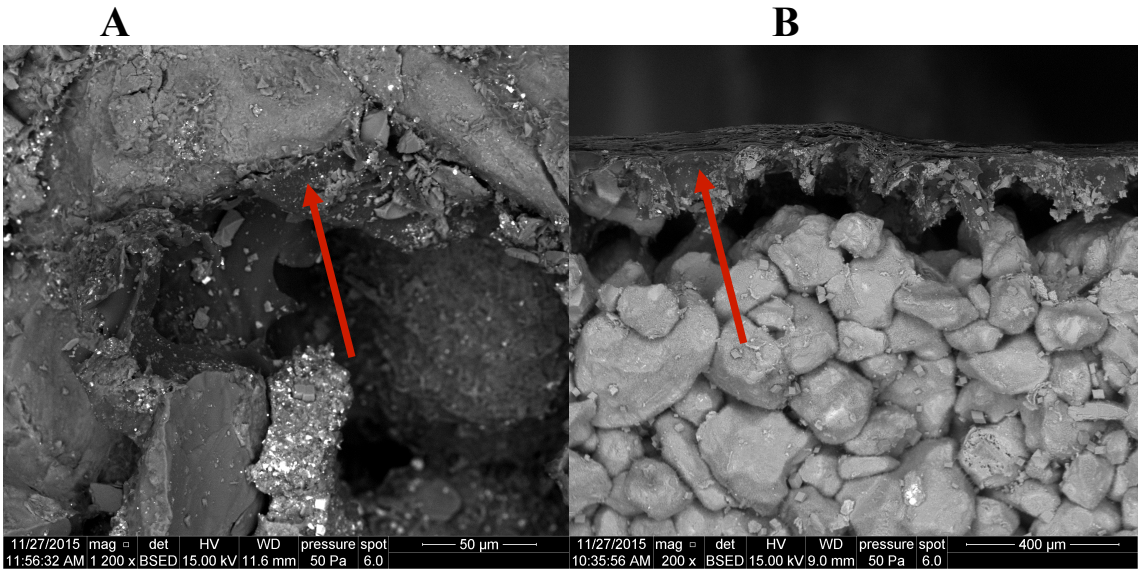

Figure 3. A-Polymer shreds (arrow) in the pore space visible even more than 3-4 mm from the front surface. B-The front surface of a core with visible polymer coating (arrow)

The level of the fracturing fluid impact on the permeability damage was confirmed by the UV tests. When using a slick water fluid, only a thin polymer coating was visible in the form of weak light blue fluorescence. Based on a linear scale visible on each image it was found that the thickness of the polymer coating is approximately 50 microns - Figure 3B. After inaction of linear polymer- based fluid, the traces of polymer were visible even at a distance of 6mm from the core surface. In the case of cross-linked polymer, the front surface of a core was covered with organic polymer layer with intensive, blue fluorescence.

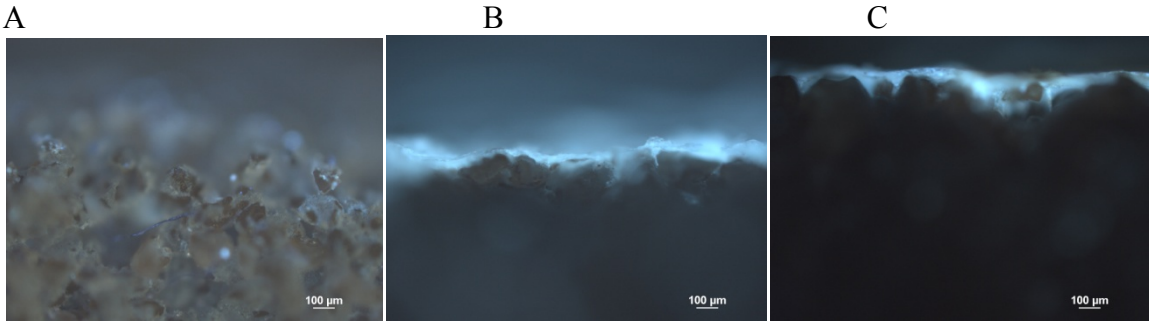

Figure 4. Core face surfaces: A-slick water, B-linear, C-cross-linked.

CONCLUSION

We defined the impact of the prepared fracking fluids on low permeability of rocks, based on experimental flow tests on natural cores. The presented fracturing fluids may damage a created fracture. The damage is caused by leak off into the rock matrix. As a result of filtrate escaping from a fracturing fluid into reservoir, the conductivity and permeability of a fracture, and the conductivity and permeability of the reservoir near the walls of the fracture can be decreased.

The tests show that this phenomenon is visible not only with cross-linked liquids, but also with linear polymer, and slick water. For this reason, when fracking low-permeability deposits, attention should be paid to fracking fluids prepared on the basis of surface-active agents, and to multi-phase fluids (the so-called energized fluids) [7].

ACKNOWLEDGEMENTS

The research leading to these results, performed within the ENFLUID Project, has received funding from the Polish-Norwegian Research Programme operated by the National Centre for Research and Development under the Norwegian Financial Mechanism 2009-2014 in the frame of Project Contract No Pol-Nor/196923/49/2013.

REFERENCES

1. Kasza P.: „Zabiegi stymulacji wydobycia w złożach niekonwencjonalnych”, Nafta-Gaz 2011, nr 10, pp. 697-701.
2. Czupski M., Kasza P., Wilk K.: „ Płyny do szczelinowania złóż niekonwencjonalnych”, Nafta-Gaz 2013, nr 1, pp. 42-50.
3. Economides M.J., Nolte K.G.: „Reservoir Stimulation” - Second edition, Houston 1989.
4. Kasza P., Wilk K.: „Technological fluids for hydraulic fracturing”, Przemysł Chemiczny 2014, nr 11, pp. 1000-1004.
5. Gandossi L.: “An overview of hydraulic fracturing and other formation stimulation technologies for shale gas production”, IPC Technical Reports 2013, pp. 7-30.
6. Chong K.K., Grieser W.V., Passman A., Tamayo C.H., Modeland N., Burke B.: “A completions Guide Book to Shale-Play Development: A Review of Successful Approaches Towards Shale-Play Stimulation in the Last Two Decades”, CSUG/SPE 133874, 2010, pp. 5-14.
7. Oilfield Services.: “Enhanced Unconventional Oil and Gas Production with Nitrogen Fracturing”. Air. Products and Chemicals 2013, pp. 1-9.

TORTUOSITY PREDICTION FROM OXYGEN DIFFUSION VIA T_2 (z, t) RELAXATION NMR

Igor Shikhov and Christoph H. Arns
University of New South Wales, Sydney, Australia

This paper was prepared for presentation at the International Symposium of the Society of Core Analysts held in Snowmass, Colorado, USA, 21-26 August 2016

ABSTRACT

Petrophysical interpretation of NMR responses may be affected by the presence of dissolved oxygen in the fluids saturating rocks. Oxygen shortens longitudinal and transverse relaxation times of liquids due to NMR paramagnetic relaxation enhancement (PRE). The presence of oxygen in solution and its effect on relaxation time of fluids is often considered unwanted requiring thorough purification and degassing of liquids for proper experimental conditions. However, the design of laboratory experiments to characterize saturated rock samples may require exposure of the bulk fluid or saturated solid sample to atmosphere while under field conditions air-saturated fluids may be introduced in the near well-bore formation. We utilize relaxation time contrast between air-saturated and oxygen-free fluids to evaluate transport properties of a porous system by observing the dynamics of oxygen concentration change and estimate the time required for equilibration. For the case of two phases, the diffusion of oxygen becomes dependent on local saturation, fluid distribution pattern and wettability since it may occur predominantly through connected continuous fluid patches. Using spatially-resolved T_2 (z, t) experiments we derived time-dependent oxygen concentration change C_{O2} (z, t) along a fully- and partially-saturated carbonate core plug exposed to air saturated oil at its inlet. This provided an effective mutual diffusion coefficient of oxygen and a tortuosity estimate. We compare with electrical tortuosity calculated on a micro-tomographic image of that core by solving the stationary Laplace equation for conductivity. We demonstrate that by solving a forward problem of finding an effective mutual-diffusion coefficient of oxygen it is possible to obtain a reasonable estimate of equilibration time and access tortuosity via NMR over longer length scales.

INTRODUCTION

Formation waters and hydrocarbons at reservoir conditions are free from oxygen. Well operations may result in introduction of oxygen into near-wellbore parts of the formation through air-saturated drilling fluids. Even more likely is that air may be introduced in the cores in the laboratory during the SCAL experiments. Oxygen dissolved in fluids affects NMR relaxation and may lead to improper petrophysical interpretation. It may diffuse inside the rock following a particular connected fluid phase or diffuse between fluid

phases through their interface. Understanding these processes enables to correct the reduction of observed NMR relaxation time. Furthermore, use of oxygen as a tracer and access to NMR relaxation resolved in time and space provides a potential for enhanced petrophysical characterization of rocks subjected to contact with oxygen-saturated fluid. Transport and evolution of oxygen concentration have been routinely studied in medicine, chemical and bioengineering, soil sciences etc. These studies typically consider diffusion of oxygen in a single phase saturating the porous medium (soil or rock) [1]. The ability of alkanes to store and conduct oxygen much faster in emulsions than in pure aqueous solutions was studied [2] who reported a so-called "shuttle mechanism". However, there is a gap in studies of oxygen as tracer in multi-phase transport through saturated porous systems in a petrophysical context. Paramagnetic species, including dissolved gaseous oxygen, are known to cause an enhanced relaxation to protons of a solvent, e.g. water or hydrocarbons. We describe the effect of paramagnetic enhancement (PRE) on observed relaxation time as a linear sum of oxygen-free bulk fluid relaxation rate and PRE related rate [3], [4]

$$\frac{1}{T_{1,2\,obs}} = \frac{1}{T_{1,2B\,pure}} + \frac{1}{T_{1,2\,O_2}}\,. \tag{1}$$

The latter term is a linear function of oxygen concentration [5], enabling direct estimation of oxygen concentration when end-point relaxation rates are known (fully oxygen saturated and oxygen free responses). We use a spatially resolved $T_2(z,t)$ experiment to measure the change of relaxation time along the core length and to estimate oxygen concentration evolution. The latter is used to derive oxygen effective diffusion coefficient using an analytical solution to 1D concentration-diffusion equation.

DIFFUSION OF A GAS TRACER IN A MULTI-PHASE SYSTEM

Oxygen present in liquids greatly increases relaxation rate of ^{1}H of a host fluid due to interaction of magnetic moments of its protons and O_2 outer unpaired electrons. Consider a rock partially saturated with oxygen-free water and oil having one boundary exposed to oil saturated with air and all other boundaries closed, (Fig.1). Air diffuses towards lower concentration along the core following two path-ways: (1) along the connected path of oil; (2) diffusion of gas across the interface is slow relative to diffusion within the continuous liquid face, yet still occurs at substantial rate. Air contained in oil will diffuse into the water and then spread along the water phase, which in water-wet rock is connected along the core length. This also offers a mechanism to connect isolated patches of oil. Diffusion of tracer dissolved gas with concentration gradient in liquid is described by Fick's second law which leads to the unsteady state diffusion equation

$$C_t = D_e\, C_{zz}\,, \tag{2}$$

where C is concentration in the solution, t is time and D the mutual diffusion coefficient of tracer in the fluid. Boundary conditions are constant inlet concentration $C(0,t) = C_0$ and

open at the outlet with side boundaries closed. For two fluids an additional boundary condition is set at the fluids interface proportional to the relative solubility gradient on both sides of the interface. We solved Eqn.2 using finite difference method on a regular mesh to calculate a change of oxygen concentration for a single fluid (Fig.1b, Fig.2a).

The solubility of oxygen in water in equilibrium with air is 8.5 mg/L at 25°C, while solubility in n-paraffins is almost an order of magnitude higher, 71 mg/L at 25°C for n-decane. Mutual diffusion coefficient of oxygen in n-alkanes is also much higher than that in water, although data **is** published only for n-hexane ($9.9 \cdot 10^{-5}$ cm^2/s) and n-hexadecane ($2.46 \cdot 10^{-5}$ cm^2/s). The expected value of oxygen diffusion in decane is in between, approximately $6 \cdot 10^{-5}$ cm^2/s. The analytical solution to Eqn.2 with relevant boundary and initial conditions is used to calibrate the numerical solution to physical dimensions

$$C(z,t) = C_0 \, (1 - \mathrm{erf}\{z/\sqrt{(4Dt)}\}) \text{ , or} \quad (3)$$

$$\ln C = a - z^2 / (4Dt) \text{ for a semi-infinite medium ([6]).} \quad (4)$$

T_2 (z, t) SIMULATION AND EXPERIMENTAL PROCEDURES

Mount Gambier limestone exhibits very high porosity, φ_{brine}=52% and permeability, k_{brine} = 4.47 D. The majority of the pore space is associated with large pores (82% effective porosity is resolved at 10.95 μm resolution). Fig.3a,b shows the effect of dissolved oxygen on NMR T_2 relaxation for fully decane saturated core. Matching modes of MICP and T_2 distributions in air-saturated and oxygen-free states requires application of a 60% lower effective relaxivity ρ_2 for O_2-free oil case (10.5 μm/s compared to 16.0 μm/s). The T_2(z,t) experiment utilizes CPMG at constant gradient 0.6 G/cm (frequency encoding) providing 3-mm spatial resolution. T_2(z) is averaged over a total acquisition time of two minutes. T_2(z) was obtained every 6, 8 or 18 minutes depending on samples.

The impact on mean relaxation time is very high when dealing with decane as a representation of light oil (Fig.3a). Interestingly, no difference between T_2 distributions obtained on fully water saturated Mount Gambier core was observed irrespectively whether or not water was deoxygenated, while bulk water $T_{2,B}$ shows an easily detectable difference (with T_{2B} of 3.2 and 2.5 sec respectively). This implies that such measurements are inherently sensitive to wettability conditions or certainly tells if rock is water-wet.

RESULTS AND DISCUSSION

The contrast offered by oxygen to relaxation times of bulk fluids and saturated Mount Gambier rock is given in Table 1. No difference in T_{2LM} was observed in case of a fully water saturated sample. Decane can carry eight times more oxygen than water and offers four times greater contrast between oxygen-free and air-saturated fluid (in our experiments oxygen is always a fraction of that gas in the air, i.e. 0.209). Expectedly, partially saturated rock, where the water phase consists of deuterium oxide (D_2O), shows

a larger difference between these states than fully decane saturated rock and less than bulk decane sample. This evidences partially oil wetting conditions.

Fig.4b,c demonstrates the time-evolution of oxygen concentration along the core (the first 6-7 3-mm thick slabs) calculated from T_2 (z, t) experiments. Initially the core was fully saturated with deoxygenated n-decane, followed by exposure of the inlet to bulk decane equilibrated with air. Fitting to analytical solution results in the following oxygen effective diffusion coefficients: (1) bulk decane $D_{e,O2} = 6.9 \cdot 10^{-5}$ cm^2/s; (2) Mt. Gambier at S_O=100% $D_{e,O2} = 6.1 \cdot 10^{-5}$ cm^2/s; (3) Mt. Gambier at S_O=51% (the rest is D_2O) $D_{e,O2} = 3.7 \cdot 10^{-5}$ cm^2/s. D_e-based tortuosity, τ_d is estimated as $\tau_d = \varphi D_e / D_o$. Another tortuosity value is obtained by solving Laplace equation for conductivity on a voxelized image, $\tau_c = \varphi c_e / c_o$ assuming perfectly water-wet conditions (see Fig. 5). Tortuosity estimate based on oxygen diffusion is expectedly higher than conductivity since some transport is possible between two phases. It reasonably well captures change of tortuosity due to saturation decrease. Factors requiring further consideration include an exposure of a core to atmosphere prior to NMR experiment; deoxygenating fluids by substitution of air with pure nitrogen, and wettability conditions which may result in better oil connectivity.

CONCLUSION

We demonstrated that the proposed approach can be applied for quantitative characterization of multi-fluid systems saturated rocks by exploiting relaxation contrast offered by oxygen solubility in aqueous and oil phases and their wettability. Interpretation of time- and spatially-resolved relaxation signal (typical in well-logging) may provide information about spatial fluid distribution. Furthermore, the approach can provide information which is difficult otherwise to obtain such as tortuosity, wettability, fluids interfacial area and potentially relative permeability. Alternatively, the approach may be used to correct NMR signal for oxygen related environmental effects.

ACKNOWLEDGEMENTS

CHA acknowledges the Australian Research Council (ARC) for a Future Fellowship and the National Computing Infrastructure for generous allocation of computing time.

REFERENCES

1. Aachib, M. *et al.*, 2004, *Water, Air and Soil Pollut.*, **156**, 163-193.
2. Bruining, W. J. *et al.*, 1986, *Chem. Eng. Sci.*, **41**, 1873-1877.
3. Chiarotti, G. *et al.*, 1955, *Il Nuovo Cimento*, **1**(5), 863–873.
4. Chen, S. *et al.*, 2004, *SPE ATCE, SPE90553, Houston, TX, USA*.
5. Parker, D. *et al.*, 1974, *Chem. Phys. Let.,* **25**(4), 505–506.
6. Crank, J., 1975, *The mathematics of diffusion.* Oxford: Clarendon Press.

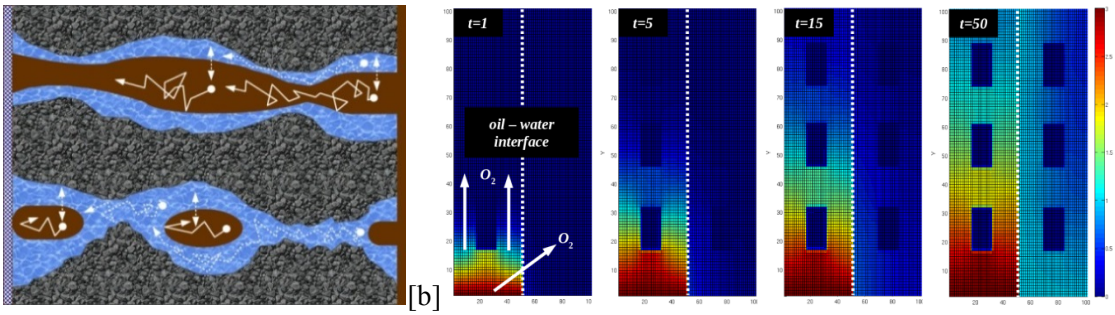

Fig.1: [a] Sketch of porous system saturated with wetting (water) and non-wetting (oil) fluids. Top: connected path of oil phase, bottom: isolated oil patches. O_2 transport is expected to be much slower in the latter case. [b] Finite difference approximation to 2D concentration-diffusion equation illustrating change of concentration with time in presence of interface and different solubility of phases. Air dissolved in the oil diffuses from the high concentration at the inlet towards the low concentration primarily along the connected oil pathway.

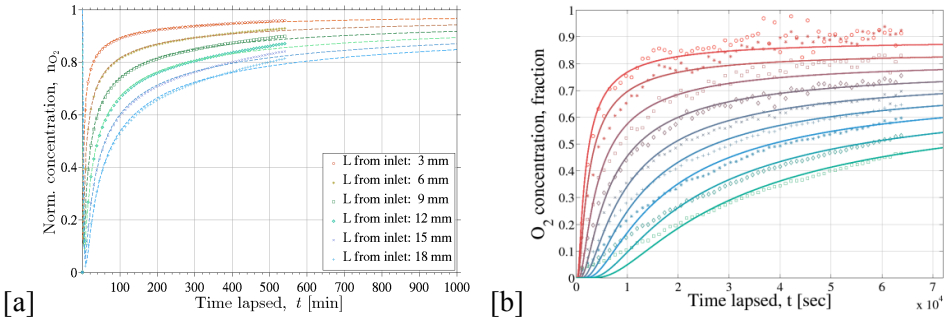

Fig.2: [a] Concentration of O_2 $C(z,t)$ calculated using a finite-difference method (FDM) for 1D time-dependent concentration-diffusion equation $C_t = D_e C_{zz}$ for six 3-mm slabs and [b] O_2 $C(z,t)$ measured for bulk decane (a soaked sponge) using a $T_2(z, t)$ experiment.

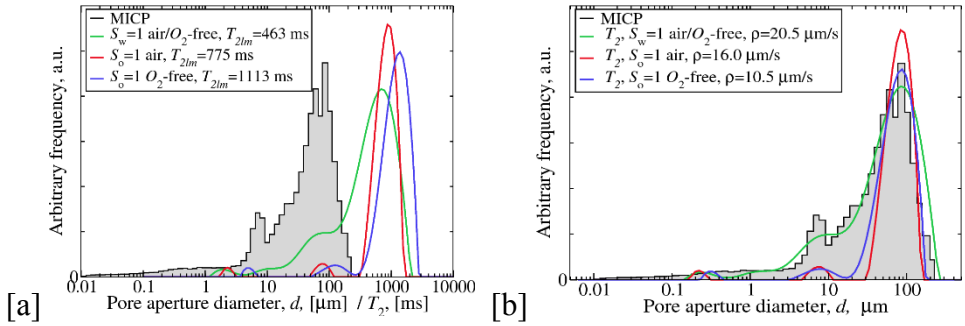

Fig.3: [a] Comparison of experimental T_2 distributions of a core fully saturated with water or oil in equilibrium with air / oxygen free state. Shift is apparent in case of oil. [b] Shift of T_2 responses to match mode MICP values at fully water and fully oil saturation states (air-saturated and O_2 free).

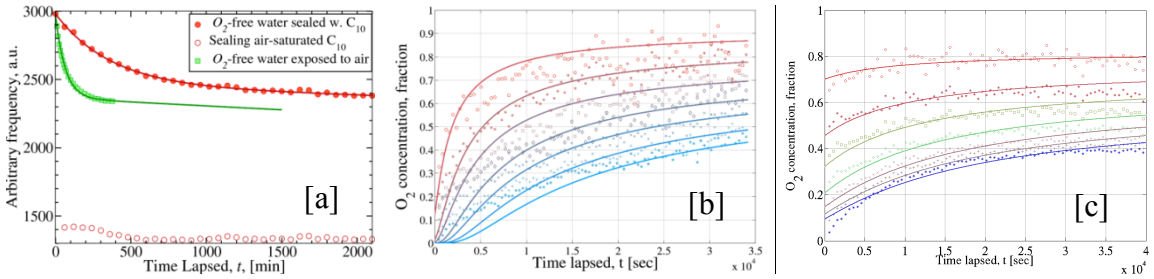

Fig.4: *Fluids only:* [a] Change of relaxation rate with time for deoxygenated bulk water sample exposed to air compared to air-saturated decane. The rate of oxygen concentration change is controlled by diffusion of air across the phases interface since the diffusion rate of oxygen in both cases is the same, $2 \cdot 10^{-5}$ cm^2/s. The change of average O_2 concentration is 6~8 times higher in an air-water system comparing to decane-water one. *Mt Gambier:* [b,c] Change of oxygen concentration $C(z, t)$ as normalized fraction of solubility with time at different distances from the core inlet evaluated from the $T_2(z, t)$ experiment for the case of [b] *S*o=100% and [c] *S*o=51%. Distances L (to the middle of 3 mm slabs) are: 3, 6, 9, 12, 15 mm, etc.

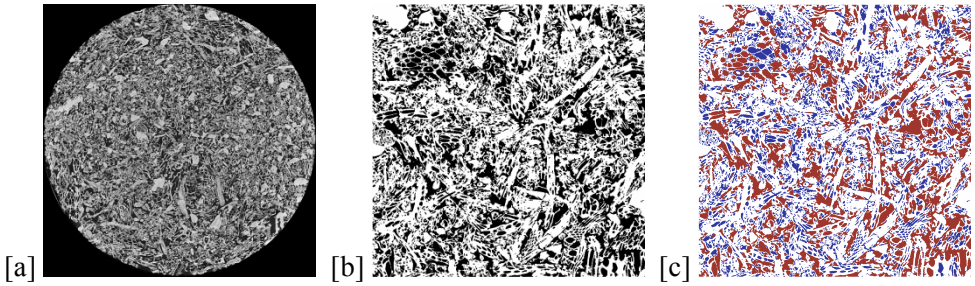

Fig.5: [a] Slice through the tomogram of Mt Gambier limestone at 10.95 µm voxel resolution (2160x2160 voxel). [b] Subsection of two-phase solid-void segmented image (1440x1440 voxel). [c] Slice through capillary drainage transformation (CDT) to set fluid distributions assuming fully water-wet rock; *S*o=48.9%.

Table 1. T_{2LM} relaxation times of bulk fluids and saturated rock.

sample	air	O_2-free	Ratio O_2-free/air
bulk water	2470	3220	1.30
MtG, Sw=100%	463	463	1.00
bulk n-decane	1250	2850	2.28
MtG, So=100%	775	1113	1.44
MtG, So=51%+D_2O	1077	1983	1.84

Table 2. Tortuosity estimated from µ-CT image and T_{2LM} experiment.

sample	MtG, So=1.0	MtG, So=0.5	ratio
$T_2(z, t)$ - $D_{e,O2}$: τ_d	0.451	0.248	1.82
Image, c : τ_c	0.186	0.054	3.44

Pore-Level Simulation of Heavy Oil and Bitumen Recovery Using the Steam Assisted Gravity Drainage (SAGD)

Arash Behrang, Sahand Etemad, Peyman Mohammadmoradi, Apostolos Kantzas

Chemical and Petroleum Engineering Department, University of Calgary

Abstract:

A CFD-based numerical solver is developed to simulate the pore-scale behaviour of SAGD process, including phase change phenomena (i.e., condensation and vaporization). During the simulation a complete set of mass conservation and Navier-Stokes momentum and energy equations under non-isothermal condition are solved simultaneously. In addition to take phase change phenomena into account, the flow pattern in porous media is well-demonstrated. Then, the solver is validated against visualization experimental studies of SAGD process available in the literature. The results include a demonstration of a series of pore-scale events particularly in the vicinity of the bitumen-steam interface. The results of this study are a part of the larger investigation the objective of which is to understand deeply physics of complex multiphase flow in heterogeneous structures.

Introduction:

Due to its high recovery, stable oil production rate and reduced environmental footprint, Steam Assisted Gravity Drainage (SAGD) recovery is one of the promising approaches developed to enhance oil recovery in heavy oil and bitumen resources (Butler, 1997; Butler *et al*., 1981). However, pore-scale physics and interactions between steam, condensed water and oil in the SAGD process are not yet fully-understood (Lee *et al*., 2015). Thus, pore-level studies of the fundamentals of complex transport phenomena (including flow pattern and heat transfer) in porous media can result in a significant improvement in understanding the field-scale macroscopic observations (Al-Bahlani and Babadagli, 2009).

The viscosity of heavy oil is very high, typically over million centipoise (Meyer and Attanasi, 2003). In order to produce heavy oil, it has to be mobilized in the reservoir. Because of extremely high viscosity, i.e. resistance to flow, fundamental recovery techniques are not applicable to improve the oil recovery factor (Hart, 2014). The key to mobilize heavy oil is to decrease its viscosity. There are two general ways to reduce heavy oil viscosity: first, heat heavy oil and second, dissolve solvent in heavy oil (Butler, 1997). The steam injection is a common way to enhance heavy oil recovery in unconventional oil resources. During steam injection, the heavy oil temperature increases sufficiently and consequently the viscosity of heavy oil drops rapidly. In contrast to non-thermal methods where viscosity reduction is very slow and depend on the diffusion and dispersion of the fluids. When steam is contact with cold heavy oil, another phase (condensate phase) is produced at the interface between the steam and heavy oil. The effect of the layer of condensate phase on the heavy oil recovery is not yet fully understood. Numerical simulation technique can be used to tackle this problem (Mohammadmoradi, 2016). Most of the previous works on the simulation of fluid flow in porous media deal with a single phase (either gas or liquid) or two phase flow. In this study a new solver is developed to study flow pattern in a porous media when the phase change occurs. The volume of fluid (VOF) approach is used to perform phase change in this study. Easy capturing of the interface during

the phase change and inherent mass conservation property are two main advantages of the VOF method (Gueyffier *et al*., 1999).

Governing equations:

To use the VOF method a volume fraction term α is defined. The volume fraction term lies between 0 and 1 and

$$\sum_{i=oil,water,steam} \alpha_i = 1$$

The continuity equation for each phase is given by (Kartuzova and Kassemi, 2011):

$$\frac{\partial(\alpha_i \rho_i)}{\partial t} + \nabla.(\alpha_i \rho_i \boldsymbol{v}) = S_i, i = oil, water, steam$$

Where ρ, **v** and t are density, velocity and time, respectively. Note that $\dot{m}$ stands for the mass transfer between phases. There are many equations to express mass transfer term. In this study, we use an empirical relation to quantify the interfacial heat and mass transfer (Lee *et al*., 2015).

$S_{\alpha_v} = -S_{\alpha_l} = r_l \alpha_l \rho_l \frac{T - T_{sat}}{T_{sat}} \quad T > T_{sat}$ evaporation process

$S_{\alpha_l} = -S_{\alpha_v} = r_v \alpha_v \rho_v \frac{T_{sat} - T}{T_{sat}} \quad T < T_{sat}$ condensation process

Where S_{α_v} is the interfacial mass transfer rate from liquid to vapor, S_{α_l} is the interfacial mass transfer rate from vapor to liquid. r denotes the mass transfer intensity factor with unit S^{-1}. The value of r is recommended to be such as to maintain the interfacial temperature reasonably close to the saturation temperature, and to avoid divergence issues. As an empirical coefficient, r is given different values for different problems. Researchers have used a very wide range of values, depending on flow regime, geometry, mesh size and time steps. (Alizadehdakhel et al., 2010; De Schepper et al., 2009; Wu et al., 2007) set $r_v = r_l$ =0.1 in their simulations for investigation of evaporation and condensation in a thermosiphon, simulating flow boiling in a hydrocarbon feedstock and flow boiling in serpentine tubes respectively.(Goodson et al., 2010; Yang et al., 2008)

For pore-scale simulation, we used $r = 100$ for both condensation and vaporization process in order to numerically maintain the consistency between saturation and temperature profiles i.e. keep the interfacial temperature around T_{sat}. It is founded that as r goes to very small values, interfacial temperature start deviating from saturation temperature and increasing r helps maintain interfacial temperature close to T_{sat}. Note that extremely large values of r cause numerical convergence problems(Yang *et al*., 2008).

The momentum equation is expressed as follow:

$$\frac{\partial(\rho \boldsymbol{v})}{\partial t} + \nabla.(\rho \boldsymbol{v}\boldsymbol{v}) = -\nabla P + \nabla.[\mu(\nabla \boldsymbol{v} + \nabla \boldsymbol{v}^T)] + \rho g + F$$

Where P is the pressure. The viscosity is denoted by μ. F and g are surface tension term and gravity respectively. Note that

$$\rho = \sum_{i=oil,water,steam} \rho_i \alpha_i$$

$$\mu = \sum_{i=oil,water,steam} \mu_i \alpha_i$$

To implement the effect of surface tension in our calculations, F is defined as follow:

$$F = \left[\sigma\kappa\boldsymbol{n} + \frac{d\sigma}{dT}\left(\sigma T - \boldsymbol{n}(\boldsymbol{n}.\nabla T)\right)\right]|\nabla\alpha|\frac{2\rho}{\rho_1 + \rho_2}$$

Where $\kappa = -\nabla.\mathbf{n}$ and σ are the curvature and surface tension terms, respectively. By T and **n**= $\nabla\alpha/|\nabla\alpha|$, the temperature and the surface normal vector are respectively defined. The energy equation is written as follow:

$$\frac{\partial(\rho C_p T)}{\partial t} + \nabla.\left(\rho\boldsymbol{v}C_p T\right) = \nabla.(k\nabla T) + Q$$

Where Q is the volumetric heat sources, k is the thermal conductivity term given by

$$\rho = \sum_{i=oil,water,steam} k_i \alpha_i$$

Using these equations, a new solver is developed in OpenFOAM solver in order to address the phase change problem.

Conclusion and Results:

Figure 1 shows a typical porous medium which is used in our study. The porous medium is fully saturated by heavy oil (T=300 K) while steam (T=400K) is injected. The saturation temperature is 373 K.

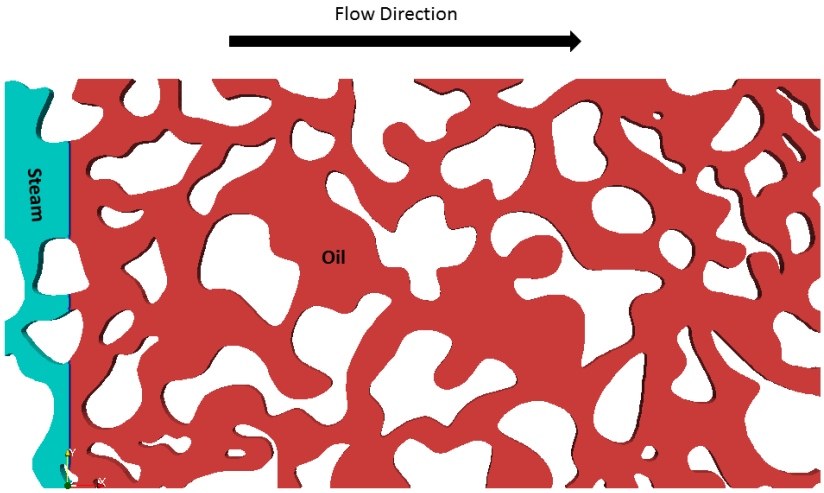

Figure 1. porous media saturated by oil and steam

The viscosity ratio and density ratio in our studies are 10000 and 1000, respectively. Material properties of water, steam and oil is provided in the table below:

Table 1. Properties of water, steam and oil

	$\rho\ [kg/m^3]$	$\mu\ [pa.s]$	$c_p\ [kj/(kg\ K)]$	$k\ [w/(m\ K)]$
Steam	1	0.0001	2100	0.02
Oil	1000	1	1900	0.3
Water	1000	0.01	4200	0.6

As illustrated in Figure 2, at the interface between oil and steam, the temperature of injected steam drops and the condensate phase is produced. Dark blue is used to present the condensate phase.

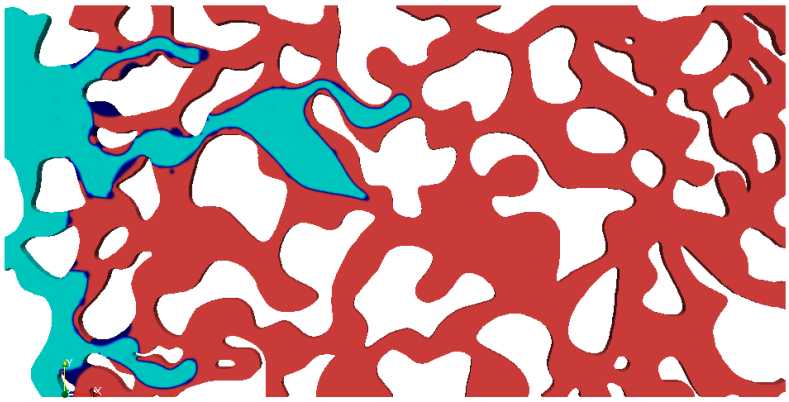

Figure 2. Displacement of oil by the injected steam. The dark blue represents the condensate phase

In the second case, a more complex medium is used to examine the oil production as a result of viscosity reduction (Figure 3). During the process starting from **a** to **f**, oil phase is heated and the production continues from the bottom face. The aqueous phase (blue color in Figure 3b) forms and disappears quickly due to condensation and evaporation phenomena.

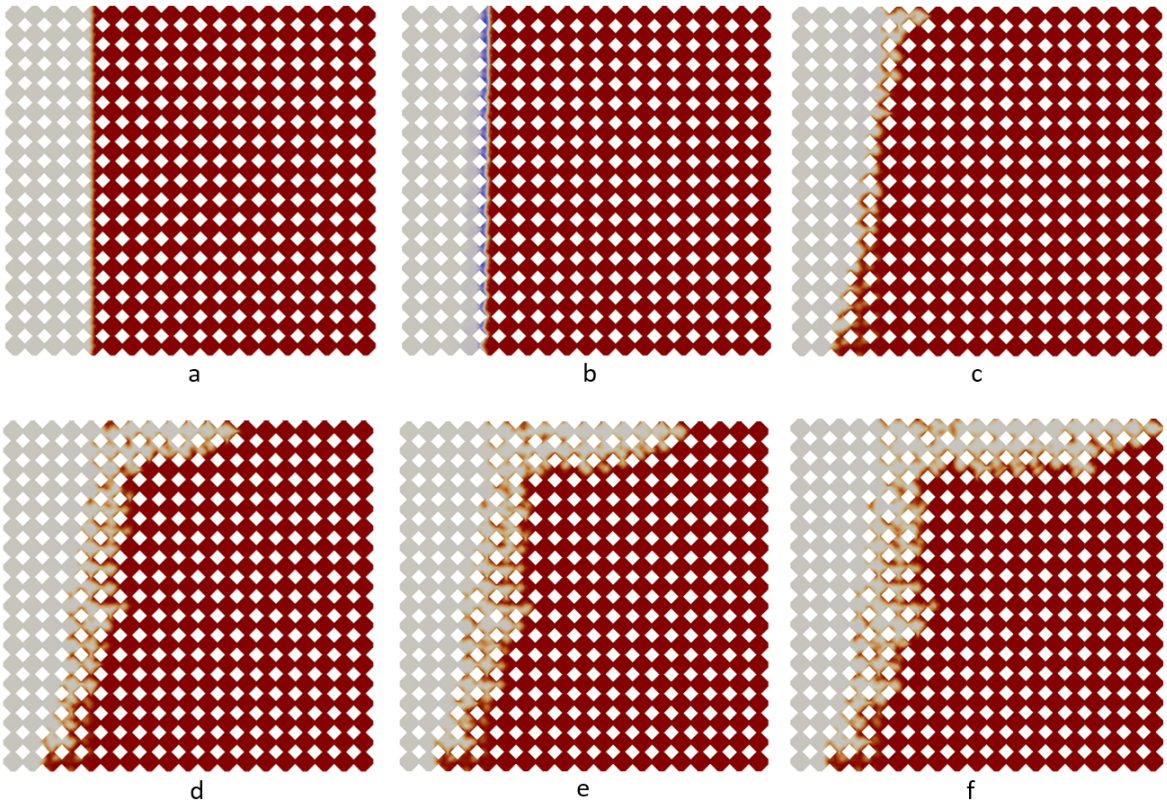

Figure 3 Simulated steam-oil interface development from (a) to (f)

The results are in a good agreement with a similar process which is conducted experimentally (Mohammadzadeh 2015) (Figure 4).

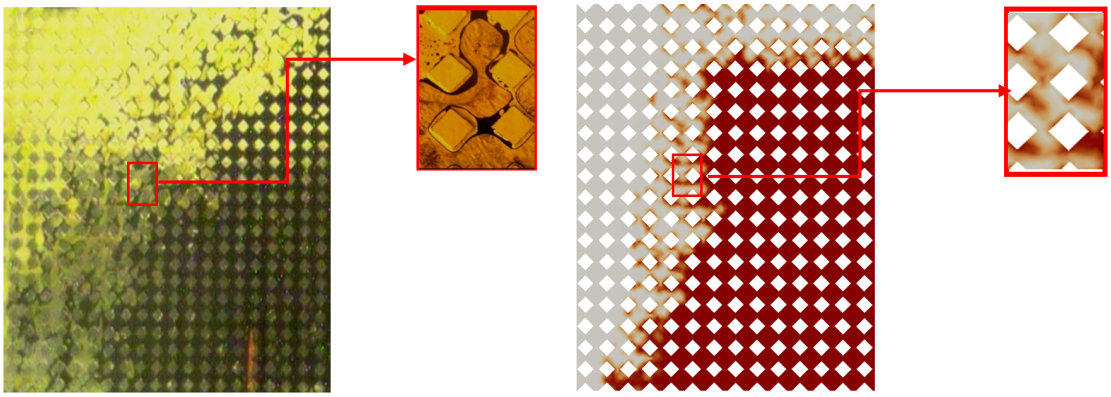

Figure 4 Residual oil pattern, (experimental (left), and simulation(right) results)

To sum up, a new solver has been developed to study phase change in porous media. This solver can help to understand complex physics which are dominated in thermal recovery approaches. Using this solver, the influence of material properties such as viscosity, density, thermal conductivity, heat capacity, interfacial tension and wettability on the phase change and consequently oil recovery can be addressed. This solver will be further modified to capture the heat transfer in grains.

REFERENCES

Al-Bahlani, A.-M., and T. Babadagli, 2009, SAGD laboratory experimental and numerical simulation studies: A review of current status and future issues: Journal of Petroleum Science and Engineering, v. 68, p. 135-150.

Alizadehdakhel, A., M. Rahimi, and A. A. Alsairafi, 2010, CFD modeling of flow and heat transfer in a thermosyphon: International Communications in Heat and Mass Transfer, v. 37, p. 312-318.

Butler, R., 1997, Thermal recovery of oil and bitumen, publ: GravDrain Inc.(2nd printing), Calgary, Alberta, 528pp.

Butler, R., G. McNab, and H. Lo, 1981, Theoretical studies on the gravity drainage of heavy oil during in-situ steam heating: The Canadian journal of chemical engineering, v. 59, p. 455-460.

De Schepper, S. C., G. J. Heynderickx, and G. B. Marin, 2009, Modeling the evaporation of a hydrocarbon feedstock in the convection section of a steam cracker: Computers & Chemical Engineering, v. 33, p. 122-132.

Goodson, K., A. Rogacs, M. David, and C. Fang, 2010, Volume of fluid simulation of boiling two-phase flow in a vapor-venting microchannel: Frontiers in Heat and Mass Transfer (FHMT), v. 1.

Gueyffier, D., J. Li, A. Nadim, R. Scardovelli, and S. Zaleski, 1999, Volume-of-fluid interface tracking with smoothed surface stress methods for three-dimensional flows: Journal of Computational physics, v. 152, p. 423-456.

Hart, A., 2014, A review of technologies for transporting heavy crude oil and bitumen via pipelines: Journal of Petroleum Exploration and Production Technology, v. 4, p. 327-336.

Kartuzova, O., and M. Kassemi, 2011, Modeling interfacial turbulent heat transfer during ventless pressurization of a large scale cryogenic storage tank in microgravity: Rep, v. 6037.

Lee, H., C. R. Kharangate, N. Mascarenhas, I. Park, and I. Mudawar, 2015, Experimental and computational investigation of vertical downflow condensation: International Journal of Heat and Mass Transfer, v. 85, p. 865-879.

Meyer, R. F., and E. D. Attanasi, 2003, Heavy oil and natural bitumen-strategic petroleum resources: World, v. 434, p. 650-7.

Mohammadmoradi, P., Behrang, A., & Kantzas, A. (2016, June 7). Effective Thermal and Electrical Conductivity of Two-Phase Saturated Porous Media. Society of Petroleum Engineers. doi:10.2118/180740-MS

Mohammadzadeh, O., Rezaei, N., Chatzis, I. , Pore-Scale Performance Evaluation and Mechanistic Studies of the Solvent-Aided SAGD (SA-SAGD) Process Using Visualization Experiments, Transport in Porous Media, June 2015, Volume 108, Issue 2, pp 437-480

Wu, H., X. Peng, P. Ye, and Y. E. Gong, 2007, Simulation of refrigerant flow boiling in serpentine tubes: International Journal of Heat and Mass Transfer, v. 50, p. 1186-1195.

Yang, Z., X. Peng, and P. Ye, 2008, Numerical and experimental investigation of two phase flow during boiling in a coiled tube: International Journal of Heat and Mass Transfer, v. 51, p. 1003-1016.

KLINKENBERG PERMEABILITY BY PRESSURE DECAY ON TIGHT ROCKS

Xiangmin Zhang and Albert Hebing
PanTerra Geoconsultants (x.zhang@panterra.nl),

This paper was prepared for presentation at the International Symposium of the Society of Core Analysts held in Snowmass, Colorado, USA, 21-26 August 2016.

ABSTRACT

Klinkenberg effect becomes more significant in tight rocks. Unsteady-state transient methods have been used in the industry to obtain Klinkenberg permeability. However, higher values are reported compared to conventional steady-state method. In this study we report measurements of Klinkenberg permeability on the same samples using three different methods 1) the steady-state method; 2) the pressure pulse decay method; and 3) the pressure decay (pressure draw-down) method. In addition to the conventional gas permeability method for steady-state measurements with mass flow meter, an accurate capillary tube soap bubble meter was used for samples with microdarcy permeability. The Klinkenberg permeability values are compared with inert oil permeability value. The pressure decay method allows permeability measurements at a wide range of mean pore pressures in a single run. Our results show that accurate Klinkenberg permeability can be obtained in a single run of pressure decay (drawdown) test using Brace's calculation, especially for tight rock samples in the permeability range of milidarcy to microdarcy.

INTRODUCTION

Gas permeability depends not only on the rock flow properties and types of probe gas, but also on the mean pore pressure at which it is measured. Gas permeability is higher than its intrinsic permeability due to the effect of "gas slippage" [1]. Hence the Klinkenberg permeability, which is independent of the type of probe gas and measuring pressures, as opposed to the gas permeability, is more commonly used in core analysis and it can be taken as inert liquid permeability.

Klinkenberg permeability can be obtained either by steady-state or unsteady-state method. Using the steady-state method, the permeability is normally obtained by measuring several gas permeability values at different mean pore pressures. The Klinkenberg permeability can then be calculated. Alternatively, unsteady-state pressure decay (draw-down) method can be used to obtain the Klinkenberg permeability by a single run [2,3]. However, as it has been reported [4,5,6], unsteady-state method gives higher Klinkenberg permeability values compared to steady-state ones. In our routine measurements, we also consistently measure much higher Klinkenberg permeability using industrial standard unsteady-state permeameter and data processing method [2], compared to those from steady-state method under similar conditions. With the increasing activities of exploration and P&D in tight gas in the permeability range of mili-micro darcy, fast and accurate methods are apparently more important than ever before.

The aim of this study is to investigate the unsteady-state method, by comparing it to the steady-state method for Klinkenberg permeability in terms of experimental setup, data processing methods, gas types under well-controlled conditions.

Our results show that the unsteady-state pressure decay method can give the same Klinkenberg permeability as the steady-state method for samples ranging from millidarcies to microdarcies, when Brace's method [7,8] is used for the calculation.

SAMPLES, METHODS AND EXPERIMENTAL

Four samples with permeabilities ranging from millidarcies to microdarcies were selected for the study. Nitrogen and Helium gases were used in unsteady-state measurements. In the steady-state measurements, only Nitrogen gas was used. The Klinkenberg permeability values obtained in the steady-state and unsteady-state measurements were compared. Oil permeability was compared as a reference to the Klinkenberg permeability on the same sample. All experiments were performed at the same effective confining pressure of 500 psi.

Klinkenberg permeability by steady-state method (SS)

For the two samples with a relative higher permeability, the steady-state gas permeability was measured using a permeameter equipped with a mass flow meter with Nitrogen as the probe gas. The volumetric gas flow rate was converted to ambient conditions of temperature (20℃) and 1 atm pressure. Gas permeability was calculated using Darcy's law. For each sample several gas permeability values were obtained at various mean pore pressures. The mean gas pressures were selected from a wide pressure range to allow for an accurate regression [9]. The gas permeability values were plotted against inverse mean gas pore pressures. The fitting line was extrapolated to zero (infinite pore pressure) to obtain Klinkenberg permeability. The slope can be used to calculate the gas slippage factor *b*.

$$K_g = k_L(1 + b/P_m) \quad (1)$$

For sample S4 with low permeability, the steady-state permeability was measured using an accurate micropipette as a gas bubble flowmeter.

Klinkenberg permeability by pressure pulse decay (PPD)

Detailed information about the pulse decay apparatus developed by PanTerra and University of Utrecht was published previously [8]. The transient pressure pulse decay setup consists of an upstream and downstream reservoir. A small pressure pulse is applied in the upstream reservoir and the differential pressure allows gas flow from the upstream reservoir, through the sample and to the downstream reservoir. The pressure changes across the sample and in the two reservoirs are recorded as a function of time.

The apparent gas permeability was then calculated based on the method originally proposed by Brace et al. [7] although many other calculation methods were proposed [10,11,12]. When a pressure pulse ΔP_0 is applied, the differential pressure $\Delta P(t)$ decays exponentially as a function of time, *t*:

$$\Delta P(t) = 2\,\Delta P_0\, V_2/(V_1 + V_2)\, e^{-mt} \quad (2)$$

Where, V_1 and V_2 are the upstream and downstream reservoir volumes and t is testing time. m is a decay time constant. Plotting the decay curve in terms of $ln[\Delta P(t)/\Delta P_0]$ vs. time t yields a straight line having a slope m. The permeability k can be determined by:

$$k = m\,\mu\beta(L/A) \times [V_1\, V_2/(V_1 + V_2)] \quad (3)$$

where
L - length of the sample,
A - cross-sectional area of the sample,
μ- Nitrogen viscosity at room temperature and mean pore pressure,
β -Nitrogen compressibility.

Four gas permeability measurements using Nitrogen (N2) were performed for sample S3 at various mean pore pressures. The Klinkenberg permeability was then calculated the same way as four-point Klinkenberg permeability by steady-state method. For sample S4, two gas permeabilities were measured at high mean pore pressures.

Klinkenberg permeability by pressure decay (draw-down) method (PD)
The pressure decay (PD) or the draw-down method can be considered as a special case of pressure pulse decay as described above with an infinitely V2 volume and a fixed down-stream pressure of 1atm.

Two permeameters were used for the pressure decay gas permeability measurements. The first one is the PanTerra in-house pressure pulse decay permeameter with down-stream reservoir open to atmosphere. Nitrogen gas was used for this apparatus. A series Nitrogen gas permeability values were calculated using the Brace method as described above at each mean pore pressure step.

The second permeameter was from an industry provider. This is a combined Helium permeameter and Helium porosimeter. The automated permeameter provides Klinkenberg permeability and gas slippage factor b for Helium. The calculation is based on the method proposed by Jones [2][3]. The Helium gas permeability values were reconstructed based on the Klinkenberg permeability, the Helium slippage factor b and the pressure decay data.

We also re-calculated the Helium gas permeability values based on the pressure decay data using the Brace method and using the equipment parameter such as V1 volume and Helium gas properties. Klinkenberg permeabilities for samples of S1, S2 and S3 were re-calculated based on the re-calculated Helium gas permeability.

Oil permeability
For the two samples of S1 and S2, the oil permeability (Kerosene lab oil) was measured after the gas permeability. For each sample four flow rates were applied in the measurements. The two samples were cleaned after oil permeability measurement and Klinkenberg permeability re-measured by the steady-state method. The same value of Klinkenberg permeability was obtained as the original one before oil permeability measurement. The oil permeability values are shown in Figure 1 and Figure 2 as inverse

of mean gas pore pressure of zero to compare with their gas permeability and Klinkenberg permeability. Please note that these mean pore pressures are only for comparison with gas and Klinkenberg permeability and not the true mean pore pressures in oil permeability tests.

DISCUSSION

For sample S1 (cf. Figure 1), the Klinkenberg permeability derived from the Brace method matches the Klinkenberg permeability from steady state measurement by using Nitrogen. The Klinkenberg permeability is close to the oil permeability. The Klinkenberg permeability by Jones method gives a value 50% higher.

For sample S2 (cf. Figure 2), four Klinkenberg permeability were obtained. Among them, three are close to the oil permeability given the experimental error. However, the Klinkenberg permeability calculated based on the Jones' method is two times higher.

For sample S3 (cf. Figure 3), the pressure pulse decay method and pressure decay (draw-down method) tested using the same apparatus and same probe gas of Nitrogen give the same results of Klinkenberg permeability considering the experimental error. The Klinkenberg permeability by a different apparatus, and different probe gas of Helium also give the same value when data is reprocessed using the Brace method. The Klinkenberg permeability by the Jones' calculation [2] gives a value two times higher compared to the rests.

For sample S4 (cf. Figure 4), the gas permeability measured by the steady-state method gives the same results as measured by single pressure decay run when compared at the same mean pore pressures. The pressure decay (draw-down) method gives comparable results with pressure pulse decay method when extrapolated to the same mean pore pressure. All measurements for sample S4 give the same single Klinkenberg permeability.

It is evident that the Klinkenberg permeability based on the pressure decay data and Jones method give a value too high. However, the same data when processed with Braces' method [8] give much close values to those obtained from steady- state method. It seems that Jones method masked the effect of "*b*" on the individual sample. By applying brace method while using the pressure decay setup, a more accurate Klinkenberg permeability can be obtained, furthermore a characterized '*b*" value can be obtained which has the potential to be used for pore characterization in tight rocks. The number and type of samples tested in this study are limited. More works are planned to continue the studies in terms of enlarging the database and refining the algorithm of Brace method et al.[7].

CONCLUSIONS

Unsteady-state pressure decay (drawdown) is a quick method to obtain accurate Klinkenberg permeability for tight rock in the permeability range of millidarcy to microdarcy. Experimental results show that the unsteady-state method gives the same Klinkenberg permeability results as steady-state method. More work needs to be done on different samples in a wider permeability range.

ACKNOWLEDGEMENTS

The authors would like to thank PanTerra Geoconsultants for permission to publish this paper. Mr. Souhail Youssef is thanked for reviewing the manuscript. Technical support from Mr. Clement Thery is acknowledged.

REFERENCES

1. Klinkenberg, L.J. , 1941, The permeability of porous media to liquids and gases, paper presented at the API 11th Mid-Year Meeting, Tulsa, OK (May 1941); in API Drilling and Production Practice (1941) 200-213.
2. Jones, S. C., 1972, A rapid accurate unsteady-state Klinkenberg permeameter, Soc. Pet. Eng. J., 12(5), 383–397.
3. Jones, S.C., 1997, A technique for faster pulse-decay permeability measurements in tight rocks, Journal of SPE Formation Evaluation, Vol 12, 19-26, DOI 10.2118/28450-PA.
4. Rushing, J., K. Newsham, P. Lasswell, J. Cox, T. Blasingame, 2004, Klinkenberg corrected permeability measurements in tight gas sands: Steady-state versus unsteady-state techniques, SPE Annual Technical Conference and Exhibition, Houston, Texas, U.S.A., 26-29 September 2004. SPE 89867.
5. Carles P, P. Egermann, R. Lenormand, JM. Lombard, 2007, Low permeability measurements using steady-state and transient methods, International Symposium of the Society of Core Analysts SCA2007-07.
6. Jannot Y., D. Lasseux, G Viz and G. Hamon, 2007, A detailed analysis of permeability and Klinkenberg coefficient estimation from unsteady-state pulse decay of draw-down experiments, International Symposium of the Society of Core Analysts SCA2007-08.
7. Brace, W. F., Walsh, J. B. and Frangos, W. T., 1968, Permeability of granite under high pressure, Journal of Geophysical Research, 73, 2225-2236, DOI: 10.1029/JB073i006p02225.
8. Zhang X., C. Spiers, C. Peach & A, Hebing, 2013, Tight rock permeability measurement by pressure pulse decay and modeling, International Symposium of the Society of Core Analysts, SCA2013-10.
9. McPhee, C. A and Arthur, K. G, 1991, Klinkenberg permeability measurements: Problems and practical solutions, Gordon and Breach Science Publishers.
10. Haskett, S. E., Narahara, G. M., and Holditch, S. A., 1988, A method for simultaneous determination of permeability and porosity in low permeability cores, SPE Formation Evaluation, 651-658.
11. Kaczmarek, M., 2008, Approximate solutions for non-stationary gas permeability tests, Transport in Porous Media, 75, 151-165.
12. Ruth, D. W., and J. Kenny, 1989, The unsteady-state gas permeameter, J. Can. Pet. Technol., 28, 67–72.

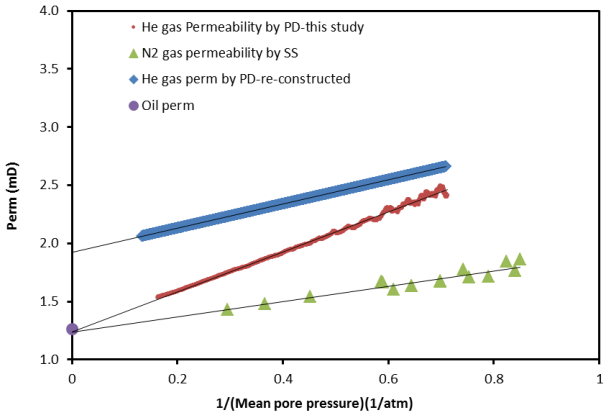

Figure 1. Sample S1: Klinkenberg permeability measured by 1) unsteady-state pressure decay (draw-down) using Helium; 2)Klinkenberg permeability measured by steady-state method using N2 gas (green triangle); 3)permeability of lab oil (purple dot).

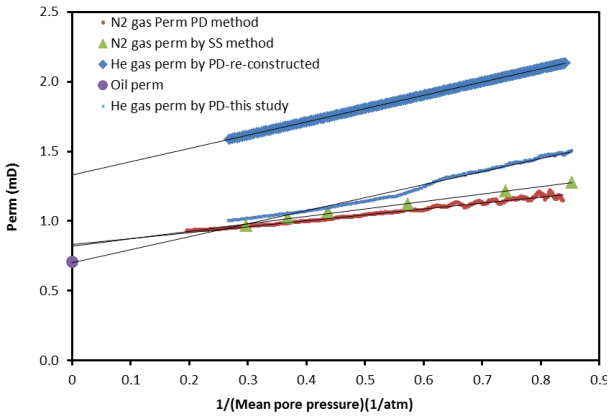

Figure 2. Sample S2: Klinkenberg permeability measured by 1) unsteady-state pressure decay (drawdown) using Nitrogen; 2)Klinkenberg permeability measured by steady-state method using N2 gas)(green triangle; 3)permeability of lab oil (dot). 4)unsteady-state pressure decay for Helium calculated by Jones method; 5) unsteady-state pressure decay (draw-down) using Helium calculated by Brace's method.

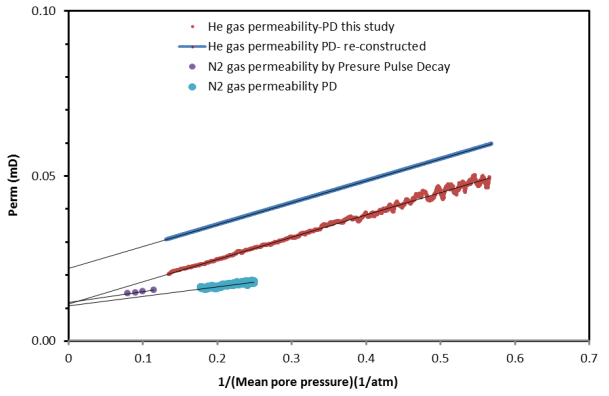

Figure 3. Sample S3: Klinkenberg permeability by 1) unsteady-state pressure decay (draw-down) using Helium; 2) unsteady-state pressure decay (draw-down) using (N2) Nitrogen; 3)Klinkenberg permeability by four pressure pulse decay measurements using N2 gas; 4)unsteady- state pressure decay for Helium calculated by Jones method.

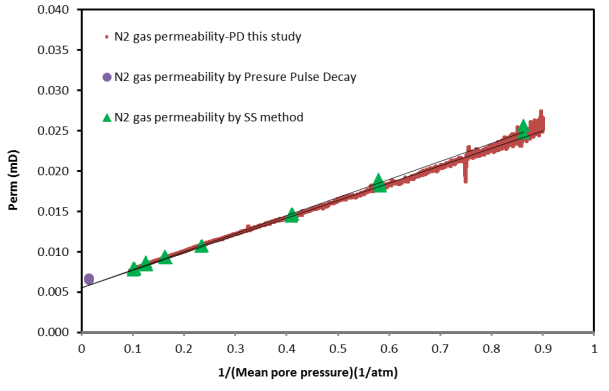

Figure 4. Sample S4: Gas permeability by 1) unsteady-state pressure decay (draw-down) using (N2) Nitrogen; 2) pressure pulse decay measurements using N2 gas; 3) gas permeability measured by steady-state method.

Fracture-Matrix Interaction during Polymer Flood

Abdullah F. Alajmi and Meshal K. Algharaib
Petroleum Engineering Department, Kuwait University, Kuwait

This paper was prepared for presentation at the International Symposium of the Society of Core Analysts held in Snowmass, Colorado, USA, 21-26 August 2016

ABSTRACT

Optimizing oil production from current resources is becoming the main strategy for many oil producing companies around the world. The applications of Enhanced Oil Recovery (EOR) techniques are encouraged by the current growing demand in producing from unconventional resources. Among EOR processes, polymer flooding which is an attractive option for many reservoirs. The objective of polymer flooding techniques is to control water mobility inside the reservoir to favor higher oil recovery. In this study, the polymer flood efficiency was evaluated in fractured system. The fluid flow interactions between the fractures and the matrix have a significant impact on displacement processes. This work focuses on multi-phase flow in the presence of a fracture tip. The impact of the fracture tip on polymer flow was studied. The fluid saturations and oil recovery information were evaluated to study the interaction of fracture-matrix environment with multi-phase flow. Polymer slug size, polymer concentration, and location of fracture tip were studies. They showed different impacts on polymer flooding performance. Fluid saturations around fracture tip were quantified with time. The diversion and convergence of polymer from and into the fracture were analyzed. Understanding the effect of these parameters on the stability and performance of polymer flood will help in designing the optimum scenario to maximize the oil recovery.

INTRODUCTION

Natural and artificially-induced fractures in a reservoir have a great impact on fluid flow patterns and on the ability to recover hydrocarbons. Fractures can have a negative effect on recovery process when they form bypass paths, especially in production-injection systems. For example, injected fluid may preferentially flow through the fractures leaving behind inaccessible and non-contacted hydrocarbons. It is important to understand the local and global effect of fractures on reservoir performance. In this paper, we are studying the effect of the presence of a fracture tip in a single fracture.

Hydrocarbon recovery depends on the interaction between fluids in the fractures and in the matrix. Polymer flooding is a chemical enhanced oil recovery (EOR) process which is used in many reservoirs to improve their productivity. In order to ensure favorable flood, polymers are used to reduce mobility ratio between water and oil and hence increase oil cut. The polymer increases the viscosity of the injected water and improves the mobility ratio, allowing for an increase in the vertical and areal sweep efficiency of the injected water and consequently, increases the oil recovery. Generally, there are two commonly used polymers in EOR applications which are the synthetic

material, polyacrylamide in its partially hydrolyzed form (HPAM) and the biopolymer, xanthan [2]. Currently, HPAM is the favorably used polymer in the industry owing to its improved characteristics.

Polymer flooding has been used for more than 20 years with an ultimate recovery expectation of 50% and 10–15% incremental oil recovery over water flood. There are several examples for field implementations of polymer flood mentioned in the literatures. Morel et al. [3] presented a planning case study for a polymer flooding in a deep offshore oil reservoir in Angola. They illustrated the feasibility of polymer flooding in such environment given the challenging space allocation for offshore injection facilities. Furthermore, Alvarado and Thyne [4] constructed a fuzzy logic and data clustering algorithm to screen chemical enhanced oil recovery techniques in Wyoming based on results reported from field cases. They concluded that chemical flooding ranks high for some of the reservoir under investigation.

Liu et al. [5] conducted a simulation study for an oil reservoir in Daqing field in China indicating that polymer flood might reach an oil recovery factor of 61% OOIP. In another work, Fulin et al. [6] presented a case study for two pilot projects in Daqing oil field which indicates that an incremental oil recovery, over water flood, of 20-23% can be achieved for the first pilot and around 20% for the second pilot. Before implementing these pilots, the results from core flood experiments showed that an incremental recovery over water flooding of more than 20% OOIP can be achieved by early time injection of high molecular weight, high concentration polymer. Tielong et al. [7] investigated the feasibility of polymer flooding in a pilot test conducted in Shuanghe reservoir located in the southeast Henan oil field in China which is known as an elevated-temperature reservoir. At the end of the pilot, a total of 10% incremental oil recovery was achieved. They concluded that polymer with extra-high molecular weight can successfully control the mobility ratio and modify the permeability profile.

The objective of this work is to investigate the polymer flood performance in a single fractured system.

MOTIVATION

Alajmi et al. [8] studied experimentally and numerically the effect of fracture tip in a single fracture during a water flood to light oil. Figure 1 presents 24 X-ray CT images along a 2-feet Berea sandstone sample. It shows the injected fluid saturations for several stages during the flooding processes. These images present the net value of the injected fluid in the core. Each stage of injection was subtracted from the initial condition. Since the fracture had high permeability, it captured the early time, as shown by the first row of images at 0.051 pore volume injected (PVI). The fluid then was transported through the fracture to the downstream tip of the fracture. At the downstream tip, the injected fluid started to diverge out from the fracture to the matrix. When the water diverged, it formed a sharp front, which moved along the core until breakthrough.

The movement of the fluid front away from the fracture was not as fast as the movement in the fracture due to the high permeability of the fracture. These differences in velocity forced a by-passed middle regions around the fracture. At later time, as injection continued, most of the by-passed region was displaced.

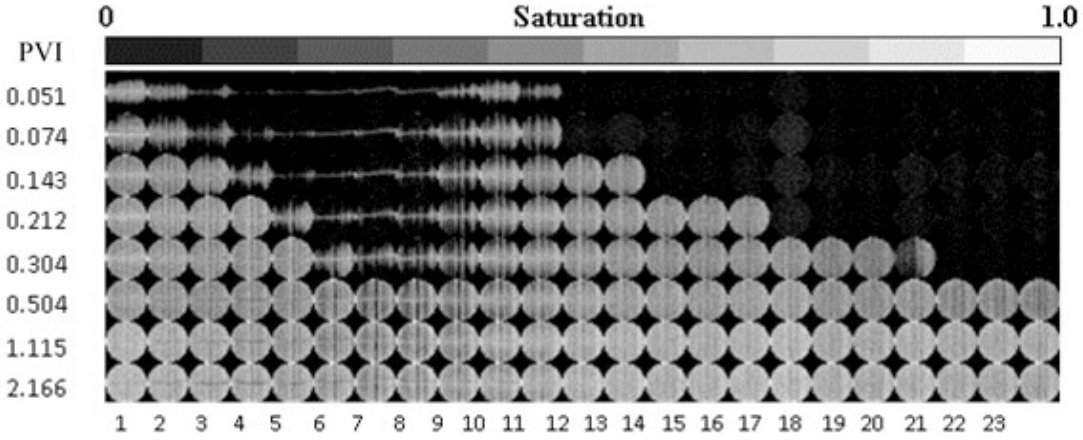

Figure 1: Injected Fluid Flow distribution.

The experimental work presented in Figure 1 was numerically simulated to understand the fracture tip effect on fluid flow. Figure 2 shows a simulated reconstruction of the net injected fluid at 0.304 pore volume injected (PVI). The injected fluid diverged from the fracture to the adjacent matrix due to the presence of the fracture tip. It shows the flow vectors direction of the fluid as the fracture is filled, the flow was then diverged to the adjacent matrix.

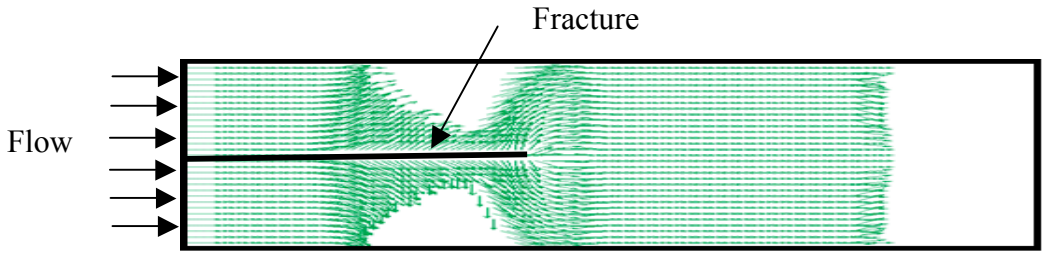

Figure 2: Flow vectors of the injected fluid.

The objectives of this paper are to investigate the efficiency of polymer flood in single fractured porous media and quantify the fracture-matrix interaction.

POLYMER FLOOD MODELLING

A numerical simulation was developed to achieve the objectives of this study. Two cases were studied, one without fracture tip (case A) and one with a fracture tip (case B).

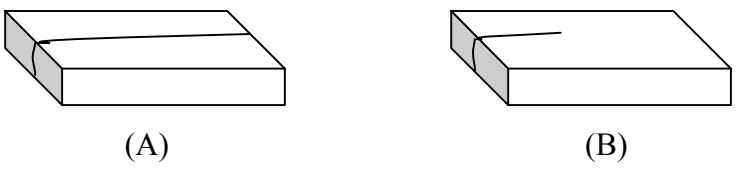

Figure 3: Schematic of the two cases.

The polymer concentration of 3000 ppm (equivalent to 10cp) was used to displace an oil with 60 cp viscosity. Water flood (1cp) was tested as a comparison to the polymer flood.

RESULTS AND DISSCUSION

Case A

In this case, the system is fully fractured with a single fracture. Two floods were preformed, water and polymer floods. Figure 4 shows the oil saturations after injecting 0.6 pore volume. The presence of the full fracture lowered the efficiencies of both floods leaving large undisplaced oil behind, which is expected. The fracture permeability is dependent of the formation stress. So average values of fracture and matrix permeabilities were selected. The fracture permeability was 10 Darcy and matrix permeability was 0.5 Darcy having a 20:1 contrast ratio.

The injected fluid moved inside the fracture much faster than in the matrix causing early breakthrough. Even though the polymer flood showed better performance and improved the mobility ratio, but still it left large oil volume behind.

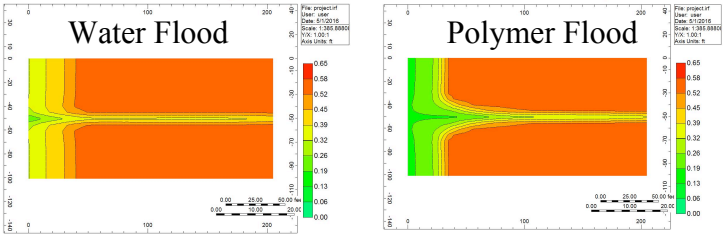

Figure 4: Oil Saturation maps for full fracture.

Case B

This case represents a system with a single fracture with a fracture tip as explained in the polymer flood modeling section.

Water Flood

Figure 5 shows the oil saturation maps during water flood. The presence of the fracture tip changed the saturation distribution compared to case A. More oil was displaced, but still the mobility ratio was not in a favorable condition. In the fracture region, the water advanced further in the matrix as the fracture was fully filled. Downstream of the fracture, since the viscosity ratio was high, the water movement was centered in the middle having difficulty to displace the oil on the sides.

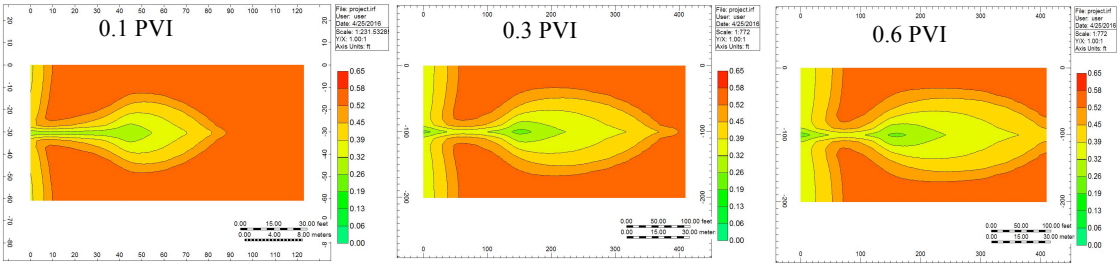

Figure 5: Oil Saturation maps during water flood.

Polymer Flood

Figure 6 shows the oil saturation maps during polymer flood. The injection of polymer improved the mobility ratio and resulted in better sweep efficiency. The same phenomena was seen as the fracture was first to be filled with the injected fluid. In the fracture region, the polymer advanced further in the matrix as the fracture was fully filled due to the improved injected fluid viscosity. Downstream of the fracture, the polymer movement was expanded across the system having a better displacing efficiency.

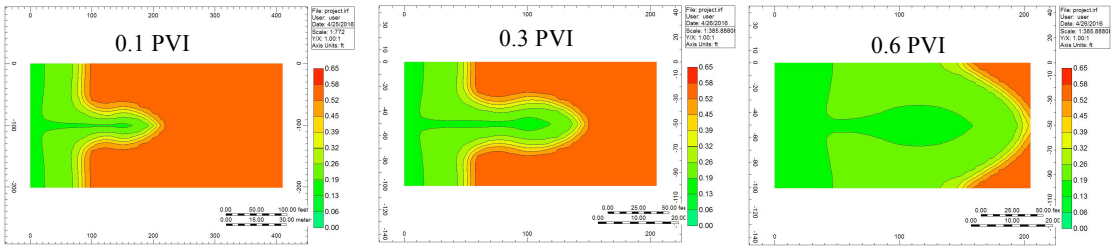

Figure 6: Oil Saturation maps during Polymer flood.

CONCLUSIONS

This study was aimed at investigating the fracture-matrix interaction assuming a permeability contrast ratio of 20:1. The performance of water and polymer floods in systems with single fracture (with and without fracture tip) were quantified. Numerical reservoir simulation was done to achieve the objectives of the study. Simulation runs were performed to determine the functional relationships between the displacement performance and fracture structure during both water flooding and polymer flooding. Results showed that the fracture structure had significant effects on the displacement performance. The displacement behavior of water flood and polymer floods can be either fracture-matrix-dominated or fracture-dominated by the presence of the fracture tip.

Results also indicated that the presence of the fracture tip allowed the polymer flood to retain it superiority and produce more oil downstream of the fracture.

ACKNOWLEDGMENT

This study was supported by Kuwait University Research Administration, Grant no. EP02/10. The authors are grateful for this support.

REFERENCES

1) Da Silva, I. P., De Melo, M. A. and Luvizotto, J., M.; "Polymer Flooding: A Sustainable Enhanced Oil Recovery in the Current Scenario", Paper SPE 107727 presented at the 2007 SPE Latin American Caribbean Petroleum Engineering Conference, Buenos Aires, Argentina, 15-18 April, 2007.

2) Sorbie, K. S. Polymer - Improved Oil Recovery. CRC Press Inc. 1991.

3) Morel, D., Vert, M., Jouenne, S., and Nahas, E.; "Polymer Injection in Deep Offshore Field: The Dalia Angola Case", Paper SPE 116672 presented at the 2008 SPE Annual Conference and Exhibition, Denver, Colorado, USA, 21 – 24 September 2008.

4) Alvarado, V., and Thyne, G.: "Screening Strategy for Chemical Enhanced Oil Recovery in Wyoming Basins" Paper SPE115940 presented at the 2008 SPE Annual Conference and Exhibition, Denver, Colorado, USA, 21 – 24 September 2008.

5) Liu, B., Sun, X., Wang, K., Xu, H., Liu, Q., Liu, X. and Song, S.: "Flooding by High Concentration Polymer Doubled Oil Recovery of Common Polymer on Field Test with 20% Closed to the Result of Lab Test in Daqing", Paper SPE 108684 presented at the 2007 International Oil Conference and Exhibition, Veracruz, Mexico, 27-30 June 2007.

6) Fulin, Y., Demin, W., Gang, W., Xinguang, S., Weijie, L., and Chunling K.: "Study on High-Concentration Polymer Flooding To Further Enhance Oil Recovery", Paper SPE 101202 presented at the 2006 SPE annual Technical Conference and Exhibition, San Antonio, Texas, 24-27 September, 2006.

7) Tielong, C., Zhengyu, S., Fan, Y., Changzhong, H., Ling, Q. and Jinxing, T.: "A Pilot Test of Polymer Flooding in an Elevated-Temperature Reservoir", Journal of SPE Reservoir Evaluation and Engineering, February 1998, pp 24-29.

8) Alajmi, A. F., and Grader, A. S., Influence of Fracture Tip on Fluid Flow Displacement. Journal of Porous Media. 12 (2009) 435-447.

FRACTAL DIMENSION: AN INDICATOR TO CHARACTERIZE THE MICROSTRUCTURE OF SHALE AND TIGHT GAS SANDS CONSIDERING DISTINCT TECHNIQUES AND PHENOMENA

Mayka Schmitt[a, b], Matthias Halisch[b], Celso P. Fernandes[a], Viviane S. S. dos Santos[c], Andreas Weller[d].

[a] Porous Media and Thermophysical Properties Laboratory (LMPT), Mechanical Engineering Department, Federal University of Santa Catarina, 88040900 Florianópolis, SC, Brazil.

[b] Leibniz-Institute for Applied Geophysics (LIAG), Dept. 5 - Petrophysics & Borehole Geophysics, 30655 Hannover, Germany.

[c] Leopoldo Américo Miguez de Mello Research and Development Center (CENPES-Petrobras), 21941598 Rio de Janeiro, RJ, Brazil

[d] Clausthal University of Technology, Institute of Geophysics, 38678 Clausthal, Zellerfeld, Germany.

This paper was prepared for presentation at the International Symposium of the Society of Core Analysts held in Snowmass, Colorado, USA, 21-26 August 2016

ABSTRACT

In this work we focused on the enhanced pore space characterization of shale and tight gas sandstones from Brazilian unconventional reservoirs, using fractal dimension determined by distinct laboratory techniques. The usage of several techniques is essential to properly cover the whole porous scale in shale and tight gas sandstone (TGS) consisting of ultra-fine (nanopore) structures, often associated with clay content and wide pore (fractures) resulting in broad pore sizes distribution. Fractal theory is an effective method that has been applied in geophysics to quantify the complexity of the rocks pore structure. As the rock pore geometry is conventionally divided into the surface geometry and the collective geometry of all the pore space, for the global description of the pore geometry a multifractal approach is presumably required. Routine core analyses, Mercury Intrusion Capillary Pressure (MICP), Nitrogen Gas Adsorption (N_2GA), X-Ray Nano- and Micro-Tomography were applied on two samples, one of each shale and TGS. From the tests statistical quantification of pore geometries and pore size distributions were acquired allowing to determine fractal dimension using, i.a., "fractal FHH" (Frenkel, Halsey, Hill), "Pittman's hyperbola" and 3D box-counting methods. The results show that fractal dimension of shale and TGS reflects their complex pore systems mainly consisting of three defined regions (D_1: macropores, D_2: mesopores and D_3: micropores). Naturally the distinct trends showed by the investigated techniques are expected as each method detects particular pore ranges and textures. In a practical manner both pore structure and surface irregularities play a role in the increases of capacity and rate flow of oil and gas reservoirs.

INTRODUCTION

Fractal analysis has proven to be useful to describe the geometric and structural properties of pores and rough surfaces. According many authors [1] there are two conventional definitions in describing the fractality of porous material: the pore fractal dimension representing the pore distribution irregularity and the surface fractal dimension characterizing the pore surface irregularity. At molecular size and microscopic range, surfaces of most materials including those of natural rocks show irregularities and defects that appear to be self-similar upon variation of resolution. A self-similar object is

characterized by similar structures at different scales. The regularity of self-similar structures can be quantified by the parameter of fractal dimension [2]. The topological dimension of a smooth surface is equal to two, while a rough surface is described by a fractal surface dimension $Ds > 2$. The fractal dimension of a volume distribution can be analyzed in a similar way. A uniform pore-size distribution corresponds to the topological dimension of three, but a variation in the pore-size distribution results in a fractal volume dimension $D_v < 3$. Many studies have shown methods that investigate the relation between capillary pressure and fluid saturation of wetting phase can be used to determine the fractal volume dimension of porous rocks [2]. The capillary pressure P_c in a cylindrical pore with radius r is related to the surface tension σ and contact angle θ between the injected and replaced fluid by:

$$P_c = (2\sigma \cos\theta) / r. \quad (1)$$

Considering the inverse proportionality $P_c \propto 1/r$ and $P_{c\ min} = 2\sigma \cos\theta / r_{max}$ being the capillary pressure related to the largest pore radius (r_{max}), the cumulative volume fraction V_c in the rock pore structure can be related to the ratio of capillary pressures $P_c/P_{c\ min}$:

$$V_c = (V (< r)) / V = (P_c / P_{cmin})^{(D-3)}. \quad (2)$$

Taking the logarithm to both sides of equation 2 results in:

$$log\ V_c = (D - 3)\ log\ P_c - (D - 3)\ log\ P_{cmin}, \quad (3)$$

which describes a linear relation between log V_c and log P_c. In the case of fractal behavior of the pore volume distribution, the slope (S) of the resulting line in double logarithmic presentation and fractal dimension is $D = 3 - S$.

For analysis of the relative pressures (P/P_o) N_2 adsorption and desorption data, the FHH (Frenkel, Halsey, Hill) equation has been widely used for calculating the fractal dimension and its simple form can be presented as follows [3]:

$$ln(V/V_o) = K\ ln(ln(P_o/P)) + C, \quad (4)$$

where P is the equilibrium pressure, P_o is N_2 saturation pressure, V is the volume of N_2 adsorbed at each equilibrium pressure and V_o is the volume of N_2 in the monolayer (cm^3/g). K is the power-law exponent, dimensionless and C is the constant of gas adsorption. In the linear relationship between $\ln(V)$ and $\ln(\ln(P_o/P))$ the slope of the plot of $\ln(V)$ versus $\ln(\ln(P_o/P))$ should be equal to K, which can be used to calculate fractal dimension D as $D=3+3K$ in the regime of capillary condensation.

The 3D X-ray Nano- and μ-CT images were reconstructed using a FDK (Feldkamp-Davis-Kress) algorithm [4], data visualization and quantification were performed with Avizo Fire 8.1.0 software [5]. Fractal Dimension (D) representing a reasonable quality index for the reconstructed image is a ratio providing a statistical index of complexity comparing how detail in a fractal pattern changes with the scale at which it is measured. In Avizo software the very popular Box-Counting method [6] is coupled and was used for D measurements.

RESULTS AND DISCUSSION

In this work we used non-wetting (Mercury Intrusion/Extrusion Capillary Pressure) and wetting (Nitrogen Gas Adsorption/Desorption) fluids phase's experiments and 3D image analysis to investigate fractal dimension of rocks from unconventional reservoirs of two basis settings in Brazil. Only the results for one sample of each oil and gas fields are shown and discussed: TGS-59 and Shale-17. Figure 1 depicts the results related to the fluid phases experiments; Figures 2 and 3 show the results obtained from the 3D X-ray Nano and μ-CT image acquisitions; Table 1 gives a summary of the all calculated fractal dimensions.

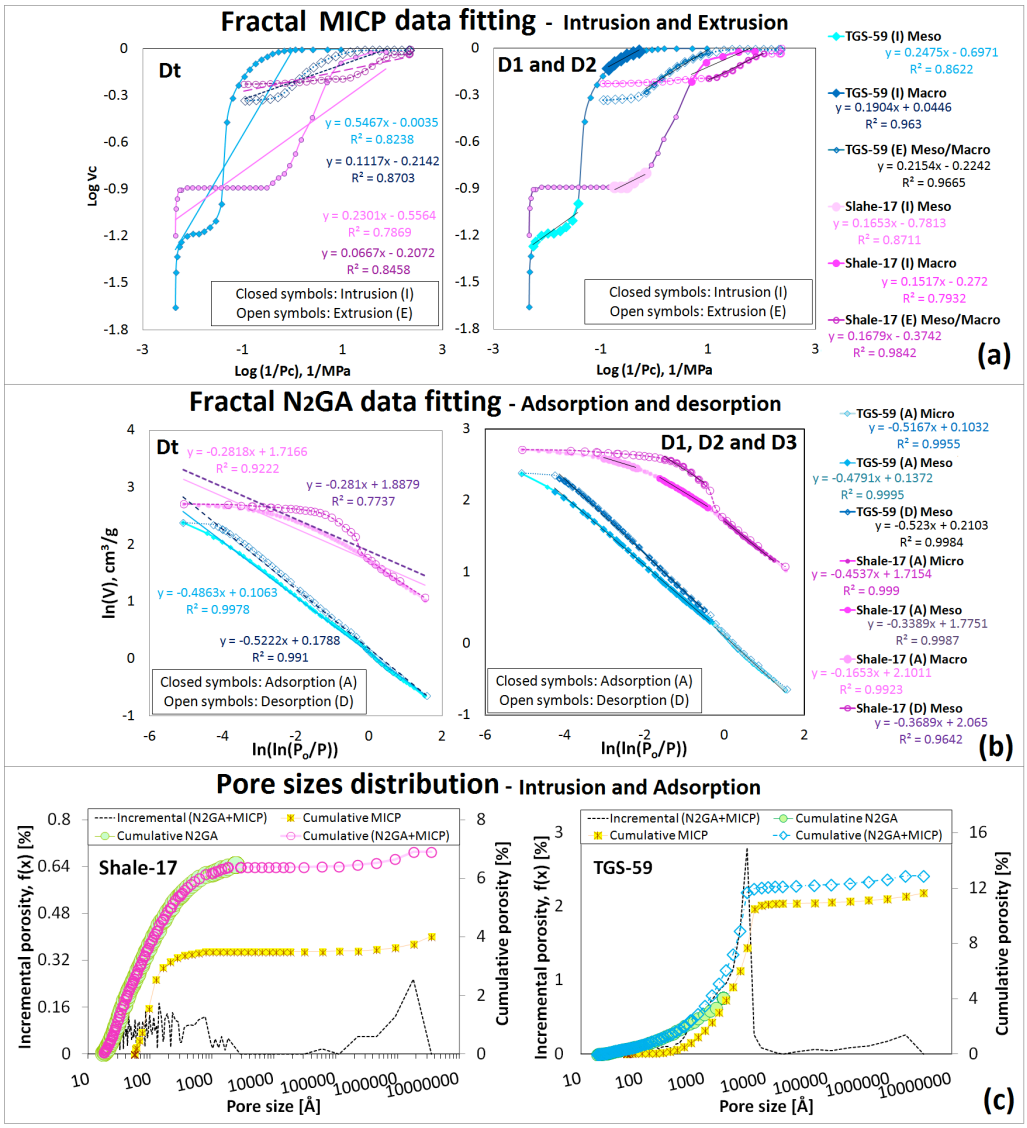

Figure 1. Slopes of the linear equations fitted to the MICP (a) and N_2GA (b) data to calculate: total fractal (Dt), fractal of the macropores (D_1), mesopore (D_2) and micropores (D_3). (c) Range of pore sizes accessed by the two techniques (intrusion and adsorption only).

Table 1. Summary of the fractal dimension values calculated from the distinct pore ranges detected using fluid phases experiment and 3D image analysis.

Samples			Fractal dimension	Shale-17				TGS-59			
Fluid saturation	Pore size range			Dt	Macro (D_1)	Meso (D_2)	Micro (D_3)	Dt	Macro (D_1)	Meso (D_2)	Micro (D_3)
	MICP	Intrusion		2.77	2.85	2.83		2.45	2.81	2.75	
		Extrusion		2.93	2.83			2.89	2.78		
	N_2AD	Adsorption		2.73	2.83	2.66	2.55	2.51		2.52	2.48
		Desorption		2.72		2.63	2.55	2.48		2.48	2.48
X-ray 3D image	Identified pore networks			Org. Matter		Main pores	Ganglia			Main pores	Ganglia
	µ-CT	VR: 0.75 µm		2.58		2.22	1.95	VR: 1.19 µm		2.43	1.87
	nano-CT	VR: 0.064 µm		2.65		2.33	1.71	VR: 0.064 µm		2.05	1.37

VR: Voxel resolution

From the Hg intrusion/extrusion and N_2 adsorption/desorption curves, samples had fractal dimension calculated according to Equation (3) – MICP and Equation (4) – N_2GA data. As shown in Figure 1 (a) and (b), for the overall pore sizes range covered by fittings in the two

techniques a total fractal value (*Dt*) is predicted; for specific pore range trends fitted separatedD_1, D_2 and D_3 fractal values are calculated. D_1 is, however, more related to the bigger pores and D_3 to the smaller ones; Thus, the relation $D_3<D_2< D_1$ is expected with the former referring more to the surface fractal dimension and the two latter describing volume fractal dimension. Figure 1 (c) depicts the pore size ranges covered by N_2GA and MICP individually and in combination [7], elucidating the presence of multimodal distributions and the distinct fractal trends found for both samples. Since the amount of micro- and mesopores (< 500 Å) are much higher for Shale-17, a defined D_1 value in the N_2GA data is also showed. The micro and mesopores of Shale-17 are in fact organic hosted pores, associated to the organic matter (OM) observed in this sample, see the darker gray regions on the 2D X-ray CT images (Figure 3). According Loucks et al., 2012 [8], shale pores are classified into: interparticle, intraparticle and organic matter pores. Because OM can be expressed as a percentage share of the mature organic matter (Total Organic Carbon, Wt % TOC) it indicates the potential of a petroleum source rock. OM is also directly related to the organic hosted pores; accordingly, fractal analyses of OM on the 3D images of Shale-17 were performed as well.

Figures 2 and 3 bring the X-ray Nano- and µ-CT results, with the 2D gray-level images and 3D renderings of segmented structures shown on the top graph and, the pore/OM volumes and calculated fractal dimension on the upper part. After performing 3D pore structure segmentation rocks showed very small disconnected pores ganglia plus main pore (MP) networks. As described by Schmitt et al., 2016 [9], the occurrence of pore ganglia obeys the relationship between a detected pore volume (V_p) and its voxel resolution (R_v); the smaller a voxel volume (N_v), the higher its undefined image's grey level and more difficult to identify a clear morphology/geometry. Therefore, a voxel pore volume is characterized as ganglia when the lower cutoff limit is $N_v=V_p/(R_v)^3 \leq 2000$. This explains the very low fractal dimension (approaching surface values) found for ganglia, as they are the smoothest and smaller pore structures identified on the analyzed images. Whereas the structures, total pores (MP+ganglias), MP and OM, showed much higher values. Additionally, fractal values increased for Shale-17 within the higher resolution since many of the smaller pores of this sample were then identified. On the other hand, for TGS-59 the 0.064 µm resolution seemed to be more related to the surface fractal dimension and very smooth and around 2 for the main pores identified. All the segmented structures of Shale-17 and TGS-59 showed a trend between the 2D fractal dimension (symbols) and porosity (dot lines) curves, indicating a directly relation. However, the increase in porosity from the 3D analysis does not imply in the rise of fractal dimension value and no correlation was observed for the analyzed samples. Any digitized image with different intensity values on its pixels is conceived as an imperfect cube in which the 3D fractal dimension should be lie in between 2 and 3; Real surfaces and images cannot be true mathematical fractal as they do not exhibit fractal behavior over several scales [10]. As we observed for our samples, fractal dimension will vary depending on the range of pore scales comprised in the acquired image. E.g., 0.064 µm resolutions include a sample with axes=32 µm; for Shale-17 this size was still enough to achieve fractal characteristics as the values found in the X-ray CT analysis increased from 2.22 (0.73 µm) to 2.33, being closer to the value observed in the micro region (D_1) of the N_2GA analysis. Nonetheless, TGS-59 showed a value decreasing from 2.43 (1.19 µm) to 2.05, beyond to the value 2.48 found for D_1. Thus, when determining fractal dimension from 3D images there will have a limited range of pore scales on each of the acquired data set, being the upper limit of this range set by the overall size of the image and lower limit is set by the voxel size.

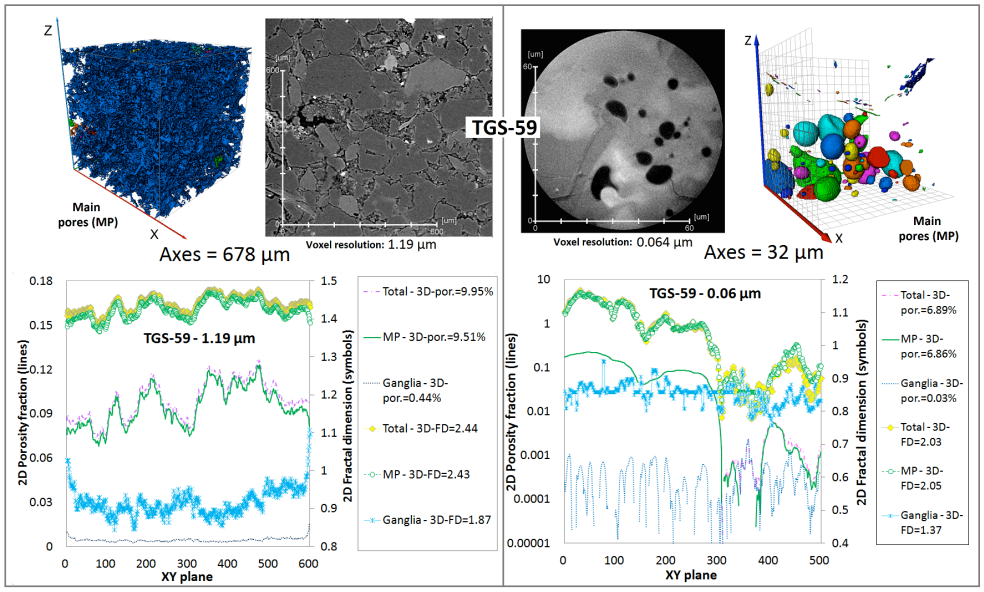

Figure 2. X-ray CT results of TGS-59: 2D gray-level images and 3D segmented pore structures (top part); 2D and 3D results for the fractal dimension and pore volume results (upper graphics).

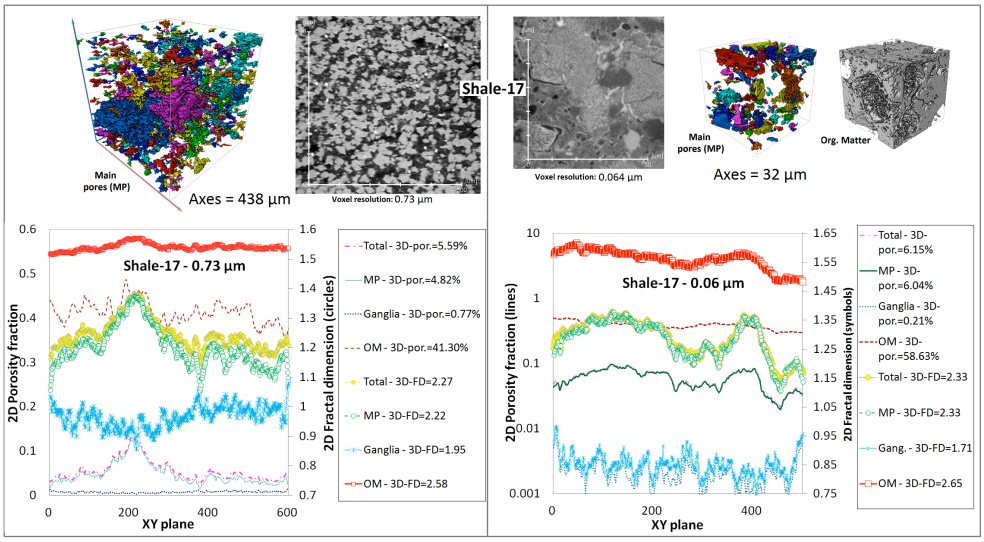

Figure 3. X-ray CT results of Shale-17: 2D gray-level images and 3D segmented pore/OM structures (top part); 2D and 3D results for the fractal dimension and pore/OM volume results (upper graphics).

CONCLUSION AND OUTLOOK

Fractal dimension of pore space in unconventional reservoirs from Brazil was investigated using fluid flow tests and X-ray CT image analyses. Fractals fitted on the drainage and imbibition overall pore size curves showed diverging values higher for MICP than for N_2GA: on Shale-17 values varied between 2.77-2.93 and 2.73-2.72; on TGS-59 from 2.45-2.89 and 2.51-48. This happens because after the imbibition process in MICP a large quantity of the mercury lost continuity and remains in the pore system after reaching atmospheric pressure, resulting in higher fractal dimensions related to the bigger amity pores. From the specific trends reveled on the data curves, macro *(D_1)* and meso *(D_2)* pore fractals were calculated from the non-wetting phase experiments and, a micro *(D_3)* pore fractal was accessed by N_2GA; In both samples $D_3<D_2<D_1$ agreeing that D_3 refers to the surface fractal and the two later are more related to the pore volume fractal dimension.

2D and 3D X-Ray Nano- and μ-CT analyses reveals that segmented pore structures seem to carry fractal behaviour; however values are lower compared with those from MICP and N_2GA curves. Because only a limited range of pores is encompassed by each X-ray CT data set, considerable information from the pore volume structures might be lost, including pore heterogeneities which result in higher fractal values.

Each method was able to reach fractal information from distinct pore ranges and textures. X-ray CT results imply that 3D image fractals are more related to the pore surface geometry as values approached D_3 from N_2GA. Also, D_2 values calculated from MICP and N_2GA (for TGS-59 equal 2.75 and 2.52, for Shale-17 equal 2.83 and 2.66) point out the resolution query, the former reports fractal dimension associated to the heterogeneous bigger pore volumes, while the later is more related to the pore surface geometry.

For the ongoing research, other samples of shale and TGS will have the fractal dimension investigated by MICP, N_2GA and X-Ray Nano- and μ-CT. Thereby, correlations within calculated fractal dimensions and laboratory measurements such as porosity, specific surface area and transient permeability, will be draw to study the role played by pore irregularities in the capacity and increase of flow rate of unconventional reservoirs.

ACKNOWLEDGEMENTS

We would like to thank CNPq, the founding agency of the Ministry of Science, Technology and Innovation of Brazil for granting the research stipend no. 207204/2014-4.

REFERENCES

[1] Pfeifer, P., Avnir, D., Chemistry in noninteger dimensions between two and three. *Journal of Chemical Physics*, 1983, **79**(7), 3369-3558.

[2] Zhang, Z., Weller, A. Fractal dimension of pore-space geometry of an Eocene sandstone formation. *Geophysics*, 2014, **79**, 6, 377-387.

[3] Liang, L., Xiong, J., Liu, X. An investigation of the fractal characteristics of the Upper Ordovician Wufeng Formation shale using nitrogen adsorption analysis. *Journal of Natural Gas Science and Engineering*, 2015, **27**(2), 402-409.

[4] Feldkamp, L.A., Davis, L.C., Kress, J.W. Practical cone beam algorithm. *Journal of the Optical Society of America A*, 1984, 1(6), 612-619.

[5] Avizo Fire 8.1.0: 1995–2014©, FEI, SAS – Visualization Sciences Group, Hillsboro, USA, www.fei.com (last access: 20 June 2016), 2014.

[6] Liebovitch, L.S., Toth, T. A fast algorithm to determine fractal dimensions by box counting. *Physics Letters A* , 1989, **141**, 386-390.

[7] Schmitt, M., Fernandes, C.P., Da Cunha Neto, J.A.B., Wolf, F.G., Dos Santo, V.S.S. Characterization of pore systems in seal rocks using Nitrogen Gas Adsorption combined with Mercury Injection Capillary Pressure techniques. *Marine and Petroleum Geology*, 2013, **39(1)**, 138-149.

[8] Louck, R.G., Reed, R.M., Ruppel, S.C., Hammes, U. Spectrum of pore types and networks in mudrocks and a descriptive classification for matrix-related mudrock pores. *AAPG Bulletin*, 2012, 96, 1071-1098.

[9] Schmitt, M., Halisch, M., Müller, C., Fernandes, C.P. Classification and quantification of pore shapes in sandstone reservoir rocks with 3-D X-ray micro-computed tomography. *Solid Earth*, 2016, **7**, 285-300.

[10] Sarkar, S., Pandey, D., Rathore, K., Munshi, P. Estimation of Moisture Content in Edible Pulses by the Application of Computerized Tomography. *NDE2015, Hyderabad*, November 26-28, 2015, 6 pages.

Water-Soluble Silicate Gelants for Disproportionate Permeability Reduction: Importance of Formation Wetting and Treatment Conditions

Reza Askarinezhad, University of Stavanger (UiS) / DrillWell; **Dimitrios G. Hatzignatiou**, UiS and International Research Institute of Stavanger (IRIS) / DrillWell

This paper was prepared for presentation at the International Symposium of the Society of Core Analysts held in Snowmass, Colorado, USA, 21-26 August 2016

ABSTRACT

Two commercial water-soluble sodium-silicate-based gelant systems, Systems A and B, were tested for their potential as Disproportionate Permeability Reduction (DPR) agents on Berea outcrop cores. The DPR experiments were conducted using a steady-state, two-phase (oil/gelant) placement method to (a) ensure the presence of moveable oil and (b) quantitatively control the placement saturation conditions at which the silicate gel sets. The treatment performance was evaluated using pre- and post-treatment two-phase (brine/oil), steady- and unsteady-state permeability measurements.

Bulk and core experiments showed that shrinkage of System B was significant in short-term tests conducted at various temperatures. System A, on the other hand, formed long-lasting, stable, rigid gels at corresponding temperatures.

Tests conducted on water-wet long-core samples at relatively low formation watercut (WC) of 22% revealed no positive DPR effect. System A was also tested in oil-wet Berea cores which were treated chemically to alter their wettability. DPR treatments at the same WC as the pre-treatment conditions (22%) resulted in an effective DPR behavior. However, DPR treatments at 22% WC in cores with pre-treatment 78% WC were more effective resulting in a lower oil-phase residual resistance factor (RRF_o) compared to the one from cases for which DPR treatments were conducted at the same pre-treatment WC.

INTRODUCTION

DPR is one method that the oil industry has used to control unwanted water production without reducing oil reserves from the treated region. Application of the DPR technology can be wide in scope with polymers or polymeric gels used traditionally as the treatment fluids. The use of an oil-soluble silicate-based system TMOS (Tetramethyl-orthosilicate) as DPR fluid has been presented previously [1, 2]. Recently, Askarinezhad *et al.* [3] provided a detailed review of the various applications of water-soluble silicate-based gelants. These fluids are environmentally friendly and require no special permissions for their use in the field. This feature serves as one of the main advantages of water-soluble silicate systems over oil-soluble ones. Iler [4] provided details on the various steps required for gel formation from monomers to large particles, and finally to a gel.

The application of water-soluble, silicate-based rigid-gels is the main focus of this work. Askarinezhad *et al.* [3] tested the potential DPR effect of a commercially-available, water-soluble, silicate-based system (System A in this work) at different wettability

conditions and presented a novel approach for DPR fluids placement, namely co-injection of oil and DPR fluid. In this work a new, water-soluble sodium silicate system (System B) is also tested its DPR effectiveness at similar treatment conditions. The most suitable silicate system, System A, was then tested as a DPR agent in oil-wet Berea cores to evaluate the effect of wettability on the DPR treatment. Experimental results showed a clear DPR effect following the formation treatment. System A was also placed at a lower watercut (22%) when the pre-treated core was producing at a 78% watercut. Treatment performance was evaluated by comparing ratios of pre- and post-treatment effective phase permeability measurements, defined as residual resistance factors (RRF). Note that DPR aims at reducing produced water without hindering, significantly, oil production; DPR treatments resulting in high RRF_w and low RRF_o values are considered as favorable.

ROCK/FLUIDS PROPERTIES – CHARACTERIZATION

Two commercially available, environmentally friendly, sodium silicate systems one with high (System A) and the other with low (System B) SiO_2:Na_2O molar ratio are used as the DPR fluids; Table 1 lists the two silicate systems' properties and activators used.

Table 1: Basic properties of the sodium silicate gelants (DPR fluids).

Silicate System	SiO_2:Na_2O Molar Ratio	pH	Gelant Viscosity (cp)	Activator	Gelant Type
A	High	10	1.7	Sodium Chloride	Newtonian
B	Low	11.5	2	Citric Acid	Newtonian

The rheology (gelation and kinetics of gelation process) of System A and formed gel properties have been investigated by Hatzignatiou *et al.* [5]. Bulk measurements showed that syneresis of gels formed using silicate System A was practically zero at different temperatures and activator concentrations, whereas System B has the tendency to shrink even by 50% of the original sample volume. In addition, bulk test observations presented by Hatzignatiou *et al*. [5] showed that the maximum compressional pressure (strength) of System A gels was significantly higher than the one of System B gels.

Strongly water-wet and (altered wettability) oil-wet Berea sandstone core samples (22-25 cm length and 3.77 cm diameter) were used in all experiments presented in this work. Filtered 0.1M sodium chloride brine and filtered isopar H (synthetic oil) with 1.29 cp viscosity at room temperature were the main "reservoir" fluids used.

Water-wet cores were treated chemically to alter their wettability to oil-wet. Measured phase-permeability curves together with recovery curves and spontaneous imbibition results were used to characterize the newly-established core wettability, which all demonstrated the water-wet and oil-wet (treated) nature of the tested core samples.

DPR TREATMENT PROCEDURE

All experiments were conducted using a steady-state, two-phase DPR placement in order to (a) better control the water/oil saturation at which the silicate gel sets (i.e., to quantitatively control the placement saturation conditions in the formation) and (b) ensure the presence of moveable oil at which the injected DPR gelant gels.

A typical DPR treatment experiment consists of three main stages. The core is first saturated with brine; pore volume (PV) and absolute brine permeability are then obtained,

and irreducible water saturation, S_{wi}, is established by single-phase oil injection. After that, a steady-state, two-phase, brine/oil injection at room temperature is initiated, at the desired water fraction (watercut), to establish the pre-treatment condition (treatment initial saturation, S_{wti}). Following that, a steady-state, two-phase, DPR-fluid/oil injection is performed at selected treatment watercut; the new saturation condition, named DPR treatment final water saturation (S_{wtf}), is established. Gelation of injected gellant and aging for one week at 60°C is then conducted. In the third, and final, stage the water residual resistance factor (RRF_w) is obtained through steady-state brine/oil injection in a step-wise fashion at several watercuts and until the residual oil saturation is reached. The last part of stage three is single-phase, oil, injection to determine approximate values for the oil residual resistance factor (RRF_o). Additional details related to the newly established procedure can be found in Askarinezhad *et al.* [3].

Table 2: Summary of DPR experiments.

Exp. #	Silicate System	Wettability condition	Porosity (%)	Absolute brine permeability (D)	Residual oil saturation - Untreated core, S_{or} (%)	Pre-treatment and DPR treatment conditions					DPR Quantification	
						Pre-treatment production watercut, WC (%)	Treatment watercut, WC (%)	Saturation			RRF_w	RRF_o
								Brine-oil	DPR fluid-oil	Water saturation shift (%)		
								S_{wti} (-)	S_{wtf} (-)			
1	A	Water wet	22.2	0.642	41.3	22	22	0.503	0.539	3.6	100	460
2	B	Water wet	23.25	0.995	41.3	22	22	0.509	0.555	4.6	2.7	3.8
3	A	Oil wet	22	0.779	30.1	22	22	0.424	0.449	2.5	14	6
4	A	Oil wet	21.4	0.667	30.1	78	22	0.506	0.4	-10.6	10.6	3.4 - 4.5

EXPERIMENTAL RESULTS AND DISCUSSIONS

Table 2 provides a summary of the four DPR experiments discussed in this work together with relevant core properties. Experiments 1 and 2 were conducted in water-wet Berea cores and Experiments 3 and 4 in oil-wet cores. It is worth mentioning that in Experiment 2, the procedure was slightly different in the post-treatment floods compared to the other three experiments (single-phase oil injection was performed prior to the two-phase brine/oil injection). System B was used only in Experiment 2; in the remaining three, System A was used as the DPR fluid. In the following subsections, the details of each experiment together with the DPR treatment results will be presented.

Experiments 1, 2: Systems A and B, water-wet cores, pre- and DPR treatments 22%

The treatment conditions in Experiments 1 and 2 were the same; the DPR treatment initial water saturation (S_{wti}) was established at WC=22% using steady-state co-injection of brine and oil (Figure 1, dashed vertical lines). DPR treatment was performed at the same WC=22%. A water saturation shift due to DPR-fluid/oil co-injection can be observed with the treatment final saturation (S_{wtf}) displayed in Figure 1. Table 2 provides additional relevant data (see also [3]). A visual inspection of the pre- and post-treatment effective permeabilities suggests that Experiment 2 could yield favorable DPR conditions, especially if one considers field-expected post-treatment flow conditions at high WCs. The results obtained will be analyzed based on the post DPR treatment RRF values (Askarinezhad *et al.* [3]). Although the treatment watercut and saturation conditions in these two experiments were practically identical, the water saturation shift

due to DPR-fluid/oil injection was more profound in Experiment 2. From the post-treatment floods, the reduction in both RRF_w and RRF_o were noticeably lower in Experiment 2 than in Experiment 1. The main reason is the significant shrinkage that occurs post-gelation with System B gels (Experiment 2). Bulk measurements at various temperatures on System B gels revealed a shrinkage of up to 50% of the total formed gel volume. The large saturation shift in post-treatment single-phase oil injection process in Experiment 2 serves as a confirmation of these observations; Bryant *et al.* [6] reported useful permeability reductions even at 95% syneresis of polymer gels. Effluent results in Experiment 2 revealed a relatively large gel erosion during the post-treatment floods.

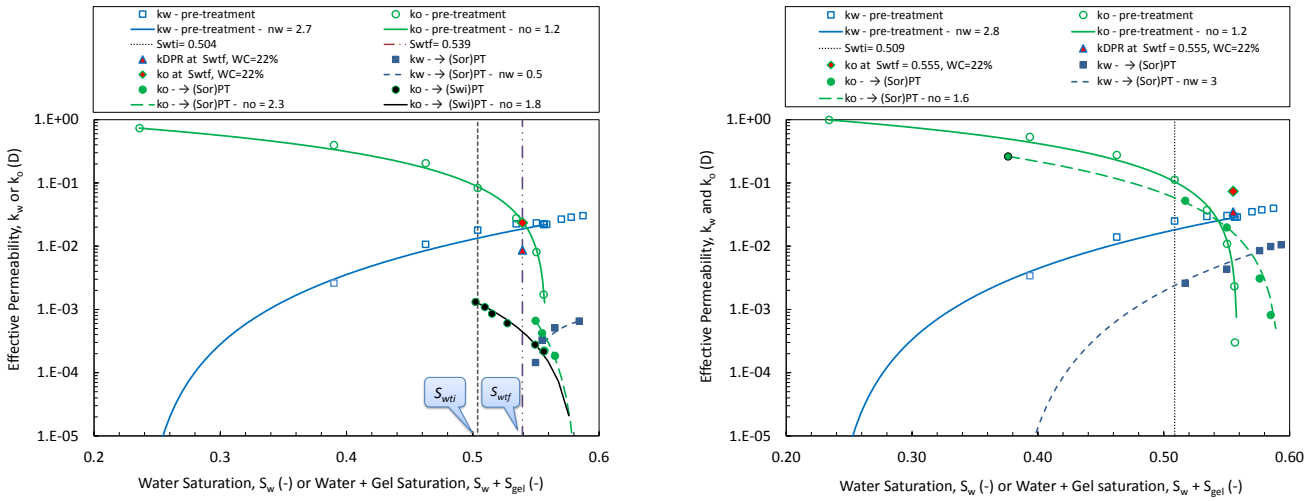

(Experiment 1) **(Experiment 2)**

Figure 1: Water-wet, pre- and DPR- treatments at WC=22% (Exp. 1) System A [3]; (Exp. 2) System B.

Gel instability and syneresis may indicate that System B is a non-favorable gelant for DPR treatments considering also the weak contrast in the two-phase RRF values. On the other hand, results in Experiment 1 showed large RRF values, which coupled with the fact that System A yields very strong gels with practically no syneresis (Hatzignatiou *et al.* [5]), the syneresis could be linked to the degree of permeability reduction. Based solely on the RRF values, it can be argued that on one hand silicate gel systems with a high degree of syneresis may not be good DPR candidates, and on the other hand strong systems, causing large oil and water RRFs, did not result in possitive DPR effects.

Experiment 3: System A, oil-wet core, pre-treatment 22%, DPR treatment 22%

The water saturation shift during treatment was less compared to water-wet cores (Figure 2 and Table 2). Based on both RRF values, which are significantly higher in the water-wet cores compared to oil-wet ones, and the visually inspected separation of the pre- and post-treatment permeability curves, it is clear that wettability has a profound impact on the DPR effectiveness, resulting in significantly more favorable DPR effects in oil-wet formations. In this experiment, the reduction of both oil and water effective permeabilities is significantly lower than the ones in water-wet cores (Experiment 1), and it can potentially yield positive DPR. Extrapolated effective oil permeabilities to S_{wti} (red curve in Figure 2) show the improvement of RRF_o with reduced water saturation.

Experiment 4: System A – Oil-wet core, pre-treatment 78%, DPR treatment 22%

The evaluation of System A as a potential DPR fluid candidate was conducted following a slightly different procedure to reflect realistic field processes and examine possible hysteresis effects. The pre-treatment WC was increased to 78% with the treatment WC been kept at 22% (Table 2). Results shown in Figure 3 demonstrate slight improvements in RRF_o compared to Experiment 3 and hysteresis effects to be practically negligible. Based on both visual inspection of the permeability curves and obtained RRF values, the achieved results demonstrated the potential for a more efficient positive DPR effect compared to the one obtained in Experiment 3. Results from this experiment serve as a starting point to the optimization of a two-phase DPR treatment in addition to serving more realistic reservoir/well conditions at which a treatment may be implemented by employing low WC treatments at realistically high pre-treatment production WCs.

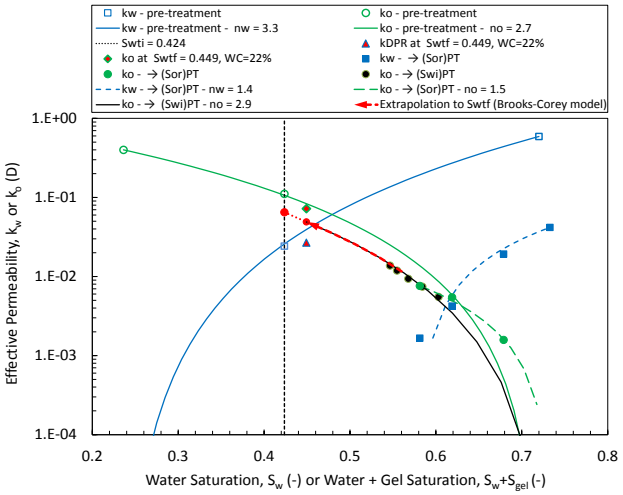

Figure 2: Experiment 3: Oil-wet, pre- and DPR treatment conditions at WC=22% [3].

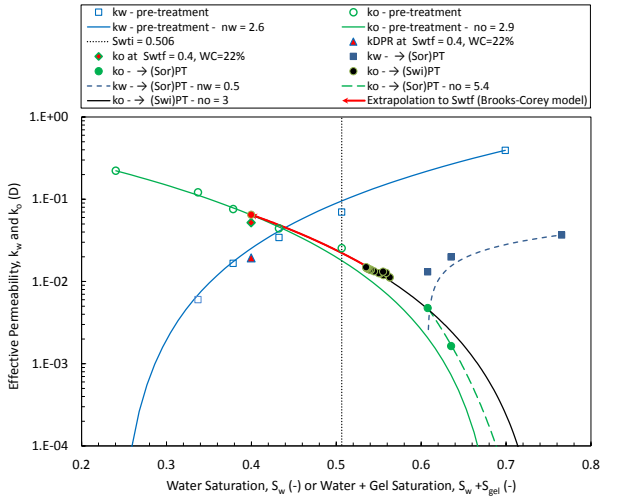

Figure 3: Experiment 4: Oil-wet, pre-treatment WC=78% and DPR treatment at WC=22%.

Discussion

DPR effectiveness was significantly different in water- and oil-wet cores mainly due to more favorable oil-phase continuity and distribution in oil-wet media compared to the corresponding one in water-wet formations. In water-wet cores, encapsulation of oil by gel may cause oil-phase discontinuities and porous medium conductivity reduction. Wettability tests have shown that silicate gel is strongly water-wet. Therefore, in oil-wet DPR treatments, formed gel in porous media yields a mixed-wet formation and a lower trapped oil saturation compared to water-wet formations. Another reason can be the lower mobile-oil saturation at S_{wtf} in the water-wet cases; the observed shift towards higher water saturations during treatment causes an even higher reduction in moveable oil saturation and a higher reduction in effective oil permeability.

In the water-wet experiment with System A, there is a rather visible hysteresis in post-treatment effective oil permeability. However, based on the qualitative analysis of our data, even if one is able to exclude the oil-permeability hysteresis effect (Experiment 1), the resulting RRF_o values are still too high to lead to an efficient positive DPR effect. Therefore, it can be argued that hysteresis effects on water and, especially, oil effective

permeabilities may not be the major reason for the observed DPR treatment results as also observed by Liang *et al.* [7]. Data from oil-wet cores showed that oil effective permeability hysteresis is much less pronounced than in water-wet ones.

CONCLUSIONS

In water-wet cores, DPR treatments resulted in high RRF values for both oil and water phases using gelant System A with absence of gel syneresis; gelant System B yielded almost identical, and low, RRF values with the formed gels displaying significant syneresis. In oil-wet cores, DPR treatments with System A resulted in significant lower oil and water RRFs than the ones observed in water-wet cores. The potential to optimize a DPR treatment effectiveness in a given oil-wet formation was demonstrated by deploying the DPR-fluid/oil mixture at low WCs when the formation produces at relatively high WCs. Generally, field executions require a careful design that balances the potential DPR treatment effectiveness with the treatment WC conditions, since low treatment WCs are also accompanied by small amounts of gel in treated porous media.

ACKNOWLEDGEMENTS

The authors acknowledge the Research Council of Norway, ConocoPhillips, Det norske oljeselskap, Lundin Norway, Statoil, Talisman (now Repsol), and Wintershall for financing the work through the research Centre DrillWell - Drilling and Well Centre for Improved Recovery, a research cooperation between IRIS, NTNU, SINTEF and UiS. The authors wish to thank A. Stavland for fruitful discussions during the course of this study.

REFERENCES

1. Thompson, K.E. and H.S. Fogler, "Pore-Level Mechanisms for Altering Multiphase Permeability with Gels". *SPE Journal,* 1997, Vol. 2 (3), 350-362. SPE-38433-PA. DOI: 10.2118/38433-PA.
2. Elewaut, K., A. Stavland, A. Zaitoun, Z. Krilov, and P.L.J. Zitha, "Investigation of a Novel Chemical for Bullhead Water Shutoff Treatments" Paper presented at the SPE European Formation Damage Conference, Sheveningen, The Netherlands, 25-27 May 2005. SPE-94660-MS. DOI: 10.2118/94660-MS.
3. Askarinezhad, R., D.G. Hatzignatiou, and A. Stavland, "Disproportionate Permeability Reduction of Water-Soluble Silicate Gelants - Importance of Formation Wettability". Paper presented at the SPE Improved Oil Recovery Conference, Tulsa, OK, USA, 11-13 April 2016. SPE-179589-MS. DOI: 10.2118/179589-MS.
4. Iler, R.K. *The Chemistry of Silica: Solubility, Polymerization, Colloid and Surface Properties, and Biochemistry*. John Wiley-Interscience, New York, USA, 1979.
5. Hatzignatiou, D.G., R. Askarinezhad, N.H. Giske, and A. Stavland, "Laboratory Testing of Environmentally Friendly Sodium Silicate Systems for Water Management through Conformance Control". *SPE Productions and Operations*. 2016. SPE-173853-PA. DOI: 10.2118/173853-PA.
6. Bryant, S.L., M.R. Rabaioli, and T.P. Lockhart, "Influence of Syneresis on Permeability Reduction by Polymer Gels". *SPE Production & Facilities*, Vol. 11 (04), 209-215. SPE-35446-PA. 1996. DOI: 10.2118/35446-PA.
7. Liang, J., H. Sun, and R.S. Seright, "Reduction of Oil and Water Permeabilities Using Gels". Paper presented at SPE/DOE Improved Oil Recovery Symposium, Tulsa, OK. 17-20 April 1992. SPE-27799-MS. DOI: 10.2118/27799-MS.

A FAST METHOD FOR HOMOGENEOUS DISSOLUTION OF CHALK SPECIMENS FOR LABORATORY EXPERIMENTS – DOCUMENTATION BY X-RAY CT-SCANNING AND SCANNING ELECTRON MICROSCOPY

Claus Kjøller,[1] Lykourgos Sigalas,[1] Helle F. Christensen,[2] and Mona Minde[3,4,5]
(1) Geological Survey of Denmark and Greenland
(2) Geo, Denmark
(3) University of Stavanger, Norway
(4) The National IOR Centre of Norway
(5) IRIS AS, The International Research Institute of Stavanger, Norway

This paper was prepared for presentation at the International Symposium of the Society of Core Analysts held in Snowmass, Colorado, USA, 21-26 August 2016

ABSTRACT

In chalk reservoirs, acid injection for well stimulation purposes as well as certain EOR methods, such as CO_2 injection, causes dissolution of the chalk matrix due to the acidic nature of fluid injected. The effects of the chalk dissolution e.g. on rock mechanical properties are currently not well understood. This is partly due to challenges with interpretation of results from laboratory experiments in the context of *in situ* reservoir conditions as laboratory experiments most often result in inhomogeneous dissolution of chalk specimens. To facilitate this challenge, we present a method for fast homogeneous dissolution of chalk specimens by a so-called retarded or heat activated acid (Acidgen™ FG) – and subsequent documentation by X-ray CT-scanning and Field Emission Gun Scanning Electron Microscopy (FEG-SEM) imaging.

The method was validated through dissolution tests using a large number of Stevns outcrop chalk specimens. Dissolution of the chalk was performed with either of two acidic or acid generating solutions: 1) Acidgen™ FG or 2) acetic acid. In both cases, the homogeneity of the chalk dissolution was investigated by image analysis of X-ray CT-scanning images, and for the Acidgen™ FG case also of FEG-SEM images.

By application of Acidgen™ FG it is possible to create homogeneous dissolution in the outcrop chalk specimens with a resulting absolute porosity change of up to at least 3.5% Likewise, the retarded acid creates homogeneous dissolution of reservoir chalk specimens. For comparison, the application of acetic acid mostly creates fast inhomogeneous dissolution from the outside of the chalk specimens. Combined image analysis of X-ray CT images and SEM images has proven a strong tool for evaluation of the homogeneity of the chalk plug specimens.

INTRODUCTION

Rock mechanical laboratory tests most often explore the rock mechanics of bulk plug specimens. As a consequence, it is important to obtain homogeneous dissolution when rock mechanical effects caused by dissolution of rocks are studied. For the purpose of establishing experimental conditions favouring homogeneous dissolution, previous studies [1-3] have applied so-called retarded acids or heat activated acids, which are organic acid pre-cursors that increase the rate of acid formation upon heat activation or in the presence of certain enzymes. Thereby, the Damköhler number [4-6] is kept low initially by a low reaction rate when the retarded acid is introduced into the core specimen. Both Egermann et al. (2010) [2] and Ott et al. (2013) [1] showed that dissolution of various limestone samples could be carried out in a reasonably homogeneous way. In both cases, the specimens dissolved were subsequently used for rock mechanical tests showing that rock mechanical properties, such as Young's modulus, in general decreased as a function of the reasonably homogeneous porosity increase. When the porosity was increased by wormhole formation i.e. inhomogeneous channel-like dissolution Ott et al. (2013) [1] found that the mechanical parameters were practically unaltered in similar rock specimens.

The goal of this paper is to pave the ground for understanding relations between chalk dissolution and rock mechanical changes. We do this by modifying the retarded acid method and comparing the results with dissolution of chalk with acetic acid. This paper presents the modified method for homogeneous dissolution of chalk specimens and documentation hereof using X-ray CT-scanning and FEG-SEM imaging.

PROCEDURE

Specimen preparation

During the first stage of the project, 98 specimens of Stevns outcrop chalk of Maastrichtian age were plugged, marked and delivered for CT-scanning. Initial state conventional core analysis (CCAL) then followed, including determination of porosity, single point N_2-gas permeability, and grain density. CT-scanning images were analysed for average Hounsfield Units (also referred to as CT-number) and standard deviation, and an initial subdivision of samples into homogeneous and less homogeneous samples was carried out qualitatively.

Subsequently, the 30 most homogeneous specimens were selected for experiments with Acidgen™ FG and acetic acid. Each test specimen was treated with Acidgen™ FG or acetic acid until up to six (6) acid solution treatment cycles were performed (the treatment cycle is described in detail below). Acidgen™ FG solutions of 2% (v/v), 5% (v/v), and 15% (v/v) were tested and compared with results from dissolution of specimens with 0.5% (v/v), 2% (v/v), and 5% (v/v) acetic acid.

In the second stage of the project, 71 reservoir chalk core specimens from undisclosed offshore chalk were cleaned using toluene-methanol interchangeable flushing at room conditions. After cleaning, the samples were CT-scanned and CCAL was carried out.

Subsequently, a set of 28 specimens from the pool of most homogeneous samples were selected for experiments with 5% (v/v) Acidgen™ FG.

General treatment procedure

The principle of the treatment is five treatment steps:

1) Vacuum saturate specimens at 5-10°C and at a duration that will ensure 100% occupation of the pore volume by the acid precursor solution.
2) Heat the specimens at 50°C for 48h, while remaining saturated with the acid solution. In case of Acidgen™ FG, heating increases the kinetics related to formation of formic acid from the acid precursor solution.
3) Flush the specimens with at least 4 pore volumes (PV) of tap water or demineralized water (DW) in order to remove the acidic solution from the pore space of the plug specimens. Complete removal of acid solution and dissolution products are documented by pH and Ca concentration measurements.
4) Dry the specimens at 75°C for at least 24h until all water is evaporated from the pore space.
5) CCAL in order to observe the effects of the treatment.

Initially, and after completion of every two (2) treatment cycles, specimens are X-ray CT-scanned for comparison.

RESULTS AND DISCUSSION

Initial CT-Scanning

We have used image analysis of X-ray CT-images to show that porosity increases homogeneously in our chalk specimens as a result of the treatment with Acidgen™ FG. However, a prerequisite for using the CT-number as a measure for the porosity distribution in a plug specimen is that it is possible to establish a correlation between the measured CT-number and the porosity. In theory, this relationship should be linear [7]. Figure 1 shows that for the set of Stevns outcrop chalk specimens, the average CT-number correlates linearly to porosity. Especially for the set of 30 most homogeneous specimens this is the case (Figure 1B).

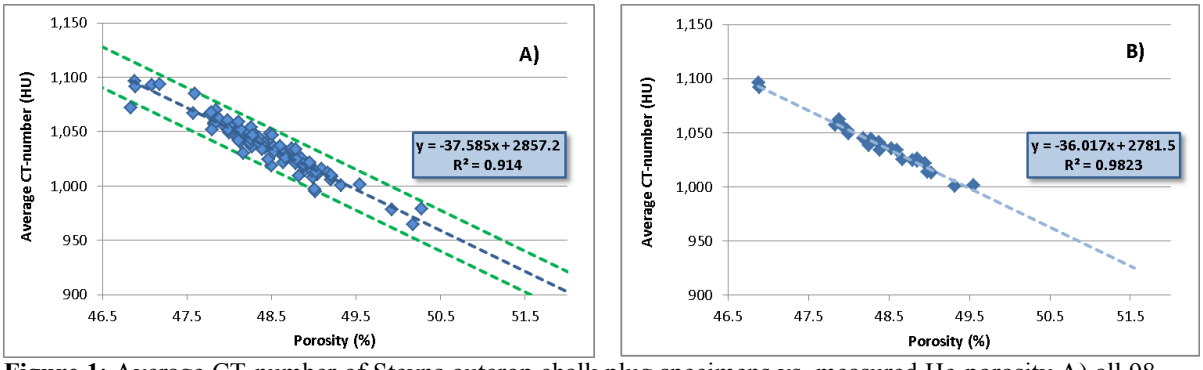

Figure 1: Average CT-number of Stevns outcrop chalk plug specimens vs. measured He-porosity A) all 98 and B) 30 selected specimens for dissolution tests.

Treatments with Acidgen™ FG

From the subset of the 30 most homogenous specimens, 18 were treated with various concentrations of Acidgen™ FG: Eight (8) specimens with 2% (v/v), six (6) specimens with 5% (v/v), and four (4) specimens with 15% (v/v). In all cases, there was a nearly linear porosity increase as a function of the number of treatments (Figure 2). In addition, the magnitude of the porosity increase was proportional to the concentration of Acidgen™ FG (Figure 2). Treatment of chalk specimens with 15% (v/v) Acidgen™ FG solution resulted in specimen failure after 2 treatments along healed hairline fractures in the specimens. This was most likely because of local pressure increase in the specimens due to CO_2 formation caused by the dissolution of the chalk. Therefore, a concentration of 5% (v/v) Acidgen™ FG was considered the upper limit for subsequent treatments according to the present method.

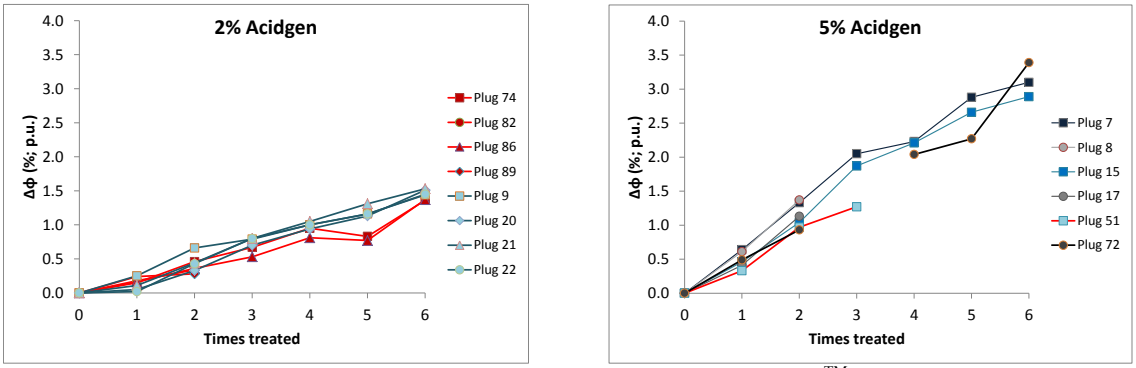

Figure 2: Absolute change in porosity as a function of number of Acidgen™ FG treatments for outcrop chalk specimens treated with Acidgen™ FG solution

The homogeneity of the dissolution is verified by X-ray CT-image analysis (Figure 3). Histogram plotting particularly helps obtaining the level of homogeneity of a specimen.

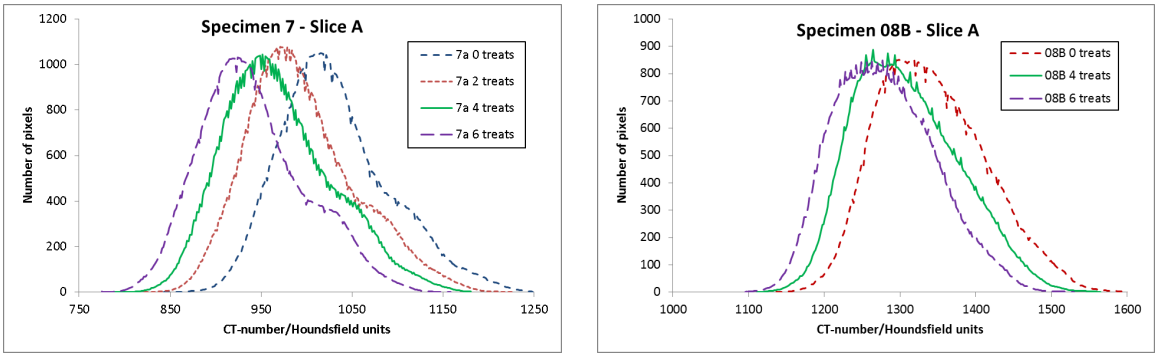

Figure 3: Histograms representing image analysis of CT-images after treatments of outcrop plug specimen # 7 and reservoir plug specimen # 08B, both treated with 5% Acidgen™ FG solution.

The CT-image histograms shift towards lower average CT-numbers as a result of the dissolution of carbonate in the specimens. In the same time, the modal distribution of CT-numbers is maintained and the standard deviation does not change considerably due to

the treatment with Acidgen™ FG. Thus, the initial porosity distribution is maintained during the Acidgen™ FG treatment, even for specimens with an initially slightly less homogeneous porosity distribution as illustrated for plug #7. Furthermore, the methodology is valid for homogeneous dissolution of both outcrop chalk specimens (plug #7, Figure 3) and reservoir chalk specimens (plug #08B, Figure 3).

Thorough analysis of 850 FEG-SEM images of treated as well as untreated outcrop chalk specimens further suggests that dissolution of the chalk specimens following the method presented herein creates a homogeneous porosity change. Thus, the main feature resulting from the dissolution is an increase in the number of partly dissolved and dismantled coccolith rings as well as the amount of smaller grains <1 μm (Figure 4).

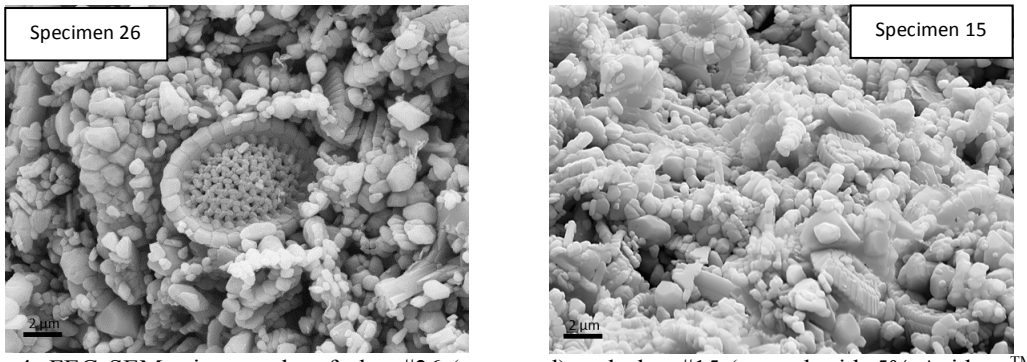

Figure 4: FEG-SEM micrographs of plug #26 (untreated) and plug #15 (treated with 5% Acidgen™ FG) showing a considerably larger number of grains in the fraction <1μm in the treated specimen.

Treatments with acetic acid

From the set of homogenous specimens, 12 were treated with various concentrations of acetic acid between 0.2% (v/v) and 5% (v/v). In all cases, chalk dissolution was observed but there was little or no porosity change due to the treatment. However, a notable change to the specimens' dimensions occurred, where length and diameter of the plug specimens were reduced (Figure 5), indicating that dissolution of the chalk occurred instantly when the specimens were exposed to acetic acid. Ca concentrations and pH levels were similar to the levels in the Acidgen™ FG experiments, indicating that comparable amounts of chalk dissolved in the two types of experiments.

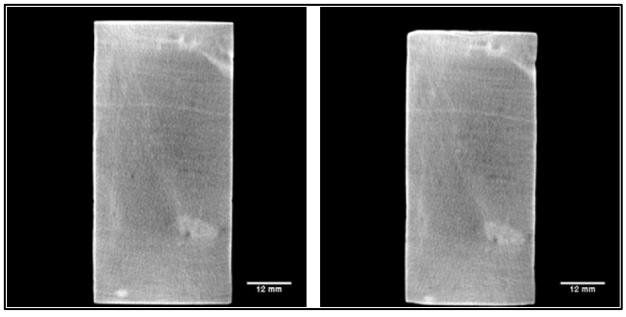

Figure 5: CT-images of plug specimen #57. A) Before treatment with 2% acetic acid. B) After 6 treatments with 2% acetic acid. Note that the specimen has become considerably smaller due to the treatment.

CONCLUSIONS

- Image analysis of CT-images of plug specimens is a powerful tool to evaluate and document homogeneity and dissolution of chalk specimens.
- Dissolution of outcrop chalk specimens can be performed in a homogeneous way with up to 5% Acidgen™ FG by application of the method presented here.
- Homogeneous dissolution of outcrop chalk specimens with acetic acid is not possible.

ACKNOWLEDGEMENTS

The research was supported by funding from the Joint Chalk Research Phase VII programme (JCR-7). Cleansorb is thanked for supplying the Acidgen™ FG used in the study.

REFERENCES

1. Ott, H., Oedai, S., Pentland, C.H., Eide-Engdahl, K., van der Linden, A.J., Gharbi, O., Bauer, A. Ott & Makurat, A., 2013. CO_2 reactive transport in limestone: Flow regimes, fluid flow, and mechanical rock properties. Paper SCA 2013-029, Proceedings of the International Symposium of the Society of Core Analysts. Napa Valley, California, USA, 16-19September, 2013. 12 pp.
2. Egermann, P., Bekri, S. & Vizika, O., 2010. An integrated approach to assess the petrophysical properties of rocks altered by rock-fluid interactions (CO_2 injection). Petrophysics, 51, 32-40.
3. Egermann, P., Bemer, E. & Binzner, E., 2006. An experimental investigation of the rock properties evolution associated to different levels of CO_2 injection like alteration processes. Paper SCA 2006-034, Proceedings of the International Symposium of the Society of Core Analysts. Trondheim, Norway, 12-16 September, 2006. 15 pp.
4. Schechter, R.S. & Gidley, J.L., 1969. The change in pore size distribution from surface reaction in porous media. AIChE Journal, 15, 339-350.
5. Daccord, G., Lenormand, R. & Lietard, O., 1993. Chemical dissolution of a porous medium by a reactive – I model for the wormholing phenomenon. Chemical Engineering Science, 48, 169-178.
6. Békri, S., Thovert, J.F. & Adler, P.M., 1995. Dissolution of porous media. Chemical Engineering Science, 50, 2765-2791.
7. Maas, J.G. & Heebing, A., 2013. Quantitative X-ray CT for SCAL plug homogeneity assessment. Paper SCA 2013-004, Proceedings of the International Symposium of the Society of Core Analysts. Napa Valley, California, USA, 16-19 September, 2013. 12 pp

Contact angle and IFT measurements at elevated temperatures for evaluating wettability in a selected carbonate reservoir in the UAE

Hazim Al-Attar, Jassim Abubacker, Abdurazak Zekri, Mohammad Khalifi, Essa Lwisa

United Arab Emirates University, UAE

This paper was prepared for presentation at the International Symposium of the Society of Core Analysts held in Snowmass, Colorado, USA, 21-26 August 2016

ABSTRACT

Waterflooding has been regarded as a well-known secondary oil recovery method. In the recent years, extensive research on crude oil, brine, and rock systems has acknowledged that the composition of the injected water can change wetting properties of the reservoir during a waterflood in a promising way to improve oil recovery. Hence, injection of "Smart Water" with correct salinity and composition is considered as a tertiary recovery method. The mechanism behind wettability alteration that is promoted by smart water injection has been a topic of discussion in carbonate and sandstone formations. In this work, some key properties of sea water and its dilutions with natural and spiked sulphate concentrations have been thoroughly investigated in the laboratory. Interfacial tension (IFT) of crude oil/brine system was monitored at ambient and high-pressure/high-temperature (HPHT) conditions. The brine with the least IFT was then used as a non-wetting phase with aged samples of rock for the measurement of contact angle at HPHT conditions. The rock samples are carbonates of a selected onshore oil field in UAE. The results of this work show that sea water of salinity 57,539 mg/l without sulphate spiking may be considered as the Smart Water for further core flooding investigation.

INTRODUCTION

Half of the world's hydrocarbon reserves is believed to exist in carbonate rocks. The mechanism that governs the recovery should be known for a successful oil production scheme. An important factor that controls the fluid distribution in a reservoir is formation wettability [1,2]. Wettability alteration studies of sea water/oil/rock systems gained momentum after the successful injection of sea water into the highly fractured Ekofisk field in the North Sea [3, 4]. Calcium and Sulphate have been found to exhibit strong potential towards the calcite surfaces [5].

It is the objective of this work to carry out extensive laboratory work on the measurements of IFT and contact angle under HPHT conditions. These two key properties are believed to have direct impact on wettability alteration of crude oil/water/rock systems. Twenty six different brines representing various scenarios of

dilution and sulphate-spiking were prepared and tested to identify the Smart Water most effective in the alteration of wettability.

PROCEDURE:

Crude Oil:
Reservoir crude oil from the Asab field was used in all experiments. The dead oil density and viscosity at 20°C are 0.8276 g/cc and 2.93 cp, respectively. The oil is sweet.

Brines:
A total of 26 brines were used in this study including formation water (FW) and injection water (IW) of Asab field. All the brines were prepared using standard procedures reported in Schlumberger manuals. Sea water was collected from the Arabian Gulf and a complete ionic analysis was performed. Sea water of Total Dissolved Solids (TDS) 57,539 mg/l was selected as the base brine and was synthetically prepared in the lab. Different brines were prepared by diluting the sea water and by spiking the sea water with sulphate. Spiking was based on the 885 mg/l of sulphate in formation water. Brines were spiked by 1,770 mg/l (x2 SO_4) and 5,310 mg/l (x6 SO_4). A sulphate spiking of x6 SO_4 was attempted in this work to see how it could alter the IFT and contact angle measurements. Asab oil field has a formation water of TDS 157,488 mg/l with a density of 1.1034 g/ml and viscosity of 1.3483 cp at ambient conditions. The Injection water of this field has a TDS of 258,250 mg/l with a density of 1.1639 mg/l and viscosity of 1.75 cp at ambient conditions. Table 1 shows the ionic composition of SW, FW and IW used in the work.

Core Samples:
Core samples were selected from Asab field. All core samples are limestone.

IFT Measurement:
All Interfacial Tension (IFT) measurements of oil/brine were carried out using Teclis Tracker which utilizes the pendant drop technique. Teclis tracker is capable of running IFT measurements at ambient and HPHT conditions. A cell capable of withstanding HPHT is used. The cell was pressurized to prevent evaporation of brine. A maximum pressure of 248 psia and maximum temperature of 90°C were implemented. The reservoir temperature of 110°C has not been achieved because of equipment limitation.

Contact Angle Measurement:
All contact angle measurements were performed on rock samples aged by fully saturating in Asab crude oil at 90°C and for 3 days, making the rock surface oil-wet with a deduced contact angle of 180°. Alotaibi et al. and Anderson classified wettability in terms of contact angle as being water-wet (0-75°), intermediate-wet (75-115°) and oil-wet (115-180°) [1, 6]. Some contact angle measurements were also carried out for brines of higher IFT values (> 8-10 dynes/cm) at HPHT conditions. All the measurements were continuously monitored for 72 hours.

RESULTS

The IFT values at HPHT conditions are shown in Table 2 and contact angle measurements at end of 72 hrs is shown in Table 3.

DISCUSSION

IFT of Brines at HPHT

Among the three brines in the category IFT 1 in Figure 1, SW corresponds to the least value of TDS and results in the least IFT. The formation and injection water, however, show high values of IFT. There is an increasing trend in IFT for the category IFT 1.

Wang and Gupta, concluded that the increase or decrease of IFT values depends on the composition of the brine [7]. From categories IFT 2 to 5, there is a decreasing trend of IFT. Category 2 shows the effect of sulphate spiking. Combined effect of dilution and sulphate spiking is observed in categories 3 to 5. The three brines in categories 2 to 5, mainly differ in the concentration of sulphate ion and an overall reduction of IFT with sulphate spiking at HPHT can be observed.

From categories IFT 6 to 8, there is an increasing trend of IFT. Categories 6 to 8 show the effect of dilution. So dilution seems to yield an increasing trend of IFT at HPHT conditions for categories IFT 6, 7 and 8. During the dilution of sulphate spiked brines, concentration of potential ions like calcium, magnesium and sulphate were reduced, diluted brines had higher sulphate compared to other ions in the brine. These higher sulphate ions alone, however, were not able to reduce the IFT of diluted brines.

Contact Angle Measurements at Single Temperature and Pressure

The results of the stabilized contact angle measurements after elapsed time of 72 hours are listed in Table 3 and presented in Figure 2.

In category CA 1, Sulphate spiking of the SW makes the rock surface more oil-wet. Also SW ($\Delta\theta = 67°$) was capable of changing the wettability from oil-wet to the border line of intermediate-wet system. In category CA 2, SW/10 ($\Delta\theta = 49°$) changed the wettability from oil wet to weakly oil wet. In category CA 3, SW/50 ($\Delta\theta = 66°$) changed the wettability from oil-wet to border line of intermediate wettability. Categories CA 1 to CA3 show that sulphate spiking increased the contact angle. Hognesen et. al reported that the ratio of calcium to sulphate ion is a key factor in altering the wettability [2]. All measurements were performed at high temperature (90°C). Categories CA 4 and CA 5 show an increasing trend of contact angle with dilution. It seems that calcium-sulphate ratio was not just good enough to alter the wettability. In category CA 6, although the contact angle has decreased but it did not change the wettability from oil wet to intermediate wet.

CONCLUSION

1. The results of IFT measurements at HPHT conditions have shown that SW, its twice and six times sulphate spiking seem to be the three best brines of least IFT. Among these three brines the SW x6 SO_4 brine has shown the least IFT.
2. From the contact angle results at HPHT, the best brines that showed the least contact angle are SW and SW/50. These brines changed the wettability of rock from oil-wet to the border line of intermediate-wet.
3. Sulphate spiking at HPHT conditions has been found to be effective in reducing IFT but not so effective in promoting favorable contact angles.
4. Brine dilution at HPHT conditions failed to reduce the IFT or the contact angle.
5. From above results and economic point of view, SW is the most likely Smart Water which has an IFT of 9.503 dyne /cm at HPHT conditions and a contact angle of 113 degrees ($\Delta\theta = 67°$).

REFERENCES

[1] M. B. Alotaibi, R. Azmy, and H. A. Nasr-El-Din, "Wettability Challenges in Carbonate Reservoirs," 2010.

[2] E. J. Hognesen, S. Strand, and T. Austad, "Waterflooding of preferential oil-wet carbonates: Oil recovery related to reservoir temperature and brine composition," 2005.

[3] O. Torsaeter, "An Experimental Study of Water Imbibition in Chalk From the Ekofisk Field," 1984.

[4] P. Zhang, M. T. Tweheyo, and T. Austad, "Wettability alteration and improved oil recovery by spontaneous imbibition of seawater into chalk: Impact of the potential determining ions Ca2+, Mg2+, and SO42−," *Colloids Surf. Physicochem. Eng. Asp.*, vol. 301, no. 1–3, pp. 199–208, Jul. 2007.

[5] A. Pierre, J. M. Lamarche, R. Mercier, A. Foissy, and J. Persello, "Calcium as Potential Determining Ion in Aqueous Calcite Suspensions," *J. Dispers. Sci. Technol.*, vol. 11, no. 6, pp. 611–635, Dec. 1990.

[6] W. G. Anderson, "Wettability Literature Survey- Part 1: Rock/Oil/Brine Interactions and the Effects of Core Handling on Wettability," *J. Pet. Technol.*, vol. 38, no. 10, pp. 1125–1144, Oct. 1986.

[7] W. Wang and A. Gupta, "Investigation of the Effect of Temperature and Pressure on Wettability Using Modified Pendant Drop Method," 1995.

CHARACTERIZATION OF INTERACTION BETWEEN OIL/BRINE/ROCK UNDER DIFFERENT ION CONDITIONS BY LOW FIELD SOLID-STATE NMR

Shijing XU[1], Xiaoliang WANG[2], Weifeng LV[1], Qingjie LIU[1],

Jiazhong WU[1], Ninghong JIA[1]

1. Research Institute of Petroleum Exploration and Development, Beijing, China

2. Nanjing University, Nanjing, China

This paper was prepared for presentation at the International Symposium of the Society of Core Analysts held in Snowmass, Colorado, USA, 21-26 August 2016

ABSTRACT

For the foreseeable future，water flooding will still remain the most economical and the most efficient way for oil field development and production. Apart from the conventional purpose of water flooding, which is to supplement energy into reservoirs and to support formation pressure, how to extend the function of water flooding is a key to enhance oil recovery while keeping the cost low enough. Currently, ions tuning water flooding (ITWF), with its function to adjust the ion strengths amongst ions of reservoir oil, clay minerals and injected fluid, rises as a hot-spot add-on that helps detach the crude oil from surfaces of clay minerals, hence enhances both micro and macro oil displacement efficiency. Quantitative investigation and evaluation of the microscopic mechanism of ITWF on oil/water/mineral is the key to the technical breakthrough. In this work, we suggested to use low field solid state NMR to evaluate the interaction between model oil compounds and inorganic rock interface under different ions tuning water. The fully refocused FID changed according to different water and ion used. Adding certain amount water weaken the interaction between model oil compounds and inorganic rock interface. However, ions strengthen the interaction between model oil compounds and inorganic rock interface, which played a negative role. The results could well guide our further application of ITWF.

INTRODUCTION

Ions Tuning Waterflooding (ITW) is a promising improved oil recovery (IOR) technology. According to our recent research work, the EOR-effect of ions tuning waterflooding is not only dependent on the low salinity but closely related to the ionic content and ionic types. Therefore, the principle of ions tuning waterflooding is not only

to dilute the salinity of the injection brine but also to adjust the salinity and composition of the injection brine[1].

In recent years, several mechanisms were proposed to account on how the ions tuning waterflooding to recover additional oil. (1) Fines migration and clays swelling caused by ions tuning waterflood are the main mechanisms of improved oil recovery[2-3]. (2) Multi-component ionic exchange between the rock minerals and the injected brine was proposed to be as the major mechanism to enhance oil recovery[4-5]. (3) Expansion of the double layer to be as the dominant mechanism of oil recovery improvement[6]. The general agreement among researchers is that ions tuning waterflooding causes reservoirs to become more water-wet[7-9]. Even though different mechanisms have been proposed to explain the wettability alternation, the primary mechanisms of which are still uncertain. Several mechanisms have been proposed to be the dominant reason to improve oil recovery by ions tuning waterflooding. Moreover, the wettability change is claimed to be the dominant reason for incremental oil recovery. However, what the main causes (electrical double layer expansion, multi-component exchange and fines migration) to improve the wettability are still uncertain. Therefore, the main objective of this paper is to investigate the fundamental mechanisms to enhance oil recovery of ions tuning waterflood by Low Field Solid-state NMR, which is established as a powerful technique to observe structure and segmental dynamics of polymers at the molecular level. [10] In principle, molecular mobility can be deduced from simple FID signals where a fast or slow decay indicates the presence of rigid or mobile components, respectively.

In this work, we suggested to use low field solid state NMR to evaluate the interaction between model oil compounds and inorganic rock interface under different ions tuning water. The results show that ions strengthen the interaction between model oil compounds and inorganic rock interface, which played a negative role, which may guide our further application of ITWF.

EXPERIMENTAL SECTION

Preparation of Samples: Desired amounts of model oil (nonanoic acid and 2-methyl quinoline), model rock (SiO_2 sphere with diameter of 10 μm and tunnel diameter of 17 nm) and deuterated water (D_2O) were combined by first dissolving the model oil in purified chloroform and then adding the model rock and D_2O.

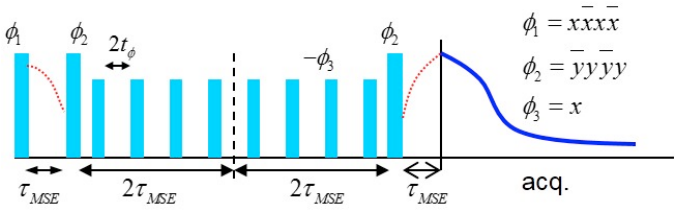

Figure 1: Magic-sandwich echo (MSE) pulse sequence for refocusing the loss of rigid-phase signal due to the dead time. [11-14].

^{1}H NMR experiments: The measurements were performed in a Bruker Minispec mq20 low-field spectrometer at 20 MHz proton resonance frequency with a typical π/2 pulse length of about 3 μs and receiver dead time of about 13 μs. Magic-Sandwich Echo (MSE, shown in Fig. 1a) could well refocus the initial FID signal, which gets lost in the single pulse experiment due to the dead time problem of the spectrometer. A Hahn Echo pulse sequence could well eliminate magnetic field inhomogeneity as well as refocus chemical shift anisotropy. We combined the MSE FID at short acquisition time (~80 μs) with ^{1}H Han Echo decay signal at long echo time (80~10^6 μs) to obtain a fully recovered FID.

RESULTS AND DISCUSSIONS

The interaction of model oil and rock results in heterogeneous mobility of the mixture: relative rigidity on the surface and mobility away from the surface. Such molecular mobility differences show up in simple FID signals. A fast decay indicates the presence of rigid components, while a slow decay is the response of mobile components. In the single pulse experiment, the spectrometer looses the initial part of the FID signals due to a long dead time and the recorded fraction of rigid components would be under-estimated in the final FID decomposition analysis. To overcome this, a MSE sequence was used to refocus the missing initial FID signals. A problem also arises at long acquisition times where the magnetic field inhomogeneity may result in a decay of FID and, thus, would obscure our analysis. Herein, Hahn echo was also utilized to record the FID signal decay with increasing echo time (80~10^6 μs), as it was able to well eliminate the magnetic field inhomogeneity and refocus the chemical shift anisotropy. A fully refocused FID with complete shape could be obtained through a combination of MSE FID and Hahn echo decay. Figure 2 shows fully refocused ^{1}H NMR FID of nonanoic acid / model rock with different nonaoic acid contents at 30 °C. With increasing nonanoic acid amount, the FID decays more and more slowly. The same thing happens in fully refocused ^{1}H NMR FID of 2-methyl quinoline / model rock with different 2-methyl quinoline contents.

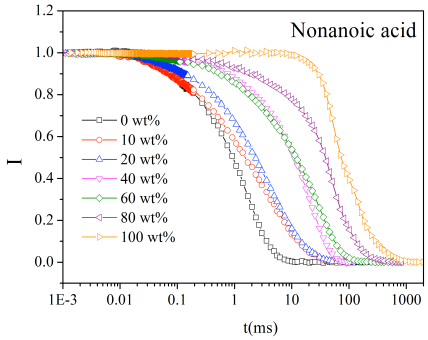

Figure 2: Fully refocused ^{1}H NMR FID of nonanoic acid/model rock with different nonaoic contents at 30 °C

To eliminate the influence of ^{1}H in water, we used D2O instead in all the following NMR experiments with 20 wt% amount of model oil. When different amount water added, the FID curves changes differently with nonanoic acid and 2-methyl quinolone added. The FID decays more slowly with increasing amount of water, as show in figure 3a. (1.0D means 1.0 amount to corresponding model oil amount) when more than 2.0D is added the FID no longer changes. On the contrary, the FID curves change very slightly in 2-methyl quonoline / model rock when different amount of water added, as shown in figure 3b. More water added only slightly increases the slowly decayed component.

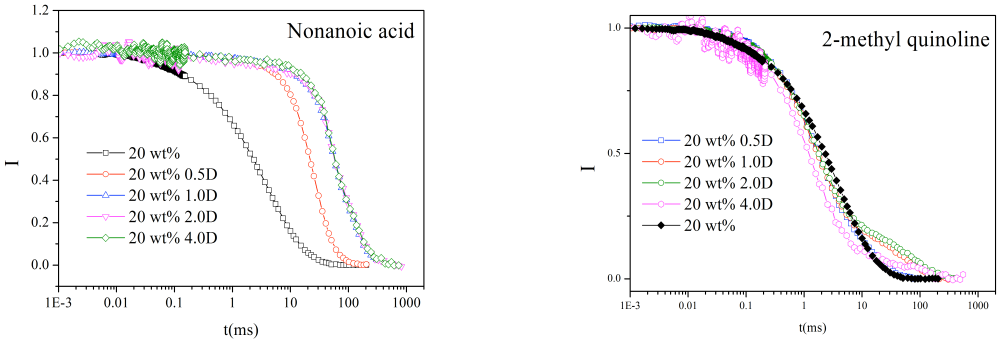

A b

Figure 3: Water added in (a) nonanoic acid/model rock (b) 2-methyl quinoline/model rock

When small amount of ions (Ca^{2+} for example) added, we can see nearly on change of FID curves in nonanoic acid system, as shown in figure 4a. If the amount is very large, 5 eqiv for example, the FID decays faster than others. In 2-methyl quinolone system, the FID decays faster with increasing ions amount, as shown in figure 4b. This suggests that ions play a negative effect.

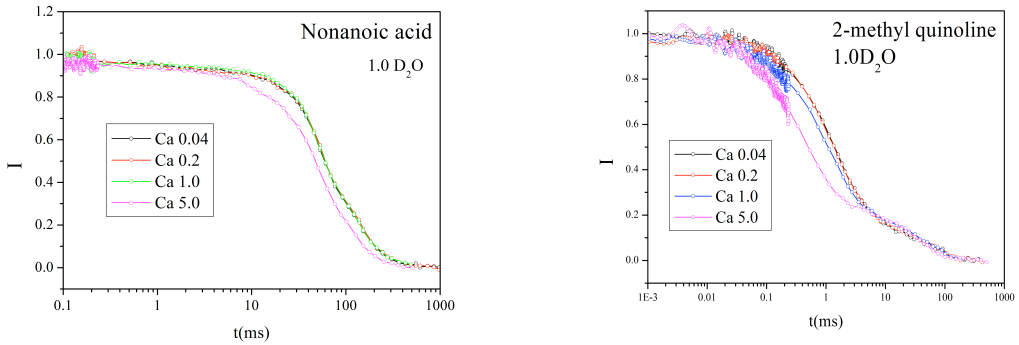

A b

Figure 4: Ca^{2+} added in (a) nonanoic acid/model rock (b) 2-methyl quinoline/model rock

CONCLUSION

In this work, the low field solid state NMR suggested a sensitive method to evaluate the interaction between model oil compounds and inorganic rock interface under different ions tuning water. The fully refocused FID changed according to different water and ion used. Adding certain amount water weaken the interaction between model oil compounds and inorganic rock interface. However, ions strengthen the interaction between model oil compounds and inorganic rock interface, which played a negative role. The results could well guide our further application of ITWF.

REFERENCES

1. Yousef, A.A., Al-Salehsalah, S.H., Al-Jawfi, M.S., 2011. New recovery method for carbonate reservoirs through tuning the injection water salinity: smart waterflooding. In: SPE EUROPEC/EAGE Annual Conference and Exhibition, Vienna, Austria.
2. Morrow, N., Buckley, J., 2011. Improved oil recovery by low-salinity waterflooding. J. Pet. Technol. 63 (5), 106–112.
3. Sohrabi, M., Emadi A., 2013. Visual investigation of oil recovery by low salinity water injection: formation of water micro-dispersions and wettability alteration. In SPE Annual Technical Conference and Exhibtion, 2013, Society of Petroleum Engineers, New Orleans, Louisiana, USA.
4. Lager, A., Webb, K.J., Black, C.J.J., Singleton, M., Sorbie, K.S., 2006.Low Salinity Oil Recovery—An Experimental Investigation, SCA2006-36.
5. Lager, A., Webb, K., Black, C.J., Singleton, M., Sorbie, K., 2008. Low salinity oil recovery—an experimental investigation. Petrophysics 49, 1.
6. Nasralla, R.A., Nasr-El-Din, H. A., 2012b. Double-layer expansion: is it a primary mechanism of improved oil recovery by low-salinity waterflooding? In: SPE Improved Oil Recovery Symposium, Society of Petroleum Engineers, Tulsa, Oklahoma, USA
7. Fjelde, I., Asen, S.M., Omekeh, A.V., 2012. Low salinity water flooding experiments and interpretation by simulations. In: SPE Improved Oil Recovery Symposium, Society of Petroleum Engineers, Tulsa, Oklahoma, USA
8. Shalabi, E.W. A., Sepehrnoori, K., Delshad, M., 2014. Mechanisms behind low salinity water injection in carbonate reservoirs. Fuel 121 (0), 11–19.
9. Sohrabi, M., Emadi A., 2013. Visual investigation of oil recovery by low salinity water injection: formation of water micro-dispersions and wettability alteration. In SPE Annual Technical Conference and Exhibtion, 2013, Society of Petroleum Engineers, New Orleans, Louisiana, USA.

10. Gao, Y.; Zhang, R. C.; Lv, W. F.; Liu, Q. J.; Wang, X. L.; Sun, P. C.; Winter, H. H.; Xue, G., J. Phys. Chem. C 2014, 118 (10), 5606-5614.
11. Zhang, R. C.; Yan, T. Z.; Lechner, B. D.; Schroter, K.; Liang, Y.; Li, B. H.; Furtado, F.; Sun, P. C.; Saalwachter, K. Heterogeneity, Macromolecules 2013, 46, 1841−1850.
12. Rhim, W. K.; Pines, A.; Waugh, J. S., Phys. Rev. B 1971, 3 (3), 684.
13. Fechete, R.; Demco, D. E.; Blumich, B., J. Chem. Phys. 2003, 118 (5), 2411-2421.
14. Mauri, M.; Thomann, Y.; Schneider, H.; Saalwachter, K., Solid State Nucl. Magn. Reson. 2008, 34 (1-2), 125-141.

ANALYZING RETENTION VIA PARTICLE MOBILITY COREFLOODING

Katherine R. Aurand, Victoria Flatås and Reidun Cecilie Aadland
Norwegian University of Science and Technology (NTNU)

This paper was prepared for presentation at the International Symposium of the Society of Core Analysts held in Snowmass, Colorado, USA, 21-26 August 2016

ABSTRACT

This paper presents a way to screen for particle retention through a core plug. Various injection rates were tested on two core plugs of different lengths to achieve base values for final saturation, differential pressure profiles, and breakthrough times. Berea sandstone cores and synthetic North Sea water were used for these tests. Final saturations were around 60% for all cores. Differential pressure profiles slightly increased throughout the duration of the core flooding tests for all scenarios except the lowest injection rate.

INTRODUCTION

As reservoir engineers develop new particles for enhanced oil recovery (EOR), certain screening criteria must be developed to determine the feasibility and potential of injecting these particles into petroleum reservoirs. If the particles have not been previously injected into reservoirs, a study should assess whether or not injection would lead to particle build-up on the rock grains, thereby causing permeability impairment and ultimately reservoir damage. The mass of the particles retained in the core can be divided into two groups: particles adhered to the solid surfaces and particles suspended in the liquid in pores spaces [1]. The objective of the method proposed in this paper is to determine the mass of the particles adhered to the solids surfaces.

The vertically-oriented particle mobility coreflooding (PMC) procedure has been developed as part of a screening program to evaluate new particles. The procedure is designed for those who have added EOR particles to an aqueous injection fluid and need to determine the particle mobility through the reservoir. Particle concentration analysis conducted on the effluent can reveal the retention of the particles in the porous media via mass balance. Retention will be primarily a result of adsorption onto rock grains if the particle diameter is smaller than the pore throat. Therefore, this procedure should be conducted after stability tests have confirmed that the particles do not aggregate during the course of the PMC tests.

The PMC tests are conducted with initially unsaturated cores. This is to mitigate the effects of diffusion on the effluent concentration. When the core is initially saturated with the base aqueous fluid prior to injection of the particle-enriched fluid, diffusion can occur into zones of flow stagnation (figure 1a). These zones occur when a pore has an opening

but not an exit. The concentration gradient at the interface between the flowing phase and the zone of stagnation causes the particle diffusion [2]. Mechanical dispersion as a result of velocity differences at the interface will result in additional particle loss to the dead-end pore [2]. However, mechanical dispersion is weaker perpendicular to the flow path, so transverse dispersion is dominated by particle diffusion until very high velocity values are reached [3].

The diffusion process would dilute the number of particles in the effluent concentration, making it difficult to determine what percentage of the lost concentration is due to diffusion into dead ends and what is due to adsorption onto solid surfaces. The core could initially be saturated with the same concentration of the EOR particle fluid which will be flooded, but then adsorption would begin prior to the flooding, making it difficult to get an accurate picture of how the adsorption capacity is changing over time due to fluid injection. This is why the core is initially unsaturated (figure 1b).

The coreholder is mounted vertically to maximize the saturation potential. When a dry core is flooded horizontally, there is a large area that remains unsaturated, especially at the outlet region (figure 2a). The vertically orientation utilizes the natural gravity segregation of the air and aqueous fluid to better saturate from the bottom and upwards (figure 2b). Pore geometry (and thereby effective porosity and permeability) plays a large role in the final saturation. The impact of the core orientation will be more pronounced with longer cores than with shorter cores and with lower flow rates than with higher flow rates. Higher flow rates will also result in a smaller value of particle retention as demonstrated with polystyrene colloids in unsaturated porous media [4] and with silica nanoparticles in saturated porous media [1]. The primary reason is because higher flow rates decrease the residence time of the particles in the porous media, giving them less time to react with the system [1].

PROCEDURE

In the PMC procedure, a dry core plug was mounted vertically in a core holder. A sleeve pressure of 20 bars was applied. The EOR fluid was injected from the bottom of the core, and effluent samples were collected from the outlet at the top (figure 3). Particle mobility and retention could be calculated by evaluating inlet and effluent particle concentration. The fluid breakthrough time, differential pressure, final saturation, and pre- and post-flooding porosity and permeability of the core were evaluated. Cores can first be tested with the aqueous dispersion fluid, rinsed and dried, and then retested with the EOR particle additive for comparison. It is important to fasten the core holder, pressure gage, reservoir, and all flow lines so that results from different tests can be confidently compared.

During the test, pressure readings were taken and samples were collected every pore volume (for the 4.5 cm core) and every half pore volume (10 cm core) for further analysis. When using a new particle-enriched EOR fluid, these effluent samples are what can be analysed for changes in pH, particle concentration, particle size distribution, etc. It

is then recommended that effluent samples are taken at higher resolutions, for example every ¼ PV, to better characterize particle mobility.

Each core was flooded such that five pore volumes of samples could be collected, resulting in six pore volumes being injected into the core. Immediately after the fifth pore volume had been collected, the core was taken out of the apparatus and weighed to determine the final saturation. The core was then placed in a soxhlet filled with methanol and rinsed for at least seven hours. It was then dried in an oven at 60 C for at least three days. Helium porosimeter and air permeameter measurements were taken after each flood. The core flooding procedure was performed using injection rates of 0.3 ml/min, 1.0 ml/min, 2.0 ml/min, and 3.0 ml/min for the 4.5 cm long core and using 1.0 ml/min and 2.0 ml/min for the 10 cm core.

MATERIALS

Two Berea sandstone cores drilled from the same block were used in this study. Both had a diameter of 3.81 cm (1.5 in.). Core 1 had a length of 4.5 cm (1.77 in.), and core 2 had a length of 10 cm (3.94 in.). Core 1 had an initial porosity of 16% and permeability of 275 mD. Core 2 had an initial porosity of 16% and permeability of 400 mD. Porosity was measured with a helium porosimeter, and permeability was measured with air and corrected by use of the Klinkenberg effect.

Synthetic North Sea water was mixed and used for the injection fluid. It was a mixture of deionized water, sodium chloride, sodium hydrogen carbonate, sodium sulfate, calcium chloride, magnesium chloride, strontium chloride, and potassium chloride. This resulted in a salinity of 3.53 wt% and a viscosity of 1.025 cP.

RESULTS

The differential pressure profiles and breakthrough times for each core flood are presented in figure 4. As expected, breakthrough times were quite consistent across all core floods. Differential pressure steeply increased at the beginning of the core flood, but then flattened out after breakthrough. For all injection scenarios except the 0.3 ml/min rate, the differential pressure continued to increase in a pattern such that there would be a plateau followed by a quick jump in pressure before plateauing again. This suggests that the core saturation is still increasing throughout water injection. The plateau regions could be where saturation has reached a pseudo-equilibrium state, and then the quick rises could be where the injected water has suddenly penetrated a previously empty zone.

The final saturation of the 4.5 cm core varied from 56 to 59%. There was no visible trend with end saturation vs. flow rate, and all the results are within the standard error. The final saturation of the 10cm core floods were 62% and 64% for the 1 ml/min and 2 ml/min floods respectively. Porosity and permeability values did not vary much between floods.

CONCLUSIONS

- This method can be useful for calculating the retention capacity of a core plug when flooded with a new particle-enriched EOR fluid.
- This method results in about a 60% final saturation. This will vary slightly with core length and injection rate. Particle retention would also alter this value when EOR fluids are injected.
- For all injection rates except 0.3 ml/min, the differential pressure profile continued to increase slightly. This suggests that the core saturation is still slightly increasing throughout the duration of the core flooding tests for all of the other scenarios.

ACKNOWLEDGEMENTS

The authors would like to thank master students Tonje Bjerga and Erik N. Pollen and engineer Roger Overå for lab assistance.

REFERENCES

1. Zhang, T., Murphy, M.J., Yu, H., Bagaria, H.G., Yoon, K.Y., Neilson, B.M., Bielawski, C.W., Johnston, K.P., Huh, C., Bryant, S.L., "Investigation of nanoparticle adsorption during transport in porous media", SPE Journal, (2015) **20**, 4, SPE-166346-PA p.

2. Sheng, J.J., "Chapter 2: Transport of Chemicals and Fractional Flow Curve Analysis" in *Modern Chemical Enhanced Oil Recovery*: *Theory and Practice*, Elsevier, Burlington, MA, (2011), p. 13-50.

3. Freeze, R.A., and Cherry, J.A., *Groundwater*, Prentice-Hall, Englewood Cliffs, NJ, (1979), 604 p.

4. Knappenberger, T., Flury, M., Mattson, E.D., and Harsh, J.B., "Does Water Content or Flow Rate Control Colloid Transport in Unsaturated Porous Media?", *Environmental Science and Technology*, (2014) **48**, 7, p. 3791-3799.

FIGURES

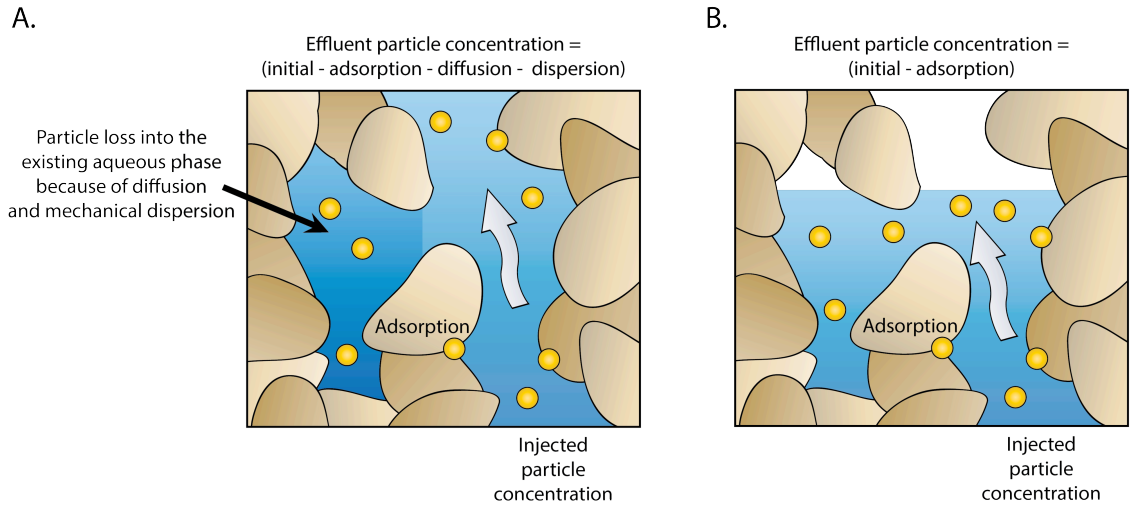

Figure 1. Conceptual drawing of how a core initially saturated with an aqueous fluid will affect the effluent concentration vs. a core initially unsaturated. **A)** When a core is initially saturated with an aqueous fluid prior to EOR fluid injection, particle diffusion and mechanical dispersion will occur, diluting the overall concentration. When the effluent sample is taken, it is impossible to determine how much of the missing concentration is from particle adsorption to the rock grains and how much is from particle loss into the aqueous fluid. **B)** When the EOR fluid is injected into a dry core, the difference in the effluent concentration from the injected concentration is solely adsorption. This figure assumes no mechanical entrapment is occurring.

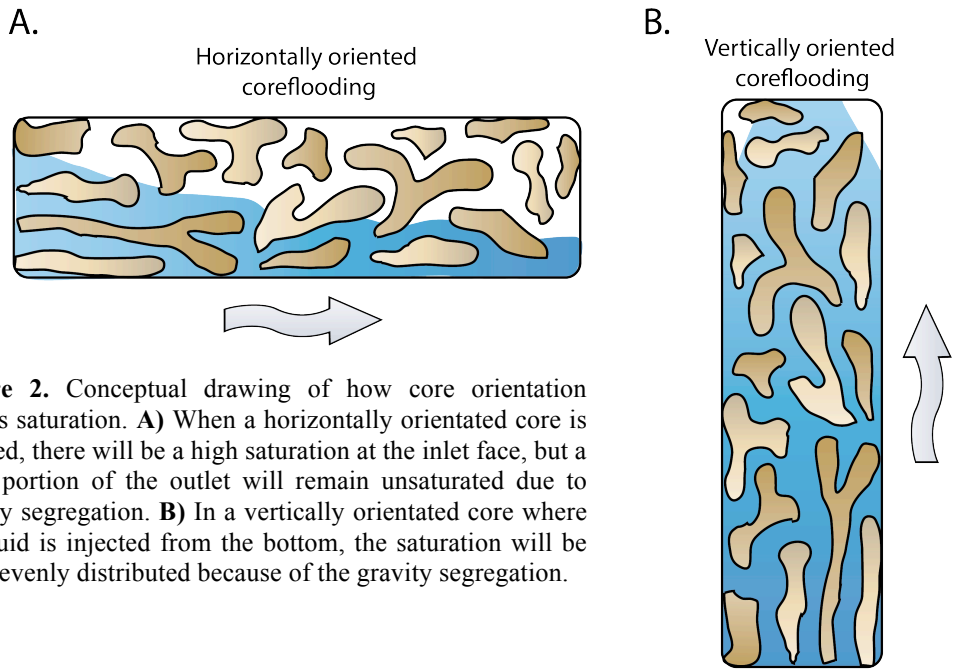

Figure 2. Conceptual drawing of how core orientation affects saturation. **A)** When a horizontally orientated core is flooded, there will be a high saturation at the inlet face, but a large portion of the outlet will remain unsaturated due to gravity segregation. **B)** In a vertically orientated core where the fluid is injected from the bottom, the saturation will be more evenly distributed because of the gravity segregation.

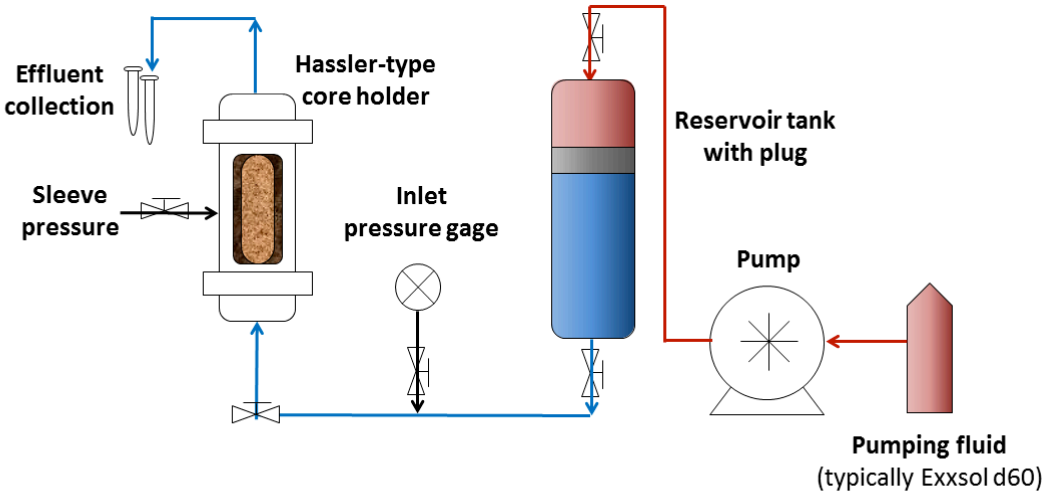

Figure 3. Schematic of the particle mobility coreflooding apparatus. The core holder, pressure gage and reservoir tank are fixed to a stand such that they have the same position for every test. The reservoir plug is not necessary if the pumping fluid and injection fluid are immiscible and it has been proved that the particles do not adhere to the liquid-liquid interface. Half of the experiments were run with the plug and half were run without. It did not affect the results because NSW and the pumping fluid are immiscible.

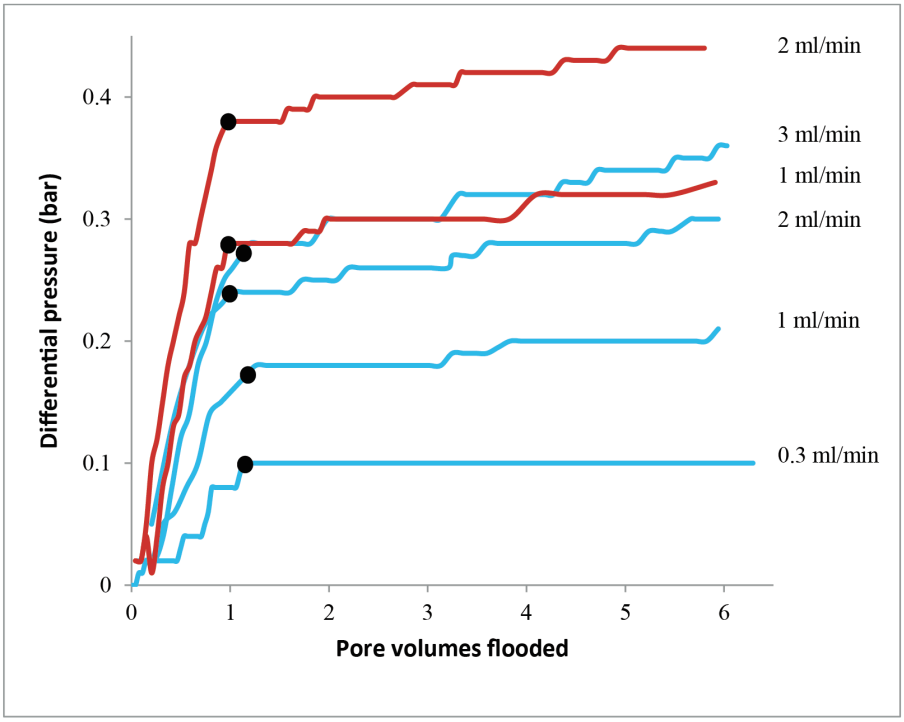

Figure 4. Differential pressure vs. pore volumes flooded for the 4.5 cm core **(blue lines)** and the 10 cm core **(red lines)** for various flow rates. Water breakthrough at the outlet is shown by black dots on the graph.

Fractal dimension of pore space in carbonate samples from Tushka Area (Egypt)

Andreas Weller [1], Yi Ding [2], Zeyu Zhang [3], Mohamed Kassab [4], Matthias Halisch [5]

[1] Technische Universität Clausthal, Institut für Geophysik, Arnold-Sommerfeld-Straße 1, D-38678, Clausthal-Zellerfeld, Germany
[2] Georg-August-Universität Göttingen, Geowissenschaftliches Zentrum, Germany
[3] Southwest Petroleum University, School of Geoscience and Technology, Chengdu, China
[4] Egyptian Petroleum Research Institute (EPRI), El Zohour Region, Naser City, Cairo, Egypt
[5] Leibniz-Institut für Angewandte Geophysik (LIAG), Stilleweg 2, 30655 Hannover, Germany

This paper was prepared for presentation at the International Symposium of the Society of Core Analysts held in Snowmass, Colorado, USA, 21-26 August 2016

ABSTRACT

The permeability of a porous rock is an intrinsic petrophysical parameter that depends on the geometry of the pore space. The pore radius distribution provides a simplified description of the pore space geometry that can be used to investigate the fractal nature of the pore space or to determine a fractal dimension. The fractal dimension is used to describe the size of geometric objects as a function of resolution. Pore volume and pore surface are typical quantities that increase with higher resolution.

A set of eight Upper Cretaceous carbonate rock samples from the Tushka area in Egypt was used to compare the pore radius distribution that was determined by mercury porosimetry (MP), nuclear magnetic resonance (NMR), and spectral induced polarization (SIP). Additionally, the parameters porosity, permeability, formation factor, and specific internal surface were available. The values of fractal dimension were determined from the pore radius distributions of the different methods. Additionally, the fractal dimension of the internal surface was derived using the effective hydraulic radius and the specific surface area per unit pore volume. The relationships between the fractal dimensions and the effective hydraulic radius are compared.

INTRODUCTION

The microgeometry of pore space in carbonates is much more complicated than that in sandstone due to the existence of biotic constituents such as shells, fossils and corals [1]. Therefore the prediction of permeability of carbonate rocks is always a challenge [2]. An accurate experimental permeability determination requires expensive methods based on the observation of fluid flow through the rock driven by a known pressure gradient.

Alternatively, physical methods that provide insight into the distribution of pore sizes enable permeability prediction using more easily accessible parameters including the fractal dimension.

The pore radius distribution provides a simplified description of the pore space geometry that can be used to investigate the fractal nature of the pore space or to determine a fractal dimension. The fractal dimension is used to describe the size of geometric objects as a function of resolution. Pore volume and pore surface are typical quantities that increase with higher resolution. The study [3] applied fractal dimension to predict the permeability of a set of sandstone samples.

We present here the pore radius distribution determined by mercury porosimetry (MP), nuclear magnetic resonance (NMR), spectral induced polarization (SIP) and specific internal surface of eight Upper Cretaceous carbonate rock samples from the Tushka area in Egypt. The parameters porosity, permeability, formation factor and the specific internal surface were available. The values of fractal dimension were determined from the pore radius distributions of the different methods. The different values were compared.

METHODS AND RESULTS

This study investigates a set of limestone samples taken from seven shallow wells in the Tushka area in south-eastern part of Egypt [4]. The Tushka basin is located in the southern part of Western Desert, approximately 250 km away from Lake Nasser and the Aswan High Dam, between the latitudes 22° 30′-22° 45′ N and longitudes 31° 45′-32° 0′ E. The region is bordered by the Sen EI-Kaddab Eocene limestone plateau to the north, by Nasser Lake to the east, by the Nubian pediplain and the political border between Egypt and Sudan to the south.

We selected eight samples from a larger set [4] for our study. All samples are cylindrical in shape and with a diameter of 25 mm and a length of about 30 mm. The measurements of petrophysical parameters such as grain density, porosity, permeability, and internal surface were performed according to acknowledged procedures. The MP experiments cover a pressure range between 0.004 and 400 MPa. The NMR T2 relaxations times were determined with a MARAN 7 equipment operating at a Larmor frequency of 7.05 MHz at room temperature and ambient pressure. The complex conductivity spectra were acquired in a frequency range between 3 mHz and 100 Hz using an impedance spectrometer with high phase accuracy. The measurements of all samples utilized the same protocols. The reproducibility of the resulting parameters has been checked.

Fractal dimension of the pore space can be characterized by the curve of cumulative volume fraction of the pores versus pore radius. For MP method, the capillary pressure shows an inverse proportionality with the pore radius. For NMR method, the proportionality between the transversal relaxation time and pore radius is used.

For SIP method, we transformed the relaxation time distribution of complex conductivity spectra determined by Debye decomposition [5] into a distribution of pore radii r. We adopt an equation proposed by [6] and applied by [7] for the Stern layer polarization model:

$$r = \sqrt{2\tau D_{(+)}} \tag{1}$$

with τ being the relaxation time and $D_{(+)}$ the diffusion coefficient of the counter-ions in the Stern layer. Originally, this equation describes the relation between the radius of spherical particles in an electrolyte solution and the resulting relaxation time [6]. Though it is questionable whether the radius of spherical grains can be simply replaced by the pore radius, we follow this approach. Additionally, we assume a constant diffusion coefficient $D_{(+)} = 3.8\times10^{-12}$ m²/s as proposed for clayey material [8]. The total chargeability is attributed to the total pore volume. The volume fraction $V_c = V(<r)/V$ is the cumulative volume fraction of pores with radii less than r, which corresponds to the ratio of cumulative intensity to total intensity.

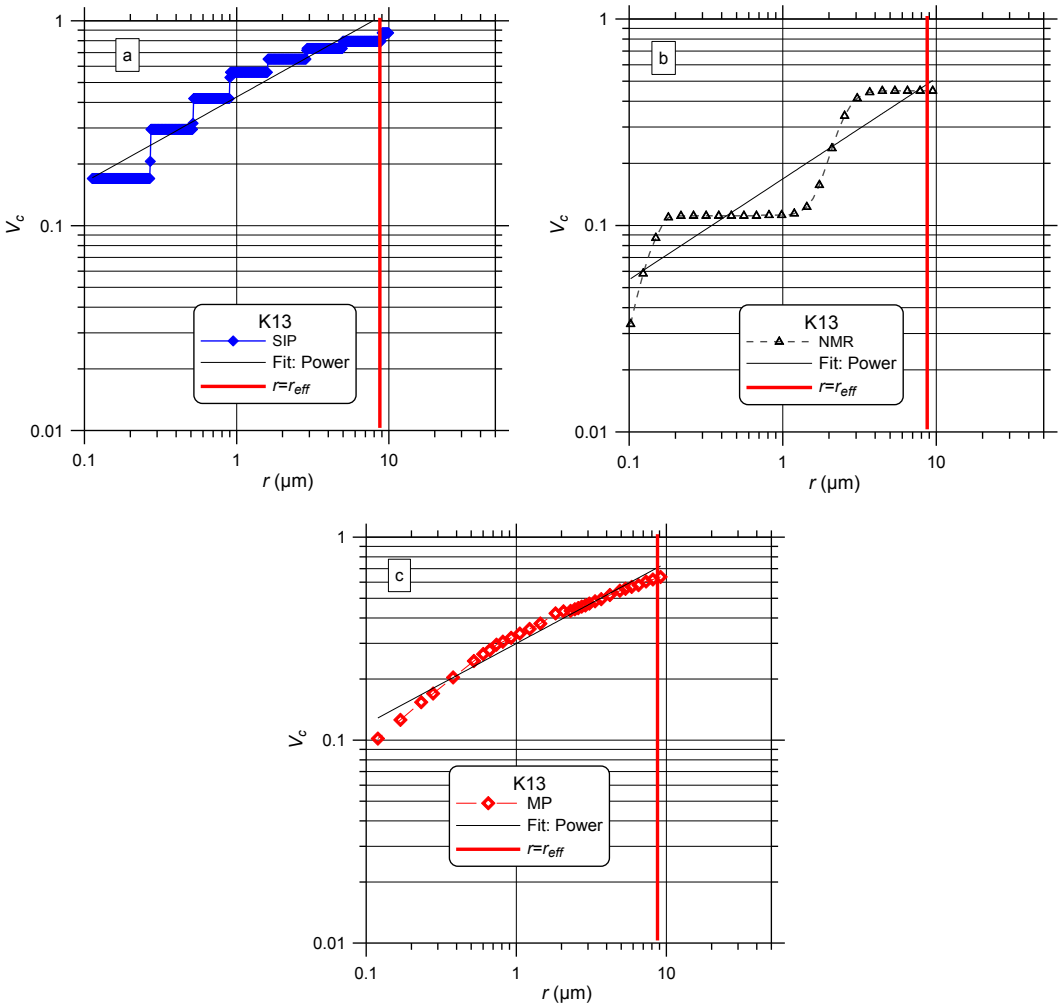

Figure 1: a) The fractal dimension D_{SIP} of sample K13. D_{SIP} is determined from the slope of the linear fitting equation $\log(V_c) = 0.416 \log(r) - 0.857$ ($R^2 = 0.915$) with $D_{SIP} = 3 - 0.416 = 2.584$, b) The fractal dimension D_{NMR} of sample K13 is determined from the slope of the linear fitting equation $\log(V_c) = 0.488 \log(r) - 1.783$ ($R^2 = 0.847$) with $D_{NMR} = 3 - 0.488 = 2.512$. c) The fractal dimension D_{MP} of sample K13 is determined from the slope of the linear fitting equation $\log(V_c) = 0.397 \log(r) - 1.207$ ($R^2 = 0.967$) with $D_{MP} = 3 - 0.397 = 2.603$. The vertical red lines indicate $r = r_{eff} = 8.44$ µm.

The cumulative curve is presented in a double logarithmic plot showing the relation log(V_c) versus log(r). Figure 1 displays the curves from SIP, NMR and MP data for sample K13. In the case of fractal behaviour of the pore volume distribution, the slope s of the fitting line is used to get the fractal dimension $D = 3 - s$. The vertical red lines in Figure 1 mark the effective hydraulic radius, which has been determined from permeability k and formation factor F:

$$r_{eff} = \sqrt{8Fk}\,. \qquad (2)$$

Following a procedure described in [3], the fractal dimension of the internal surface (D_{Spor}) was derived using the effective hydraulic radius and the specific surface area per unit pore volume determined from the nitrogen adsorption method.

Figure 2 displays the relation between pore radii determined at V_c = 0.5 (with $r = r_{50}$) from MP method and r_{eff}. The comparison indicates a good agreement between r_{eff} and r_{50}. The median pore radius r_{50} from MP can be regarded as suitable parameter to estimate the effective hydraulic radius r_{eff}. This estimate can be used if the values of permeability and formation factor are not available for the rock samples.

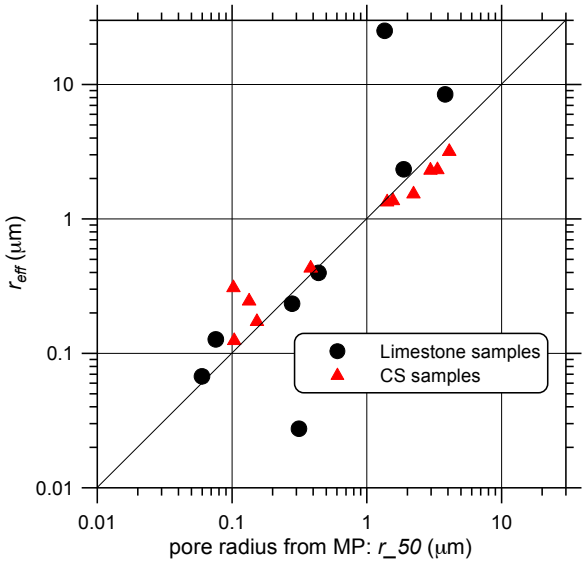

Figure 2: Relation between r_{eff} and r_{50} for the limestone samples in this study and 11 sandstone samples (CS) in [3]. The diagonal line indicates r_{eff}=r_{50}.

For the carbonate samples with effective pore radius r_{eff} > 1 µm, the V_c-r curves of the methods NMR, MP and SIP show similar characteristics. The best agreement exists for sample P3 with all cumulative pore radii curves indicating the steepest slope close to r_{eff} as shown in Figure 3a. The smallest effective pore radius was determined for sample K34 with r_{eff} = 0.028 µm. A shift between the different curves becomes visible in Figure 3b. The curves of MP and SIP indicate much larger pore radii. The curve of SIP can be shifted to smaller pore radii if a lower value of the diffusion coefficient is used in equation 2. But it should be noted that a shift does not affect the slope of the curve and the resulting fractal dimension.

Figure 4a displays the relation between the effective pore radius r_{eff} and the fractal dimension derived from NMR, MP, SIP and the specific internal surface. The values of fractal dimensions D_{NMR}, D_{MP}, and D_{SIP} indicate a slight decrease with rising effective pore radius, while the fractal dimension D_{spor} shows an increasing trend as the effective pore radius rises.

Figure 4b displays the comparison between the fractal dimension D_{SIP} with the fractal dimension derived from MP and NMR. In order to enable an unbiased comparison, the same r-range of 0.1 to 10 µm was applied for all methods. The fractal dimension derived from SIP and NMR are close to each other. The pore radius distribution of MP results in slightly larger values of fractal dimension.

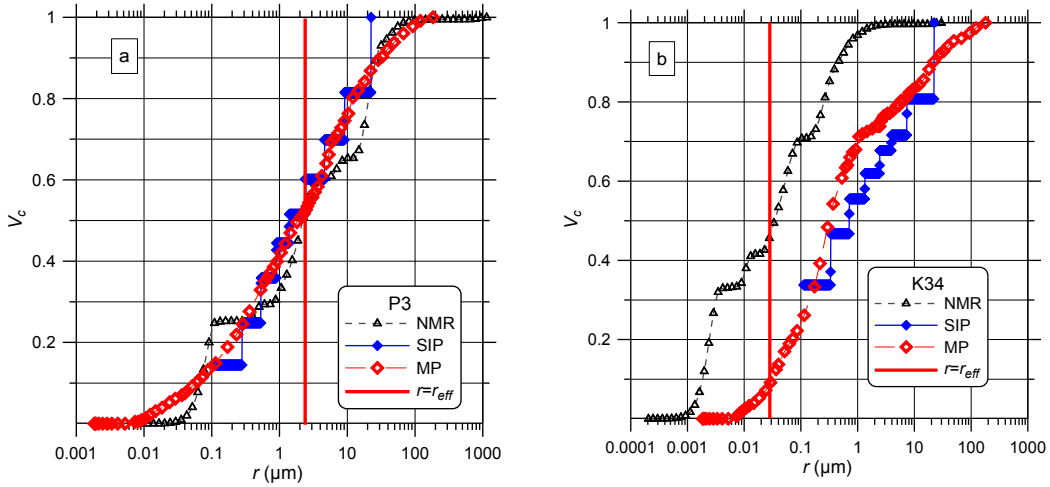

Figure 3: a)The comparison of V_c-r curves determined from NMR, MP, and SIP for sample P3. The vertical red line indicates $r = r_{eff} = 2.34$ µm. b) The comparison of V_c-r curves determined from NMR, MP, and SIP for sample K34. The vertical red line indicates $r = r_{eff} = 0.028$ µm.

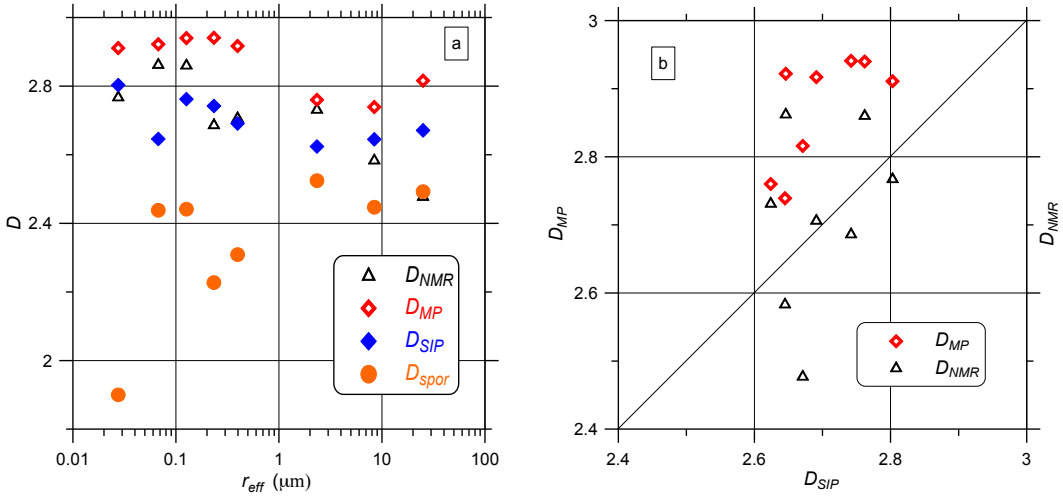

Figure 4: a) Relation between effective pore radius and fractal dimension determined from NMR, MP, SIP and nitrogen adsorption method. b) Comparison of fractal dimensions determined from NMR, MP and SIP. The diagonal line indicates $D_{SIP} = D_{NMR}$ and $D_{SIP} = D_{MP}$.

CONCLUSION

Our study demonstrates that the relaxation time distribution of complex conductivity spectra can be used to derive the fractal dimension. The resulting values, which vary in a range between 2.62 and 2.80, are comparable with those derived from NMR and MP for a set of eight limestone samples. The fractal dimension that is determined from the specific internal surface and the effective hydraulic radius indicates lower values in a range between 1.90 and 2.52. The comparison of fractal dimension determined by the different methods indicates a differentiation into "surface dimension" and "volume dimension". The fractal dimension resulting from NMR, SIP, and MP reflects a volume dimension, while the fractal dimension determined from the specific internal surface data represents the roughness of pore surface.

The fractal dimension that describes pore space geometry as a function of resolution is a useful parameter for upscaling and downscaling pore size for different applications.

ACKNOWLEDGEMENTS

The authors thank Sabine Kruschwitz, Wolfgang Debschütz, Mostafa Behery and Sven Nordsiek for supporting the measurements and data processing of this study.

REFERENCES

1. Clark, B., and R. Kleinberg, 2002, *Physics in oil exploration*: Physics Today, 55, 48–53.
2. Westphal, H., I. Surholt, C. Kiesl, H. F. Thern, and T. Kruspe, 2005, *NMR measurements in carbonate rocks: problems and an approach to a solution:* Pure and Applied Geophysics, 162, 3, 549–570.
3. Zhang, Z., and A. Weller, 2014, *Fractal dimension of pore-space geometry of an Eocene sandstone formation*: Geophysics, 79, 6, D377-D387. doi: 10.1190/geo2014-0143.1.
4. Öner, Ü., A. Weller, C.-D. Sattler, and M. A. Kassab, 2016, *Petrographic and petrophysical investigation on carbonate samples (Upper Cretaceous) from the Tushka Area (Egypt) with special focus on the effective pore radius*: Arabian Journal of Geosciences 9:229. doi: 10.1007/s12517-015-2212-x.
5. Nordsiek, S., and A. Weller, 2008, *A new approach to fitting induced-polarization spectra*: Geophysics, 73, No. 6, F235-F245, doi: 10.1190/1.2987412.
6. Schwarz, G., 1962, *A theory of the low-frequency dielectric dispersion of colloidal particles in electrolyte solution*: Journal of Physical Chemistry, 66, 2636-2642, doi: 10.1021/j100818a067.
7. Revil, A., K. Koch, and K. Holliger, 2012, *Is it the grain size or the characteristic pore size that controls the induced polarization relaxation time of clean sands and sandstones?*: Water Resources Research, 48, W05602, doi:10.1029/2011WR011561.
8. Revil, A., 2013, *Effective conductivity and permittivity of unsaturated porous materials in the frequency range 1 mHz-1GHz*: Water Resources Research, 49, 306-327, doi: 10.1029/2012WR012700.

EFFECT OF BEDDING PLANES ON ROCK MECHANICAL PROPERTIES ANISOTROPY OF SANDSTONE FOR GEOMECHANICAL MODELING

Dee Moronkeji, Richard Shouse and Umesh Prasad
Baker Hughes, Houston, TX, USA

This paper was prepared for presentation at the International Symposium of the Society of Core Analysts held in Snowmass, Colorado, USA, 21-26 August 2016

ABSTRACT

Side wall cores have become a routine coring operation in conventional and unconventional formations. The recent departure from drilling vertical wells to directional drilling of wellbores in unconventional wells has led to side wall cores that are acquired in different directions to bedding planes. Studies have shown that rock mechanical properties can be affected by bedding planes. Consequently, side wall cores retrieved from unconventional wells that are used for rock mechanical properties (RMP) estimation for geomechanical modelling can lead to unrealistic models, depending on the coring direction.

The main purpose of this study is to examine the effect of bedding planes on RMP, especially from side wall cores. Depending on the well inclination to the bedding plane, core plugs are taken along three orthogonal directions and at intermediate orientation with respect to bedding and tested at unconfined and confined conditions to obtain unconfined compressive strength (UCS) and confined compressive strength (CCS) for sandstone samples with bedding planes.

This study is an effort to characterize strength anisotropy using orthotropic considerations and to examine the source of anisotropy and determine if it is stress induced. Berea sandstone with bedding planes was selected to perform a series of UCS and CCS tests. The rock strength was observed to be highest in the plugs drilled perpendicular to bedding (ZZ) and consistently lowest in the horizontal plugs drilled parallel across the bedding (YY) compared to the horizontal plugs drilled parallel along (XX) the beddings. The difference in the rock strength measured in the plugs parallel along and across the bedding could be due to the pre-existing stress anisotropy and can be a clue to the horizontal stress orientation in bedded formations as result of depositional environment and existing tectonic stresses.

This knowledge will help in planning coring operations, completion, and production processes and better sand production prediction in bedded formation with significant bedding plane in which side wall cores are taken that can significantly alter the RMP and geomechanical modeling predictions.

INTRODUCTION

Rock mechanical properties are key parameters in geomechanical models and their subsequent use to plan and design drilling, evaluation, completion, and production

processes. RMP such as elastic properties of Young's modulus (EMOD) and Poisson's ratio (PR) and UCS or CCS are regularly used for geomechanical investigation, and assume rocks to be continuous, homogenous, linearly elastic and isotropic. Traditionally, isotropic considerations can be assumed based on the level of variation in RMP of elastic and peak strength beyond an accepted threshold level (say 5% or 10%). However, if the variation is beyond the threshold level, an anisotropic consideration has to be applied, originating from vertical transverse isotropy (VTI) or orthotropic considerations. Luckily, the recent technological advancement of dipole or quadrupole acoustics has enabled the industry to characterize the VTI anisotropic behavior from logs together with laboratory-based measurements to supplement or calibrate log measurements. Orthotropic considerations have also been tried based on extensive lab-based measurements, but their use has been limited because they require extensive lab testing to supplement the log measurements.

Studies have shown that RMP can be affected significantly due to intrinsic features such as laminations, foliations, bedding planes or extrinsic stressed-induced anisotropy. Due care should be taken to utilize the typical rock mechanical behavior in deciding drilling trajectory, quantifying suitable mud weight windows for mitigating wellbore stability issues, or planning and design of perforation or hydraulic fracturing.

The effect of bedding planes as a source of intrinsic properties on strength and elastic properties on sedimentary rocks carried out on vertical, inclined, or horizontal plugs are discussed in detail by Jaeger and Cook [1], and Zoback [2]. Other earlier work on shale, sandstone and limestone was performed by Chenevert, M. and Gatlin, C. [3] and McLamore, R. and Gray, K. [4] on slate. However, very limited work has been done to characterize full anisotropy, especially in visually isotropic looking sandstone. Some study on anisotropy in sandstone was performed by Holt, R.M et al. [5] and Yasar [6].

TESTING PROGRAM

A large number of core plugs were taken according to the direction of bedding plane and loading direction (plug axis). The plugs were drilled from the same Berea sandstone block to examine if the RMP would be different (see Figure 1) and grouped according to the orientation of the loading direction with respect to the bedding plane.

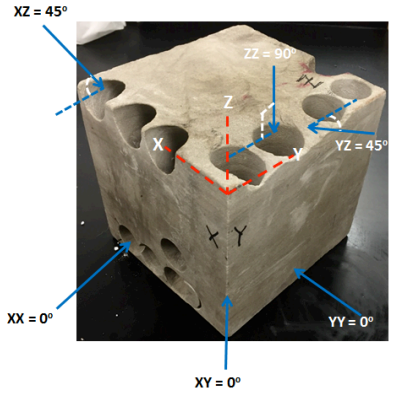

Figure 1: Berea Sandstone Block with Drilling Directions with Respect to Bedding Plane

The ZZ axis (90^o) is perpendicular to horizontal bedding, XX, YY and XY (0^o), are parallel along (X-axis), across (Y-axis) and inclined (45°) on the horizontal plane to the bedding, respectively, XZ and YZ (45^o) are inclined along and across the bedding, respectively.
The bulk density of all plugs was measured. Mineralogical and microstructural properties were measured by X-ray diffraction (XRD) and scanning electron microscope (SEM) on selected samples to see the samples mineralogical composition homogeneity. UCS and CCS tests at 5500 psi confining pressure were carried out using a TerraTek 880 triaxial load frame with an MTS servo-digital control system, confining pressure intensifier, hydraulic service manifold, and a Silent-flow hydraulic power unit. The tests met the ASTM standard D4543-04 [7].
Axial and radial strain measurements were performed using linear variable displacement transducers and a circumferential extensometer, respectively, at a circumferential strain rate of 1.69×10^{-5} cm/sec. (0.0004-in./min.) for all tests.

RESULTS

The SEM analysis on the Berea sandstone shows that there are pore-filling vermiculites of kaolinite and corroded sodium feldspar. The vermiculites, confirmed by using XRD, as 4% kaolinite with the Berea sandstone predominantly composed of 88% quartz minerals. The XRD result is shown in Table 1 and the SEM plots are shown in Figure 2.
The results of the triaxial testing at UCS and CSS are shown in Table 1 for all orientations with a standard deviation of one. The perpendicular sample has the highest peak strength in UCS and CCS tests than the parallel or inclined samples, showing that strength anisotropy is also present under confining conditions. This was also observed by Holt, R. M., et al. [5] and Zetian Zhang et al. [8] as it is more difficult for the failure plane to develop and cross through (perpendicular) the bedding plane than it is to develop along (parallel) the bedding plane as shown by the axial strain at failure in Table 1. The standard deviation shows that statistically the errors were 8% and 4% on the vertical and horizontal plugs with an average UCS of 48 MPa and 38 MPa in ZZ and XX, respectively, except in the YY (15% difference), where the error was even lower in CCS with 2% and 1%, respectively, for the ZZ and XX direction, showing good testing repeatability.
Figure 3 for the UCS and CCS tests, respectively, show that the YY samples peak strength, with average values of 33 and 186 MPa, is lower than the 38 and 191 MPa in the XX. This shows that strength anisotropy exists in bedded Berea sandstone.
It can be assumed to be either a VTI or orthotropic rock. If we ignore the outlier from the XX and YY data sets and take only two concurrent values, then it further shows that YY cores are weakest. UCS, CCS and EMOD at 0 psi and 5500 psi show that this can only be explained that there is one plane of symmetry, so the pre-existing stress condition must be the cause of the weaker plane along YY. The weakest YY is also evident from CCS and EMOD data. Figure 4 show that EMOD increases linearly with the UCS at each plug orientation to bedding, and as a whole with a high linear regression correlation (R^2 of 0.85). A similar observation is also seen for the CCS. The effect of bedding planes on EMOD shown in Figure 5 for UCS and CCS were higher in the perpendicular direction to

bedding (90^o) compared to the other directions. This was also observed by Zetian Zhang et al. [8] in their testing.
Figure 6 shows there are no distinct patterns of the shear plane failure based on the loading direction with respect to the bedding orientation; all samples show a clear shear failure plane. A typical stress-strain plot is shown in Figure 7 at three directions (ZZ, XX and YY) with respect to bedding. The plot clearly shows that the CCS is clearly lower on the YY than in the other directions.

CONCLUSION

The testing results show that it is possible that the stress anisotropy and bedding direction of oriented cores can indicate the direction of the principal stresses due to
pre-existing stress orientations. The maximum stress direction caused ZZ to be the strongest. Further, if we ignore the outlier, YY was the weakest. This could only be explained by the influence of intermediate or least principal stress influence in alignment of foliation or microcracks.
The stress anisotropy inferred by the testing in the Berea sandstone clearly shows that anisotropic consideration should be used in bedded sandstones formation as indicated by the results because bedded sandstone formation are more stress sensitive.
Future testing will include conducting P&S wave measurements, to see if the non-destructive testing can also validate the finding in this testing program, and applying this methodology to a wellbore with known stress orientation. Finally, the data obtained will help in planning coring operations in the bedded formation because the strength anisotropy measured can be a clue to the in-situ stress orientation and help in building realistic geomechanical model in these types of formations.

ACKNOWLEDGEMENTS

The authors would like to thank Baker Hughes for the permission to publish the results. We also thank Amber Koch and BJ Davis for the XRD & SEM testing and interpretation.

REFERENCES

1. T Jaeger, JC & NGW Cook; 1979. Fundamentals of Rock Mechanics. Chapman & Hall.
2. Zoback, M.D.; 2008. Reservoir Geomechanics, Cambridge University Press.
3. Chenevert, M.E. and C. Gatlin. 1964. Mechanical anisotropies of laminated sedimentary rocks. 39th Annual SPE Meeting, Houston, TX., Oct. 11-14. 67–77.
4. McLamore, R.T. and K.E. Gray. 1967. A Strength Criterion for Anisotropic Rocks Based Upon Experimental Observations. 96th Annual AIME Meeting, Los Angeles, California, Feb. 19-23. SPE 1721.
5. Holt, R. M., et al., 1987. Anisotropic Mechanical Properties of Weakly Consolidated Sandstone. ISRM Congress 177.
6. Yasar, E. 2001. Failure and Failure Theories for Anisotropic Rocks. 17th international Mining Congress and Exhibition of Turkey- IMCET 2001.
7. ASTM, 2004. Standard Practices for Preparing Rock Core Specimens & Determining Dimensional and Shape Tolerances. D4543-04. Annual Book of ASTM Standards.

8. Zetian Zhang et al. (2014). Effect of Bedding Structure on Mechanical Property of Coal. *Advances in Materials Science and Engineering, Volume 2014, Article 952703.*

Table 1. Berea Sandstone UCS and CCS Triaxial Test Results and XRD Analysis

Sample ID	Sample Orientation		D	L	Den	UCS	EMOD	PR	Strain corresponding to Peak Stress (in)			STDEV UCS	STDEV EMOD	STDEV POIS	XRD Results	Sample AE-4	XRD Mineral
	X-Y-Z	Deg	in	in	g/cc	MPa	GPa		Axial Strain	Circum. strain	Volum. strain	MPa	GPa			%	
UCS																	
BV-5	ZZ	90	1.00	1.99	2.17	44.0	11.2	0.25	0.0049	-0.0019	0.0010	3.8	0.7	0.03		88	Quartz
BV-2	ZZ	90	0.99	1.96	2.17	47.5	11.3	0.21	0.0050	-0.0014	0.0022						
BV-3	ZZ	90	0.98	1.95	2.20	51.6	12.4	0.26	0.0059	-0.0021	0.0017						
Average			**0.99**	**1.96**	**2.18**	**47.7**	**11.6**	**0.24**	**0.0052**	**-0.0018**	**0.0016**					0	Albite
HC-6	XX	0	0.98	1.96	2.21	36.6	10.0	0.28	0.0042	-0.0022	-0.0002	1.5	0.6	0.05			
HC-3	XX	0	1.00	1.97	2.19	37.9	11.1	0.30	0.0040	-0.0019	0.0002						
HC-2	XX	0	0.99	1.98	2.18	39.6	10.9	0.37	0.0041	-0.0029	-0.0017						
Average			**0.99**	**1.97**	**2.20**	**38.0**	**10.7**	**0.32**	**0.0041**	**-0.0023**	**-0.0006**					2	Plagioclase-Feldspar
HB-4	YY	0	0.99	2.01	2.12	27.2	7.6	0.19	0.0047	-0.0028	-0.0008	4.9	1.2	0.05			
HB-2	YY	0	0.99	1.90	2.11	34.5	9.4	0.28	0.0047	-0.0024	0.0000						
HB-6	YY	0	1.00	2.03	2.17	36.6	10.0	0.27	0.0045	-0.0024	-0.0004						
Average			**0.99**	**1.98**	**2.13**	**32.7**	**9.0**	**0.25**	**0.0046**	**-0.0025**	**-0.0004**					3	Potassium-Feldspar
ID-1	XY	0	1.00	1.95	2.17	36.7	10.9	0.29	0.0042	-0.0021	0.0000	2.2	1.0	0.07			
ID-3	XY	0	0.99	1.94	2.16	33.3	9.1	0.34	0.0036	-0.0016	0.0003						
ID-5	XY	0	0.99	2.01	2.16	32.5	9.1	0.20	0.0045	-0.0014	0.0016						
Average			**0.99**	**1.97**	**2.16**	**34.2**	**9.7**	**0.28**	**0.0041**	**-0.0017**	**0.0006**					2	Mica-Illite-Smectite
IC-2	XZ	45	1.00	1.95	2.17	34.9	10.0	0.26	0.0042	-0.0020	0.0002	4.8	0.9	0.02			
IC-1	XZ	45	1.00	2.04	2.15	42.0	11.5	0.26	0.0046	-0.0021	0.0004						
IC-8	XZ	45	0.99	1.96	2.21	44.0	11.6	0.22	0.0051	-0.0014	0.0023						
Average			**1.00**	**1.99**	**2.17**	**40.3**	**11.0**	**0.24**	**0.0046**	**-0.0018**	**0.0010**					0	Chlorite
IB-5	YZ	45	0.99	1.95	2.18	37.1	9.8	0.21	0.0048	-0.0014	0.0020	5.2	1.1	0.03			
IB-1	YZ	45	0.98	1.90	2.15	41.6	10.5	0.25	0.0052	-0.0036	-0.0021						
IB-4	YZ	45	0.99	1.99	2.18	47.5	11.9	0.26	0.0054	-0.0021	0.0011						
Average			**0.99**	**1.95**	**2.17**	**42.0**	**10.7**	**0.24**	**0.0051**	**-0.0024**	**0.0003**					4	Kaolinite
5500 psi Confining																	
BV-4	ZZ	90	1.00	1.97	2.19	191.8	17.5	0.11	0.0114	-0.0015	0.0085	3	1.0	0.02			
BV-6	ZZ	90	1.00	2.04	2.19	192.6	18.2	0.08	0.0122	-0.0039	0.0043						
BV-8	ZZ	90	0.99	1.99	2.22	197.7	19.6	0.13	0.0092	-0.0015	0.0063						
Average			**0.99**	**2.00**	**2.20**	**194.0**	**18.4**	**0.11**	**0.0109**	**-0.0023**	**0.0064**					-	Calcite
HC-8	XX	0	0.99	1.98	2.16	188.6	16.6	0.14	0.0119	-0.0024	0.0071	3	0.4	0.01			
HC-7	XX	0	0.99	1.89	2.18	191.9	16.7	0.13	0.0122	-0.0026	0.0071						
HC-5	XX	0	0.99	1.96	2.24	193.8	17.2	0.15	0.0112	-0.0023	0.0065						
Average			**0.99**	**1.94**	**2.19**	**191.4**	**16.8**	**0.14**	**0.0118**	**-0.0024**	**0.0069**					-	Dolomite
HB-5	YY	0	0.99	1.98	2.19	173.2	16.9	0.11	0.0107	-0.0015	0.0076	11	0.8	0.06			
HB-1	YY	0	0.98	1.92	2.19	188.9	17.0	0.23	0.0119	-0.0021	0.0078						
HB-8	YY	0	0.99	1.83	2.19	194.4	18.4	0.13	0.0106	-0.0020	0.0067						
Average			**0.99**	**1.91**	**2.19**	**185.5**	**17.4**	**0.15**	**0.0110**	**-0.0018**	**0.0074**					0	Anatase
ID-2	XY	0	0.99	1.88	2.14	173.8	17.0	0.12	0.0110	-0.0021	0.0069	1	0.3	0.01			
ID-4	XY	0	0.99	1.95	2.18	175.4	16.5	0.13	0.0116	-0.0022	0.0071						
Average			**0.99**	**1.92**	**2.16**	**174.6**	**16.8**	**0.13**	**0.0113**	**-0.0022**	**0.0070**					0	Apatite
IC-5	XZ	45	1.00	1.96	2.13	185.8	16.9	0.13	0.0113	-0.0021	0.0071	7	0.9	0.01			
IC-6	XZ	45	0.99	1.96	2.17	195.3	18.3	0.11	0.0135	-0.0017	0.0101						
IC-9	XZ	45	0.99	1.96	2.18	199.1	18.6	0.12	0.0120	-0.0018	0.0084						
Average			**0.99**	**1.96**	**2.16**	**193.4**	**17.9**	**0.12**	**0.0123**	**-0.0019**	**0.0085**					0	Halite
IB-3	YZ	45	0.99	2.01	2.20	178.2	18.5	0.11	0.0086	-0.0012	0.0062	12	0.1	0.01			
IB-6	YZ	45	0.99	1.98	2.19	195.4	18.6	0.12	0.0107	-0.0016	0.0075						
Average			**0.99**	**1.99**	**2.19**	**186.8**	**18.6**	**0.12**	**0.0096**	**-0.0014**	**0.0068**					0	Anhydrite

- Trace amount

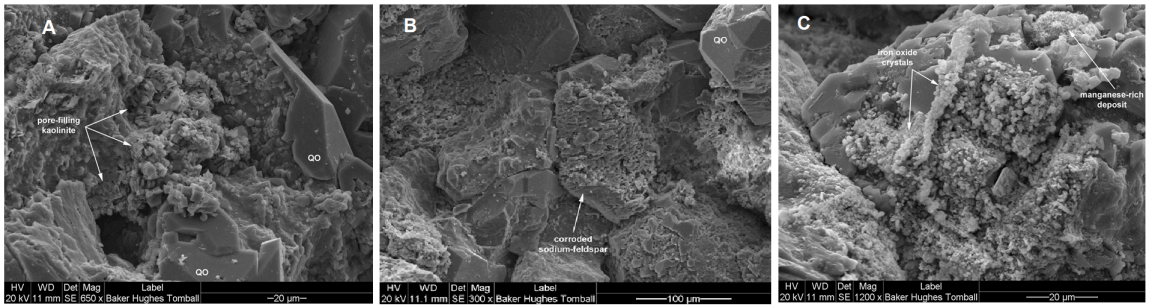

Figure 2: SEM showing (A) Pore-filling vermiculite kaolinite (B) Corroded sodium feldspar and (C) iron oxide crystals and manganese-rich deposit

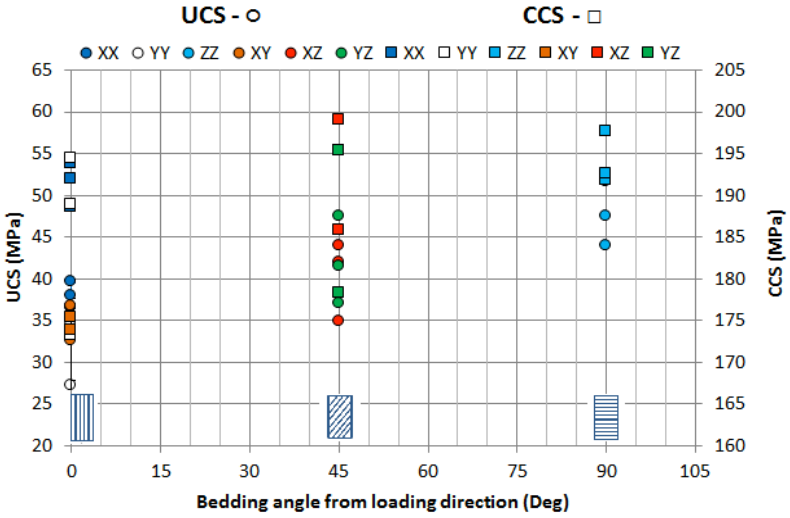

Figure 3: Effect of Bedding Plane on Unconfined and Confined Compressive Strength (UCS and CCS)

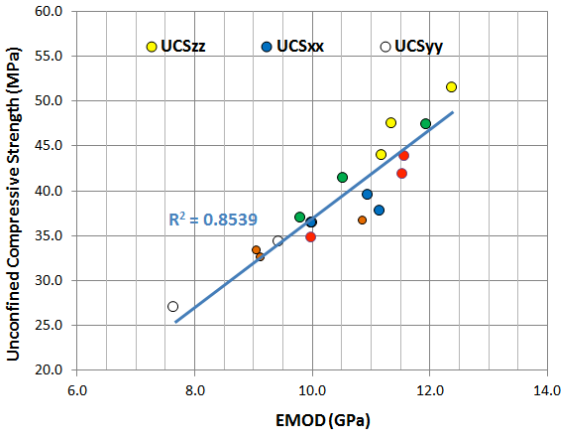

Figure 4: Young's Modulus at Uniaxial Testing Conditions (UCS) with respect to Bedding Plane From Loading Direction

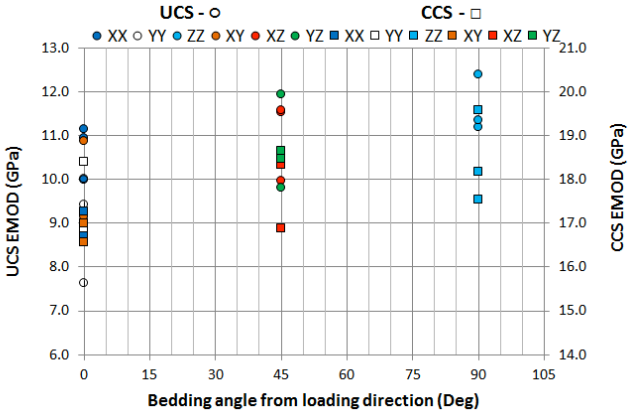

Figure 5: Effect of Bedding Plane on Young's Modulus during Uniaxial and Triaxial Testing Conditions (UCS and CCS)

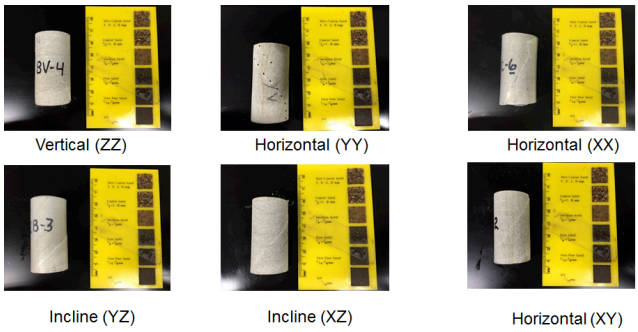

Figure 6: Shear Plane Failure Pattern on Post Triaxial Testing

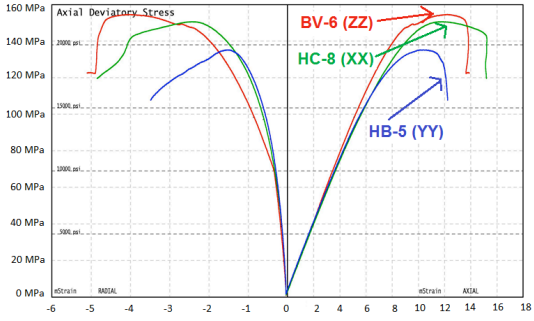

Figure 7: Stress-Strain Plots of Three Different Orientations to Bedding Plane

Fracture stratigraphy: Predicting fractures from small-scale lithologic and textural changes

Laura Kennedy, Jack Beuthin, and Jaime Kostelnik; Weatherford Laboratories

This paper was prepared for presentation at the International Symposium of the Society of Core Analysts held in Snowmass, Colorado, USA, 21-26 August 2016

ABSTRACT

Fracture prediction in hydrocarbon reservoirs remains problematic, despite advances in an understanding of mechanical properties and fracture development. We investigate two structurally and stratigraphically complex cores in the Heath Formation to address the growing need for knowledge of fracture stratigraphy as a tool for fracture prediction. We observed five major stratigraphic units hosting drastically different fracture patterns where changes in fracturing can be correlated to stratigraphic and diagenetic variation down to the microscopic scale.

INTRODUCTION

Natural fractures are necessary for enhanced production of unconventional oil reservoirs. Regardless, natural fractures remain difficult to predict. Gale (2014) states that *"Being able to predict fracture-size ranges, and thereby the natural fracture porosity and permeability enhancement, requires an understanding of the fracture stratigraphy; assumptions about size ranges and mechanical stratigraphy may lead to large errors in estimates of these parameters."* As more vertically heterogeneous reservoirs are targeted for oil and gas production, studies of fracture stratigraphy become more useful for fracture prediction, and thus a production prediction tool within fractured reservoirs. We analyzed two densely fractured cores in the Heath Formation from central Montana to show how geologic data including stratigraphy, mineralogy, fracture characterization, and petrography can be used to resolve and understand fracture stratigraphy.

The Mississippian-age Heath Formation recently has been targeted as a tight-oil play. It is a known source of oil for the overlying Tyler Formation, and has generated over 30 billion barrels of oil (Bottjer, 2014). The Heath is a lithologically variable unit that comprises organic-rich mudstones/marlstone, limestone, dolomite, anhydrite, and coal. Deposition occurred largely in an east-west trending, shallow marine embayment that extended across Montana. Formation-scale heterogeneity is largely a product of shoreline fluctuations and climate change during deposition.

PROCEDURES

Natural Fracture Characterization

Natural fractures were logged in cores from two wells in the Heath Formation, the Reese 1 and the Padre 1A. Fracture data collected included fracture depth (top and bottom),

length, dip-angle, aperture (healed and open), spacing, mode (opening or shearing), shear-sense, termination style, fill mineralogy, and intersection-angle with other fractures, obtained using manual standard fracture measurement techniques. The fractures measured were then separated into fracture domains based on their characteristics and integrated with other geologic data outlined in this report to determine a fracture stratigraphy.

Core Description

The sedimentologic features of each core were logged at a scale of 1 inch = 2 feet. Observations included general lithology, texture, bedding and sedimentary structures, fossil content, and bioturbation intensity. Data were plotted as a graphic log.

Thin Section Analysis

Twelve thin sections were cut from the Reese 1 core and produced using standard techniques. Nine were oversized thin sections and four were standard sized. Thin sections were stained for calcite and ankerite. Sample selection was focused on fractured intervals, and major fractures were the central focus thin section analysis.

X-ray Diffraction Analysis

X-ray diffraction (XRD) samples were sampled based on lithology changes at a 3 to 37 foot spacing with an average spacing of ~14 ft. Fifteen bulk and clay samples were analyzed for mineralogy. Clay samples were analyzed using both glycolated and heat treated samples to calculate expandability for montmorillonite (mixed layer illite/smectite). XRD peaks were picked manually and subsequently verified using Topaz® analysis software. Data were normalized for total clay, total carbonate, anhydrite, and other (quartz, feldspar, etc.) based on the common lithologies observed in the cores.

Core Panel Integration

All data were compiled into a core panel as a visual representation and integration tool for both cores. Components of the core panel include core gamma log, a drafted core description and fracture sketch, XRD data represented as pie charts, and thin section photographs with descriptions plotted with respect to depth. The core panels were divided into intervals separated by flooding surfaces, significant changes in lithology and/or texture, and structural detachment surfaces for analysis. Components of each interval were then analyzed for structural, mineralogical, and stratigraphic elements.

RESULTS

Natural Fracture Results

The major natural facture types observed include: 1) vertical mineralized joints (Fig. 1b); 2) inclined, slickensided shear fractures (Fig. 1a); 3) short, bed-limited, fracture sets; 4) bed-parallel shears; 5) bedding-parallel veins with fibrous mineral fill (termed “beef” by Buckland and De la Beche, 1835) (Fig. 1a); 6) pre-compaction fractures (Fig. 1c); and 7)

fracture zones/swarms (Fig. 1a). Similar fracture styles tend to cluster in zones, confined to a specific stratigraphic unit.

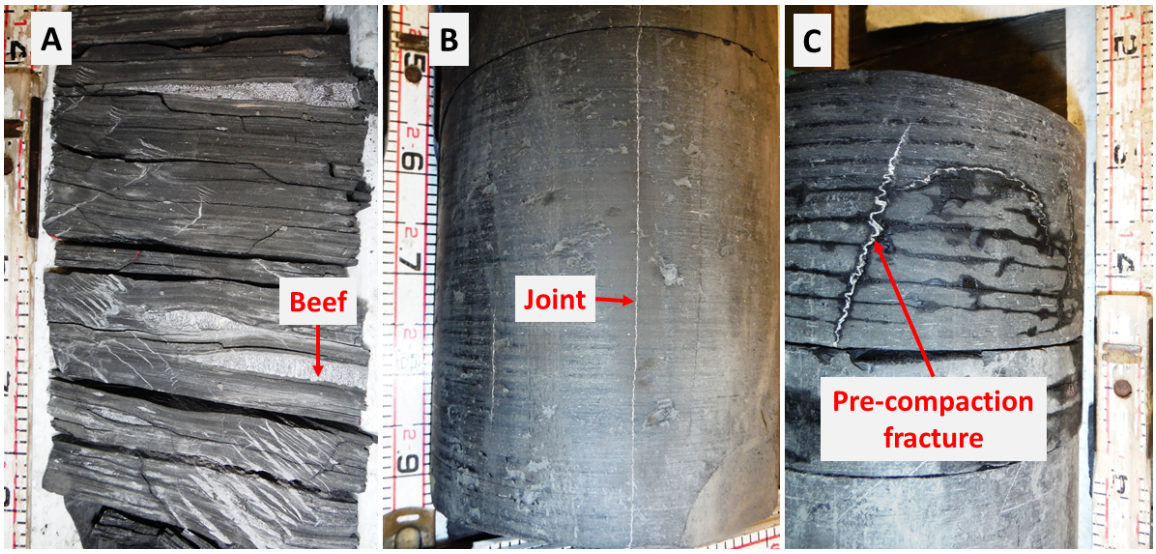

Figure 1. Some fracture types including A) a shear fractures (as seen by lamination offset) and beef zone, B) a mineralized vertical joint, and C) a pre-compaction fracture.

In both cores, natural fractures are organized into distinct fracture domains that correspond to lithologic units. In stratigraphic order, these fracture domains are: 1) densely-spaced cleats in coal; 2) dominantly joints; 3) mostly shear fractures; 4) short, bed-limited fractures; and 5) highly variable fracturing. The highly variable fracture interval is subdivided into four subintervals – two intervals of joints, one interval of shear fractures, and the upper-most interval of both shear fractures and beef. Two low-angle detachments, defined by densely spaced low-angle shear fractures and intersecting bed-parallel shears, are present in both cores.

Changes in fracturing are abrupt across sharp lithologic boundaries, ranging from the half-meter to millimeter scale. The conventional wisdom that fracture spacing decreases with decreasing fractured bed or lamination thickness (Ladeira and Price, 1981) holds true in thinly laminated intervals (for vertical fractures), however this relationship is less evident in intervals with low-angle shear fractures, bed-parallel shears, and beef.

Core Description Results

Combined, the two cores comprise four informal members of the Heath Formation: the Potter Creek coal, the Cox Ranch shale, the Heath limestone, and the upper shale member.

The Potter Creek coal, observed only in the Reese 1 core, is one foot thick and overlies a root-penetrated mineral paleosol developed in siliciclastic facies. This member is an impure/argillaceous coal that comprises 58% TOC by weight.

The Cox Ranch shale, present in both cores, ranges from 57 to 70 ft thick. This member consists of organic-rich, calcareous mudstone to marlstone with intercalated limestone and dolostone. Shelly, marine bioclasts are abundant and are commonly densely concentrated in the laminae and layers. Bioturbation is variable, ranging from absent to intense. Flooding surfaces within the Cox Ranch interval are recognizable in both cores and provide high-resolution correlations.

The Heath limestone, present in both cores, is about 20 feet thick. This member consists of anhydritic, calcareous dolostone to dolomitic limestone that grades up into crystalline anyhydrite. Some calcareous mudstone/marlstone beds are also present. Anhydrite in the carbonate beds is largely displaced. The crystalline anhydrite ranges from laminated to brecciated. In the Padre 1A, some crystalline anhydrite appears replaced by silica/clay.

The upper shale member is present in both cores, but the entire thickness of the unit is not represented. The cored section ranges 9 to 14 feet thick. This unit comprises calcareous mudstone/marlstone with interbedded marine limestone and dolostone. Bioclastic, shelly laminae are locally present in the mudstone facies.

Thin Section Analysis Results

Twelve thin sections from the Reese 1 core reveal complex fracturing and diagenesis. Fracture-parallel layers of mineral fill suggest crack-seal mechanisms for fracture development with up to three different layers of minerals. This indicates mineral replacement within fractures, (e.g. calcite and chlorite). Petrographic analysis supports observations in core suggestive of multiple deformation events. Younger fractures abut into older fractures in core and thin section. These same fractures show small amounts of fill from the younger fractures bulging into older, orthogonal fractures (Fig. 2).

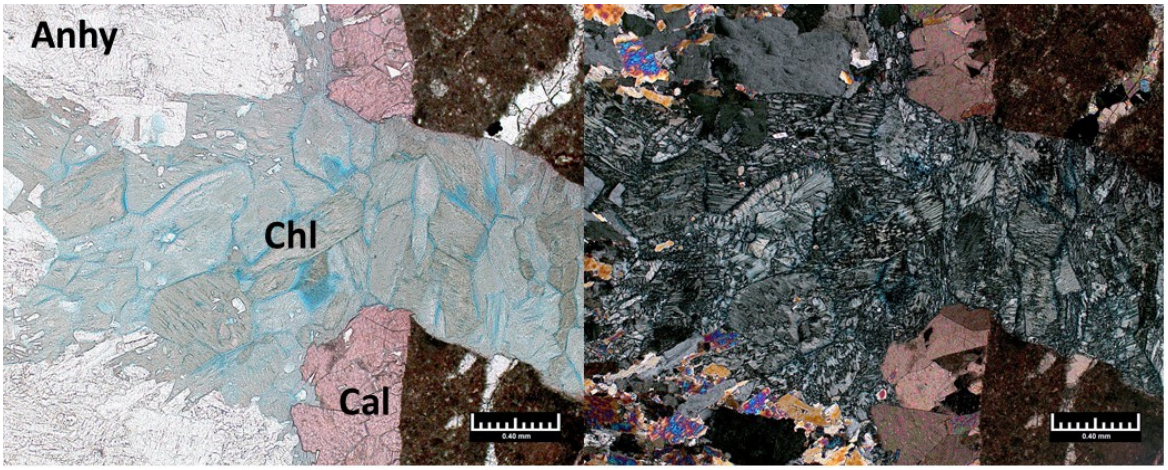

Figure 2. Thin section photomicrographs showing a younger fracture bulging into an older fracture partially reopening the older fracture. Anhy = anhydrite; Chl = chlorite; Cal = calcite; Magnification = 50X; Left is PPL; Right is XPL.

Further evidence of a relationship between fracturing and diagenesis is found in thin sections from the upper shale and Cox Ranch. In the upper shale, a relatively large-aperture fracture has up to four mineral fills including chlorite, dolomite, anhydrite, and calcite, partially due to mineral-replacement. In the Cox Ranch, a discontinuous fracture crosses a succession of three laminae: shale, organic silty shale, and dolomite. The fracture is fully healed by dolomite and calcite in the lower shale lamina. The intervening clay/organic silty shale lamina is not fractured. The fracture reappears and is propped open by euhedral dolomite crystals in the dolomite lamina preserving fracture porosity.

X-Ray Diffraction Analysis Results

Thirteen samples were analyzed for XRD mineralogy – 11 from the Reese 1 well and four from the Padre 1A well. The major mineralogical components include clay, carbonate, anhydrite, and quartz (Fig. 3). Small amounts of plagioclase, pyrite, apatite, analcime, celestine, gypsum, and barite were also found. The major component averages are: 19% clay (ranging 0-51%), 43% carbonate (ranging 2-89%), 19% quartz (ranging 1-44%), and 13% anhydrite (ranging 0-88%). In the Padre 1A core, samples were not taken from facies with abundant anhydrite; hence, this mineral phase is underrepresented in the XRD data. Differentiation of clays shows the dominant clays as mixed-layer illite/smectite and illite with trace amounts of chlorite and kaolinite in most samples.

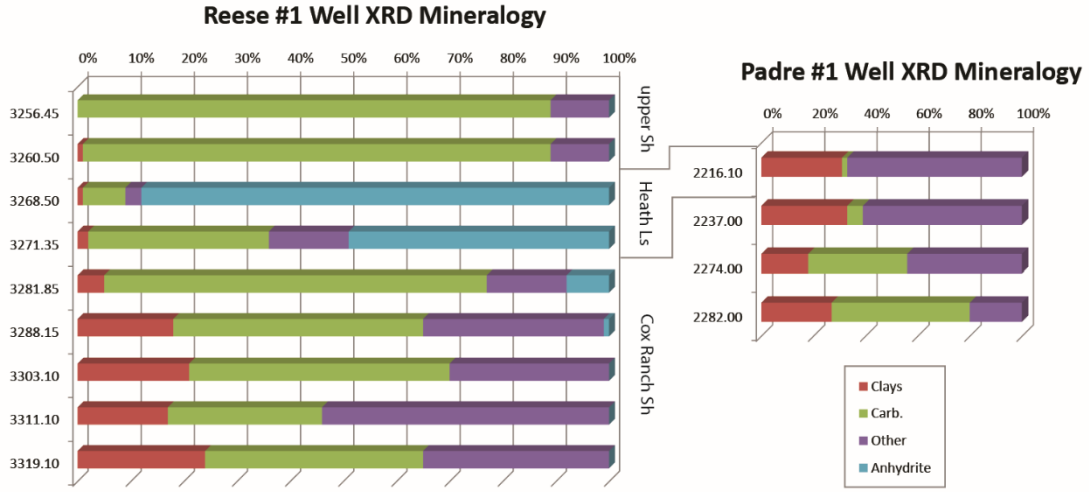

Figure 3. XRD mineralogy (total clay, total carbonates, anhydrite, and other (including quartz) for samples in the Reese 1 and Padre 1A wells. Not to scale.

DISCUSSION

A distinct fracture stratigraphy exists within the Heath Formation. Fractures within each interval (listed in stratigraphic order) are: 1) Potter Creek coal — closely spaced cleats; 2) lower Cox Ranch shale — mostly planar, vertical, mineralized joints; 3) upper Cox Ranch shale — mostly shear fractures and bed-parallel shears; 4) Heath limestone —

variable but prominent bed-limited fractures, mostly within thin, dolostone beds and laminations; and 5) upper shale member — mixed, highly variable fractures including bed-parallel shears, shear fractures, short, mineralized and unmineralized joints, and beef.

Densely-spaced cleats are expected in coals such as the Potter Creek. The presence of mostly planar joints in the lower Cox Ranch shale may be related to the calcareous nature (possibly increased due to the presence of calcareous bioclasts as a source of carbonate) of the marlstones and limestones, raising the shear strength of the interval, and inhibiting the development of shears. Conversely, the lower carbonate percentage (also lower calcareous bioclast concentration) within the upper Cox Ranch likely promoted development of shear fractures and bed-parallel shears. Both the thinly-bedded nature of the Heath limestone, and the alternating layers of ductile anhydrite with the more brittle dolostone, promoted the development of closely-spaced, bed-limited fractures. The argillaceous and laminated character of the mudstone facies in the upper shale may explain the presence of beef and dense shears. These changes show that facies and diagenesis, control the distinct differences in fracture characteristics including fracture mode (opening, shearing, etc) and geometry.

CONCLUSION

Data from two heterogeneous "shale" cores from the Heath Formation in Montana provided an opportunity to better understand fracture stratigraphy. Clear correlations exist between stratigraphy, texture, mineralogy, diagenesis, and fracturing. Ultimately, this and similar studies will make natural fracture prediction models more geologically accurate, increasing production in fractured shale plays.

REFERENCES

Bottjer, R., Stratigraphy and oil resource potential of the Mississippian Heath Formation, Central Montana, USA, Search and Discovery Article #50914, (2014), presented at AAPG Rocky Mountain Section Meeting, Salt Lake City, Utah, September 22-14, 2013.

Buckland, W., and De la Beche, H. T., On the geology of the neighborhood of Weymouth and the adjacent parts of the coast of Dorset, *Transactions of the Geological Society of London*, (1835) **v. 2-4**, p. 1-46.

Gale, J. F. W., Laubach, S. E., Olson, J.E., Eichhubl, P., and Fall, A., Natural fractures in shale: A review and new observations, *AAPG Bulletin*, (2014) **v.98**, no.11, p.2165–2216.

Ladeira, F. L., and Price, N.J., Relationship between fracture spacing and bed thickness, *Journal of Structural Geology*, (1981) **v.3**, no. 2, p. 179-183.

DRILL CUTTINGS AS AN ECONOMIC TOOL TO UNDERSTAND THE PETROLEUM SYSTEM FOR EXPLORATORY AND DEVELOPMENT WELLS

[1]Rushdi Ali, [2]Ibrahim Ghiniwa
(1) Reservoir Geology Team Leader, Corex Services LTD., (Egypt Branch)
(2) Core Analysis Manager, Corex Services LTD., (Egypt Branch)

This paper was prepared for presentation at the International Symposium of the Society of Core Analysts held in Snowmass, Colorado, USA, 21-26 August 2016

ABSTRACT

The geological studies (petrographical analyses) can be applied on drill cuttings (old/new, dry/wet sets) recovered from un-cored intervals, in order to help the oil and gas companies to understand the characteristics of their source rock, reservoirs and seals, with special focus on the reservoir quality.

Drill cutting samples are as useful for geological studies as core or side wall core samples. These types of samples are recovered each 3-5m or 10-15 ft, from each well. Their availability, nature and sample volume would dictate the amount of geological and geophysical data resulted from various types of analyses as petrography, scanning-electron microscopy (SEM), X-ray diffraction analysis (XRD), grain size analysis (include sieving and laser particle "LSPA" analyses) and mercury injection capillary pressure analysis (MICP). Petrographical analyses include identification and description of the detected rock types by quantitative (point counted) or qualitative petrographic thin-section analysis; whereas MICP is considered a useful tool for improved understanding of porosity and matrix permeability distributions of petroleum systems (including source rock, reservoirs and seals). Thin section analysis performed on selected drill cutting pieces aims to identify rock types and to define their mineralogy, texture and composition, and the evaluation of mineralogical and diagenetic controls on porosity and permeability (reservoir quality). This type of study could focus on individual wells or multi wells (exploratory and/or development wells). Based on petrographical results a rock type scheme could be built and applied on a regional scale to better interpret the electric logs (Gamma-Ray) in terms of reservoir/seal intervals and their potentials. Each identified rock type could be further analysed by applying SEM and XRD analyses. Each special petrographical test provides more and more details with regard to the pore geometry, pore occluding minerals, clay minerals differentiation and quantification. In addition to that, MICP can provide data that are equally suitable for the calibration of porosity logs and has the added advantage that the analysis can be done on fresh or archived cuttings samples as well as core. Potentiality of sandy intervals and their characteristic grain size distribution is also possible to be determined by performing sieve and/or laser particle (LSPA) analyses.

INTRODUCTION

Drill cuttings are the broken bits of solid material removed from a borehole drilled by rotary or percussion methods. Boreholes drilled in this way include oil and/or gas wells for exploratory and/or development stages. The drill cuttings are commonly examined to make a record (a well/mud log) of the subsurface materials penetrated at various depths recovered each 3-5m or 10-15 ft. Drill cuttings are produced as the rock is broken by the drill bit advancing through the rock; the cuttings are usually carried to the surface by drilling fluid circulating up from the drill bit. Drill cuttings can be separated from liquid drilling fluid by shale shakers, by centrifuges, or by cyclone separators [1].

Objective of the Study

The main objective of this study is to provide the importance of applying and integrating the lithological description, with petrographical characteristics and the rock properties of the drill cutting samples and to interpret the gained information with regard to reservoir quality. Petrographical analyses were performed (special attention to thin section and scanning-electron microscope) of the selected drill cutting samples from different parts of petroleum systems, with the aim to identify and characterise their mineralogy, texture and composition, which further allows the petrographical classification of rock types and the evaluation of mineralogical controls on porosity and permeability, and could be supported with mercury injection capillary pressure (MICP) data.

ANALYTICAL PROCEDURES AND RESULTS

As a part of this study the lithological description and petrographical analyses (thin section “TS” and scanning-electron microscope “SEM”) were carried out on drill cuttings. A brief description of the analytical procedures is as follows:

Samples Preparation and Lithological Description

When received the cutting samples are cleaned first using water depending on the nature of the samples. If the samples contain swelling clays, we won’t wash them with water but we will crush them and try to blow the drilling mud that coats the grains. If the samples are sandstone or carbonate or normal clays, we will wash them gently with water. Figure 1A shows the samples laid out after washing and ready for petrophysical analysis and description. After cleaning the samples are studied macroscopically (naked eye) and microscopically (by using binocular microscope, Figure 1B).

The available material of each sample was inspected with regard to its overall condition (degree of recovery) and the nature and relative abundance of components. Rock types distinguished within the cutting samples have been lithologically classified according to their specific characteristics and were further described considering their colour, composition, textures and percentages; then facies schemes (lithologically) can be established by preparing a log description (e.g., by using canvas software) and integrated / interpreted with the electric logs (Gamma-Ray) in terms of reservoir/seal intervals and their potentiality (Figure 2).

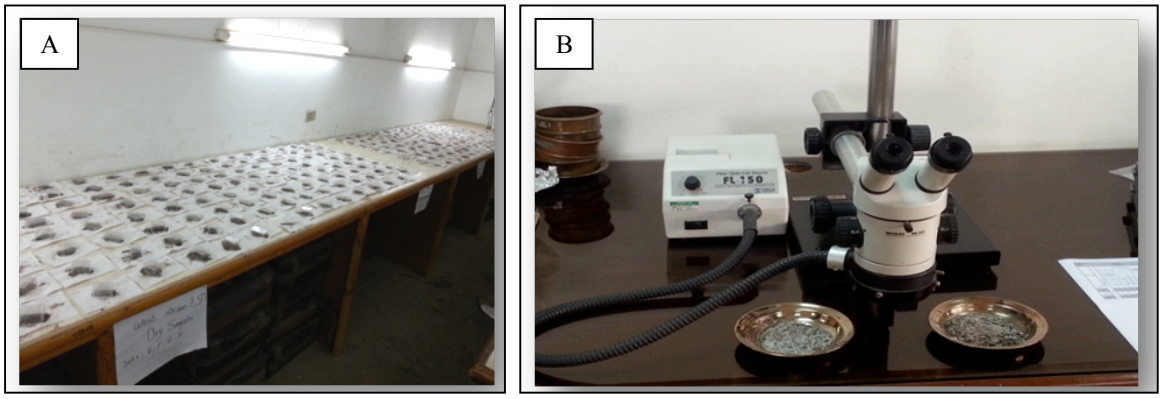

Figure 1. A) Showing the samples layout after washing and ready for description. B) Showing the Binocular microscope used in describing the samples.

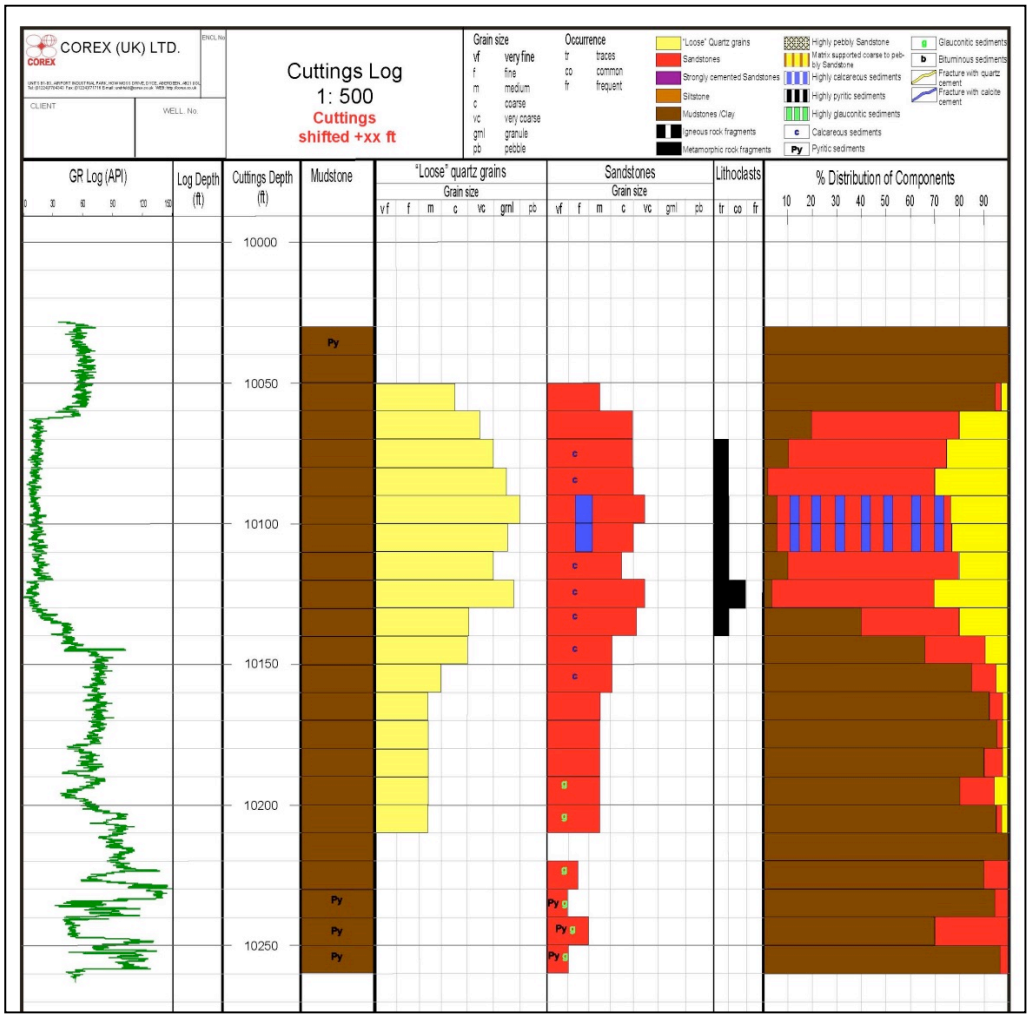

Figure 2. Example for cuttings log description integrated with Gamma-Ray (GR) log, by using Canvas software.

Petrographical Analyses (TS and SEM)

After lithological description we pick the cutting samples for petrographical analyses (thin section and SEM) to cover all the represented lithotypes, in order to built-up microfacies types integrated with lithofacies types. During the selection process we divide the material into three parts: 40% for thin section; 40% for SEM and 20% as a reference for quality control, and try to avoid additives (such as calcite pieces of drilling).

Thin Section (TS)

Thin section preparation involved vacuum impregnation with blue dyed resin to facilitate the recognition of porosity and staining with a mixed Alizarin Red-S and potassium ferricyanide solution to allow the identification of the carbonate minerals. In addition, samples were stained with a sodium cobaltinitrite solution to aid the recognition of alkali feldspars [2]. The thin sections were examined under plane- and cross-polarised light with a petrographic polarising microscope. Different lithologies (microfacies) were selected from each thin section and separately analysed. The texture, mineralogy and porosity of each lithology (microfacies) were described and the relative abundances (in % by volume) of detrital and authigenic components and pore spaces were determined by either point counting (quantitative descriptions: 50, 100, or 200 counts) in some pieces/samples or estimated (qualitative descriptions) in other parts depending on the quality of the cuttings. Due to the poor nature of some analysed samples, point counts couldn't be applied. Instead quantification of minerals and porosity was achieved through visual estimation. Rock types were petrographically classified according to an established rock classification scheme (such as sandstone classification scheme, after Dott [3]). The results of the thin section analyses are summarised on a petrographic data sheet (Figures 3 and 4). The specific characteristics of the samples are further illustrated by coloured photomicrographs for each sample depending on the number of microfacies distinguished in each individual sample (Figure 4).

DEPTH [ft]	SAMPLE TYPE	TEXTURAL DATA: Grain Size Min.	Grain Size Av.	Grain Size Max.	GRAIN SORTING	GRAIN ROUNDNESS	GRAIN CONTACTS	Pore System: AV. PORE SIZE (µm)	Pore System: AV. PORE CONNECTIVITY	Pore System: PORE TYPES	ROCK NAME (After Dott, 1964)	POINT COUNTED / ESTIMATED DATA [% BY VOLUME] — DETRITAL COMPONENTS: Quartz: POLYCRYSTALLINE	Quartz: MONOCRYSTALLINE	LITHIC FRAGMENTS	Feldspars: K-FELDSPARS	Feldspars: PLAGIOCLASE FELDSPARS	Accessory Minerals: MICAS	Accessory Minerals: OPAQUES	Accessory Minerals: HEAVY MINERALS	GLAUCONY	BIOCLASTS	PHOSPHATIC FRAGMENTS	CARBONACEOUS DEBRIS	Matrix: DETRITAL CLAYS	AUTHIGENIC COMPONENTS: QUARTZ OVERGROWTHS	FELDSPAR OVERGROWTHS	Carbonates: CALCITE	Carbonates: FERROAN CALCITE	Carbonates: DOLOMITE	Carbonates: FERROAN DOLOMITE	Carbonates: SIDERITE	Clay Minerals: KAOLINITE	Clay Minerals: ILLITE	Clay Minerals: CHLORITE	PYRITE	SPHALERITE	Evaporites: ANHYDRITE	Evaporites: GYPSUM	Evaporites: BARITE	SECONDARY SILICA	Organic Matter: RESIDUAL HYDROCARBONS	Organic Matter: HYDROCARBON STAINS	POROSITY	TS-PLATE NUMBERS
9900		vfL	fU mL	cU	MS WS	SA SR	P, L, F, C	10 50	Very Poor	SBP, FR	*Fe-Dolomitic Sublithic Arenite	1.5	39	10	1	8	1	1	1	2	_	_	_	2.5	2.5	_	_	1.5	_	22	_	_	TR	TR	4.5	_	_	_	_	_	1	TR	1.5	13
9910		silt	fU mL	mU	WS	SA SR	P, L, F, C	_	_	_	***Fe-Calcitic Subfeldspathic Arenite	1	38	6	_	10	2	1	1	2	4	_	_	_	2	_	_	26	_	1	_	_	TR	TR	6	_	_	_	_	_	_	_	_	14a
		vfL	mL mU	cL	MS WS	SA SR	P, L, F, C	10	Very Poor	FR	**Fe-Dolomitic Sublithic Arenite	3	31	12	_	8	2	1	1	2	1	_	_	2	2	_	_	2	_	27	_	_	TR	TR	4	_	_	_	_	_	_	_	2	14b
9920		silt	fL fU	mL	WS	SA SR	P, F, L	_	_	_	Fe-Calcitic Subfeldspathic Arenite	2	37	8	5	6	1	0.5	1	1	0.5	_	_	_	1	_	_	33	_	2	_	_	TR	TR	2	_	_	_	_	_	TR	TR	_	15a
		silt	fL fU	mL	WS	SA SR	P, L, F	_	_	_	Fe-Dolomitic Subfeldspathic Arenite	2	38	7	3	5	1	0.5	0.5	1	7	_	_	6	1	_	_	4	_	20	_	_	_	_	4	_	_	_	_	_	TR	TR	_	15b
		silt	mL	cL	WS	SA SR	P, F, L	_	_	_	Lithic Wacke	3	20.0	10	1	5	_	_	_	1	4	_	_	51	1	_	_	_	_	3	_	_	TR	TR	1	_	_	_	_	_	TR	TR	_	15c

Figure 3. Example for petrographical data sheet (TS) of cutting samples (* 200 point counts; ** 100 point counts; *** 50 point counts; % by volume – whereas the rest of samples were visually estimated.

Distinguished Lithologies	%	*Distinguished Lithologies*	%
Fe-Dolomitic Sandstone	27	Loose Quartz Grains	3
Fe-Calcitic Sandstone	40	Loose Bioclasts	1
Argillaceous Sandstone	5	Porosity	3
Porous Sandstone	10	**Pore Type:** Secondary Inter- and Intraparticle.	
Mudstone	6	**Pore Size:** 10-100 µm	
Bioclastic Mudstone	4	**Pore Connectivity:** Poor-Moderate	
Calcitic/Limestone	1		
Total			**100%**

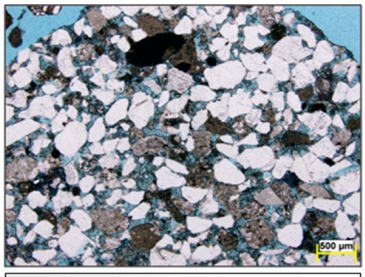

(Photo A; PPL): Fe-Dolomitic Sandstone.

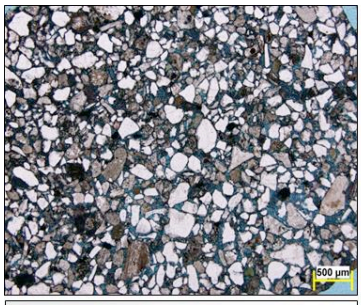

(Photo B; PPL): Fe-Calcitic Sandstone.

(Photo C; PPL): Porous Sandstone.

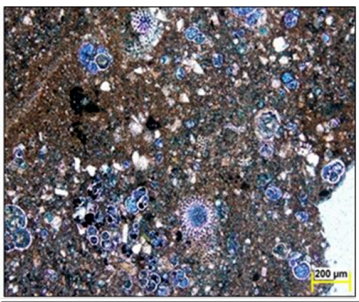

(Photo D; PPL): Bioclastic Mudstone.

Figure 4. Another example for lithology definition in thin section by % by volume / sample (visual estimation) and examples for thin section photomicrographs representing different types of microfacies.

Scanning Electron Microscopy (SEM)

SEM examination can be carried out on selected lithofacies types from cutting samples, where the samples are mounted on standard aluminum SEM stubs and coated with gold using a sputter coater. SEM analysis involved detailed description of the cutting material with a special focus on the pore geometry, composition and morphology of the main pore-occluding clays / carbonate cement minerals. Figure 5 shows examples of the quality and resolution of SEM images for cutting pieces.

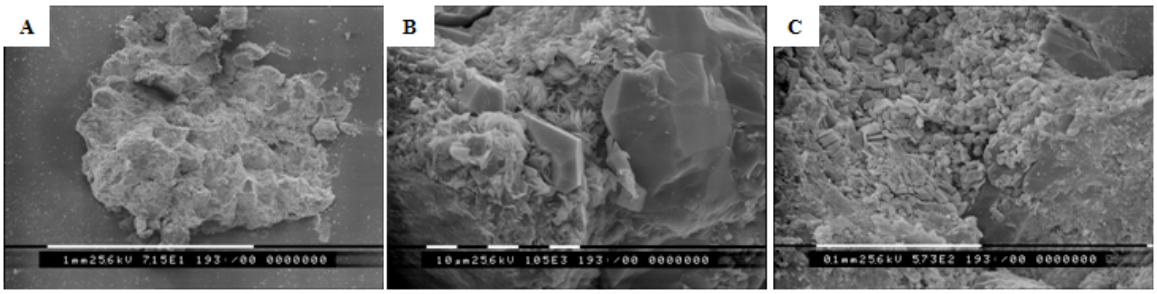

Figure 5. Examples for SEM images of cutting pieces: A) shows the quality of cutting sample in SEM. B) shows euhedral, smooth-faced and pyramidal quartz overgrowths, locally enclosed with moderately crystallised chlorite plates (card-house texture). C) shows moderately crystallised pore filling kaolinite booklets of partly corroded pseudohexagonal basal plates.

RESERVOIR QUALITY

Petrographical analyses (TS and SEM) on cutting samples can help clarify the reservoir quality from the mineralogical and textural composition of detected microfacies/lithofacies types from cutting samples, and their effects on porosity types and

distributions. The importance of MICP on cutting samples is shown in Figure 6 for improved understanding of porosity and matrix permeability distributions of reservoirs [4], and integrated with the observations of the petrographical analyses.

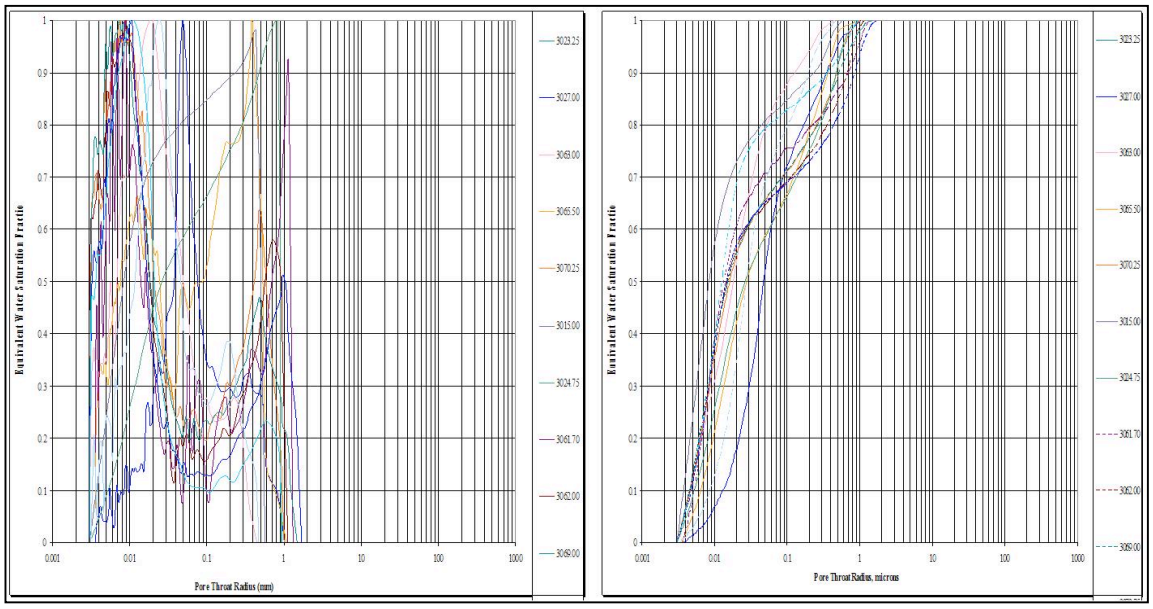

Figure 6. Example for MICP data for different samples that shows smaller pore throat radius and strong positive skewness, where GeoMean Permeability = 0.12mD and Average He Porosity = 10.7%.

CONCLUSION

Drill cutting samples are recovered as a minimum record of rock material from each well. Petrographical and petrophysical studies can be applied to them and offer a continuous record of lithologies over wide depth ranges where cores are not recovered. Comparison and correlation of wells over an entire field area can also be undertaken.

ACKNOWLEDGEMENTS

We would like to thank Corex for access to their various experimental facilities.

REFERENCES

1. Schlumberger: Oilfield Glossary. (http://www.glossary.oilfield.slb.com/Display.cfm?Term=cuttings)
2. Tucker, M. E., ed., *Techniques in Sedimentology*, Blackwell Scientific Publications, (1988), 394p.
3. Dott, R.H., "Wacke, greywacke and matrix: what approach to immature sandstone classification?" *Journal of Sedimentary Petrology*, (1964) **volume**, 34, pp.623-632.
4. Olson, R.K. and Grigg. M.W., "Mercury Injection Capillary Pressure (MICP) a useful tool for improved understanding of porosity and matrix permeability distributions in shale reservoirs", *oral presentation at AAPG Annual Convention, San Antonio, Texas,* (2008), 31p.

Geomechanical Simulation of Core Microfractures While Pulling Out Of Hole

Rahman Ashena*, Gerhard Thonhauser*, Walter Vortisch*,
Michael Prohaska*, Rasoul Arabjamaloei**
*Chair of Drilling and Completion, Petroleum Engineering Department, Montan University of Leoben, Austria
** University of Manitoba, Winnipeg
This paper was prepared for presentation at the International Symposium of the Society of Core Analysts held in Snowmass, Colorado, USA, 21-26 August 2016

ABSTRACT

When the core is retrieved to the surface, it undergoes pressure and temperature drop. Due to pressure and temperature drop, some micro fractures may be created in the core if the pressure and temperature change occurs too rapidly. This is because basically the hydrocarbon inside the core cannot exit the core fast enough and thus pressure inside the core cannot drop as fast as the pressure outside. This causes a pressure difference between the inside and outside of the core. If the pressure difference is excessively high, it can simply cause creation of microfractures throughout the core.

Therefore, in this paper, the effect of stress changes outside of the cylindrical core while retrieval is simulated in order to obtain the inside core pressure, difference between inside and outside pressure, and the induced circumferential stresses in a time based manner. In this work, geomechanical poroelastic models have been modified and merged with finite element modeling and thus a new model has been reached. Having inserted the inputs into the developed model and interpretation of outputs, the creation of tensile microfractures is simulated. Thus, initiation time of microfractures and their radial locations in the core can be reported.

INTRODUCTION

Microfractures in cores are known as small cracks with high fracture length to width. Microfractures can be natural or induced. Induced microfractures occur while coring, core retrieval, recovery or handling. The aperture of microfractures is considered in the order of 0.1 mm in geophysics and petroleum engineering.

Induced microfractures created during core retrieval can be severe (as typically shown in **Figure-1**) if safe tripping procedures for core quality is disregarded. If core tripping speed is too high, the pore pressure does not reach equilibrium with outside pressure fast enough. This can cause stress-release induced microfractures.

Indeed, microfractures cause irreversible damage to the core, but there is little knowledge about their creation time and their locations. Obtaining this knowledge contributes to preventing induced microfractures in some cases (e.g. by controlling tripping rate). It can also contribute to the detection and discrimination in the core.

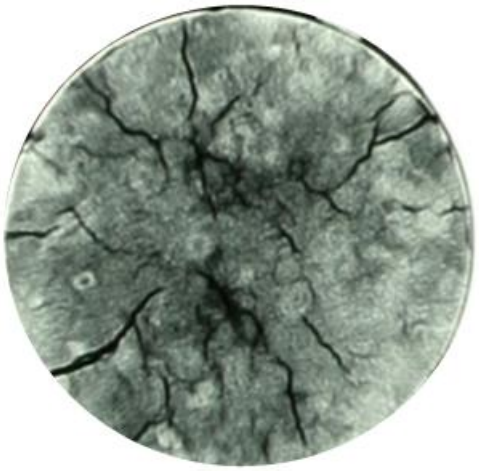

Figure 1: Typical large sized microfractures created in the core during tripping

Poroelastic Modeling and Solution

In elasticity modeling of cores, the effect of pores is ignored. Poroelastic models are modeling the effects of change in induced stress and pore pressure. Based on solid to fluid coupling, a change in stress causes a resultant change in pore pressure and also fluid volume. Conversely, a change in pore pressure causes a change in effective stress and rock mass volume. Poroelasticity depicts the interactive effects of pore pressure, increment of fluid content, strain and effective stress as follows (*Wang, 2000*):

$$\zeta = \alpha\epsilon + \frac{\alpha}{K_u B} p \tag{1}$$

The parameters in equation-1 are named in .

While core retrieval to the surface, outside pressure is reduced from bottomhole to atmospheric pressure gradually depending on retrieval speed. The same effect occurs for temperature.

The following equation depicts the relation between the Laplace transform of increment of fluid content (ζ) with radius and time (*Wang, 2000*, *Detournay and Cheng, 1993*):

$$\frac{d^2 L(\zeta)}{dr^2} + \frac{1}{r}\frac{dL(\zeta)}{dr} - \frac{s}{c} L(\zeta) = 0 \tag{2}$$

The above equation is solved to yield the solution of increment of water content in Laplace form ($L(\zeta)$). Then, using Stehfest algorithm, the inverse of Laplace is taken to

yield water content. Unlike many other geomechanical works, in this paper the compressive and tensile stresses are respectively considered positive and negative.
Original poroelasticity has an innate assumption that stress change occurs instantly. Thus, the core is instantly retrieved for the core retrieval case. This questions the validity of the model. Therefore, in this paper, finite element modeling is merged with poroelastic models. Thus, the incremental values are calculated and summed up to yield the final inside pore pressure at each stage, and circumferential stress.

Fracture Criteria

The creation of microfractures while core is being retrieved is considered tensile. Basically, tensile fracture occurs when the effective tensile stress across a plane in the core becomes greater than the rock critical tensile strength (T_0).

Table 1: Geomechanical Parameters Used and their Values

Parameter	Relation	Values
α (Biot's Coefficient):	$c = \frac{K}{\mu S}$, $c = (4.083e-7)\frac{K}{\emptyset \mu C_t}$	0.74
c1 (initial hydraulic diffusivity):		6e-8 m^2/s (Shale)
μ (dynamic viscosity) at downhole conditions:	$S = \frac{1}{K_v} + \varphi \frac{1}{K_f}$ $K_f = \frac{1}{C_f}$ $C_t = (4.083e-7)\frac{K}{\emptyset \mu c}$	0.02 cp
S (uniaxial specific storage):		
K_f (fluid bulk modulus):		
C_t (total compressibility) at reservoir conditions:		85.06 1/Pa (Shale)
UCS (Uniaxial Compressive Strength):		20 MPa
Estimated Tensile Strength (T_0):	$T_0 = \frac{1}{8} UCS$	2.5 MPa
υ (Poisson's Ratio):		0.18
υ_u(undrained Poisson's Ratio):	$\upsilon_u = \frac{3\upsilon + \alpha B(1-2\upsilon)}{3 - \alpha B(1-2\upsilon)}$	0.28
B (Skempton's coefficient):	$B = \frac{3(\upsilon_u - \upsilon)}{\alpha(1-\upsilon)(1+\upsilon_u)}$	0.49

To detect the time and location of microfractures created in the core, two criteria are conceived in this paper to be effective:
1) Griffith criteria (*Griffith 1921*):

$$\sigma'_{\theta\theta} = -T_0 \quad (3)$$

2) When difference between inside pore pressure ($P_{p,c}$) and outside pressure exceeds critical tensile strength (T_0):

$$P_{p,c} - P_m > -T_0 \quad (4)$$

The second criterion was utilized by Zubizarreta et. al. (2013) to simulate microfractures created while core retrieval using computational fluid dynamic modeling.

Case Study

To evaluate the developed model function, one typical case study is investigated in this paper. The parameters and their corresponding values are given in **Table-1.** The controlling variables are pull-out-of-hole time or speed, hydraulic diffusivity (*c*), and mud cake pressure drop which have been simulated.

Results and Discussion

After inserting the input data in the developed model, the two mentioned criteria of initiation of microfractures (***equation-3 and 4*** respectively) are considered to detect the time and location of microfractures. The results of the simulation for a typical *shale gas formation* case have been shown in **Table 2**. The simulation results using the two tensile failure criteria respectively for the time and location of fracture initiation have been plotted in **Figure 2**. As can be seen in **Figure 3**, the time of creation of microfractures in shales is almost instant. As can be seen in **Figure 3**, most microfractures are concentrated near the boundary.

Table 2: Results of Model on the Case Study

	Controlling Variables		**Results**	
Shale Core	POOH schedule:	T1=2 min/stand T2=12 min/stand T3=18 min/stand	Microfractures?	Yes
	Hydraulic diffusivity (c):	6e-8	Time(s):	t≥0.5e3 s
	Mud cake pressure drop (psi):	0%	Location(s):	0≤r/R≤1
	Total time (hr):	25.55 hr	Damage:	Severe
	Tensile strength (MPa):	2.5 MPa	Effect:	+

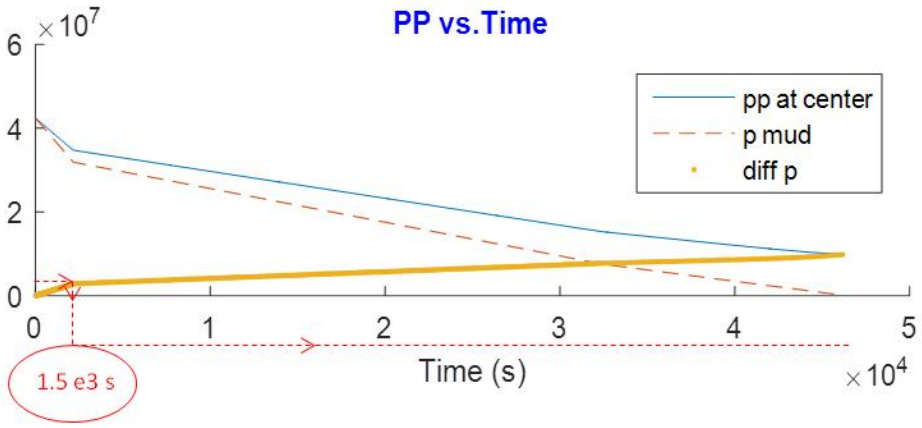

Figure 2: Results of application of the First Tensile Failure Criterion for Detection of Microfracture Initiation Time (Equation-3)

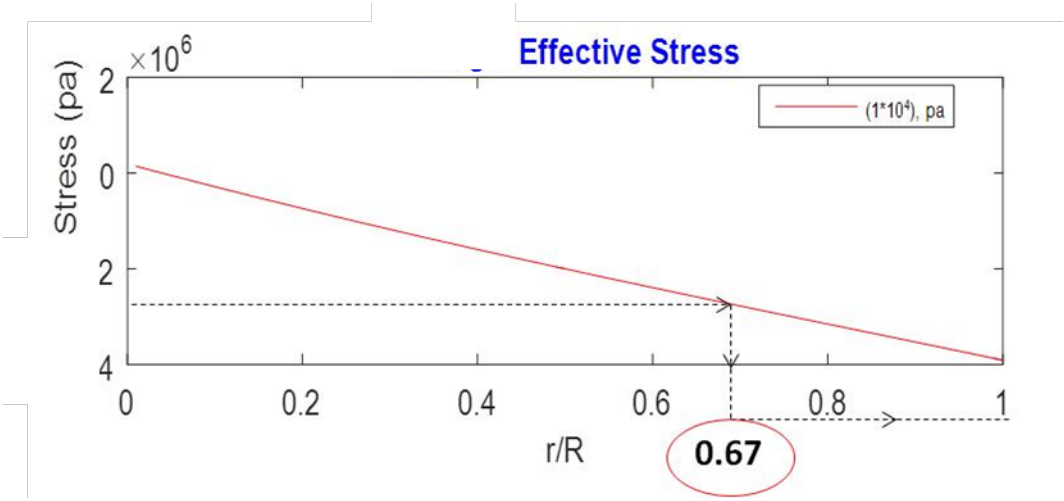

Figure 3: Results of application of the Second Tensile Failure Criterion for Detection of Radial Locations of Microfractures in the Core (Equation-4)

CONCLUSION

In this paper, it is attempted to detect the initiation time and radial locations of microfractures created in the core when it is retrieved to the surface. Using poroelastic modeling of stress change and merging it with finite element modeling, it is possible to evaluate inside pore pressure and circumferential stresses around the core while retrieval. For shale cores, the microfractures are created almost instantly due to their minimal permeability and hydraulic diffusivity. In addition, most microfractures are distributed near the boundary.

ACKNOWLEDGEMENTS

I would like to appreciate Chair of Drilling and Completion, Petroleum Engineering Department, University of Leoben for the support and permission to publish this paper.

REFERENCES

Ahmed, T. (2000) Reservoir Engineering Handbook, Gulf Professional Publishing.

Andres, M.H., Laubach, S.E., Scholz, C.H. (2014) Microfractures: A Review, Journal of Structural Geology, Volume 69, part B, Dec. 2014, p. 377-394.

Kieschnick, J. and Suarez-Rivera, R. TerraTek Fundamentals for Reservoir Quality Assessment and Completion Analysis, Core Technology for Evaluating the Bakken.
(http://pttc.mines.edu/casestudies/Bakken/BakkenCore.pdf, last accessed on Jan. 2016)

Detournay, E., Cheng, A. (1993) Fundamentals of Poroelasticity, Comprehensive Rock Engineering, Pergamon Press.

Fjaer, E., Holt, R.M. and Horsrud, P. (1992) Petroleum Related Rock Mechanics, 2nd edition, p.59.

Griffith, A.A. (1921) The phenomena of rupture and flow in solids, The Philosophical Transactions of the Royal Society London (Series A), 221 (1921), pp. 163–198

Grover, P.W. (2011) Petrographic Recognition of Artificially Induced Microfractures Versus Natural Microfractures in Oil/Gas Shales, AAPG Annual Conference and Exhibition, April 10-13, 2011, Houston, Texas, USA.

Rezaee, R. (2015) Fundamentals of Gas Shale Reservoirs, Wiley Press, p. 343.

Wang, H. (2000) Theory of Linear Poroelasticity with Applications to Geomechanics and Hydrogeology, Princeton University Press.

Zubizarreta, I., Byrne, M., Sorrentino, Y., Rojas, E. (2013) Pore Pressure Evolution, Core Damage and Tripping Out Schedules: A Computational Fluid Dynamics Approach, SPE-163527-MS, SPE/IADC Drilling Conference, 5-7 March, Amsterdam, The Netherlands.

Manufacture of water wet artificial core by chemical modification method

Haojun Xie[1], Aifen Li[1], Jianfei Qin[2], Bonifasi Lazaro[1]
1-School of Petroleum Engineering, China University of Petroleum (East China)
2- Shengli Oilfield, Sinopec
This paper was prepared for presentation at the International Symposium of the Society of Core Analysts held in Snowmass, Colorado, USA, 21-26 August 2016

ABSTRACT
A limited number of reservoir rocks can be drilled for laboratory experiments, so artificial core is often used to study the multiphase flow and EOR mechanism during physical simulation experiments. Artificial core manufacturing method includes epoxy cementing and high temperature sintering processes. Conventional epoxy resin cement core used was commonly oil wet. By adopting the method of high temperature sintering or surfactant cementation, the wettability requirements of reservoir rocks can be satisfied; however, it may have water sensitivity and unstable hydrophilicity issues.

The traditional process of epoxy cement is improved on the basis of above mentioned facts. In this paper the method of manufacturing water wet artificial core was improved and simplified by chemical modification. The non-ionic hydrophilic group for epoxy molecule is added by the chemical reaction of E-51(epoxy) and glycine, and then the chemically modified epoxy and curing agent can cement quartz sands directly. The mixture of chemically modified epoxy resin and curing agent before solidification can be diluted by water directly instead of acetone which is toxic for human body. The test of contact angle shows that cured epoxy resin and cemented core slice are both water wet. Strength, porosity and permeability of cementing core are essentially the same with the conventional cementing one; moreover, the pore distributions by NMR test are the same. Furthermore, the water sensitivity phenomenon does not exist, and its' properties (strength, porosity and permeability) basically remain unchanged after soaking by kerosene or water for 48 hours. This kind of water wet core manufacturing method is simple since the process doesn't need high temperature curing and it's more suitable to study the fluid flow in porous media and EOR method in light of the stable property.

INTRODUCTION
Most scientists working on the problem have concluded that it is difficult to obtain valid measurements without operating under conditions as close as possible to those in the reservoir. In the field of reservoir engineering, it is important for the core samples used in laboratories to have properties representing the real reservoir. Although often neglected, core samples always degrade to some degree in the process of cutting the core, handling it, and studying it. This necessitate for artificial core sampling as an alternative. Artificial core manufacturing methods which include high temperature sintering or surfactant

cementation improve wettability requirements of reservoir rocks and makes the sample representative. Unfortunately, water sensitivity and unstable hydrophilicity is still challenging under this method.

Most scholars generally change additives or processing methods to meet the requirements of different wettability [1]. For the core produced by epoxy cement, the method of adding clay and surfactant substances, is generally adopted to change the wettability (weak oil-wet is changed into weak water-wet) [2-3]. For the high-temperature sintering core and natural water-wet core, the method of silicone oil immersion is generally adopted to change the wettability (weak oil-wet is changed into weak water-wet). However, silicone oil and surfactant can be removed by core flooding. When clay is added, there is strong water-sensitivity. Moreover, the acid and alkali resistance of high-temperature sintering core is poor [5-6]. Therefore the reusability and wetting stability of core are still unresolved.

Chemical modification is a common way to change the surface properties in material science field, and water-borne epoxy resin technology has been developed in these years [7-8]. So chemical modification adopted as remedy to improve and simplify the method of manufacturing water wet artificial core and hence give solution for the above mentioned challenges. The traditional process of epoxy cement is improved on the basis of the above mentioned criteria.

PROCEDURES

Chemical Modification of Epoxy

The cement and quartz sand should be sufficiently stirred and cured during core manufacturing process. The thin film is formed by cement on the surface of quartz sand. The ordinary epoxy is oil-wet; as a result, the cemented core is also oil-wet. The core's wettability can be influenced by properties of epoxy and curing agent.

Bisphenol-A-type epoxy resin E-51(Epoxy value: 0.48-0.54, industrial products with lower viscosity) and glycine (analytically pure) were selected for chemically modified epoxy resin manufacturing. Mole ratio is n (epoxy group): n (glycine) = 3:1 (mass ratio is about 8:1). E-51 epoxy resin, the glycine and surfactant were mixed together and heated to 80°C (keep 3.5 hours for reaction). Using sodium hydroxide solution to neutralize the mixture and therefore the water-based epoxy system was produced [6]. The equation for the chemical reaction is:

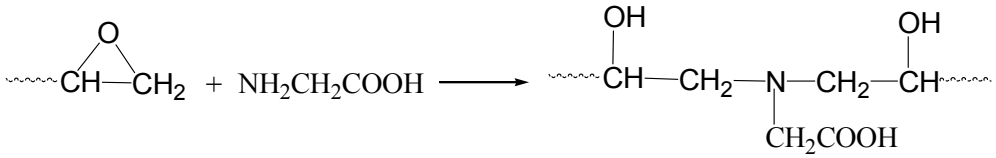

(1)

Modified epoxy resin is transparent liquid with light yellow color. Triethanolamine (TEA, industrial product) is used as a curing agent. The equation for the cure reaction is:

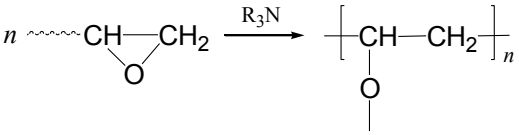

(2)

Solidification of Epoxy and Artificial Core

Firstly, mix ordinary epoxy or modified epoxy resin with TEA adequately and smear the mixture evenly on the glass. Then place it into a thermostat (65°C) for 5 hours to solidify. After the solidification, measure the solid-oil-water contact angle for cured epoxy and modified epoxy resin.

Secondly, mix ordinary epoxy or modified epoxy resin with TEA and quartz sand adequately. Quartz sand of 100~120 mesh was used as cement particles and the mass ratio of epoxy (including curing agent) to quartz sand is 0.07:1. Then push the mixture into the cylindrical mould (diameter = 1 inch, pressure = 10MPa) and place it into a thermostat (65°C) for 5 hours to solidify. After the solidification, we get the artificial core and then measure the contact angle, stability in oil or water (valued by stress sensitivity) and pore structure using NMR.

RESULTS AND DISCUSSION

Wettability

Using water and kerosene (dyed by Sudan III), the oil-water contact angle on the solid surface for different epoxy coatings at 20°C was measured. The results are given by Fig 1 and Fig 2. The contact angle of oil-water on ordinary epoxy coating surface is about 106° which is the critical value between weakly oil-wet and oil-wet. But the contact angle on water-wet epoxy coating surface reaches about 40.5°, which shows that it is strongly water-wet or hydrophilic.

The artificial cores were cut into small slices with a thickness of 3mm and the contact angle results of oil-water phase on the surface are given in Fig 3 and Fig 4. Since ordinary epoxy resin core is oil-wet, slow spontaneous imbibition will occur to the oil drop, so ought to measure the contact angle when the kerosene were just touching the slice. Contact angle on ordinary epoxy resin core slice is 103^{o}, which shows that it is weak oil-wet. On the other hand, contact angle on waterborne epoxy resin core slice is 47^{o}, which shows that it is stronger water-wet than the previous.

The analysis of results show that the contact angles of cement core are very close to epoxy resin. Although quartz is hydrophilic, after mixing the epoxy resins and curing agent, cementing agent will form the thin film on the surface of quartz particle. After the cementing agent solidified, the quartz particles will be brought together to form the core. So the surface properties of cemented core are related closely with curing agent.

Core stability

8 artificial cores were made at same conditions, but with different epoxy. The permeability and porosity were tested by N_2 at 20°C. Table 1 shows that these cores have

basically the same permeability and porosity. After soaking in kerosene and brine (5%wt) for 48 hours, stress sensitivity of cores was tested by changing confining pressure, the results were used to value the core stability. In Fig 5 and Fig 6, k and k_i represent permeability under different confining pressure and initial permeability respectively. The stress sensitivity curves are very similar and close for cores soaked in kerosene or brine for both kind of cores. Therefore the kerosene and brine have little effect on the strength of this kind of cores. Stress sensitivity is low for both cases since the permeability under 10MPa is still above 85% of initial permeability. Comparing Fig 5 and Fig 6, the oil-wet core has a higher permeability than water-wet core at the same effective stress. In particular, when stress is 15MPa for both cases, the permeability for oil-wet is 5% higher as compared to that of the water-wet core.

The cured epoxy resin ensured the strength and weak stress sensitivity for the artificial cores. Since some epoxy groups of chemical modified epoxy have been replaced by hydrophilic groups, the strength of cured resin modified epoxy becomes lower and the effective stress of water-wet core stronger. However, the difference of 5%, which is shown in the results has little influence on normal displacement experiment.

Pore structure

Finally, the NMR tests were conducted for two kinds of cores (O4, W4) as shown in Table1 and Fig7. They all have the feature of single crest in the NMR spectrum. Since the pore samples were made of sand and epoxy of the same size and amount, the porosity, permeability and proportion distributions is almost the same. So a better comparability for the influence of wettability on multiphase flow in porous media is shown.

CONCLUSION

(1) The wettability of core mainly depends on the surface characteristics of epoxy. Using chemically modified epoxy the manufacture of water wet artificial cores becomes simple and convenient

(2)Artificial core has low stress sensitivity and better stability even when soaked in oil or water.

(3)Generally, artificial cores have almost the same properties except for wettability, so they are more suitable for porous media flow under different wettability.

ACKNOWLEDGEMENTS

This work is supported by National Science and Technology Major Project (2016ZX05009-001-007 and 2016ZX05014-003-002).

REFERENCES

1. Tang Renqi, Zeng Yuhua, Yao Fengying. “The Manufacture and Study of HNT Artificial Rock Sample” .*Oil Drilling & Production Technology*, (1998) 20, 1, 98-102

2. Yan Fu, P. I. "Technology and Application of Making Artificial Cores by the Cementation of Quartzite and Colophony." *Science Technology & Engineering*. (2010)10, 28, 6998-7010.
3. Liang, Wanlin. "Study on preparing artificial cores." *Petroleum Instruments* (2008) 22, 2, 72-74.
4. Xu, Hongbo, et al. "Research and evaluation of the manufacturing methods of the mineral-wide simulated core in sandstone reservoir." *Offshore Oil* (2009) 29, 3, 19-25.
5. Xie Haojun, Li Aifen, Song Haopeng, Li Gangzhu "A New Method of Manufacturing Hydrophilic Artificial Core." *Science Technology & Engineering.* (2015) 15, 20, 234-237.
6. Zhou, Yingying, et al. "Preparation of Diethanolamine Modified Waterborne Epoxy Resin." *Paint & Coatings Industry* (2011)41.1:48-51.
7. Gans, Adam, and J. L. Corvec. "Epoxy core with expandable microspheres." US, EP2281680. 2011.
8. Shikha, Deepti, P. K. Kamani, and M. C. Shukla. "Studies on synthesis of water-borne epoxy ester based on RBO fatty acids." *Progress in Organic Coatings* (2003)47, 2, 87-94.

Tab 1. Properties of artificial cores

Core number	Length /mm	Diameter /mm	Gas Permeability /$10^{-3}\mu m^2$	Porosity	Processing mode	Wettability
W1	62.43	25.02	1453	0.352	-	water-wet
W2	59.40	24.96	1512	0.357	Soaked in kerosene for 48h	water-wet
W3	60.88	25.08	1478	0.353	Soaked in brine (5%wt) for 48h	water-wet
W4	21.02	24.88	1512	0.354	-	water-wet
O1	61.52	24.86	1450	0.353	-	oil-wet
O2	62.34	24.96	1489	0.355	Soaked in kerosene for 48h	oil-wet
O3	61.72	25.12	1503	0.354	Soaked in brine (5%wt) for 48h	oil-wet
O4	20.56	24.90	1485	0.358	-	oil-wet

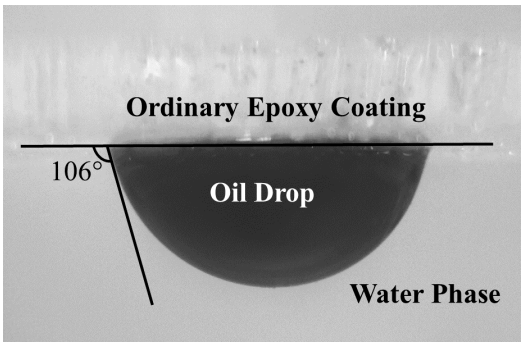

Fig 1. Contact angle on ordinary epoxy coating surface

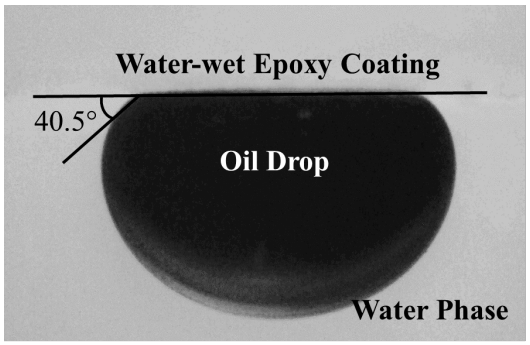

Fig 2. Contact angle on modified epoxy coating surface

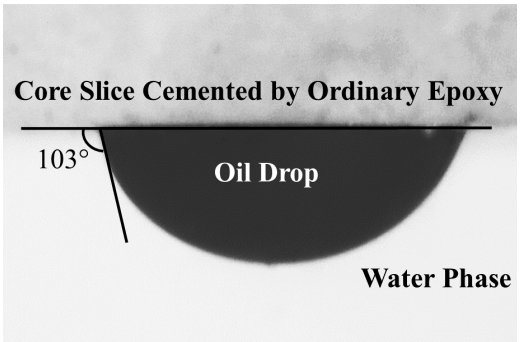

Fig 3. Contact angle on surface of core slice cemented by ordinary epoxy

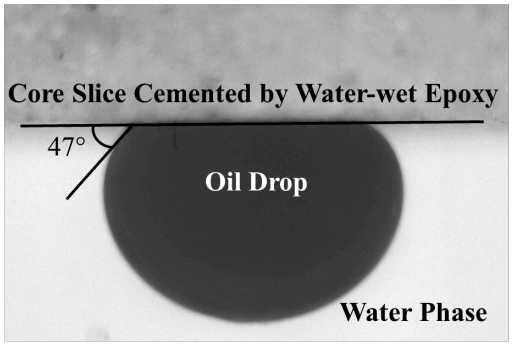

Fig 4. Contact angle on surface of core slice cemented by modified epoxy

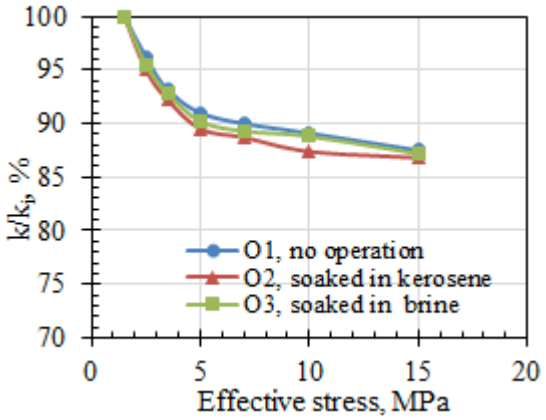

Fig 5. Stress sensitivity of oil-wet cores using ordinary epoxy

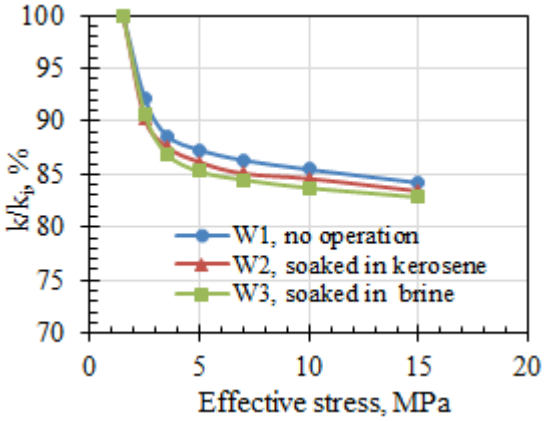

Fig 6. Stress sensitivity of water-wet cores using modified epoxy

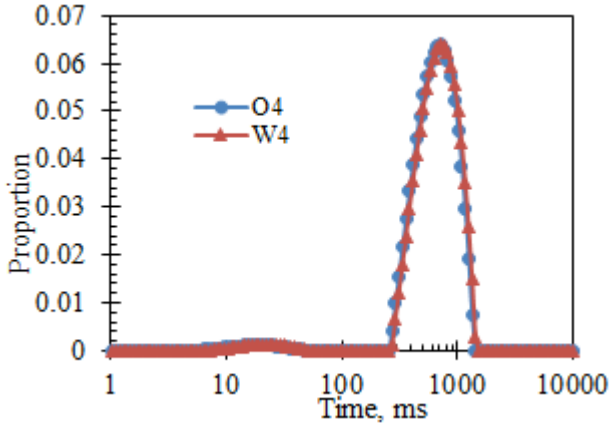

Fig 7. NMR result (proportion distribution) for two kind of cores

OFFSHORE WIRELINE CORING – CLOSING TECHNICAL AND ECONOMIC GAPS

Dave Whitby – Coring Technical Director
National Oilwell Varco, Drilling and Intervention, Coring Services

This paper was prepared for presentation at the International Symposium of the Society of Core Analysts held in Snowmass, Colorado, USA, 21–26 August 2016

ABSTRACT

Wireline retrievable coring has advanced markedly in recent years in terms of system reliability, core quality, application range, safety and general oilfield acceptance — especially in the unconventional sector. The industry has yet to fully exploit the information benefits and economic savings of wireline coring technologies for conventional reservoirs, in particular for offshore applications.

To properly communicate the positive attributes of wireline coring systems and ask why it is not employed more frequently in place of conventional cores, sidewall cores or electric wireline logging, the historical challenges and objections should be clearly laid out and examined properly from three key aspects: safety, core quality and technical limitation. For example, misconceptions around core degradation while tripping are unfounded given current knowledge around tripping programmes and the trip management resources available. The industry needs to reconsider what was once perhaps true, otherwise the cost- and time-saving benefits of reducing or replacing several conventional core trips per well will not be capitalised upon.

21st century coring industry and related tubular, wireline handling / surface pressure control, and fishing companies have developed solutions that may be applied to overcome past challenges, such as large bore drillpipe, drill collars, hydraulic and mechanical jars to allow for a larger core diameter; rotating and circulating arrangements for wireline surface pressure control and minimisation of differential sticking; slimhole electric wireline logging systems conveyed through the corehead; drilling insert technology that allows cycling infinitely between coring, drilling or logging as desired; and non-critical path core surface logging options.

Recent application of wireline coring technology offshore not only proves cores of excellent condition are obtainable, but that even with extremely conservative tripping practices, substantial economic savings can be realised, whilst at the same time delivering more useable bulk volume samples than any other coring method.

HISTORICAL CHALLENGES AND OBJECTIONS

Wireline Coring, also referred to as Continuous Coring, is the method by which core samples are cut downhole, similar to conventional coring, with the key difference being the method for recovering the core. As the name suggests, wireline cores are retrieved through the bottom-hole-assembly and drill string to surface by a wireline winching unit, negating the requirement to trip the entire drill string and BHA; this translates to much faster tripping – commonly at a retrieval rate average of around 70m/min. Many modern oilfield wireline coring systems also allow for the downhole fitment of a drilling insert that permits drilling ahead conventionally to further reduce drill pipe trips to core point, between core points or to drill to total depth.

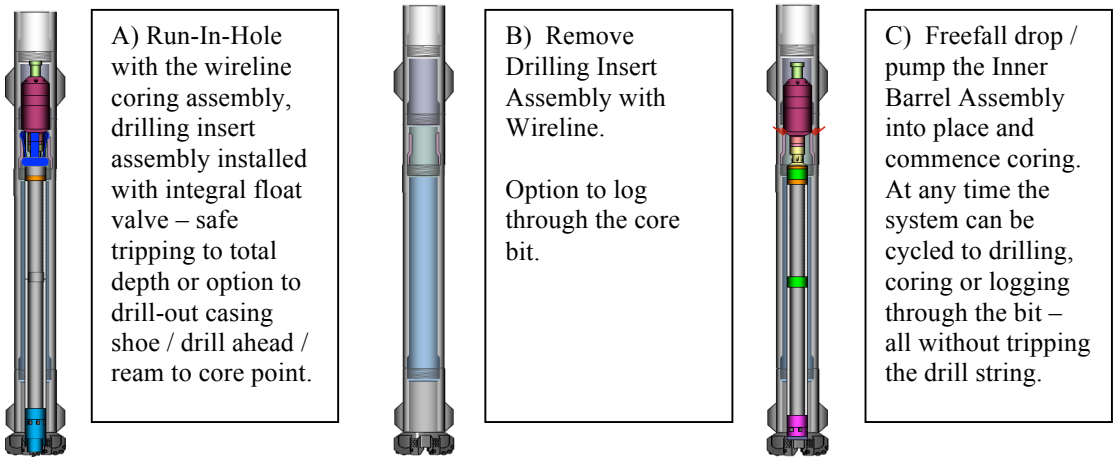

Figure 1. General Wireline Coring Operating Principle.

Perception is one of the largest challenges facing wireline coring acceptance in modern-day oilfield operations. Although large diameter rotary wireline retrievable coring technology was first introduced to the US oilfield in 1928 [1] and enjoyed popularity right up through the 1950s and 1960s [2], it was the mineral exploration sector that truly invested in and further developed the system for slimhole use from the 1950s onwards [3]. Some assume that wireline coring is non-oilfield in origin and therefore something to be viewed sceptically.

Numerous times in the late 20th century, there was some re-invention of small core diameter systems for operation within standard drill pipe and bottom hole assembly internal diameters, predominantly confined to use in land operations [4]. These systems saw limited success with many operators perceiving the 2 in. or smaller diameter cores [5, 6] to be of little analytical value. In addition to working within the confines of less than ideal diameter limitations, this translated to general system weaknesses, often evident when attempting long coring / drilling intervals (with drilling insert), hard or soft formation intervals, casing shoe drill-out, or limited inner assembly length capacity.

Operationally, wireline coring has often been at odds with established drilling practices, in particular concerning how to minimise the chances of differential sticking when the

drillstring is stationary during the core retrieval process [7], swabbing when retrieving the core [6], and means to effect general well control / cure losses with the lack of a float valve and or circulation sub in the bottom hole assembly. Additionally, surface pressure control equipment and the ability to pass through certain diameters, maintain sufficient working pressure capacity, rig-up time / cost, and ambiguous industry guidelines are all additional factors that in the past have attempted to push wireline coring aside as being too challenging.

From a sub-surface perspective, the coring industry in general has preached the importance of engineered trip-out rates to avoid cores being retrieved back to surface too quickly and suffering irreversible damage from gas break-out, in addition to the associated safety aspects of allowing venting and dissipation of gases released during the trip out of hole [6].

INDUSTRY SOLUTIONS

Driven primarily by the unconventional sector since the turn of the century, general wireline coring system specifications, capacities, diameters and associated technologies and processes have in most cases solved the challenges mentioned above, but have not been communicated adequately across to the exploration and appraisal stakeholders concerned with conventional and offshore operations that could benefit the most economically from wireline retrievable coring technology.

The ability to cut and recover large diameter wireline cores of up to 3 ½ in. diameter and 56m in length has been made possible by the innovation and investment of some key coring service providers, along with the ever increasing range of proprietary drillstring connections with large internal diameters available on rental strings and engineering efforts to produce mechanical and hydraulic coring jars / drill collars.

Although not specifically designed for wireline coring, there are a number of modern surface pressure control systems with certified working pressures of up to 15,000psi that are beneficial for offshore operators considering wireline coring. There are a wide range of configurations that offer the ability to circulate, rotate and or reciprocate drillpipe whilst wire is within the drillstring, reducing risks of differential sticking, cuttings pack-off, swabbing, and enabling safe retrieval of the inner barrel assembly; and well control at any point in the coring process.

Properly developed, tested and critically reviewed operational procedures based off risk assessment and hazard analysis then provide the remainder of controls to ensure a safe coring operation that delivers quality core. Some general examples include properly calculated circulation periods after each core is cut, tripping drillstring back inside the casing shoe where warranted, pulling the inner assembly to surface against swabbing calculations and core decompression programme, removal of the inner assembly from the surface arrangement, and well control procedures at each stage of the process.

REDUCING WELL CONSTRUCTION TIME, WHILST OBTAINING MORE CORE

Aside from the time-saving benefits of wireline coring versus conventional coring – especially over long intervals or where multiple trips are required — there are other less tangible savings that are no less significant:

1. More core can be taken for the same cost or less. In a conventional coring scenario, a conventional drill bit is used to drill out the casing shoe and onto core point, a round trip is required to core, then post coring another conventional drill bit trip is required to drill the electric logging rathole (even more costly is a sidetrack to core scenario). With this method, core point may be selected incorrectly due to the formation tops uncertainty, resulting in a wasted trip to core formation of little value, or could also result in core point being picked low, missing critical formation information (e.g. reservoir seal.). With wireline coring, the assembly has the capability to drill out the casing shoe and ahead to core point (drilling mode). Where there is depth uncertainty, coring can commence high to be sure to capture the interval of interest. The operation is economically favourable to do this as a full trip is already saved before coring commences. Once coring is finished, the drilling insert can be reinstalled to allow for drilling to TD / logging rathole, all with a single BHA trip.

   If deemed necessary, an electric, wireline-conveyed logging tool may be run out of the bottom of the coring assembly [12] to identify positional markers, or to log the target formation a mere hour or two after coring it — without tripping drillpipe.

2. The underexplored possibility of inverse logging (logging the core on surface as opposed to logging the borehole) [8], or at minimum reducing the number of suites required, can all be conducted off critical path and delivered in semi-real time, allowing for logging as coring / drilling is still in progress. This would also be a major boon for decision making. As each wireline core is retrieved to surface it can be instantly logged on a core exposed to mud for a very short period of time, as opposed to formation logged days later downhole.

   Some basic surface logging examples available include [8] gamma ray, magnetic susceptibility, infrared mineralogy, ultraviolet fluorescence, nuclear magnetic resonance porosity, pyrolysis, gas chromatography, digital photography / video, resistivity, P-wave velocity, and X-ray diffraction, not to mention the opportunity for obtaining immediate trimmed plug samples with the absolute minimum of filtrate invasion.

3. Smoother, constant rate tripping of the core (profiled trip out programme) with no setting of slips is beneficial to avoid damage to weak formation cores.

4. By not tripping pipe as often, certain projects in populated areas may be able to maintain 24 hour operations through reduced noise pollution.

5. By reducing trips, wear and tear on the drillstring and rig equipment is reduced in addition to minimising the potential for personnel injury during one of the most hazardous rig operations, tripping the drill string.

6. Wireline coring can eliminate the need for sidewall cores by taking cores on the fly and providing wider coverage over the drilled / cored interval.

Wireline coring also allows for jammed or problem core runs to be aborted and addressed in a matter of an hour or two as opposed to a similar issue with a conventional coring system being measured in days.

FUTURE OF WIRELINE CORING

Long term, the future of conventional and in particular wireline coring system technology is clear: real-time logging capability whilst coring [9, 10, 11, 13]. Other electronic real-time transmitted measurements such as jam detection, core position, pressure, temperature, downhole dynamics and general inner barrel behaviour are all expected to be forerunner coring technologies in the near term.

CONCLUSION

Wireline retrievable coring has developed into a simple, robust and reliable option for operators to obtain a larger volume of quality core samples safely and economically. The status quo of how formation evaluation is commonly applied across the industry should be called into question. More physical samples are always preferable over inferred electric log interpretation data, notwithstanding the associated "flat time" critical path time taken to wireline log the well and the fact that the data is often taken from the reservoir section days after it was drilled. The cost savings are tangible and have been proven onshore in thousands of wells. Though offshore uptake has been limited to date, favourable results and positive upsides are reported in those instances [10, 11, 12, 14].

ACKNOWLEDGEMENTS

Thanks to Alan Norrie (Senior Product Line Director for Coring) and Simon Wilde (Technical Support Manager for Dynamic Drilling Solutions – Australasia), both from National Oilwell Varco, for their valued assistance with this paper.

REFERENCES

1. Forbes R.J. and O'Beirne D.R., *The Technical Development of the Royal Dutch / Shell 1890 – 1940.* Brill, Leiden, The Netherlands, 1957, page 204.
2. Gow S. *Roughnecks, Rock Bits and Rigs: The evolution of oil well drilling technology in Alberta, 1883 - 1970.* University of Calgary Press, Calgary, Alberta, Canada. 2005. Page 248.

3. Boart Longyear Website, *Boart Longyear's 125 Year History.* http://www.boartlongyear.com/company/corporate-profile/history Accessed 11th April 2016. Section 1950 to 1970.
4. Warren T (SPE), Powers J (SPE), Bode D (SPE / Amoco), Carre E (SPE / Security DBS), Smith L (SPE / Security DBS). *Development of a Commercial Wireline Retrievable Coring System.* SPE 36536. SPE annual Technical Conference & Exhibition, Denver, Colorado 6th to 9th October 1996. Page 1.
5. Rowley D.S. *Vertical and Horizontal Coring and Sampling.* (*Background Papers for Drilling Technology Workshop* – Park City, Utah. 25th to 27th June 1975*)* National Academy of Sciences, Washington, D.C. 1975. Page 145
6. American Petroleum Institute, Exploration and Production Department, *Recommended Practice for Core Analysis – Recommended Practice 40*. 2nd Edition, February 1998. Pages 1-4 and 2-4.
7. Randolph S.B. (Amoco Production Co.) and Jourdan A.P. (Elf Aquitaine) *Slimhole Continuous Coring and Drilling in Tertiary Sediments*. SPE / IADC 21906. SPE / IADC Drilling Conference 1991. Page 1.
8. Spain D.R, Morris S.A, Penn, J.T. *Automated Geological Evaluation of Continuous Slim-Hole Cores.* SPE 23577. Amoco Production Company Research Centre, Tulsa, Oklahoma. 1991.
9. Fate T. ChevronTexaco. *DI-110 – Deepwater Improved Coring Efficiency with Real-Time Data Collection.* Drilling Engineering Association (DEA), presented 19th Feb 2004. Website accessed 12th April 2016. http://dea-global.org/?p=609
10. Goldberg D, Myers G – Lamont Doherty Earth Observatory. Grigar K, Pettigrew T – Texas A&M University. Mrozewski S, Arceneaux C, Collins T – Schlumberger D & M and Shipboard Scientific Party, ODP Leg 204. *Logging-while-Coring, New Technology Advances Scientific Drilling.* SPWLA, 2003.
11. Van Puymbroeck L. G, Deshotels K, Fletcher D - Baker Hughes INTEQ. *A Technology to Selectively Core and Drill with Realtime Wireline Retrievable MWD Applied in Deepwater.* AADE 01-NC-HO-03. AADE National Drilling Conference, "Drilling Technology, The Next 100 years", Omni, Houston, Texas. 27th to 29th March 2001.
12. Shankel C.P, Chachula R – EnCana Corp. *Improved Decision Making During Drilling Operations: Using a Wireline Coring System, Offshore Brazil.* SPE 97615. SPE Latin America and Caribbean Petroleum Engineering Conference, Rio De Janeiro, Brazil. 20th to 23rd June 2005.
13. Myers G, Keogh W, Masterson W – Lamont-Doherty Earth Observation; Schroeder D, Grigar K – Texas A&M University. *Coring Dynamics; Data Acquisition While Coring.* OTC 17920. Offshore Technology Conference, 1st to 4th May 2006.
14. Performance Summary, *Corion Express 4.0 – Premium Wireline Coring – SFNY-1040.* http://www.docfoc.com/corion-express-4-0-performance-summary-sfny-1040 Accessed 20th April 2016.